

**Preclinical Evaluation of Protein Disulfide Isomerase Inhibitors for the Treatment of Glioblastoma**

By

Andrea Shergalis

A dissertation submitted in partial fulfillment  
of the requirements for the degree of  
Doctor of Philosophy  
(Medicinal Chemistry)  
in the University of Michigan  
2020

Doctoral Committee:

Professor Nouri Neamati, Chair  
Professor George A. Garcia  
Professor Peter J. H. Scott  
Professor Shaomeng Wang

Andrea G. Shergalis

ashergal@med.umich.edu

ORCID 0000-0002-1155-1583

© Andrea Shergalis 2020

All Rights Reserved

## ACKNOWLEDGEMENTS

So many people have been involved in bringing this project to life and making this dissertation possible. First, I want to thank my advisor, Prof. Nouri Neamati, for his guidance, encouragement, and patience. Prof. Neamati instilled an enthusiasm in me for science and drug discovery, while allowing me the space to independently explore complex biochemical problems, and I am grateful for his kind and patient mentorship. I also thank my committee members, Profs. George Garcia, Peter Scott, and Shaomeng Wang, for their patience, guidance, and support throughout my graduate career. I am thankful to them for taking time to meet with me and have thoughtful conversations about medicinal chemistry and science in general.

From the Neamati lab, I would like to thank so many. First and foremost, I have to thank Shuzo Tamara for being an incredible, kind, and patient teacher and mentor. Shuzo is one of the hardest workers I know. In addition to a strong work ethic, he taught me pretty much everything I know and laid the foundation for the article published as Chapter 3 of this dissertation. The work published in this dissertation really began with the initial identification of PDI as a target by Shili Xu, and I am grateful for his advice and guidance (from afar!). His preliminary experiments to validate PDI as a target made this work possible. I must thank all of the co-authors of the work in this dissertation, including Ana Kyani, Bikash Debnath, and Armand Bankhead III for their assistance with computational chemistry and bioinformatic analysis, Soma Samanta for her guidance, Yuting Kuang for her graduate school advice, and Urarika Luesakul for teaching me how to make really cool figures in Adobe Illustrator. Ding Xue and Suhui Yang were the lead chemists responsible for synthesizing and characterizing most of the compounds for my

dissertation, and I am forever grateful for their triumphs and struggles. Dan Lu, Ziwei Liu, Shuai Mao, and Yuning Shen also prepared compounds and were very helpful. Additionally, Christine Cuthbertson, Shuai Hu, and Maha Hanafi are incredible lab mates and survivors. All of the postdoctoral researchers in the Neamati lab over the years, including Tiangong Lu and Yibin Xu, have been incredibly helpful and have brought a bright and cheerful atmosphere into the lab. Of course, much of this would not be possible without the help of all the talented undergraduate students in the Neamati lab, including Kirin Cromer, Hannah Driks, and Amina Tanweer, who sacrificed time they could be studying to come in and perform screening campaigns.

I also want to thank our collaborators, specifically Bonnie Liu, an incredibly talented biochemist, for preparing many of the cell lines and biochemical tools that we used to study PDI, Jenn Schmidt, for helping me with protein mass spectrometry experiments, and the Ljungman lab for all their Bru-seq efforts. I want to extend a special thank you to the members of the Stuckey lab, including Dr. Stuckey, Jennifer Meagher, Elyse Petrunak, and Pryia Chinnaswamy for teaching me the basics of crystallography and being an amazing support system as I troubleshooted my crystallography project (even though I never succeeded).

Finally, I want to thank my fiancé for his patience and support. I could not have done this without him. My parents have also been very supportive, even though I am pretty sure they still think I am just getting a master's degree. Furthermore, volleyball and soccer games were a welcome break from the lab, and, in addition to lab mates, Nick Ragazzone, Lindsey Drake, Amy Fraley, Sumit Bandekar, Sarah Burris, and everyone in our cohort made graduate school more fun.



## Table of Contents

ACKNOWLEDGEMENTS .....	ii
LIST OF FIGURES .....	v
LIST OF TABLES .....	x
LIST OF ABBREVIATIONS.....	xii
ABSTRACT.....	xv
CHAPTER I Current Challenges and Opportunities in Treating Glioblastoma.....	1
CHAPTER II Protein Disulfide Isomerase .....	75
CHAPTER III Discovery and Mechanistic Elucidation of a Class of PDI Inhibitors for the Treatment of Glioblastoma .....	96
CHAPTER IV Design, Synthesis, and Biological Evaluation of Novel Allosteric Protein Disulfide Isomerase Inhibitors.....	131
CHAPTER V Characterization of Alpha-Aminobenzylphenol Analogues in Glioblastoma Cell Lines.....	188
CHAPTER VI Concluding Summary.....	264

## LIST OF FIGURES

### Figure

Figure I-1 Classification of brain tumors as reported from the Central Brain Tumor Registry of the United States. ....	6
Figure I-2 Common characteristics of glioblastoma.....	8
Figure I-3 Canonical gliomagenesis mediators EGFR, P53, and RB1 are important for cancer signaling.....	9
Figure I-4 Signaling pathways involving membrane proteins upregulated in GBM as determined by LC-MS/MS and iTRAQ.....	11
Figure I-5 Twenty genes associated with reduced survivability in the TCGA GBM patient cohort profiled with RNASeq expression data.....	15
Figure I-6 Hierarchical clustering of 20 genes .....	17
Figure I-7 Expression of 20 genes significantly associated with reduced survivability in GBM across 33 TCGA diseases.....	22
Figure I-8 The blood-brain barrier protects the brain from foreign material with a layer of endothelial cells bound by adherens junctions (i.e. vascular endothelial (VE)-cadherin) and tight junctions (i.e. junction adhesion molecules (JAMs), endothelial cell adhesion molecule (ESAM), claudins, and occludins).....	42
Figure I-9 CNS MPO Version 2 scores were calculated for 73 GBM drug candidates. ....	46

Figure II-1 Domain structure of PDI family members. ....	80
Figure II-2 PDI structure.....	81
Figure II-3 Role of PDI in the endoplasmic reticulum. ....	83
Figure II-4 Multifunctional roles of the PDI family. ....	84
Figure II-5 PDI plays an important role in various disease states. ....	87
Figure III-1 Discovery of <b>35G8</b> .....	99
Figure III-2 <b>35G8</b> destabilizes PDI.....	100
Figure III-3 DFO decreases the potency of <b>35G8</b> . ....	105
Figure III-4 Effects of <b>35G8</b> treatment on cellular pathways.....	108
Figure III-5 Effect of <b>35G8</b> treatment on RNA synthesis in U87MG cells.....	110
Figure III-6 ROS induction of <b>35G8</b> analogues at (A) 4 hours, (B) 6 hours, and (C) 24 hours. ....	111
Figure III-7 PAINS characteristics of <b>35G8</b> do not interfere with PDI activity in the insulin turbidity assay. ....	113
Figure III-8 Venn diagram for the genes with greater than two-fold change in <b>35G8</b> and erastin treatments.....	116
Figure IV-1 Chemical structures of chalcones that have been marketed or clinically tested, and the hit compound <b>BAP2</b> as a PDI inhibitor. ....	133
Figure IV-2 Summarized SAR of synthesized <b>BAP2</b> analogues.....	145
Figure IV-3 Optimized <b>BAP2</b> analogues inhibit colony formation and PDI activity. ....	150
Figure IV-4 Optimized <b>BAP2</b> analogues stabilize PDI.....	153
Figure IV-5 <b>BAP2</b> analogues inhibit protein synthesis via EIF2 $\alpha$ pathway.....	154
Figure IV-6 <b>BAP2</b> analogues inhibit cell migration in a dose-dependent manner.....	156

Figure IV-7 <b>BAP2</b> analogues induce transcription of ER stress genes and downregulate DNA damage response genes <i>RAD51</i> and <i>E2F1</i> .....	158
Figure IV-8 Upregulated GSEA of <b>18</b> treatment.....	159
Figure IV-9 Downregulated GSEA of <b>18</b> treatment.....	160
Figure IV-10 Upregulated GSEA of <b>46</b> treatment.....	160
Figure IV-11 Downregulated GSEA of <b>46</b> treatment.....	161
Figure IV-12 GSEA analysis of proteome perturbation by <b>BAP2</b> and <b>18</b> reveals increased expression of G2M checkpoint and arsenic trioxide response and reduced expression of proteins involved in ribosome and DNA replication.....	162
Figure IV-13 <b>BAP2</b> analogues synergize with As <sub>2</sub> O <sub>3</sub> .....	163
Figure IV-14 <b>BAP2</b> and analogue <b>68</b> synergize with radiation to inhibit clonogenic growth. ..	164
Figure IV-15 <b>BAP2</b> analogues interact with the b' domain of PDI.....	166
Figure IV-16 <b>BAP2</b> analogues interact with the b' domain of PDI.....	167
Figure V-1 Previously reported PDI inhibitors studied in the context of ovarian cancer ( <b>PACMA31</b> ), Huntington's disease ( <b>LOC14</b> ), brain cancer ( <b>BAP2</b> and <b>35G8</b> ), thrombosis ( <b>Bepristat 1a</b> and <b>isoquercetin</b> ), and multiple myeloma ( <b>CCF642</b> ).....	190
Figure V-2 Discovery and characterization of <b>AS15</b> and <b>CD343</b> .....	193
Figure V-3 <b>AS15</b> selectivity for PDIA1.....	194
Figure V-4 Structure-activity relationship analysis of <b>AS15</b> analogues in the PDI reductase assay. .....	196
Figure V-5 Activity of additional <b>AS15</b> analogues in the PDI reductase assay (IC <sub>50</sub> ) and MTT assay (in U87MG cells). .....	204

Figure V-6 SAR indicates that compounds are covalent PDI inhibitors. ....	214
Figure V-7 Spectrum of inactive <b>AS15</b> analogue, <b>DX1-69</b> .....	215
Figure V-8 Recovery of PDI activity upon treatment with <b>PACMA31</b> (A), <b>BAP2</b> (B), <b>AS15</b> (C), or <b>CD343</b> (D).....	217
Figure V-9 N-Acetyl cysteine and glutathione inactivate <b>AS15</b> analogues. ....	218
Figure V-10 Dimerized analogue is less sensitive to GSH treatment.....	221
Figure V-11 Colony formation assay of PDI inhibitors in combination with BSO in (A) U118MG and (B) A172 cells. ....	223
Figure V-12 <b>AS15</b> analogues bind serum albumin.....	225
Figure V-13 Activity of <b>DX3-159</b> against wild-type PDIA1 in the PDI reductase assay .....	226
Figure V-14 <b>DX3-159B</b> protein band migrates higher than PDI.....	226
Figure V-15 DTT outcompetes <b>DX3-173B</b> for binding to PDI.....	227
Figure V-16 <b>AS15</b> analogues bind multiple proteins. ....	228
Figure V-17 <b>DX3-59</b> competition with BODIPY-labeled probe.....	229
Figure V-18 Competitive inhibition of BODIPY-labeled <b>AS15</b> analogue.....	230
Figure V-19 Competitive inhibition of 20 $\mu$ M BODIPY-labeled <b>AS15</b> analogue in BSA. ....	230
Figure V-20 Cell-based binding of BODIPY-labeled <b>AS15</b> analogues <b>DX3-159</b> (left) or <b>DX3-173B</b> (right) in U118MG cells in the presence of 20 $\mu$ M BSO or 10 % FBS. ....	231
Figure V-21 Confocal microscopy images at 60X magnification of A172 cells treated with 10 $\mu$ M <b>DX3-159B</b> (A) or 2 $\mu$ M <b>DX3-173B</b> (B) for 24 h prior to fixation and staining for PDI.....	242
Figure V-22 <b>DX1-202</b> upregulates transcription of genes involved in the unfolded protein response.....	244

Figure V-23 Compound <b>DX1-202</b> treatment.....	245
Figure VI-1 Potential drivers of GBM tumors based on TCGA analysis.....	269
Figure VI-2 PDI modulators in different diseases .....	270
Figure VI-3 Discovery of <b>35G8</b> as a PDI inhibitor .....	271
Figure VI-4 Lead compound <b>BAP2</b> optimization .....	272
Figure VI-5 Identification of <b>AS15</b> analogues that covalently bind PDI .....	273

## LIST OF TABLES

### Table

Table I-1 Gene descriptions from DAVID bioinformatics database .....	18
Table II-1 Function and subcellular localization of 22 PDI isoforms .....	78
Table III-1 PDI inhibitory activity of <b>35G8</b> analogues .....	101
Table III-2 <i>In vitro</i> cytotoxicity of <b>35G8</b> analogues in a panel of human glioblastoma cell lines .....	104
Table III-3 Cell death rescue from <b>35G8</b> treatment.....	105
Table IV-1 PDI inhibitory activity of the synthesized <b>BAP2</b> derivatives <b>5-36<sup>a</sup></b> .....	139
Table IV-2 PDI inhibitory activity of the synthesized <b>BAP2</b> derivatives .....	141
Table IV-3 PDI inhibitory activity of the synthesized <b>BAP2</b> derivatives .....	144
Table IV-4 Cytotoxicity of the 23 selected <b>BAP2</b> analogues in a panel of human GBM cell lines <sup>a</sup> .....	147
Table IV-5 Cytotoxicity of 6 <b>BAP2</b> analogues in a human fibroblast cell line HFF-1 .....	149
Table V-1 SAR of compounds with 5-hydroxybenzo[ <i>d</i> ][1,3]dioxole and saturated cyclic amine moieties.....	197
Table V-2 SAR of compounds with 5-hydroxy benzo[ <i>d</i> ][1,3]dioxole and other amine moieties .....	199
Table V-3 SAR of compounds with 8-hydroxyquinoline and 2-aminopyridine moieties.....	201

Table V-4 SAR of compounds with 8-hydroxyquinoline and aniline moieties.....	203
Table V-5 SAR of compounds lacking the tertiary amine.....	205
Table V-6 SAR of Type I compounds .....	208
Table V-7 SAR of Type II compounds.....	210
Table V-8 SAR of Type III compounds .....	211
Table V-9 Percent inhibition of <b>AS15</b> analogues in the absence or presence of 5 mM GSH in the PDI reductase assay .....	219
Table V-10 Most abundant proteins around 40 kDa in A172 cells .....	233
Table V-11 Most abundant proteins around 55 kDa in A172 cells .....	235
Table V-12 Most abundant proteins around 57 kDa in A172 cells .....	237
Table V-13 PDI family members and molecular weight .....	239
Table V-14 Known targets of similar inhibitors.....	240
Table V-15 STRING process terms for significantly affected genes upon <b>DX1-202</b> treatment.	245
Table V-16 Top 25 compounds that positively correlate with <b>DX1-202</b> treatment in CMap. ...	247
Table V-17 Top 25 compounds that negatively correlate with <b>DX1-202</b> treatment in CMap. ..	248



## LIST OF ABBREVIATIONS

GBM – Glioblastoma

CNS – Central nervous system

TCGA – The Cancer Genome Atlas

FDA – Food and Drug Administration

IC50 - Half maximal inhibitory concentration

PDI – Protein disulfide isomerase

SAR – Structure activity relationship

PAINS – Pan-assay interference compounds

BSO – Buthionine sulfoximine

GPCR – G protein-coupled receptor

BBB – Blood-brain barrier

MGMT – O-6-Methylguanine-DNA methyltransferase

VEGF – Vascular endothelial growth factor

RB – Retinoblastoma

RTK – Receptor tyrosine kinase

PI3K – Phosphoinositide 3-kinase

AKT – Protein kinase B

EGFR – Epidermal growth factor receptor

RPPA – Reverse phase protein array

MAPK – Mitogen-activated protein kinase

IDH1 – Isocitrate dehydrogenase 1

ATRX – ATP-dependent helicase ATRX, X-linked helicase II

HIST1H3A – Histone cluster 1 H3 family member A

NF1 – Neurofibromin 1

NF- $\kappa$ B – Nuclear factor kappa-light-chain-enhancer of activated B cells

PDGFRA – Platelet derived growth factor receptor alpha

CSF – Cerebrospinal fluid

2-HG – 2-hydroxyglutarate

RSEM – RNA-seq by expectation maximization

ROS – Reactive oxygen species

2DGE – Two-dimensional gel electrophoresis

GEMM – Genetically engineered mouse models

ClogP – Calculated partition coefficient

TKI – Tyrosine kinase inhibitor

ER – Endoplasmic reticulum

UPR – Unfolded protein response

ERO1 – Endoplasmic reticulum oxidase 1

FAD – Flavin adenine dinucleotide

PERK – Protein kinase RNA-like endoplasmic reticulum kinase

eIF2 $\alpha$  – Eukaryotic initiation factor 2 alpha

GRP78 – Glucose-regulated protein 78

PRDX4 – Peroxiredoxin 4

DARTS – Drug affinity responsive target stability

CETSA – Cellular thermal shift assay

DAVID – Database for annotation, visualization and integrated discovery

GSEA – Gene set enrichment analysis

## ABSTRACT

Cancer cells require increased rates of protein synthesis to sustain rapid cell growth and proliferation. Increased secretory and membrane protein synthesis relies on an upregulation of the translational and protein folding machinery in the endoplasmic reticulum to aid tumor growth. For example, many critical cancer signaling kinases, such as EGFR (epithelial growth factor receptor), function as membrane proteins. Protein disulfide isomerase (PDI) is the major enzyme responsible for disulfide bond formation in the endoplasmic reticulum, and knockdown of PDI halts tumor progression. Thus, the goal of this dissertation project was to identify novel PDI inhibitors and provide an extensive preclinical evaluation of their activity for the treatment of cancer, specifically glioblastoma.

Through a phenotypic screening approach, we identified the pyrimidotriazinedione **35G8** as a potent cytotoxic agent that inhibited PDI. Because of its known pan-assay interference (PAINS) properties, we first validated that the activity of **35G8** was not due to its redox cycling characteristics and used a variety of assays to confirm PDI inhibition. **35G8** destabilized PDI in cell-based target-engagement assays and had a transcriptomic profile similar to PDI knockdown. These results demonstrated the ability of **35G8** to inhibit PDI and potently kill cancer cells.

The chalcone **BAP2** was also identified through a phenotypic screening approach, and an initial structure-activity relationship (SAR) campaign with 67 analogues revealed important binding characteristics that allowed us to hypothesize that the compounds were binding in the b' domain of PDI. Mutation of His256 to Ala abolished **BAP2** activity and confirmed the binding hypothesis. Furthermore, **BAP2** and analogues inhibit glioblastoma cell growth, induce ER stress, increase expression of G2M checkpoint proteins, and reduce expression of DNA repair proteins. **BAP2** and analogues also sensitized glioblastoma (GBM) cells to radiation. These results establish the **BAP2** series as PDI inhibitors and support their further study as a novel strategy to treat glioblastoma.

Finally, a manual biochemical screen of over 1,000 compounds in the PDI reductase assay produced a benzyl-benzodioxole, **AS15**, as a potent hit with an IC<sub>50</sub> value under 1 μM. SAR analysis was performed with over 100 analogues of **AS15**. The SAR indicated that the compounds were binding PDI via a retro-Michael addition onto the cysteines, and protein mass spectrometry confirmed covalent binding. Cytotoxicity of the **AS15** analogues was improved when combined with glutathione synthesis inhibitor buthionine sulfoximine (BSO), which confirmed that PDI competed with glutathione for binding the **AS15** series in the cells. Thus, this study provides an excellent foundation to build analogues that are less sensitive to glutathione and more selective for PDI in the cells.

The work as a whole provides an extensive characterization of PDI inhibition and its role in cancer. We were able to provide extensive preclinical evaluation of lead PDI inhibitors identified from medium throughput screens. This work provides the foundation for a guided optimization of the PDI inhibitors discovered to further improve the potency and selectivity of the compounds and design a PDI inhibitor for testing in clinical trials.

## CHAPTER I

### Current Challenges and Opportunities in Treating Glioblastoma

#### Introduction<sup>1</sup>

Glioblastoma (GBM) is the most malignant primary central nervous system tumor, and the prognosis for patients is often bleak. Currently, there are no curative treatment options for GBM, and despite rigorous therapeutic research, the survival rate of patients diagnosed with GBM remains low. Median overall survival is 15-23 months and five-year survival is less than 6 %, which is the lowest long-term survival rate of malignant brain tumors.<sup>1</sup> An estimated 79,270 new cases of primary brain and other central nervous system (CNS) tumors were expected to be diagnosed in 2017.<sup>1</sup> To improve therapeutic options, studies to identify and validate single protein targets are underway. However, in most cases, targeted compounds that perform well in preclinical studies have failed expensive Phase III clinical trials in humans. Ultimately, several major factors are responsible for drug failure, including poor pharmacokinetic properties, emergence of resistance pathways, complex intratumoral heterogeneity, and suboptimal clinical trial design. Thus, there is a desperate need for an efficient approach to identify and vet potential drugs at the preclinical stage, to prevent late stage failure. Genomic- and proteomic-scale analysis can identify

---

<sup>1</sup> This work has been published and is being reprinted with permission from Shergalis, A., Bankhead, A., Luesakul, U., Muangsin, N., & Neamati, N. (2018). Current challenges and opportunities in treating glioblastoma. *Pharmacological reviews*, 70(3), 412-445.

**Author contributions:** Andrea Shergalis was the primary author, Armand Bankhead III generated figures I-5, I-6, and I-7. Urarika Luesakul generated figure I-10. Nouri Neamati is the corresponding author.

proteins and pathways involved in the development of chemotherapeutic resistance mechanisms responsible for recurrent disease.

With the advent of TCGA (The Cancer Genome Atlas) consortium and resources, genomic analysis of cancers is at the forefront of drug discovery. Additionally, proteomics is gaining widespread use in drug discovery efforts. Quantitative proteomics can measure the expression and, in some cases, post-translational modification status of up to and over 8,000 proteins in the cell at any given time. The advent of novel proteomic techniques in the last decade, in tandem with the resources allocated to address the lack of a cure for GBM, will accelerate the discovery of a treatment and shed light on the feasibility of precision medicine.

The target and mechanism of action of many Food and Drug Administration (FDA)-approved drugs are not fully established. Of the approximately 1,600 FDA-approved drugs with known targets, most belong to four classes: GPCRs (33 %), ion channels (18 %), nuclear receptors (16 %), and kinases (3 %).<sup>2</sup> This suggests uncharted proteomic space exists in which novel drug targets may be identified. Of the six drugs approved for the treatment of GBM, three act as DNA alkylators, two are kinase inhibitors, and one is a tubulin inhibitor. Burgeoning research efforts in novel treatment areas, including alternating electric field therapy (tumor-treating fields), immunotherapy, and antibody-drug conjugates are improving patient outcomes. Much of the challenge in developing a GBM therapy lies in reaching therapeutic concentrations at the target site. Few drug molecules cross the blood-brain barrier (BBB), and those that do may be exported via efflux pumps. Therefore, valid target selection, permeability, and drug pharmacokinetics are important considerations in GBM drug design.

In this review, we highlight the importance of genomic and proteomic research on identifying novel biomarkers and drug targets for GBM treatment. Additionally, we demonstrate a genomic approach to drug discovery and uncover novel potential drug targets by performing bioinformatics analysis of TCGA data. While further validation is necessary and increased expression of some of these targets may be a response to oncogenic stress, this approach provides a list of proteins that, if inhibited alone or in combination with other targets, could effectively treat GBM. Furthermore, we address the challenges faced in the drug discovery and delivery process and discuss potential solutions to those problems. In particular, we focus on the challenge of BBB permeability, nanocarrier design, and the application of computational methods to aid compound optimization. In recent years, major clinical trials for small molecule treatment of GBM have failed because the compounds did not reach effective concentrations in the brain (i.e. gefitinib and erlotinib).<sup>3, 4</sup> Thus, an understanding of BBB function and physiology is crucial for the development of efficacious small molecule treatment strategies and the avoidance of failed expensive clinical trials. The lack of effective treatment options for GBM emphasizes the unmet need for successful target inhibition and drug delivery strategies.

### **Current treatment options for glioblastoma**

Upon diagnosis, GBM treatment includes maximal surgical resection, followed by temozolomide and radiation.<sup>5</sup> Due to the invasive nature of GBM, surgical resection rarely eliminates all tumor cells, and post-surgical treatment is usually necessary to prevent recurrence. Treatment varies based on the age of the patient and stage of the disease. Depending on the overall health of the patient and disease status, they may also be enrolled in relevant ongoing clinical trials.



The standard-of-care temozolomide is a DNA-alkylating agent discovered in the 1970s and approved in 2005 by the FDA to treat newly diagnosed brain tumors. The first clinical trial with temozolomide was conducted in 1993, and, of the ten patients who received adjuvant temozolomide, five patients showed significant clinical and radiographic improvement.<sup>6</sup> The success of this initial study prompted further successful studies of temozolomide treatment in GBM patients. In these studies, subsets of patients were more responsive to temozolomide treatment than others. Responsive patients had methyl-guanine-methyltransferase (*MGMT*) genes with methylated promoters and showed higher survival rates than patients with hypomethylated *MGMT* genes.<sup>7</sup> *MGMT* is a DNA repair enzyme that repairs the N7 and O6 positions of guanine alkylated by temozolomide. While *MGMT* depletion does not seem to be an effective treatment strategy,<sup>8,9</sup> *MGMT* gene methylation status nevertheless remains an important biomarker for GBM prognosis. Although temozolomide is part of the standard chemotherapeutic regimen for GBM, it presents unwanted toxicity and does not eliminate the disease. As an alternative approach, targeted therapies may limit unwanted toxicity and more effectively block tumor proliferation.

A promising targeted treatment is the anti-vascular endothelial growth factor (VEGF) monoclonal antibody bevacizumab. Bevacizumab was first approved by the FDA in 2004 to treat metastatic colorectal cancer. Since then, it has been approved for several different types of cancer, including GBM in 2009. Angiogenesis is a key survival feature of many cancers as tumors rely on nutrients from the vasculature to proliferate. VEGF is a broad mediator of tumor neovascularization, and VEGF expression is linked with GBM tumorigenicity.<sup>10</sup> Bevacizumab was first tested in 21 patients with malignant glioma in 2004. Patients were treated with bevacizumab at 5 mg/kg and irinotecan at 125 mg/m<sup>2</sup> every two weeks producing a significant 43 % response

rate.<sup>11</sup> However, the Phase III “Avaglio” trial, conducted on 921 patients with newly diagnosed GBM, resulted in no overall survival benefit in bevacizumab-treated versus placebo-treated patients (median overall survival of 16.8 months for bevacizumab-treated patients and 16.7 months for placebo-treated patients).<sup>12</sup> A second Phase III trial, the RTOG 0825 trial, produced similar results. Out of 637 patients receiving either 10 mg/kg bevacizumab every two weeks or placebo, there was no significant difference in overall survival between the two groups (median overall survival of 15.7 months for bevacizumab-treated patients vs. 16.1 months for the placebo group).<sup>13</sup> Therefore, bevacizumab treatment is an option reserved for patients with recurrent GBM.

Almost all GBM tumors that respond to first-line therapy recur. There is no standard approach for a successful treatment of recurrent GBM. Second-line treatment may take several directions, depending on factors such as tumor size and location, previous treatments, age, and time from initial diagnosis. Treatment can include surgical resection, reirradiation, nitrosoureas, temozolomide rechallenge, bevacizumab, or tyrosine kinase inhibitors.<sup>14</sup> Even with these treatments, median overall survival after recurrence is 6.2 months.<sup>15</sup> In a Phase II study that led to conditional FDA approval, the longest median progression-free survival (5.6 months) was seen with a combination of bevacizumab and irinotecan,<sup>16</sup> while longest overall survival (12 months) resulted from CCNU + bevacizumab.<sup>17</sup>

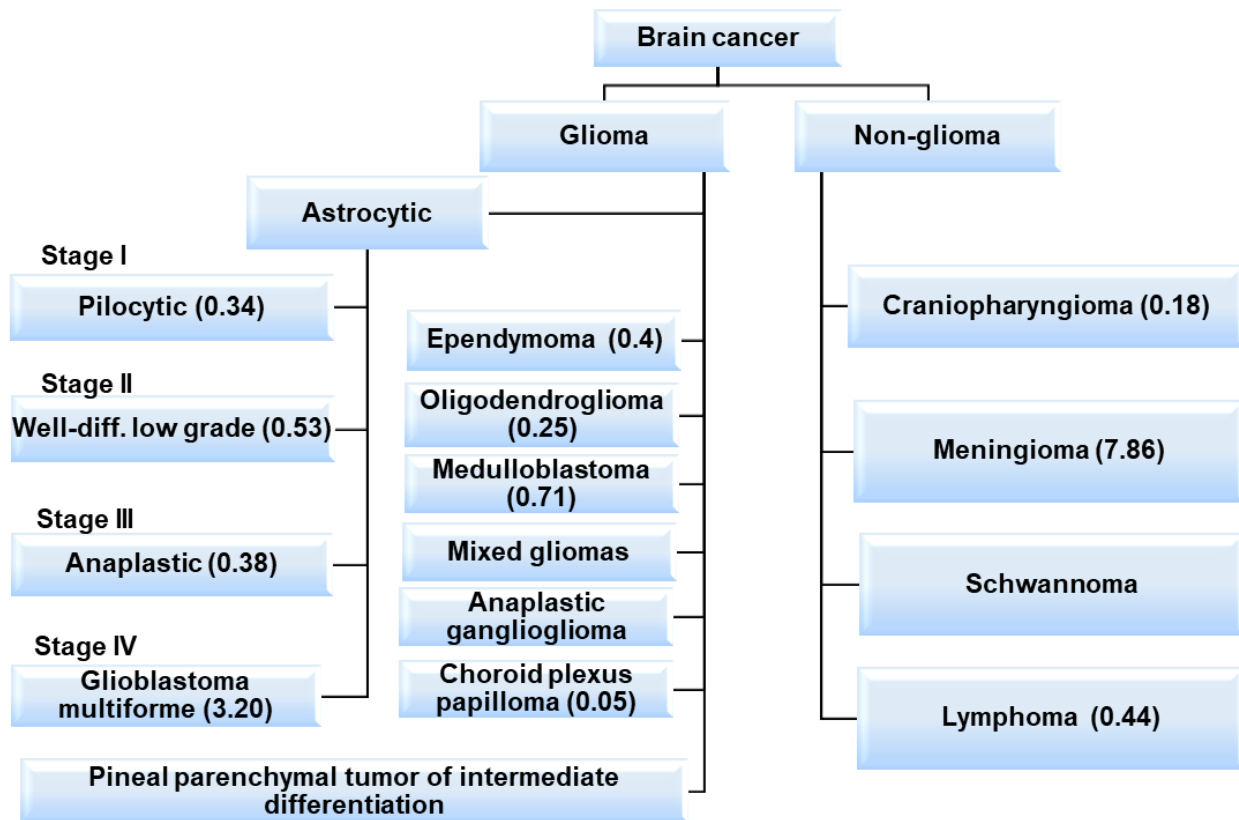


Figure I-1 Classification of brain tumors as reported from the Central Brain Tumor Registry of the United States.<sup>18</sup> Numbers in parentheses indicate incidence or cases per 100,000 individuals and are age-adjusted to the 2000 United States standard population.

### Molecular diagnostic signature of glioblastoma

Glioblastoma is a grade IV glioma and the most malignant astrocytoma (Figure I-1).<sup>19</sup> GBM tumors consist of a complex mixture of heterogeneous cells, complicating the search for the cell of origin. Previously, GBM was thought to originate from neural stem cells. However, studies have suggested that gliomas may differentiate directly from progenitor cells, and the type of progenitor cell each tumor originates from dictates their chemosensitivity.<sup>20</sup> Until recently, GBM tumors have been diagnosed histologically and are characterized by increased cell density, abnormal cell types (atypia), areas of necrosis, and robust angiogenesis (Figure I-2). This

histological diagnosis hinders therapeutic approaches at personalized therapy. TCGA project improved characterization of GBM tumors with whole genome sequencing and identified key oncogenic signaling pathways to further classify tumor types. The molecular aberrations required for gliomagenesis include: mutations in the P53, retinoblastoma (RB), and receptor tyrosine kinase (RTK)/Ras/phosphoinositide 3-kinase (PI3K)/protein kinase B (AKT) signaling pathways (Figure I-3).<sup>21</sup> RB and P53 are tumor suppressors that lose function in several cancers.<sup>22, 23</sup> Additionally, epithelial growth factor receptor (EGFR) expression is amplified in some GBM tumors, leading to increased cell proliferation through the RTK/Ras/PI3K/AKT signaling pathway.<sup>24</sup> Through TCGA project, tumors were also profiled with Reverse Phase Protein Array (RPPA), a high-throughput technique similar to Western blotting that detects and quantifies protein expression levels. Out of 171 antibodies, 127 correlated with transcriptomal subtype, and signaling pathway alterations were confirmed, including increased EGFR, Notch1, and Notch3 expression and activated MAPK pathway signaling.<sup>21</sup> While this is a useful tool, only 171 antibodies were used in this study and therefore only 171 gene products could be profiled, providing a limited scope of potential novel drug targets. TCGA results were used by the World Health Organization to describe novel guidelines for GBM diagnosis to supplement histological findings with the mutation status of several biomarkers of GBM, including *IDH1/2*, *ATRX*, and Histone Cluster 1 H3 Family Member A (HIST1H3A or H3F3A) (mutation at position K27M or simply H3-K27M mutation).<sup>25</sup> The novel classification of GBM subtypes will aid patient stratification and the development of targeted therapeutics based on genetics.

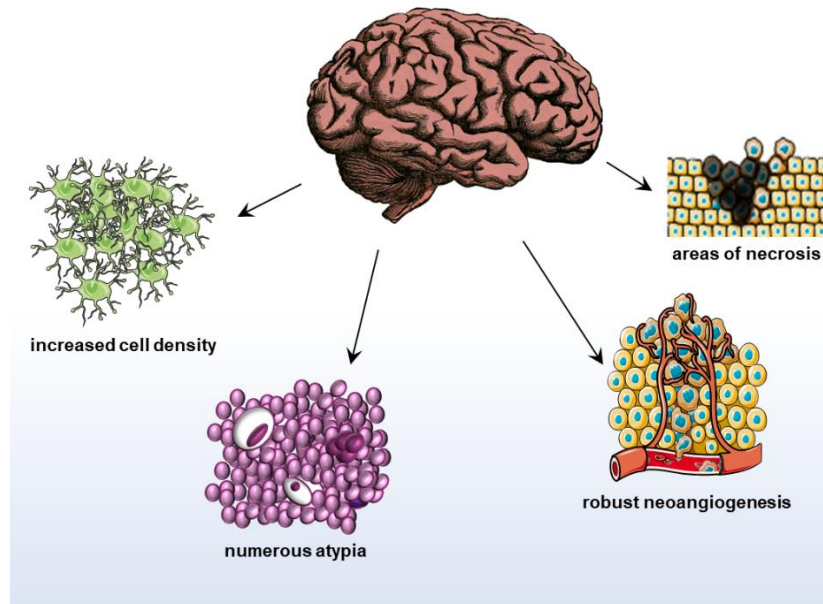


Figure I-2 Common characteristics of glioblastoma. Object images obtained from Servier Medical Art by Servier.

Molecular profiling has been used to classify GBM into four subtypes: Classical, Mesenchymal, Proneural, and Neural. Expression and aberrations of specific genes associated with each subtype have been identified.<sup>26</sup> All Classical GBM tumors contain chromosome 7 amplification and chromosome 10 loss, and almost all (97 %) display *EGFR* amplification.<sup>26</sup> Mesenchymal GBM tumors show loss of *NF1*, contain markers of epithelial-to-mesenchymal transition (*CD44* and *MERTYK*), and highly express genes in the tumor necrosis factor super family and NF- $\kappa$ B pathways. Alterations of *PDGFRA* and point mutations in the *IDH1* gene are characteristic of Proneural subtypes. Tumors with expression of neural markers *NEFL*, *GABRA1*, *SYT1*, and *SLC12A5* are classified as the Neural subtype. Of these subtypes, patients classified with the Proneural subtype generally had a longer overall survival, though the results were not statistically significant. Furthermore, the Proneural subtype is most common in younger patients. However, of the four subtypes, the Proneural subtype seemed the least responsive to aggressive

treatment (concurrent chemo- and radiotherapy, or more than three subsequent cycles of chemotherapy).<sup>26</sup>

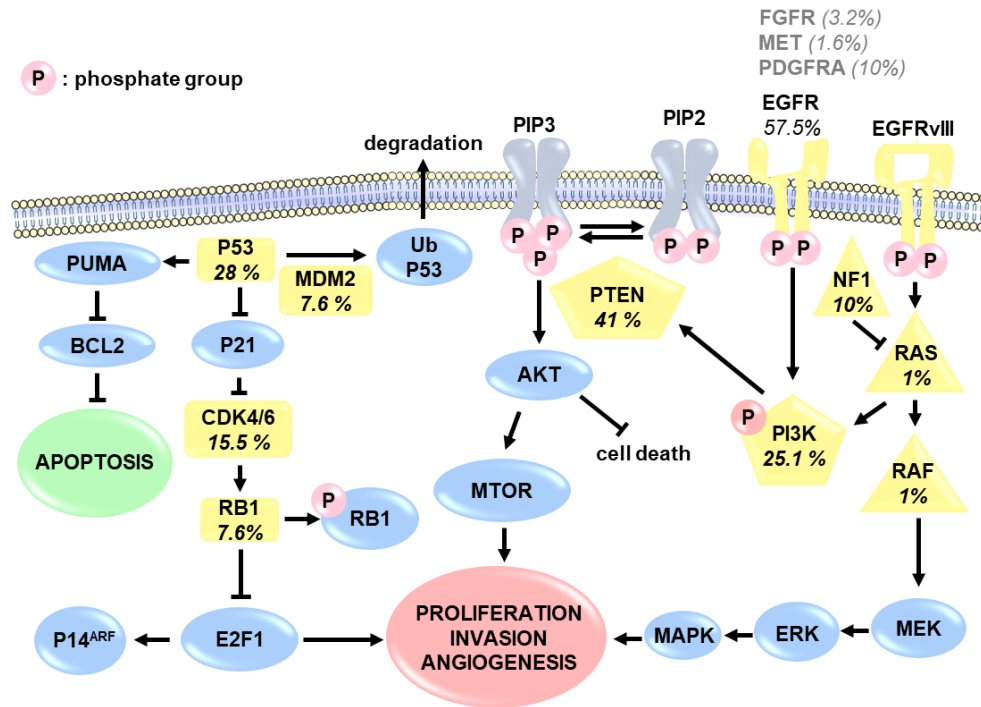


Figure I-3 Canonical gliomagenesis mediators EGFR, P53, and RB1 are important for cancer signaling. EGFR is amplified or mutated to the constitutively active EGFRvIII and propagates kinase signaling cascades to promote proliferation, invasion, and angiogenesis. P53 is a tumor suppressor that is mutated in GBM, allowing BCL2 to inhibit apoptosis. RB is another tumor suppressor gene that, when inactivated, releases E2F1 to activate cell cycling and growth. Percentages of aberrations of commonly mutated genes (in yellow) are reported, determined from TCGA analysis of patient samples.<sup>21</sup>

Improvements in tumor profiling may drastically alter how GBM is treated and may improve the fidelity of new diagnoses. Furthermore, treatment of each tumor subtype may be individualized for optimal success. Although no targeted therapies have been approved for GBM yet, these diagnostic criteria may lead to more effective personalized treatments. Moreover, targeted therapies should be evaluated in a specific GBM subtype for optimal response. Further complicating the development of targeted treatments is the fact that a single cell of origin may not exist because of the cellular complexity of GBM. Conversely, multiple factors lead to the disease,

and, in fact, the cell of origin may not be the cell type that contains the transforming mutation. However, deciphering the cell of origin of GBM may be important to properly identify targets for drug discovery, stratify patient diagnosis, and optimize an effective treatment strategy.

### **Characteristics of protein expression in glioblastoma**

Dynamic signaling pathways govern cancer cell proliferation. A major consequence of cancer signaling is an imbalance in protein expression to allow the cells to evade apoptosis, proliferate, and metastasize. Approximately 40% of GBM tumors are characterized by amplification and overexpression of EGFR, an effector of several signaling cascades that aid tumor growth, angiogenesis, migration, and metastatic spread.<sup>21</sup> EGFR is a receptor tyrosine kinase that, upon ligand binding, dimerizes and activates downstream signaling through the Ras/PI3K/AKT pathway. EGFR overexpression and EGFRvIII amplification may be prognostic markers that correlate with decreased overall survival of GBM patients<sup>27</sup>; however, a recent meta-analysis disputes this claim.<sup>28</sup> Nevertheless, because EGFR amplification and mutations promote glioma growth and survival, EGFR has been proposed as an attractive therapeutic target. Unfortunately, several clinical trials with EGFR inhibitors have failed, likely due to poor BBB permeability, intratumoral heterogeneity, and the difference between local versus systemic administration.<sup>29</sup> Gliomagenesis is driven by mutations such as EGFRvIII, and those gene mutations promote tumor growth and proliferation through protein expression networks.

Large-scale proteomic research has shown that GBM tumors have increased expression of membrane proteins involved in cellular function and maintenance ( $p = 2.03 \times 10^{-8}$ ), protein synthesis ( $p = 7.74 \times 10^{-11}$ ), cell-to-cell signaling and interaction ( $p = 1.82 \times 10^{-10}$ ), cellular movement ( $p = 1.34 \times 10^{-8}$ ), and antigen presentation ( $p = 2.24 \times 10^{-7}$ ) compared to normal brain

tissue (Figure I-4).<sup>30</sup> More specifically, GBM tumors had increased expression of membrane proteins involved in acute phase response signaling, caveolar-mediated endocytosis signaling, and calcium signaling.<sup>30</sup>

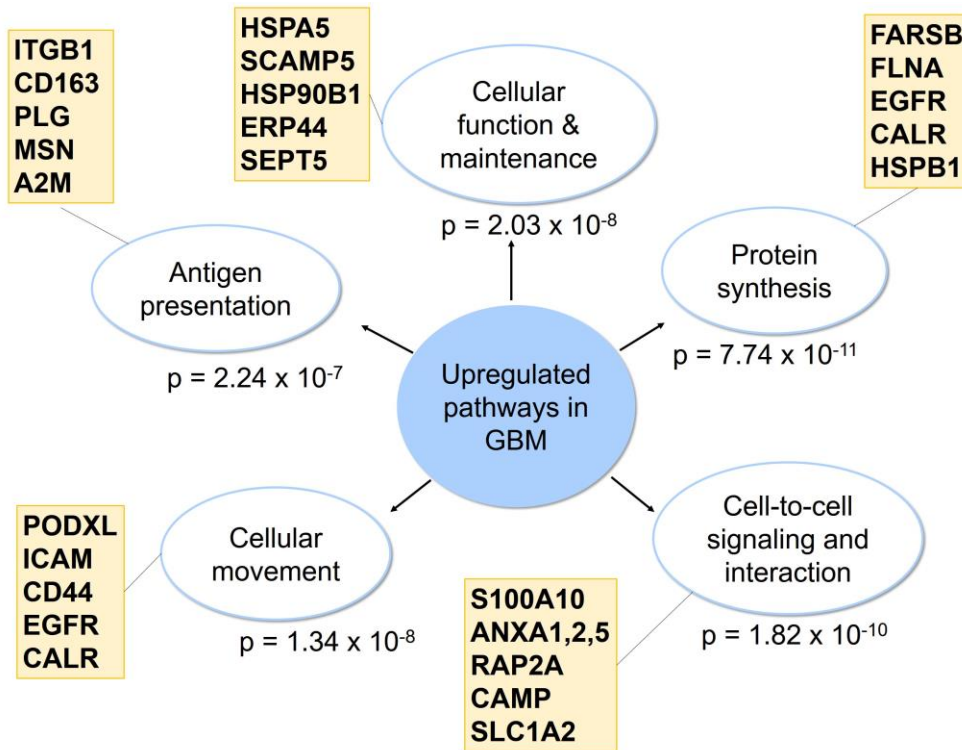


Figure I-4 Signaling pathways involving membrane proteins upregulated in GBM as determined by LC-MS/MS and iTRAQ. Results are from proteomics analysis of human GBM tumors with Ingenuity Pathway Analysis software.<sup>30</sup> Representative genes from each category are shown.

Proteomic approaches have identified proteins that are involved in chemotherapeutic resistance. For example, a study using 2D gel electrophoresis (2DGE) and mass spectrometry identified that lipocalin 2 (LCN2) and integrin  $\beta$ 3 (ITGB3) were downregulated in BCNU-resistant rat models of glioma.<sup>31</sup> Furthermore, 2DGE coupled with liquid chromatography-mass spectrometry analysis identified several proteins important for the invasive properties of gliomas.<sup>32</sup> In particular, annexin A2 was highly expressed in an angiogenesis-dependent cell line,<sup>32</sup> and its overexpression further correlated with tumor aggressiveness and patient survival.<sup>33</sup>



Although many other proteins have been found to contribute to GBM tumor growth, for this review, we will focus on targets that have been discovered through proteomic approaches and TCGA data mining. Some examples of proteins overexpressed in GBM that may represent novel drug targets that were not discovered via proteomic approaches include heat-shock protein 47 (HSP47),<sup>34</sup> cathepsin L (CTSL),<sup>35</sup> glycoprotein nonmetastatic melanoma protein B (GPNMB),<sup>36</sup> transcription factor 12 (HEB),<sup>37</sup> targeting protein for Xenopus kinesin-like protein 2 (TPX2),<sup>38</sup> and B-cell CLL/lymphoma 3 (BCL3).<sup>39</sup> Due to the characteristic intratumoral heterogeneity of GBM, it is likely that a single target approach will not be effective, and appropriate drug combinations will be necessary.

### **Emerging targets in glioblastoma**

Numerous proteins are overexpressed in GBM, and abundant research has identified potential targets; however, extensive genomic and proteomic research suggests that tumor heterogeneity will likely render GBM unresponsive to single agent therapy. Of equal importance to target discovery is biomarker identification. Disease biomarkers can be used for early diagnosis and monitoring responsiveness to treatment.

### **Biomarker identification**

Biomarkers have been used successfully as tools for cancer diagnosis. Prostate cancer was one of the first to benefit significantly with the discovery of prostate specific antigen to inform early diagnosis and response to treatment. In addition, biomarkers have been discovered for ovarian, head and neck, lung, and breast cancer, among others.<sup>40-43</sup> Gliomas are characterized in the clinic by *IDH1* and *IDH2* mutations and *MGMT* gene promoter methylation status to better inform treatment strategies; however, for GBM, proper prognostic biomarkers do not yet exist. By

studying glioma tumorigenesis in detail, prognostic markers can be identified. Better prognostic markers would allow physicians to diagnose and begin treatment of GBM at early onset, possibly preventing disease progression.

Several groups have used proteomic techniques to analyze GBM and identify potential biomarkers for early diagnosis. For example, small extracellular vesicles transporting RNA and protein between cells can help clinicians diagnose and begin treatment of GBM at an earlier stage. Small extracellular vesicles in the cerebrospinal fluid (CSF) carry important microRNA that could be used as biomarkers.<sup>44</sup> In addition, the oncometabolite 2-hydroxyglutarate (2-HG) has been studied as a noninvasive biomarker in gliomas. In one study, urinary 2-HG levels were elevated in patients diagnosed with *IDH1*-mutant gliomas.<sup>45</sup> However, it is still unclear whether 2-HG levels could be used as a diagnostic measure for *IDH1*-mutant GBM, and whether 2-HG levels could determine patient health outcome in response to chemotherapy and radiation. A computational approach was used to identify dysregulated pathways associated with short-term survival including proteins associated with gene ontology terms “protein kinase cascade” and “NFκB pathway.”<sup>46</sup> Despite this research, novel disease biomarkers identified with mass spectrometry-based proteomics have yet to reach the clinic.<sup>47</sup>

### **Drug discovery targets**

Genomic and proteomic techniques inform the development of precision medicine. The evolution of large-scale proteomic efforts is likely to benefit future drug discovery, and information on genomic events in GBM could lead to valuable insights about protein target candidates. Using TCGA GBM project cohort genomic analysis, we identified 20 genes with high expression that correlates with poor overall survival. These genes encode for proteins that promote

the aggressive nature of GBM tumors and therefore may be important drug targets. However, further validation is necessary to confirm that the increased expression is not a response to oncogenic stress.

### **Gene expression associated with reduced patient survival**

In an effort to better understand the landscape of known and unknown GBM drug targets based on available gene expression data, we performed an analysis on 141 GBM samples from the TCGA cohort with both survival metadata and RNASeq expression data (<http://cancergenome.nih.gov/>). Patient sample RNASeq RSEM-normalized gene expression values and survival metadata were sourced from the TCGA GDAC Firehose.<sup>48</sup> When multiple samples were available for a given patient, barcodes were sorted alphabetically and the first was selected for analysis.

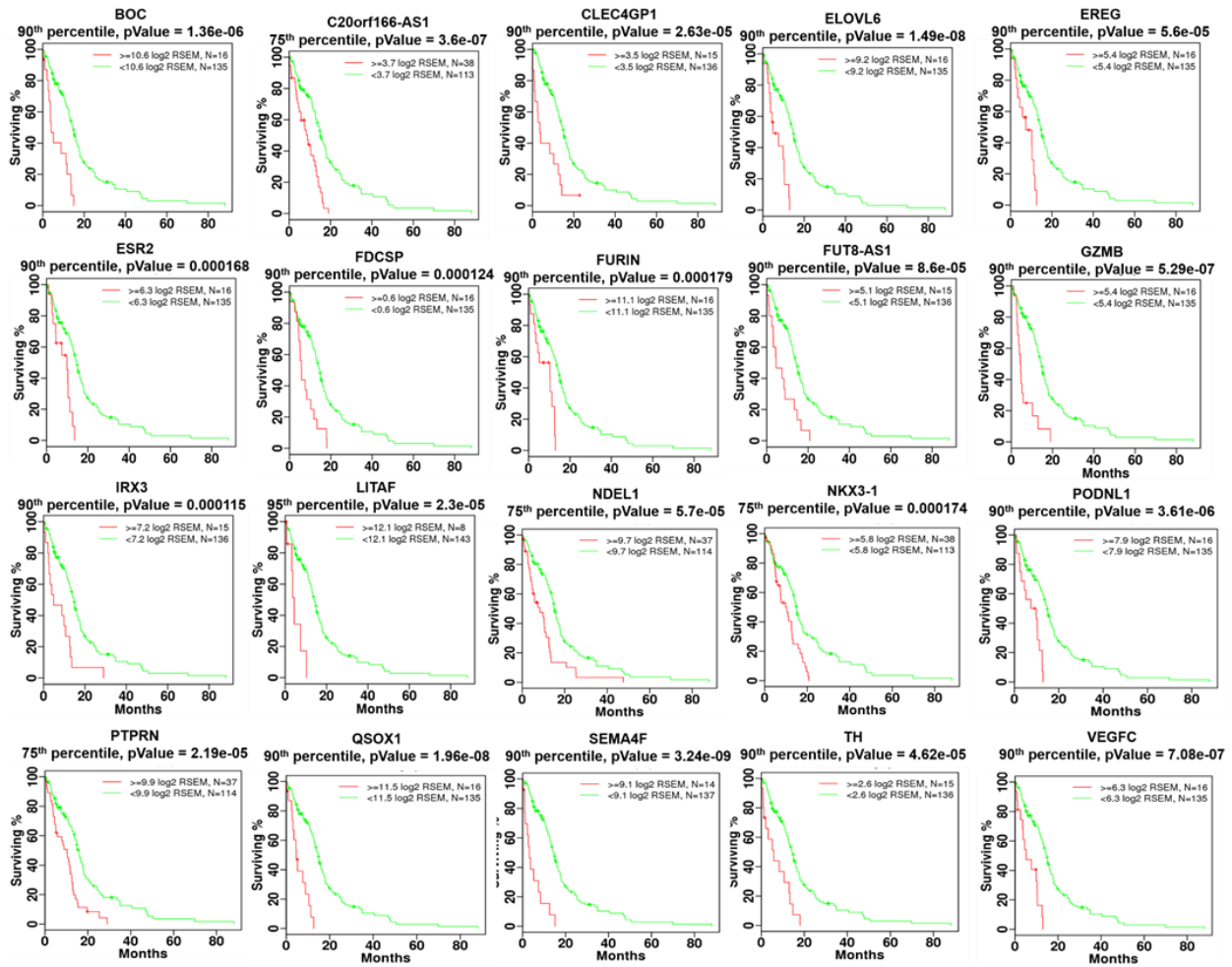


Figure I-5 Twenty genes associated with reduced survivability in the TCGA GBM patient cohort profiled with RNASeq expression data. Patients were stratified by high and low gene expression based on one of five expression percentile thresholds. Kaplan-Meier survival plots are shown with patients having increased expression in red and all other GBM patients shown in green. Non-adjusted p-values generated using the log-rank test are shown. All p-values shown survived multiple testing corrections (qValue  $\leq 0.1$ ) across all 5 percentile thresholds and 20,531 genes.

GBM patient samples were evaluated for reduced survivability by comparing survival outcomes for patients with high and low expression of each gene (Figure I-5). Thresholding for high and low expression patient populations was evaluated using five different quantile cutoffs: 95%, 90%, 75%, 50%, and 25%. A log-rank test statistic was calculated for each cutoff to compare the survival distributions of high and low expression patient populations with the null hypothesis that there was no difference in survival curves. *P*-values were FDR-adjusted across all diseases,

quantile cutoffs, and genes evaluated. To reduce over-fitting of a single cutoff per gene, genes for which the high expression population was associated with reduced survivability were required to have FDR-adjusted  $p$ -values  $\leq 0.1$  for at least two quantile cutoffs. Survival test statistics were calculated in R using the survival package.<sup>49</sup>

Twenty genes were identified as significantly associated with reduced survivability using the criteria described in the previous paragraph. Several of the 20 significant genes encode proteins involved in EGFR signaling. Our results reveal novel EGFR signaling proteins that may have more prominent roles than previously thought. These proteins include proteases (FURIN, GZMB, and NDEL1), transcription factors (LITAF, IRX3, NKX3-1, and VEGFC), and receptors (ER $\beta$ , BOC, EREG, and PTPRN). Agglomerative hierarchical clustering was performed using the 20 significant genes across TCGA GBM patients, and patients were stratified based on cluster membership. One cluster group had higher average expression across the 20 genes, and this higher expression corresponded with reduced time to death and disease-free survival (Figure I-6). Patients belonging to the cluster group with higher average expression had significantly reduced survival compared to those not included. Survival stratification significance ( $p = 5.59 \times 10^{-11}$ ) was greater when evaluating by cluster group across all 20 genes compared with any of the 20 genes separately (Figure I-6). Gene expression association with poor overall survival was further validated by applying survival test statistics to samples from three independent GBM cohorts.<sup>50-52</sup> Eight of the 20 genes (*LITAF*, *FURIN*, *VEGFC*, *C20orf166-AS1*, *ELOVL6*, *PODNLI*, *ESR2*, and *QSOX1*) were significantly associated with reduced survivability in at least one additional GBM cohort. This additional validation supports the importance of the overexpression of these genes in the context of GBM.

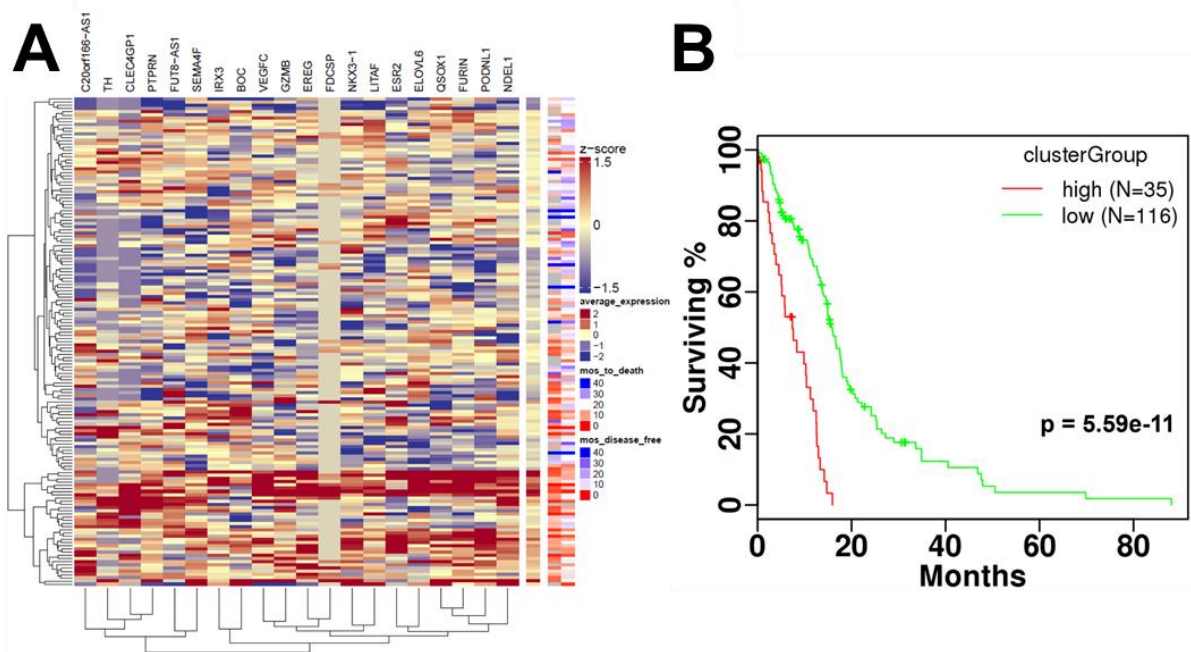


Figure I-6 Hierarchical clustering of 20 genes (A) Hierarchical clustering was performed to identify groups of patients with similar RNASeq expression of 20 genes associated with reduced survivability in the TCGA GBM patient cohort. (B) Patients stratified using clustering dendrogram assignment into high and low expression groups showed significant differences in survival. Heatmap z-scores were calculated per gene. Agglomerative hierarchical clustering with complete linkage was performed using Euclidean and Pearson correlation distance metrics on rows and columns respectively.

Further validation of the proteins was performed with the open-access resource Pharos.<sup>53</sup>

The majority of the identified genes (12) had Tbio classifications while two (ESR2 and TH) had Tclin classifications and three (ELOVL6, FURIN, GZMB) were assigned a Tchem classification. All targets that were mapped to GTEx expression were classified as having high or medium expression levels in normal brain tissue. From the analysis, 21 out of 25 genes in Figure I-4 and 12 out of 20 genes (Table I-1) have a known link to brain cancer. Of the 12 genes, seven are linked to GBM: *BOC*, *ELOVL6*, *IRX3*, *LITAF*, *NDEL1*, *PTPRN*, and *QSOX1*. Furthermore, *ELOVL6* small molecule probes have been identified and could be used to validate *ELOVL6* as a drug target. Given that *ELOVL6*, *ESR2*, *TH*, *FURIN*, and *GZMB* have probes or inhibitors identified, these proteins could be a starting point for validation of our TCGA data mining.

Table I-1 Gene descriptions from DAVID bioinformatics database (<https://david.ncifcrf.gov>).

No.	Name	Full Name	Description	Refs.
1	<i>BOC</i>	BOC cell adhesion associated, oncogene regulated	Component of a cell-surface receptor complex that mediates cell-cell interactions between muscle precursor cells	54
2	<i>CLEC4GP1</i>	C-type lectin domain family 4 member G pseudogene 1	function unknown	N/A
3	<i>ELOVL6</i>	ELOVL fatty acid elongase 6	Fatty acid elongase specific to C12-C16 saturated and monounsaturated fatty acids	55
4	<i>EREG</i>	epiregulin	May be a mediator of localized cell proliferation	56
5	<i>ESR2</i>	estrogen receptor 2	Nuclear hormone receptor that binds estrogens with an affinity similar to that of ESR1 and activates expression of reporter genes containing estrogen response elements in an estrogen-dependent manner	57, 58

6	<i>FDCSP</i>	follicular dendritic cell secreted protein	Can bind to the surface of B-lymphoma cells, but not T-lymphoma cells, consistent with a function as a secreted mediator acting upon B-cells	59, 60
7	<i>FURIN</i>	furin, paired basic amino acid cleaving enzyme	Release of mature proteins from their proproteins by cleavage of -Arg-Xaa-Yaa-Arg- -Zaa- bonds, where Xaa can be any amino acid and Yaa is Arg or Lys and regulates TGF- $\beta$ bioavailability	61
8	<i>FUT8-ASI</i>	fucosyltransferase 8 antisense RNA 1	Fucosylation of proteins, including EGFR	62
9	<i>GZMB</i>	granzyme B	This enzyme is necessary for target cell lysis in cell-mediated immune responses. It cleaves after Asp. Seems to be linked to an activation cascade of caspases (aspartate-specific cysteine proteases) responsible for apoptosis execution. It has been associated with both tumor progression and regression, in a case-dependent manner.	63, 64
10	<i>IRX3</i>	iroquois homeobox 3	Belongs to the TALE/IRO homeobox family and may have a direct functional relationship to both obesity and type 2 diabetes. IRX3 is a proneural gene important for neuronal differentiation.	65, 66



11	<i>LITAF</i>	lipopolysaccharide induced TNF factor	Probable role in regulating transcription of specific genes. May regulate through NFκB1 the expression of the CCL2/MCP-1 chemokine. May play a role in tumor necrosis factor alpha (TNF-alpha) gene expression	67
12	<i>NDELI</i>	nudE neurodevelopment protein 1 like 1	Facilitates the polymerization of neurofilaments from the individual subunits NEFH and NEFL. Required for organization of the cellular microtubule array and microtubule anchoring at the centrosome	68
13	<i>NKX3-1</i>	NK3 homeobox 1	Transcription factor, which binds preferentially the consensus sequence 5'-TAAGT[AG]-3' and can behave as a transcriptional repressor. Could play an important role in regulating proliferation of glandular epithelium and in the formation of ducts in prostate	69
14	<i>PODNL1</i>	podocan like 1	Belongs to the small leucine-rich proteoglycan (SLRP) family	70-72
15	<i>PTPRN</i>	protein tyrosine phosphatase, receptor type N	Implicated in neuroendocrine secretory processes. May be involved in processes specific for neurosecretory granules, such as their biogenesis, trafficking or regulated exocytosis or may have a general role in neuroendocrine functions	73, 74

16	<i>QSOX1</i>	quiescin sulfhydryl oxidase 1	Catalyzes the oxidation of sulfhydryl groups in peptide and protein thiols to disulfides with the reduction of oxygen to hydrogen peroxide. May contribute to disulfide bond formation in a variety of secreted proteins	75
17	<i>SEMA4F</i>	semaphorin 4F	Estrogen-regulated semaphorin ligand with growth cone collapse activity against retinal ganglion-cell axons	76
18	<i>TH</i>	tyrosine hydroxylase	Plays an important role in the physiology of adrenergic neurons	77
19	<i>VEGFC</i>	vascular endothelial growth factor C	Growth factor active in angiogenesis and endothelial cell growth, stimulating proliferation and migration. Has effects on the permeability of blood vessels. May function in angiogenesis of the venous and lymphatic vascular systems during embryogenesis, and in the maintenance of differentiated lymphatic endothelium in adults	78, 79
20	<i>C20orf166AS1</i>	chromosome 20 open reading frame 166 antisense RNA 1	long non-coding RNA	80

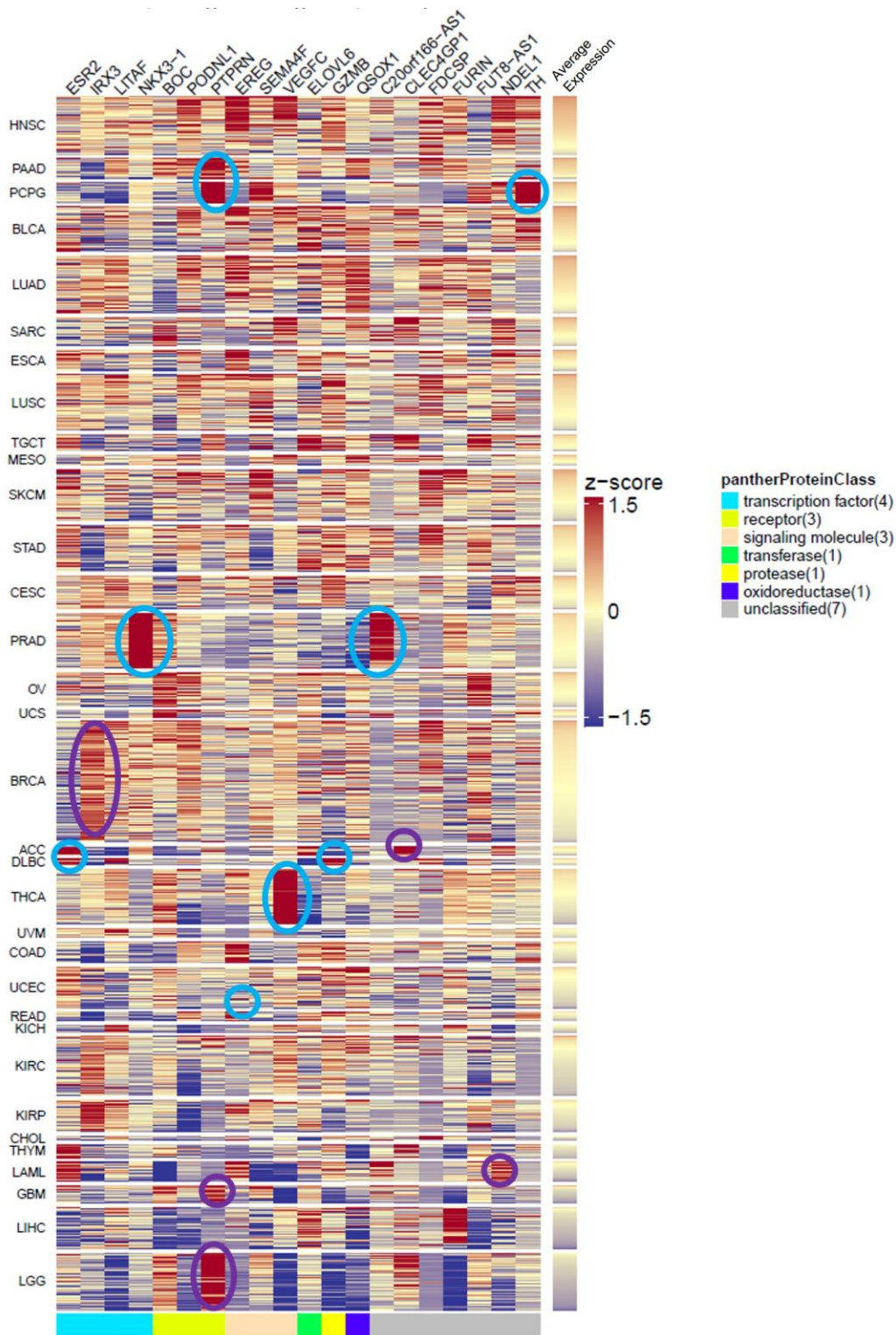


Figure I-7 Expression of 20 genes significantly associated with reduced survivability in GBM across 33 TCGA diseases. Gene expression from each patient sample was converted to a z-score, and z-scores were re-calculated across all diseases for each gene

to show relative expression. Regions of the heatmap are circled to highlight genes with consistent higher expression (10th percentile > 0.5) and previously published support for relevance to disease progression (cyan) or high expression without previously published support for disease progression (purple). Diseases are ranked by decreasing average expression and ribbon on the right is colored to indicate average expression per patient sample.

We expanded our analysis of the 20 genes to include 33 TCGA diseases (Figure I-7). Head and neck squamous cancer had the highest average expression of the 20 genes in the analyzed patient samples. In addition, several genes were identified that have consistently higher expression in several cancers. For example, *PTPRN* was highly expressed in pancreatic adenocarcinoma and the pheochromocytoma and paraganglioma cohort; and therefore, those cancer subsets may be more sensitive to targeted PTPRN therapy. Several of the genes are involved in the transcriptional regulation of EGFR, including *ESR2*, *EREG*, and *VEGFC*. In addition, several genes are indirectly involved in EGFR regulation, including *FUT8*, *LITAF*, *FURIN*, *NKX3-1*, and *TH*. Upon further validation, these transcription factors may prove to be relevant to the progression and recurrence of GBM.

Below, we briefly summarize the 20 genes significantly associated with reduced survivability and discuss current research on the link between each gene and cancer. Further validation of each target is necessary to confirm the importance of each gene in the context of GBM. Inhibiting the activity or expression of one, or a combination, of the proteins discussed below may prove to be a viable treatment strategy for GBM.

#### **BOC cell adhesion associated, oncogene regulated (BOC)**

BOC is a member of the immunoglobulin/fibronectin type III repeat family and promotes myogenic differentiation. During oncogenesis, BOC promotes hedgehog pathway signaling by sustaining a feedback mechanism that enhances the concentration of Sonic hedgehog (Shh) ligand.<sup>54</sup> The hedgehog signaling pathway is necessary for normal cellular processes such as

embryogenesis and growth of hair follicles and taste papillae in adults.<sup>81</sup> In the absence of the Shh ligand, the GPCR Ptch is active, which blocks Smo signaling. When Shh ligand is present, it inactivates Ptch, allowing Smo to signal transcription of target genes. Since BOC activates hedgehog pathway signaling, it likely contributes to GBM progression and may be a potential drug target. In our analysis, increased *BOC* expression is strongly associated with poor overall survival ( $p = 1.36 \times 10^{-6}$ ). This is the first report, to our knowledge, of *BOC* associated with GBM.

#### **C-type lectin domain family 4 member G pseudogene 1 (CLEC4GP1)**

CLEC4G is a 32.6-kDa membrane-bound protein expressed in the liver and lymph nodes and plays a role in T-cell immune response. TCGA whole-genome sequencing revealed *CLEC4G* was downregulated in hepatocellular carcinoma tissue.<sup>82</sup> As a pseudogene, *CLEC4GP1* is likely a non-functional copy of the enzyme. Pseudogenes can arise during duplication if a mutation occurs in the DNA, or with retrotransposition, in which the cDNA product of the reverse-transcribed mRNA becomes incorporated in the genome. In our analysis, increased *CLEC4GP1* expression is strongly associated with poor overall survival ( $p = 2.63 \times 10^{-5}$ ). *CLEC4GP1* is located on chromosome 19. In one study, *CLEC4GP1* mRNA expression increased in response to an mRNA-based vaccine encoding influenza A hemagglutinin from a pandemic strain.<sup>83</sup> Additionally, expression of *CLEC4GP1* is high in samples from patients diagnosed with adenoid cystic carcinoma (Figure I-7).

#### **ELOVL fatty acid elongase 6 (ELOVL6)**

ELOVL6 is highly expressed in the brain, and the gene is often hypomethylated in GBM.<sup>84</sup> This enzyme performs the first and rate-limiting step of fatty acid elongation, with malonyl-CoA as a 2-carbon donor and is important for insulin sensitivity and energy metabolism.<sup>85</sup>

Phospholipids containing longer acyl chains are abundant in cancer tissue, and ELOVL6 is the main enzyme responsible for fatty acid elongation in cancer.<sup>86</sup> The gene is located on chromosome 4q25, adjacent to the *EGF* gene. Expression of *ELOVL6* may be high because it shares an enhancer region with *EGF*. Enhancers perform complex functions and can activate transcription of specific genes upstream or downstream, by engaging the transcriptional machinery. In acute myeloid leukemia, a novel chromosomal rearrangement was found to activate *ELOVL6* and *EGF*.<sup>87</sup> *ELOVL6* has been studied in the context of many cancers. Increased *ELOVL6* mRNA expression was found in triple-negative breast cancer tissue.<sup>88</sup> Additionally, *ELOVL6* and lipid composition may be regulated by the RB-E2F1 pathway.<sup>89</sup> An *ELOVL6* inhibitor, Compound A, inhibited tumor growth in an *in vivo* model of squamous cell carcinoma,<sup>86</sup> and therefore validation and pursuit of *ELOVL6* inhibition in GBM is warranted.

### **Epiregulin (EREG)**

EREG is a 19-kDa peptide hormone that acts as a ligand for the EGF receptor and ErbB4. When cleaved by a disintegrin and metalloproteinase (ADAM) enzyme from the transmembrane pro-peptide to an active soluble form, EREG binds EGFR family members and initiates the signaling cascade. *EREG* expression is upregulated in gastric,<sup>90</sup> colon,<sup>90</sup> lung,<sup>91</sup> and head and neck<sup>92</sup> cancers, among others. In a colon cancer xenograft model, *EREG* expression correlated with a positive response to the anti-EGFR monoclonal antibody cetuximab, suggesting the tumors were dependent on the EGFR signaling pathway activated by EREG.<sup>93</sup> *EREG* transcription is regulated by insulin, Sp1, NFκB, and AP-2.<sup>94-96</sup> Silencing of *EREG* in a breast cancer cell line inhibited metastasis, angiogenesis, and tumor cell extravasation.<sup>97</sup> EREG is a partial agonist of EGFR dimerization and induces differentiation in breast cancer cells.<sup>98</sup> The emerging role for

EREG as a key activator of EGFR signaling driving cancer cell proliferation suggests that inhibition of EREG binding to EGFR is a potential targeted cancer treatment. In our analysis, *EREG* expression was associated with poor overall survival in GBM patients ( $p = 5.6 \times 10^{-5}$ ). High *EREG* expression was also found in TCGA samples from patients diagnosed with rectum adenocarcinoma (Figure I-7). Furthermore, EREG activates the ERK/MAPK pathway in GBM suggesting inhibition of the EREG-EGFR interaction may be a strategy for EREG-overexpressing GBM patients.<sup>99</sup>

### **Estrogen receptor 2 (ESR2)**

*ESR2* encodes the gene for estrogen receptor  $\beta$  (ER $\beta$ ), a nuclear hormone receptor for estrogen, is considered a tumor suppressor in the context of GBM and other cancers,<sup>58, 100</sup> and enhances chemosensitivity in NSCLC.<sup>101</sup> Treatment with ER $\beta$  agonist, LY500307, is efficacious in a GBM tumor-bearing mouse model.<sup>58</sup> Additionally, ER $\beta$  expression, analyzed immunohistochemically, declines as brain astrocytic tumors progress.<sup>57</sup> In our analysis, increased *ESR2* expression is strongly associated with poor overall survival ( $p = 1.68 \times 10^{-4}$ ), which is in contrast with the tumor suppressing effects of the protein. Furthermore, expression of *ESR2* is high in TCGA samples from patients diagnosed with diffuse large B-cell lymphoma (Figure I-7). The tumor-suppressing characteristics of ESR $\beta$  may prevent it from being a potential anticancer target.

### **Follicular dendritic cell secreted protein (FDCSP)**

FDCSP (C4orf7) is a 9.7-kDa peptide that promotes invasion and metastasis of tumor cells. While relatively little is known about this peptide, overexpression of FDCSP is common in tumorigenesis, especially in ovarian cancer.<sup>60</sup> FDCSP expression has also been implicated as a marker of follicular dendritic cell sarcoma.<sup>102</sup> The position, on chromosome 4q13, and

characteristics, including amino acid composition, molecular mass, and isoelectric point suggest *FDCSP* may be similar to the inflammatory C-X-C chemokines, such as IL-8.<sup>103</sup> In our analysis, increased *FDCSP* expression is strongly associated with poor overall survival ( $p = 1.24 \times 10^{-4}$ ). *FDCSP* expression may be important for GBM progression.

### **Furin**

Furin is a protease that activates matrix metalloproteinases including parathyroid hormone, transforming growth factor beta 1 precursor, proalbumin, pro-beta-secretase, membrane type-1 matrix metalloproteinase, beta subunit of pro-nerve growth factor, and von Willebrand factor. Furin is linked with tumor progression in several cancers including head and neck squamous cell carcinoma, breast cancer, and rhabdomyosarcoma.<sup>104</sup> In astrocytoma cells, inhibition of furin decreases cell proliferation and invasiveness.<sup>105</sup> Furthermore, furin promotes activation of pro-TGF $\beta$ 1 and pro-TGF $\beta$ 2, demonstrating a tumorigenic role in glioma-initiating cells.<sup>106</sup> In our analysis, increased furin expression is strongly associated with poor overall survival ( $p = 1.79 \times 10^{-4}$ ). Transcription of furin is promoted by AP-1 (activator protein-1), c-Jun, and ATF-2. Proteolysis is important in cancer, and furin activates several enzymes via proteolysis that contribute to cell migration and survival, including protein kinase C.<sup>107</sup> Combined inhibition of furin, ADAM, calpain, and another serine protease is necessary to prevent glioma migration and slow growth mediated by protein tyrosine phosphatase  $\mu$ .<sup>61</sup> Inhibitors of furin demonstrate antiproliferative effects and are being optimized in the context of inhibition of viral replication.<sup>108</sup>  
<sup>109</sup> The extensive evidence of the tumorigenic role of furin in several cancers, including brain cancer, suggests it may be a promising therapeutic target, and inhibitors of furin may improve treatment outcomes.



### **Fucosyltransferase 8 antisense RNA 1 (FUT8-AS1)**

FUT8 is a 66.5-kDa enzyme located in the Golgi apparatus and extracellular space and catalyzes the transfer of fucose from GDP-fucose to N-linked type complex glycopeptides. Fucosylation is an important post-translational glycosylation event that regulates cancer signaling processes including metastasis and epithelial-to-mesenchymal transition. The expression of *FUT8-AS1* suggests *FUT8* expression may be downregulated in GBM patients. In our analysis, increased *FUT8-AS1* expression is strongly associated with poor overall survival ( $p = 8.6 \times 10^{-5}$ ). *FUT8* function has been studied in the context of several cancers. For example, knockdown of *FUT8* halted growth of *in vitro* and *in vivo* models of lung cancer.<sup>110</sup> Additionally, inhibitors have been developed that block fucosylation in models of cancer.<sup>111</sup> While *FUT8* expression has been studied in the context of lung, liver, colon, and other cancers, it has not been evaluated in GBM.

### **Granzyme B (GZMB)**

*GZMB* is a serine protease in the peptidase S1 family and is involved in mediating apoptosis. This enzyme cleaves after aspartate and plays a role in the cellular caspase cascade that leads to apoptosis. *GZMB* is the most abundant enzyme in cytotoxic granules responsible for the clearance of tumor cells, as well as cells infected with intracellular pathogens and allogeneic cells.<sup>112, 113</sup> It is also a prognostic marker in colorectal cancer.<sup>114</sup> In our analysis, increased *GZMB* expression is strongly associated with poor overall survival ( $p = 5.29 \times 10^{-7}$ ). Additionally, there is high expression of *GZMB* in TCGA samples from patients diagnosed with diffuse large B-cell lymphoma (Figure I-7). *GZMB* transcription is regulated by nuclear factor of activated T cells, Ikaros, and AP-1.<sup>115</sup> *GZMB* gene transcription is also activated and enhanced by NF- $\kappa$ B, which

binds approximately 10 kilobases downstream from the *GZMB* transcription start site,<sup>116</sup> and by JAK1/STAT signaling.<sup>117</sup> The role of *GZMB* in apoptosis makes it an attractive anticancer target.

### **Iroquois homeobox 3 (*IRX3*)**

*IRX3* is a 5.2-kDa transcription factor in the Iroquois homeobox family of developmental factors and is involved in Shh-dependent neural patterning. *IRX3* belongs to class I proteins of neural progenitor factors and is repressed by Shh signals. *IRX3* contains transcription factor binding sites for ER $\alpha$ , Pax-5, AP-2 $\alpha$ , AP-2 $\beta$ , AP-2 $\gamma$ , FOXD1, and C/EBP, among others. In our analysis, increased *IRX3* expression is strongly associated with poor overall survival ( $p = 1.15 \times 10^{-4}$ ). In addition, consistently higher expression of *IRX3* is observed in TCGA samples from patients diagnosed with breast cancer (Figure I-7). *IRX3* is a target gene of *WHSC1L1* (Wolf-Hirschhorn syndrome candidate 1-like 1 gene, or NSD3), a known oncogene in breast cancer, and may be a regulator of WNT signaling.<sup>66</sup> DNA methylation profiling of an oligodendroma-derived cell line revealed hypermethylation of the CpG island on an *IRX3* exon, consistent with overexpression of *IRX3* in tumor tissue compared to normal brain samples.<sup>118</sup> Although *IRX* transcription factors have been identified in multiple genome-wide sequencing studies in cancer, they specifically hamper the tumor-suppressing activity of the TGF- $\beta$  pathway.<sup>119</sup> Therefore, blocking *IRX3* expression, or inhibiting its ability to suppress the TGF- $\beta$  pathway, may be an option for GBM treatment.

### **Lipopolysaccharide-induced tissue-necrosis-factor factor (*LITAF*)**

*LITAF* is a lipopolysaccharide-regulated transcription factor located on chromosome 16 that regulates VEGF and plays a role in angiogenesis and inflammatory response.<sup>120</sup> *LITAF* contains a small integral membrane protein of lysosome/late endosome (SIMPLE)-like domain

(SLD) with a YXX  $\phi$  motif that mediates transport of membrane proteins to and from the endosome, Golgi apparatus, and lysosomes. In several cancers, LITAF induces inflammation and promotes cancer cell survival. Stimulation by lipopolysaccharide (LPS) causes LITAF to translocate from the cytoplasm with its partner protein STAT6(B) to the nucleus to promote gene expression.<sup>67</sup> In our analysis, increased *LITAF* expression is strongly associated with poor overall survival ( $p = 2.3 \times 10^{-5}$ ). Furthermore, *LITAF* was in the top 30 overexpressed genes in GBM in a large-scale expression analysis study.<sup>121</sup> Therefore, blocking the LITAF-STAT6(B) protein-protein interaction may be a viable treatment strategy. However, LITAF possesses a tumor-suppressing role in pancreatic cancer,<sup>122</sup> and its expression can be induced by P53.<sup>123</sup> *LITAF* knockdown promoted tumor malignancy and growth in nude mice injected subcutaneously with prostate cancer cells.<sup>124</sup> Overall, LITAF plays a complex role in the progression of cancer.

#### **NudE neurodevelopment protein 1 like 1 (NDEL1)**

NDEL1 is a 38-kDa cytoskeletal protein that contains an N-terminal coiled coil NUDE domain and is important for the regulation of microtubule organization to promote neuronal migration. Expression of NDEL1 is highest during mitosis, and it is necessary for mitotic cell division.<sup>125</sup> In our analysis, increased *NDEL1* expression is strongly associated with poor overall survival ( $p = 5.7 \times 10^{-5}$ ), and consistently higher expression is found in acute myeloid leukemia (Figure I-7). NDEL1 has also been implicated in the development of schizophrenia via its protein-protein interactions with Disrupted-in-Schizophrenia 1 (DISC1).<sup>126</sup> NDEL1 associates with microtubules, dynein, CENPF, and ZNF365. Additionally, the *NDEL1* gene contains P53, c-myc, and ARP-1 transcription factor binding sites. With an increased understanding of the role of

NDEL1 in cancer migration, effective, targeted inhibitors could be developed to control tumor growth.

### **NK3 homeobox 1 (NKX3-1)**

NKX3-1 is a transcription factor that negatively regulates epithelial cell growth in prostate tissue. Loss of *NKX3-1* is common in prostate cancer patients.<sup>69, 127</sup> NKX3-1 negatively regulates the PI3K-AKT pathway to suppress tumor growth, and heterozygous deletions of *NKX3-1* and *PTEN* cause prostate adenocarcinomas in mice.<sup>128</sup> Additionally, NKX3-1 functions as a tumor suppressor in hepatocellular carcinoma.<sup>129</sup> In our analysis, increased *NKX3-1* expression is strongly associated with poor overall survival ( $p = 1.74 \times 10^{-4}$ ), and consistently higher expression is also found in prostate adenocarcinoma (Figure I-7). To our knowledge, NKX3-1 has not yet been studied in the context of GBM.

### **Podocan like 1 (PODNL1)**

PODNL1 is an extracellular protein expressed in tibial nerves, coronary arteries, and bone marrow mesenchymal stem cells and is involved in proteinaceous extracellular matrix formation. It belongs to the small leucine-rich proteoglycan (SLRP) family of 17 genes and is a member of Class V SLRPs, residing on chromosome 19q. SLRPs also act upstream of signaling cascades, including receptor tyrosine kinases like ErbB family members.<sup>130</sup> Interestingly, the Class V SLRPs bind collagen I and inhibit cell growth by inducing p21 expression.<sup>131</sup> Additionally, another SLRP family member, decorin, binds to EGFR and lowers receptor levels by caveolin-mediated internalization.<sup>132-134</sup> High expression of PODNL1 correlates with poor prognosis in ovarian cancer.<sup>71</sup> Methylation of the *PODNL1* gene may be important for phenotypic changes that occur during aging,<sup>70</sup> and *PODNL1* expression is associated with high-grade glioma.<sup>72</sup> Our analysis

supports these findings; increased *PODNL1* expression is strongly associated with poor overall survival ( $p = 3.61 \times 10^{-6}$ ). Because several proteins in the SLRP family play a role in cancer progression, *PODNL1* may have an important function as well.

### **Protein tyrosine phosphatase, receptor type N (PTPRN)**

*PTPRN* (also known as islet antigen-2 or IA-2) is a gene encoding a 105.8-kDa protein in the protein tyrosine phosphatase family responsible for signaling processes related to cell growth, differentiation, and oncogenic transformation. Hypermethylation of *PTPRN* in ovarian cancer patients was associated with shorter survival.<sup>73</sup> It was initially discovered as a gene differentially expressed in human pancreatic beta islet cells and is localized on the plasma membrane and in endosomes. *PTPRN* depletion reduced small cell lung cancer cell growth.<sup>135</sup> Valproic acid induced the expression of *PTPRN* as a result of increased acetylation in the promoter region.<sup>136</sup> Analysis of TCGA samples from patients with pancreatic adenocarcinoma, pheochromocytoma, paraganglioma, GBM, and LGG revealed consistently higher expression of *PTPRN* (Figure I-7). In our analysis, increased *PTPRN* expression is strongly associated with poor overall survival ( $p = 2.19 \times 10^{-5}$ ). While PTP family proteins have been well-studied in the context of cancer, little work has been done to elucidate the role of *PTPRN* in brain cancer.

### **Quiescin sulfhydryl oxidase 1 (QSOX1)**

QSOX1 is a FAD (flavin adenine dinucleotide)-dependent 82.6-kDa enzyme that forms disulfide bonds in proteins by oxidizing sulfhydryl groups. It is found in the extracellular space, Golgi apparatus, and endoplasmic reticulum, where it functions alongside protein disulfide isomerase to fold nascent proteins.<sup>137</sup> QSOX1 contains one thioredoxin domain and one ERV/ALR sulfhydryl oxidase domain. In pancreatic cancer, *QSOX1* expression correlates with cell migration

and survival, and QSOX1-mediated migration of pancreatic ductal carcinoma cells may be activated by MMP-2 and MMP-9.<sup>75</sup> Interestingly, loss of *NKX3-1* expression correlates with an increase in *QSOX1* expression in prostate cancer.<sup>138</sup> In our analysis, increased *QSOX1* expression is strongly associated with poor overall survival ( $p = 1.96 \times 10^{-8}$ ). Proteomic analysis using iTRAQ identified that QSOX1 expression was upregulated in hepatocellular carcinoma.<sup>139</sup> Furthermore, knockdown of QSOX1 sensitizes nasopharyngeal carcinoma cells to radiation.<sup>140</sup> Ebselen, a covalent inhibitor of QSOX1, suppressed pancreatic tumor growth *in vivo*.<sup>141</sup> Much work has been done to elucidate the complex role of QSOX1 in several cancers, and it clearly plays an important role in disease progression.

#### **Semaphorin 4F (SEMA4F)**

SEMA4F is a membrane-bound glycoprotein in the semaphorin family of receptors. Semaphorins are involved in eliciting intracellular signaling cascades and may be receptors for EGFR signaling ligands. Therefore, semaphorins are important regulators of tumor growth, angiogenesis, migration, and apoptosis.<sup>142</sup> For example, SEMA3B was found to be a marker for poor survival in patients over 50 diagnosed with GBM.<sup>143</sup> In contrast, SEMA4D can stimulate or inhibit breast cancer cell migration and adhesion, depending on the presence of receptor tyrosine kinases ERBB2 and MET.<sup>144</sup> In our analysis, increased *SEMA4F* expression is strongly associated with poor overall survival ( $p = 3.24 \times 10^{-9}$ ). SEMA4F is linked to the induction of prostate cancer neurogenesis<sup>145</sup> and may be important for breast cancer progression.<sup>146</sup> SEMA4F knockdown was linked to Schwann cell proliferation in the development of neurofibroma downstream of the loss of NF1 tumor suppressor function.<sup>76</sup> The molecular mechanisms driving the function of this signaling receptor in cancer are complex.

### **Tyrosine hydroxylase (TH)**

TH, as its name suggests, hydroxylates tyrosine to form the precursor for dopamine, l-dopa, and is induced by hypoxic stress via HIF1 $\alpha$ , common in the tumor microenvironment. TH is also a marker for neurons containing downstream products dopamine, norepinephrine, and epinephrine. In our analysis, increased *TH* expression is strongly associated with poor overall survival ( $p = 4.62 \times 10^{-5}$ ). *TH* gene expression is also significantly increased in pheochromocytoma and paraganglioma (Figure I-7). To date, eight inhibitors of TH have been studied. One of the inhibitors, alpha-methyl-p-tyrosine (AMPT), was used to treat pheochromocytoma; however, use was discontinued because of severe side effects. In general, inhibition of TH may rely on a small therapeutic window for safe usage, because of the crucial role of the enzyme in dopamine synthesis.

### **Vascular endothelial growth factor C (VEGFC)**

VEGFC is a dimeric, secreted growth factor in the VEGF (vascular endothelial growth factor) family. The VEGF family contains five members, VEGFA, placenta growth factor (PGF), VEGFB, VEGFC, and VEGFD, and acts by binding tyrosine kinase VEGF receptors on the cell surface. VEGFC binds and activates VEGFR-2 and VEGFR-3. VEGFC is overexpressed in peripheral blood mononuclear cells and plays an important role in lymphoangiogenesis.<sup>147</sup> *VEGFC* is also strongly overexpressed in patients with thyroid cancer (Figure I-7). Furthermore, VEGFC expression is upregulated in brain tumors including GBM and haemangioblastomas, suggesting this protein is important for tumor-associated inflammation.<sup>148</sup> In our analysis, increased *VEGFC* expression is strongly associated with poor overall survival ( $p = 7.08 \times 10^{-7}$ ). Expression of *VEGFC* is associated with poor overall survival in GBM ( $p < 0.001$  and  $p = 0.023$ ).<sup>149, 150</sup> *VEGFC*

is targeted by microRNA-144 and microRNA-186 to halt tumor growth in cervical and bladder cancer, respectively.<sup>151, 152</sup> High expression of this protein in GBM suggests VEGFR-3 plays a vital role in cancer proliferation, potentially as much as VEGFR-1. CS2164 is a novel multi-kinase inhibitor that targets VEGFR1, VEGFR2, VEGFR3, PDGFR alpha, c-Kit, Aurora kinase b, and CSF-R1, and exhibited anti-tumor potency in mouse xenograft models of colon, lung, liver, and stomach cancer.<sup>153</sup> Inhibitors of VEGFR-1 or VEGFR-3, or inhibitors of the maturation of VEGFC, could be efficacious in GBM, based on the strong correlation between poor prognosis in several cancers and VEGFC expression.

#### **Chromosome 20 open reading frame 166 antisense RNA 1 (C20orf166AS1)**

*C20orf166AS1* is an 8.5-kb long noncoding RNA (lncRNA). *C20orf166AS1* was reported as a prostate-cancer-specific lncRNA that was negatively correlated with prostate cancer.<sup>80</sup> Analysis of TCGA samples supports these findings; *C20orf166AS1* is consistently higher in prostate adenocarcinoma patient samples than in normal tissue (Figure I-7). In our analysis, increased *C20orf166AS1* expression is strongly associated with poor overall survival ( $p = 3.6 \times 10^{-7}$ ). Aside from its possible role in prostate cancer, *C20orf166AS1* function has not been fully elucidated.

#### **Protein targets identified via proteomic approaches**

Although the application of modern proteomic approaches has yet to reach its full potential in GBM research, several important studies have identified potential drug targets. Traditionally, proteomics has been performed with 2DGE and mass spectrometry. While useful, 2DGE has several major limitations. For example, 2DGE cannot detect low abundance proteins, proteins with a molecular weight greater than 100 kDa, or hydrophobic membrane proteins.<sup>154</sup> In addition,



proteins with isoelectric point (pI) values outside the pH range go undetected, including important GBM proteins such as EGFR and VEGFR.<sup>155</sup> Proteomic technologies have overcome these challenges with several methods, namely targeted mass spectrometry via Selected Reaction Monitoring (SRM), iTRAQ, and SWATH-MS (Sequential Window Acquisition of All Theoretical Mass Spectra). Here we discuss several preclinical protein targets involved in GBM identified via proteomic approaches.

Several GBM proteomic studies have identified annexin A2 as a possible drug target.<sup>30, 32, 156</sup> Annexin A2 is a calcium-binding cytoskeletal protein expressed in cancer cells and is strongly correlated with tumor aggression, metastasis, and glioma patient survival.<sup>33</sup> The protein aids the conversion of plasminogen to plasmin, a serine protease that activates metalloproteinases and degrades the extracellular matrix to promote cell metastasis.<sup>157</sup> Consistent overexpression of annexin A2 emphasizes its role in various subtypes of GBM. Thus, annexin A2 may be a promising drug target. Small molecule annexin A2 inhibitors have been developed to prevent human papilloma virus.<sup>158, 159</sup> Further validation of annexin A2 inhibitors in models of GBM is warranted.

One study identified nine potential GBM targets by comparing microarray data sets of neural stem cells and GBM stem cells and further validating the findings with RT-PCR and Western blot.<sup>160</sup> Nine overexpressed proteins: PBK, CENPA, KIF15, DEPDC1, CDC6, DLG7, KIF18A, EZH2, and HMMR, correlated with poor patient survival and are potential GBM drug targets. CENPA was further validated as a potential target in GBM initiating cells.<sup>161</sup> PBK is a MAPKK involved in p38-mediated cell motility and DNA damage response<sup>162</sup> and has been validated *in vivo* as a GBM target.<sup>163</sup> EZH2 has also been validated as a target in GBM, and overexpression is associated with poor prognosis.<sup>164, 165</sup> CDC6, a gene involved in the RB/E2F

pathway, was associated with decreased astrocytic glioma patient survival.<sup>166</sup> Additionally, HMMR was validated as a potential target for GBM stem cell inhibition.<sup>167</sup> The other proteins have not been validated further in the context of GBM but may also represent potential drug targets.

Proteomic approaches may also explain potential reasons for drug or target failure. To determine why anti-angiogenic therapies failed, a proteomic approach based on SRM was employed on patient-derived intracranial GBM xenografts in rodents.<sup>49</sup> Levels of tricarboxylic acid cycle enzymes such as isocitrate dehydrogenase and aldehyde dehydrogenase decrease in response to anti-angiogenic therapy, suggesting the cells evade death by increasing glycolysis.<sup>49</sup> Additionally, a systems-based statistical analysis of a proteomic and transcriptomic signature of GBM was identified, concluding a strong link between GBM invasive properties and the TGF- $\beta$  signaling pathways.<sup>168</sup> Targeting these pathways may inhibit GBM proliferation; however, target validation is necessary to rule out proteins that do not drive tumor growth.

### **Target validation**

Correlation between gene expression and patient survival does not necessarily indicate the gene (or protein) is critical for tumor progression, or a viable drug target. For example, tyrosine hydroxylase is required for the synthesis of dopamine, and inhibition of TH, at least by the reported inhibitors, showed significant adverse effects. Therefore, rigorous validation of the 20 genes determined from TCGA analysis is crucial to move forward and develop a viable treatment option for GBM.

Clinical trials fail often due to insufficient target validation in the preclinical stage of the drug discovery process. To validate each target appropriately, CRISPR-Cas9-mediated gene

knockdown can be used to assess tumor growth *in vitro* and *in vivo*. Gene knockouts that significantly inhibit tumor growth would be pursued for druggability. High throughput small molecule binding screens of each target could be run, using differential scanning fluorimetry or other binding determination methods. For targets with selective inhibitors, further validation can be performed. While our TCGA analysis results demonstrate a potential direction for GBM drug discovery research, target validation is required before further effort is used to develop inhibitors of these targets.

### **Synthetic lethality**

GBM tumor heterogeneity will likely render single target inhibition ineffective. In general, combination therapies are necessary to halt tumor growth. A potential approach to identify synergistic interactions is to perform “synthetic lethal” screens. Synthetic lethality is the concept that a combination of two or more gene mutations or alterations is necessary for cell death, and the mutation or inhibition of only one of the genes allows tumor cells to survive.<sup>169</sup> Synthetic lethal combinations can be identified via several strategies. For example, large, short hairpin RNA (shRNA) libraries can be used to screen cell lines with an inhibitor, that, when in combination with certain shRNAs, causes a lethal phenotype. Synthetic lethal pairs can also be discovered computationally, by mining large datasets. Using this method, the known synthetic lethal relationship between *P53* and *PLK1* was validated by comparing patient survival data with pairs of genes in which the expression of one of the genes was under-represented.<sup>170</sup>

Several other synthetic lethal combinations have been identified in the context of GBM. Large-scale, shRNA library screening identified that the inhibition of *MYC*, *P38MAPK*, or *ERK* signaling pathways may be synthetically lethal with PI3K inhibitor PX-866.<sup>171</sup> EGFR inhibition is

synthetically lethal with pharmacological stabilization of *P53*.<sup>172</sup> *P53* mutations have also sensitized GBM cells to combined p-AKT inhibition and radiation, by antagonizing DNA repair.<sup>173</sup> Furthermore, *IDH1*-mutated gliomas are potentially more susceptible to BCL-xL inhibition than other gliomas.<sup>174</sup> Continued work in this area is expected to generate novel effective treatment strategies for GBM.

### **Preclinical models of glioblastoma**

Preclinical *in vivo* models of GBM can recapitulate hallmarks of cancer including tissue invasion, sustained angiogenesis, evasion of apoptosis, and cancer-specific metabolism that cannot be modeled *in vitro*. Robust models of GBM that mimic the human tumor microenvironment are needed to assess drug safety profiles and reduce clinical trial failure. There are three major types of preclinical GBM models: chemically induced models, xenograft models, and genetically engineered mouse models (GEMMs). Some of the current and state-of-the-art strategies for developing animal models of GBM will be summarized here.<sup>175, 176</sup>

GBM mouse models have evolved in an attempt to mirror human tumor characteristics and microenvironment. One of the earliest models, the chemically induced GBM tumor, is generated by treating rats with N-nitroso compounds. The spontaneity of tumor generation in this model provides insight about the underlying molecular pathways involved in chemically induced mutagenesis. However, the rat tumors generally do not model human GBM histological characteristics, and cell lines suffer from genetic drift.<sup>175</sup> Xenografts of human tumor cell lines injected into immunodeficient mice have also been used. However, these models can be difficult to establish and do not factor in immune response or changes in stromal environment.<sup>175</sup> Therefore, GEMMs are excellent as *in vivo* GBM models because of the extensive molecular characterization

of the human GBM tumor genome, which confirmed key mutations that drive oncogenesis. Compounds of interest can be tested on several variations of GEMMs, including those generated via combinations of *P53*, *PTEN*, *NF1*, *RB*, and PDGF alterations.<sup>177</sup> GEMMs have also provided valuable insight on the cell of origin of GBM. For example, GBM tumors can form in mice with conditional tumor suppressor alleles of *NF1*, *P53*, and *PTEN* that are injected with cre recombinase-expressing adenovirus.<sup>178</sup> The downsides of GEMMs are that they can be costly and time-consuming, and do not exhibit the heterogeneity of human GBM tumors. Additional *in vivo* models include orthotopic models in which GBM cells are injected intracranially, and patient-derived xenograft (PDX) models, in which primary patient tumors are cultured and implanted in mice subcutaneously.<sup>179</sup> Furthermore, a Human Glioblastoma Cell Culture (HGCC) open resource has been organized to promote *in vitro* and *in vivo* testing.<sup>180</sup> The HGCC resource contains a bank of 48 GBM cell lines derived from patients, for translational research use. This bank allows robust *in vivo* representations of GBM to promote new discoveries. Numerous *in vivo* models of GBM exist, but none perfectly capture the complexity of tumor biology and microenvironment.

Because each GBM tumor model has its shortcomings, there remains a need for better preclinical models for compound screening. One strategy to meet this need involves avatar mice and co-clinical models of GBM.<sup>181</sup> The mouse avatar allows efficient testing of different treatment strategies by implanting GBM tumor tissue resected from the patient into mice with the goal of selecting a promising therapy for each individual patient.<sup>181</sup> Unfortunately, grafted PDX tumors are altered by the mouse biology and do not predict response to treatment with great accuracy.<sup>182</sup> CRISPR/Cas9 technology was previously used to generate *P53*, *PTEN*, and *NF1* gene deletions in mice.<sup>183</sup> While the CRISPR/Cas9 system represents a more convenient model for *in vivo* tumor

development, the need for an accurate model of GBM still exists. In general, *in vivo* models that mimic human intratumoral heterogeneity, tumor initiation, and tumor microenvironment are needed to accurately assess *in vivo* efficacy of a drug.

## **Blood-brain barrier**

### **Characteristics of the blood-brain barrier**

The BBB is responsible for nutrient transport, homeostasis, and communication between the body and the brain and also prevents foreign substances from reaching the brain. Research on the BBB dates to the 1880s, when a barrier to the transport of solutes from the blood to the brain was discovered. Paul Ehrlich furthered BBB research with experiments demonstrating that passage into the brain of peripherally injected dyes was impeded. Small molecule permeability of the BBB is an important consideration for drug development. Not only does the BBB impede small molecule transport, but active BBB transporters clear foreign material that passes the protective layers. The BBB is a dynamic, flexible interface between the brain and the body.

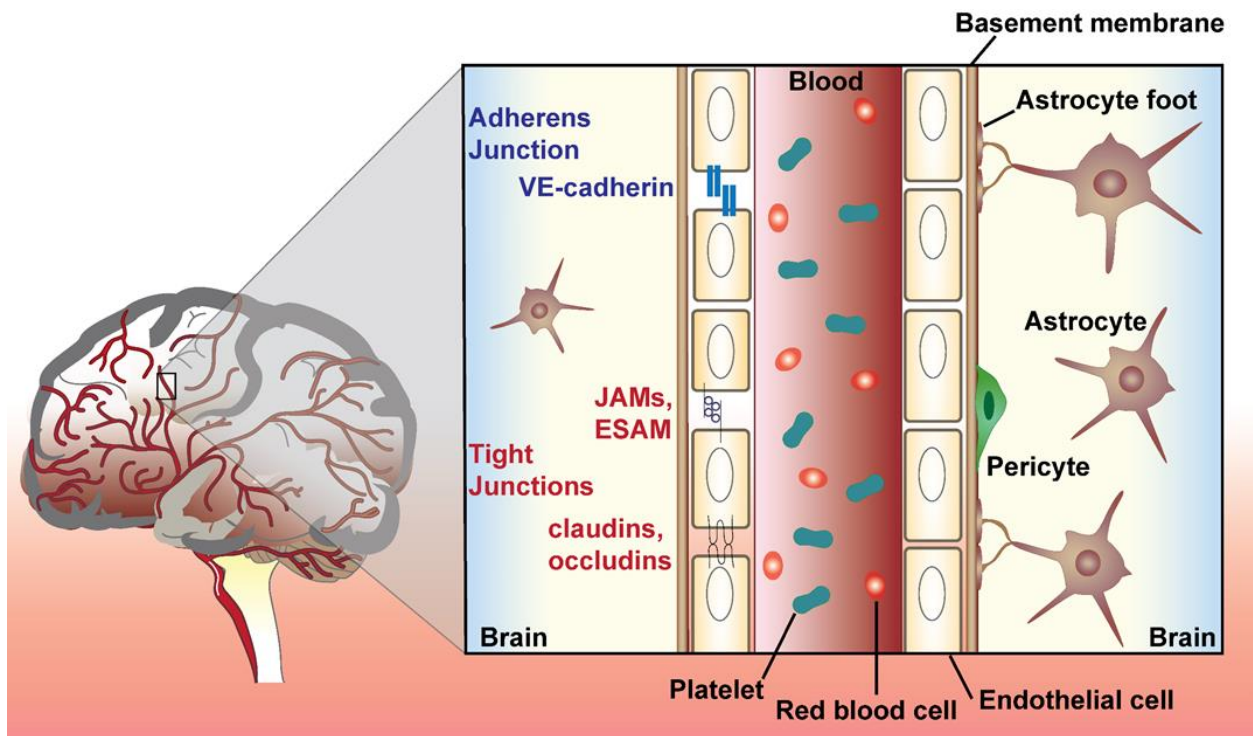


Figure I-8 The blood-brain barrier protects the brain from foreign material with a layer of endothelial cells bound by adherens junctions (i.e. vascular endothelial (VE)-cadherin) and tight junctions (i.e. junction adhesion molecules (JAMs), endothelial cell adhesion molecule (ESAM), claudins, and occludins).

The BBB is composed of a monolayer of endothelial, endepithelial, and pericytic cells held together by restrictive tight junctions (Figure I-8). Two types of cellular junctions halt passive diffusion and prevent leakiness between the endothelial cells: intercellular adherens junctions and paracellular tight junctions. Adherens junctions are composed of vascular endothelium, cadherin, actinin, and catenin.<sup>184</sup> Tight junctions consist of three major proteins: occludin, claudin, and junction adhesion molecules. Occludins are regulated by phosphorylation of serine, tyrosine, and threonine residues. Junction adhesion molecules regulate the formation of tight junctions during the acquisition of cell polarity.<sup>185</sup> Furthermore, there are several other important cytoplasmic accessory proteins including zonula occludens and cingulin. Altogether, these proteins maintain the integrity of the BBB.

Nutrients and small molecules may be transported in and out of the brain by various methods, including passive diffusion, carrier-mediated transport, endocytosis, and active transport. Small biomolecules, such as water and various lipid-soluble molecules, are transported by passive diffusion. Typically, small lipophilic compounds will diffuse through the BBB; however, these properties make compounds more likely to be P-glycoprotein (Pgp) substrates or be taken up by peripheral tissues.<sup>186</sup> Thus, while lower molecular weight and ClogP values are often optimal in theory for CNS drug discovery, the determination of appropriate values is a balancing act. Carrier-mediated transport is driven by two major protein families, the solute carrier (SLC) superfamily and ATP binding cassette (ABC) transporters. The main function of these transporters is to carry essential amino acids and glucose from the blood to the brain. Carrier-mediated transport may be hijacked by drug delivery. For example, System L has a broad substrate specificity for large molecules, and, therefore, can transport levodopa.<sup>187, 188</sup> Endocytosis imports nutrients such as insulin via the formation of intracellular transport vesicles.<sup>189</sup> Active transport requires energy in the form of ATP hydrolysis; the  $\mu$ -opioid agonist fentanyl is likely taken up into the brain via active transport mechanisms.<sup>190</sup> However, due to the complexity of the BBB neovascular unit, drug uptake and efflux likely proceed via multiple transport pathways.

The BBB poses several challenges for effective drug discovery. One challenge is reaching and maintaining effective CNS permeation and drug concentration. The brain uses efflux pumps at the luminal side of the BBB to recognize and remove foreign substances. In particular, ABC transporters prevent a large influx of lipophilic molecules, xenobiotics, toxic metabolites, and drugs.<sup>191</sup> CNS tumors compromise the structural integrity of the BBB, causing it to be leaky at the tumor core.<sup>192</sup> While this may suggest that small molecules may be more permeable at the tumor



site, the BBB surrounding the proliferating cells at the tumor's edge remains intact.<sup>193</sup> Thus, BBB physiology and compound permeability are critical considerations for the CNS drug discovery process.

BBB transporters may provide an opportunity for the pursuit of alternative drug targets. L-dopa, melphalan, baclofen, and gabapentin are examples of drugs that cross the BBB via neutral amino acid transporters. Organic cation-carnitine transporters are used by verapamil, levofloxacin, and cephaloridine.<sup>194</sup> Generally, compounds that use these transporters are similar in size and shape to the endogenous substrate of the protein. Additionally, uptake and efflux transporters can be inhibited by saturating the transporters. For example, saturating the LNAA (large neutral amino acid) transporter with LNAA competes off the excess branched chain amino acids that enter the brain and cause neurotoxicity in maple syrup urine disease.<sup>195</sup> Furthermore, a recent study demonstrated that metastasizing cells may signal to break down the BBB with microRNA-181c, allowing the cells to propagate in the brain.<sup>196</sup> As a whole, successful drug discovery and development will involve efficient and reliable drug delivery methods to significantly improve treatment.

### **Blood-brain barrier computational modeling for drug discovery**

Lipinski et al. developed a groundbreaking method of screening for orally bioavailable, drug-like molecules by using physicochemical properties known as the "Rule of Five."<sup>197</sup> Traditional CNS drugs are biased toward targeting monoamine GPCRs, transporters, and ion channels. Therefore, an assessment of the physicochemical properties of CNS drugs would conclude that CNS drugs should be small lipophilic compounds. Generally, CNS drugs are smaller and more lipophilic than oral non-CNS drugs, and have fewer hydrogen bond donors and a lower

topological polar surface area.<sup>198</sup> However, with increasing drug discovery efforts focused on non-traditional CNS targets, understanding of CNS-penetrant compounds could expand. To ameliorate this problem, a CNS multiparameter optimization (CNS MPO) algorithm was designed by Pfizer scientists, with the goal of streamlining the CNS drug discovery process.<sup>199</sup> The CNS MPO algorithm involves six physicochemical parameters (lipophilicity (ClogP), distribution at pH = 7.4 (ClogD), molecular weight (MW), topological polar surface area (TPSA), most basic center (pK<sub>a</sub>), and the number of hydrogen bond donors (HBD)) relative to CNS penetration and success. The value of each parameter is weighted (0-1) based on the probability of the compound crossing the BBB (0 = low probability; 1 = high probability). For example, it is well known that a compound with a ClogP value less than 0 will be less likely to cross the BBB, therefore a compound with a ClogP value less than zero would receive a 0 for the ClogP parameter. The total CNS MPO desirability score is the summation of the weighted scores based on each of the six properties, with a range from 0 to 6. An analysis of FDA-approved CNS drugs demonstrated 74 % have a CNS MPO desirability score  $\geq 4$ .<sup>199</sup> To assess the BBB permeability of novel GBM clinical candidates, we applied the algorithm to 73 of the small molecule compounds currently undergoing clinical trials related to GBM treatment.

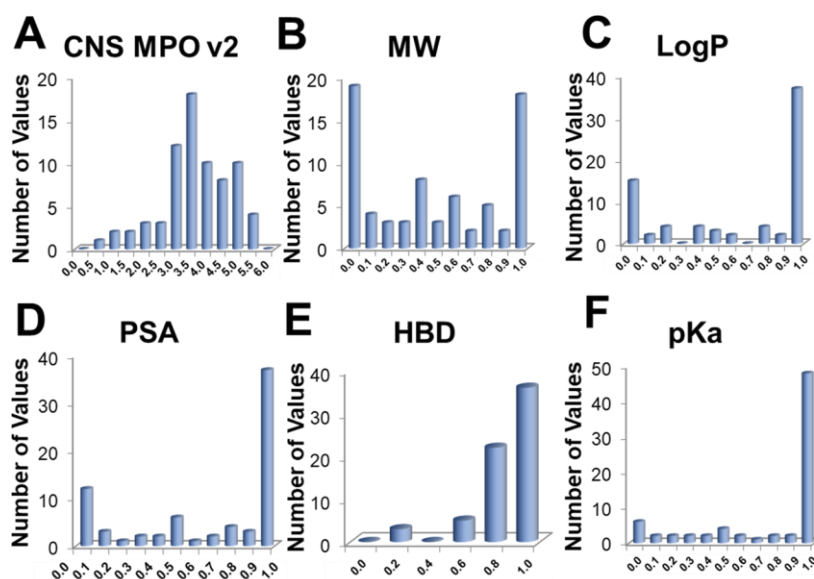


Figure I-9 CNS MPO Version 2 scores were calculated for 73 GBM drug candidates. Plots are shown for scores calculated for (A) Total CNS MPO score, (B) Molecular weight distribution, (C) LogP value distribution, (D) Polar surface area value distribution, (E) Hydrogen bond donor total distribution, and (F) pK<sub>a</sub> value (of the most basic center) distribution.

We determined the CNS desirability score for 73 GBM drug candidates in clinical trials, using the CNS MPO.v2 algorithm (Figure I-9).<sup>200</sup> The CNS MPO.v2 desirability score weighs five important CNS physicochemical properties: molecular weight, lipophilicity (ClogP), number of hydrogen bond donors, topical polar surface area, and pK<sub>a</sub> (of the most basic center), from 0 to 1. These properties were calculated with ADMET Predictor Version 8. The desirability score was the summation of the weighted score of each component, with the number of HBD score doubled. The HBD value was found to correlate strongly with BBB permeability, whereas ClogD, a variable used in the original equation, was somewhat redundant to ClogP and removed.<sup>200</sup> Interestingly, only 37 % of the small molecule candidates in clinical trials currently have a score  $\geq 4$ , a much lower percentage than the 74 % of FDA-approved CNS drugs. This may highlight the significance of emphasizing BBB permeability in early-stage drug discovery and may explain future clinical trial failures (or highlights the use of novel drug delivery methods). The compound that scored

highest, LB100 with a 5.68 out of 6, is a protein phosphatase 2A inhibitor. Compounds with a desirable molecular weight (score = 1) made up 23 % of the group, while an almost equal amount (25 %) had higher-than-optimal molecular weight values, over 500 Da. Most of the compounds (48 %) had a ClogP score of 1. A large portion of the compounds had a favorable TPSA (45 % between 40 and 90 Å<sup>2</sup>). Several of the compounds had an appropriate number of hydrogen bond donors as well (36 % with scores > 0.8). The majority of the compounds (64 %) had a pK<sub>a</sub> desirability score of 1 (pK<sub>a</sub> < 8 for the most basic center). Use of this CNS MPO algorithm together with other useful tools for predicting biological behavior of small molecules could enhance and accelerate the drug discovery process.

### **Drug discovery challenges in GBM**

CNS drugs typically have a lower FDA-approval rate than non-CNS drugs. Additionally, oncology drug discovery attrition rates are characteristically high, second only to the therapeutic area of woman's health.<sup>201</sup> Thus, brain tumor drug discovery is characterized by major obstacles and historical failure.

In a study of CNS drugs entered into clinical trials from 1990-2012, CNS drugs were 45 % less likely to pass Phase III trials than non-CNS drugs, with 46 % failing to show improved efficacy over placebo.<sup>202</sup> Even though bevacizumab received FDA approval, other anti-angiogenesis drug candidates have been less effective. The Phase III "REGAL" (Recentin in Glioblastoma Alone and With Lomustine) trial comparing cediranib and cediranib + lomustine versus placebo in patients with recurrent GBM failed to reach the primary endpoint of progression-free survival (PFS) prolongation.<sup>203</sup> Using a different approach, rindopepimut, a conjugate of the EGFRvIII mutation site with an immunogenic carrier protein keyhole limpet hemocyanin, demonstrated efficacy in

Phase I and II trials in combination with temozolomide. PFS and median overall survival (OS) were 10-15 and 22-26 months, respectively, compared to 6 and 15 months in historical controls.<sup>204</sup> Unfortunately, in the Phase III study, rindopepimut failed to meet OS endpoint criteria; however, this was due to a significant outperformance of the control arm (median OS = 21.1 months) compared to the treatment arm (median OS = 20.4 months).<sup>205</sup> Trials with rindopepimut will continue, but this failure highlights an important obstacle faced when bringing a novel therapy to the market.

Several obstacles impede the drug discovery process for GBM treatment. Challenges include identifying an effective target at the early research stages amidst the complex intratumoral molecular heterogeneity, identifying a therapy that is permeable to the BBB, and developing robust clinical trials to assess the effectiveness of the potential treatment. Furthermore, a recent study highlighted the variation in the epigenetic tumor microenvironment of *in vitro* and *in vivo* models, suggesting that research with *in vitro* cancer cell lines is a “therapeutic roadblock” to GBM drug discovery.<sup>206</sup> This study identified a single gene, jumonji C-domain-containing protein 6 (JMJD6), as a potential target. JMJD6 interacts with bromodomain containing 4 (BRD4), and JMJD6 shRNA knockdown was lethal in both *in vitro* and *in vivo* models.<sup>206</sup>

As for the pharmacokinetics of the drug, there are several important limitations to consider for any drug candidate. First, the compound must reach the tumor site without diffusing into other tissue and must reach therapeutic concentrations. For example, a retrospective pharmacokinetic analysis of lapatinib after a failed Phase I/II clinical trial revealed that therapeutic concentrations of the drug were not reached.<sup>207</sup> Additionally, CNS drugs must be able to cross the BBB, which means they must have appropriate lipophilicity and size. Lipophilicity is measured by the octanol-

water partition coefficient of a compound (ClogP), and CNS drugs optimally have a ClogP = 2. The size of a compound is measured by its molecular weight and polar surface area, which are optimal below 450 g/mol and 90 Å<sup>2</sup>, respectively, for CNS drugs.<sup>208</sup> This is a large obstacle for biologics, since EGFR antibodies cannot cross the BBB. Generally, only 0.1 - 0.2 % of an administered antibody crosses the BBB and reaches the tumor site.<sup>209</sup> (Here, it should be noted that bevacizumab likely does not need to cross the BBB to target the VEGF receptors in the lumen of capillaries of blood vessels in the brain.) Drugs could be administered intratumorally, as with the case of DNX-2401. In a Phase I trial, DNX-2401, an oncolytic adenovirus, demonstrated antitumor activity with no dose-limiting side effects.<sup>210</sup> Intratumoral injections, while effective, may be time-consuming, unfamiliar to oncologists, and pose biosafety concerns. Another consideration is the presence of Pgp efflux pumps that remove foreign material escaping past the BBB. While the BBB is impaired at the tumor site, allowing for increased permeability, the dense endothelium of vasculature providing nutrients to the tumor is not compromised, and therefore most of the BBB remains intact.<sup>211</sup> These issues should be addressed in the preclinical phase, before bringing drug candidates into clinical trials.

Retrospective analysis of EGFR inhibitors provided insight into their failure in GBM clinical trials. EGFR inhibitors are widely and effectively used in preclinical models of GBM; however, clinical trials with these inhibitors failed to detect any improvement in outcome. These tyrosine kinase inhibitors (TKI), namely erlotinib and gefitinib, likely failed clinical trials due to limited brain exposure from Pgp and ABCG2-mediated efflux.<sup>3,4</sup> Additionally, gefitinib inhibits signaling of EGFR proteins with mutations in exons 19 and 21 of the TK domain that are often

absent in gliomas.<sup>212</sup> This phenomenon suggests more rigorous preclinical research should be conducted before expensive clinical trials are initiated.

A few recent successes in TKIs, osimertinib and GDC-0084, should be noted. The third generation EGFR inhibitor osimertinib (AZD9291) has been studied for its efficacy against non-small cell lung cancer (NSCLC) and is undergoing a large Phase I/II trial to determine the maximum tolerated dose in patients with advanced NSCLC (NCT01802632). Preclinical evaluation of osimertinib demonstrated the compound is more BBB-permeable than gefitinib and other TKIs.<sup>213</sup> Another TKI, GDC-0084, was demonstrated to cross the BBB in a first-in-human Phase I dose-escalation study in patients with high-grade glioma.<sup>214</sup> Extensive structure-activity relationship analysis on the dual PI3K/mTOR inhibitor revealed that removal of a methyl group at the 2 position of the pyridine side chain of the purine-based scaffold increased cellular potency and human metabolic stability and decreased efflux ratios.<sup>215</sup> Since BBB permeability has been a major problem with current EGFR TKIs, osimertinib and GDC-0084 both represent exciting inhibitors that have the potential to become efficacious treatments for brain and potentially other cancers.

While recent efforts have advanced GBM drug discovery, non-pharmacokinetic problems, including clinical trial organization, remain a large obstacle to drug development. Because GBM is an orphan disease, clinical trial participation is low, which prevents the detection of subtle differences in treatment with statistical significance. Other challenges include determination of appropriate controls, stratification according to prognostic factors, and definition of clinical endpoint.<sup>216</sup> In addition, it is difficult to monitor the molecular signature of a brain tumor because surgeries are expensive and risky. It will be important to establish non-imaging methods of

determining drug efficacy because targeted therapies may be cytostatic. In addition, biomarkers to measure treatment response will be useful for GBM clinical trials.

### **Conclusions and future directions**

Treatment of GBM is a complex and formidable, but not unsolvable, problem. The girth of available genomic information directs research strategies, allowing researchers to pursue meaningful hypotheses supported by patterns in population-level genomics. In tandem, novel proteomic tools are a valuable resource that will enhance our understanding of GBM tumor complexity. Genomic methods have already revealed a molecular fingerprint of the disease and pathways on which to focus our research efforts. Despite the emergence of more specific molecular classifications of GBM, targeted therapies to treat specific GBM subtypes are not yet realized. Numerous failed clinical trials suggest combination therapies will likely be the most promising method of GBM treatment, and emphasis should be applied to drug design and pharmacokinetic properties. With this study, we have identified 20 genes that may play important roles in GBM progression. These genes should be validated as potential targets for GBM drug discovery, as they correlate with poor overall patient survival. We have also uncovered novel transcription factors and signaling molecules involved in GBM that may regulate EGFR signaling. Targeting transcription factors and membrane proteins upstream of EGFR signaling may prove a promising therapeutic strategy for the treatment of GBM. Several genes identified in our analysis have been linked with GBM or EGFR signaling in previous studies. It should be noted that gene expression of the 20 targets could be a consequence of oncogenic stress, rather than tumor growth and further target validation is necessary. This analysis may reorganize research priorities towards targeting receptors and proteins involved in glioma progression. In the future, both genomic and proteomic



approaches will be standard tools not only to identify novel drug targets, but also to identify non-invasive biomarkers for diagnosis and treatment response.

## Notes

The article in which the rationale for the CNS MPO.v2 algorithm was published was retracted in February 2019 by Eli Lilly in order to validate substantial changes made to the manuscript.<sup>200, 217</sup> Thus, until the updated CNS MPO.v2 manuscript is published, caution should be used when interpreting scores calculated with the CNS MPO.v2 algorithm.

## References

1. Ostrom, Q. T.; Gittleman, H.; Liao, P.; Vecchione-Koval, T.; Wolinsky, Y.; Kruchko, C.; Barnholtz-Sloan, J. S. CBTRUS statistical report: Primary brain and other central nervous system tumors diagnosed in the United States in 2010-2014. *Neuro Oncol* **2017**, *19*, v1-v88.
2. Santos, R.; Ursu, O.; Gaulton, A.; Bento, A. P.; Donadi, R. S.; Bologa, C. G.; Karlsson, A.; Al-Lazikani, B.; Hersey, A.; Oprea, T. I.; Overington, J. P. A comprehensive map of molecular drug targets. *Nat Rev Drug Discov* **2017**, *16*, 19-34.
3. Agarwal, S.; Sane, R.; Gallardo, J. L.; Ohlfest, J. R.; Elmquist, W. F. Distribution of gefitinib to the brain is limited by P-glycoprotein (ABCB1) and breast cancer resistance protein (ABCG2)-mediated active efflux. *J Pharmacol Exp Ther* **2010**, *334*, 147-55.
4. de Vries, N. A.; Buckle, T.; Zhao, J.; Beijnen, J. H.; Schellens, J. H.; van Tellingen, O. Restricted brain penetration of the tyrosine kinase inhibitor erlotinib due to the drug transporters P-gp and BCRP. *Invest New Drugs* **2012**, *30*, 443-9.
5. Stupp, R.; Mason, W. P.; van den Bent, M. J.; Weller, M.; Fisher, B.; Taphoorn, M. J.; Belanger, K.; Brandes, A. A.; Marosi, C.; Bogdahn, U.; Curschmann, J.; Janzer, R. C.; Ludwin, S. K.; Gorlia, T.; Allgeier, A.; Lacombe, D.; Cairncross, J. G.; Eisenhauer, E.; Mirimanoff, R. O. European Organisation for Research and Treatment of Cancer Brain Tumor and Radiotherapy Groups; National Cancer Institute of Canada Clinical Trials Group. Radiotherapy plus concomitant and adjuvant temozolomide for glioblastoma. *N Engl J Med* **2005**, *352*, 987-96.
6. O'Reilly, S. M.; Newlands, E. S.; Glaser, M. G.; Brampton, M.; Rice-Edwards, J. M.; Illingworth, R. D.; Richards, P. G.; Kennard, C.; Colquhoun, I. R.; Lewis, P.; Stevens, M. F. G. Temozolomide: A new oral cytotoxic chemotherapeutic agent with promising activity against primary brain tumours. *Eur J Cancer* **1993**, *29*, 940-2.
7. Hegi, M. E.; Diserens, A. C.; Gorlia, T.; Hamou, M. F.; de Tribolet, N.; Weller, M.; Kros, J. M.; Hainfellner, J. A.; Mason, W.; Mariani, L.; Bromberg, J. E.; Hau, P.; Mirimanoff, R. O.; Cairncross, J. G.; Janzer, R. C.; Stupp, R. MGMT gene silencing and benefit from temozolomide in glioblastoma. *N Engl J Med* **2005**, *352*, 997-1003.
8. Quinn, J. A.; Jiang, S. X.; Reardon, D. A.; Desjardins, A.; Vredenburgh, J. J.; Rich, J. N.; Gururangan, S.; Friedman, A. H.; Bigner, D. D.; Sampson, J. H.; McLendon, R. E.; Herndon, J. E.; Walker, A.; Friedman, H. S. Phase II trial of temozolomide plus O(6)-benzylguanine in adults with recurrent, temozolomide-resistant malignant glioma. *J Clin Oncol* **2009**, *27*, 1262-7.

9. Robinson, C. G.; Palomo, J. M.; Rahmathulla, G.; McGraw, M.; Donze, J.; Liu, L.; Vogelbaum, M. A. Effect of alternative temozolomide schedules on glioblastoma O-6-methylguanine-DNA methyltransferase activity and survival. *Br J Cancer* **2010**, 103, 498-504.
10. Cheng, S. Y.; Huang, H. J.; Nagane, M.; Ji, X. D.; Wang, D.; Shih, C. C.; Arap, W.; Huang, C. M.; Cavenee, W. K. Suppression of glioblastoma angiogenicity and tumorigenicity by inhibition of endogenous expression of vascular endothelial growth factor. *Proc Natl Acad Sci U S A* **1996**, 93, 8502-07.
11. Stark-Vance, V. Bevacizumab and CPT-11 in the treatment of relapsed malignant glioma. *Neuro Oncol* **2005**, 7, 369.
12. Chinot, O. L.; Wick, W.; Mason, W.; Henriksson, R.; Saran, F.; Nishikawa, R.; Carpentier, A. F.; Hoang-Xuan, K.; Kavan, P.; Cernea, D.; Brandes, A. A.; Hilton, M.; Abrey, L.; Cloughesy, T. Bevacizumab plus radiotherapy-temozolomide for newly diagnosed glioblastoma. *N Engl J Med* **2014**, 370, 709-22.
13. Gilbert, M. R.; Dignam, J. J.; Armstrong, T. S.; Wefel, J. S.; Blumenthal, D. T.; Vogelbaum, M. A.; Colman, H.; Chakravarti, A.; Pugh, S.; Won, M.; Jeraj, R.; Brown, P. D.; Jaeckle, K. A.; Schiff, D.; Stieber, V. W.; Brachman, D. G.; Werner-Wasik, M.; Tremont-Lukats, I. W.; Sulman, E. P.; Aldape, K. D.; Curran, W. J., Jr.; Mehta, M. P. A randomized trial of bevacizumab for newly diagnosed glioblastoma. *N Engl J Med* **2014**, 370, 699-708.
14. Tosoni, A.; Franceschi, E.; Poggi, R.; Brandes, A. A. Relapsed glioblastoma: Treatment strategies for initial and subsequent recurrences. *Curr Treat Options Oncol* **2016**, 17, 49.
15. Gorlia, T.; Stupp, R.; Brandes, A. A.; Rampling, R. R.; Fumoleau, P.; Ditttrich, C.; Campone, M. M.; Twelves, C. C.; Raymond, E.; Hegi, M. E.; Lacombe, D.; van den Bent, M. J. New prognostic factors and calculators for outcome prediction in patients with recurrent glioblastoma: A pooled analysis of EORTC Brain Tumour Group phase I and II clinical trials. *Eur J Cancer* **2012**, 48, 1176-84.
16. Friedman, H. S.; Prados, M. D.; Wen, P. Y.; Mikkelsen, T.; Schiff, D.; Abrey, L. E.; Yung, W. K.; Paleologos, N.; Nicholas, M. K.; Jensen, R.; Vredenburgh, J.; Huang, J.; Zheng, M.; Cloughesy, T. Bevacizumab alone and in combination with irinotecan in recurrent glioblastoma. *J Clin Oncol* **2009**, 27, 4733-40.
17. Taal, W.; Oosterkamp, H. M.; Walenkamp, A. M.; Dubbink, H. J.; Beerepoot, L. V.; Hanse, M. C.; Buter, J.; Honkoop, A. H.; Boerman, D.; de Vos, F. Y.; Dinjens, W. N.; Enting, R. H.; Taphoorn, M. J.; van den Berkmortel, F. W.; Jansen, R. L.; Brandsma, D.; Bromberg, J. E.; van Heuvel, I.; Vernhout, R. M.; van der Holt, B.; van den Bent, M. J. Single-agent bevacizumab or lomustine versus a combination of bevacizumab plus lomustine in patients with recurrent glioblastoma (BELOB trial): A randomised controlled phase 2 trial. *Lancet Oncol* **2014**, 15, 943-53.

18. Ostrom, Q. T.; Gittleman, H.; Xu, J.; Kromer, C.; Wolinsky, Y.; Kruchko, C.; Barnholtz-Sloan, J. S. CBTRUS statistical report: Primary brain and other central nervous system tumors diagnosed in the United States in 2009-2013. *Neuro Oncol* **2016**, 18, v1-v75.
19. Siegel, R. L.; Miller, K. D.; Jemal, A. Cancer statistics, 2016. *CA Cancer J Clin* **2016**, 66, 7-30.
20. Persson, A. I.; Petritsch, C.; Swartling, F. J.; Itsara, M.; Sim, F. J.; Auvergne, R.; Goldenberg, D. D.; Vandenberg, S. R.; Nguyen, K. N.; Yakovenko, S.; Ayers-Ringler, J.; Nishiyama, A.; Stallcup, W. B.; Berger, M. S.; Bergers, G.; McKnight, T. R.; Goldman, S. A.; Weiss, W. A. Non-stem cell origin for oligodendroglioma. *Cancer Cell* **2010**, 18, 669-82.
21. Brennan, C. W.; Verhaak, R. G. W.; McKenna, A.; Campos, B.; Nounshmehr, H.; Salama, S. R.; Zheng, S. Y.; Chakravarty, D.; Sanborn, J. Z.; Berman, S. H.; Beroukhi, R.; Bernard, B.; Wu, C. J.; Genovese, G.; Shmulevich, I.; Barnholtz-Sloan, J.; Zou, L. H.; Vegesna, R.; Shukla, S. A.; Ciriello, G.; Yung, W. K.; Zhang, W.; Sougnez, C.; Mikkelsen, T.; Aldape, K.; Bigner, D. D.; Van Meir, E. G.; Prados, M.; Sloan, A.; Black, K. L.; Eschbacher, J.; Finocchiaro, G.; Friedman, W.; Andrews, D. W.; Guha, A.; Iacocca, M.; O'Neill, B. P.; Foltz, G.; Myers, J.; Weisenberger, D. J.; Penny, R.; Kucherlapati, R.; Perou, C. M.; Hayes, D. N.; Gibbs, R.; Marra, M.; Mills, G. B.; Lander, E.; Spellman, P.; Wilson, R.; Sander, C.; Weinstein, J.; Meyerson, M.; Gabriel, S.; Laird, P. W.; Haussler, D.; Getz, G.; Chin, L.; Network, T. R. The somatic genomic landscape of glioblastoma. *Cell* **2013**, 155, 462-77.
22. Freed-Pastor, W. A.; Prives, C. Mutant p53: One name, many proteins. *Genes Dev* **2012**, 26, 1268-86.
23. Weinberg, R. A. The retinoblastoma protein and cell cycle control. *Cell* **1995**, 81, 323-30.
24. Huang, P. H.; Xu, A. M.; White, F. M. Oncogenic EGFR signaling networks in glioma. *Sci Signal* **2009**, 2, re6.
25. Reifenberger, G.; Wirsching, H. G.; Knobbe-Thomsen, C. B.; Weller, M. Advances in the molecular genetics of gliomas - implications for classification and therapy. *Nat Rev Clin Oncol* **2016**, 14, 434-52.
26. Verhaak, R. G. W.; Hoadley, K. A.; Purdom, E.; Wang, V.; Qi, Y.; Wilkerson, M. D.; Miller, C. R.; Ding, L.; Golub, T.; Mesirov, J. P.; Alexe, G.; Lawrence, M.; O'Kelly, M.; Tamayo, P.; Weir, B. A.; Gabriel, S.; Winckler, W.; Gupta, S.; Jakkula, L.; Feiler, H. S.; Hodgson, J. G.; James, C. D.; Sarkaria, J. N.; Brennan, C.; Kahn, A.; Spellman, P. T.; Wilson, R. K.; Speed, T. P.; Gray, J. W.; Meyerson, M.; Getz, G.; Perou, C. M.; Hayes, D. N.; Canc Genome Atlas Res, N. Integrated genomic analysis identifies clinically relevant subtypes of glioblastoma characterized by abnormalities in PDGFRA, IDH1, EGFR, and NF1. *Cancer Cell* **2010**, 17, 98-110.
27. Shinojima, N.; Tada, K.; Shiraishi, S.; Kamiryo, T.; Kochi, M.; Nakamura, H.; Makino, K.; Saya, H.; Hirano, H.; Kuratsu, J.; Oka, K.; Ishimaru, Y.; Ushio, Y. Prognostic value of

epidermal growth factor receptor in patients with glioblastoma multiforme. *Cancer Res* **2003**, *63*, 6962-70.

28. Chen, J. R.; Xu, H. Z.; Yao, Y.; Qin, Z. Y. Prognostic value of epidermal growth factor receptor amplification and EGFRvIII in glioblastoma: Meta-analysis. *Acta Neurol Scand* **2015**, *132*, 310-22.

29. Wen, P. Y.; Chang, S. M.; Lamborn, K. R.; Kuhn, J. G.; Norden, A. D.; Cloughesy, T. F.; Robins, H. I.; Lieberman, F. S.; Gilbert, M. R.; Mehta, M. P.; Drappatz, J.; Groves, M. D.; Santagata, S.; Ligon, A. H.; Yung, W. K.; Wright, J. J.; Dancey, J.; Aldape, K. D.; Prados, M. D.; Ligon, K. L. Phase I/II study of erlotinib and temsirolimus for patients with recurrent malignant gliomas: North American Brain Tumor Consortium trial 04-02. *Neuro Oncol* **2014**, *16*, 567-78.

30. Polisetty, R.; Gautam, P.; Sharma, R.; Harsha, H.; Nair, S.; Gupta, M.; Uppin, M.; Challa, S.; Puligopu, A.; Ankathi, P.; Purohit, A.; Chandak, G.; Pandey, A.; Sirdeshmukh, R. LC-MS/MS analysis of differentially expressed glioblastoma membrane proteome reveals altered calcium signaling and other protein groups of regulatory functions. *Mol Cell Proteomics* **2012**, *11*, M111.013565.

31. Suk, K. Proteomic analysis of glioma chemoresistance. *Curr Neuropharmacol* **2012**, *10*, 72-9.

32. Maruo, T.; Ichikawa, T.; Kanzaki, H.; Inoue, S.; Kurozumi, K.; Onishi, M.; Yoshida, K.; Kambara, H.; Ouchida, M.; Shimizu, K.; Tamaru, S.; Chiocca, E.; Date, I. Proteomics-based analysis of invasion-related proteins in malignant gliomas. *Neuropathology* **2013**, *33*, 264-75.

33. Maule, F.; Bresolin, S.; Rampazzo, E.; Boso, D.; Della Puppa, A.; Esposito, G.; Porcu, E.; Mitola, S.; Lombardi, G.; Accordi, B.; Tumino, M.; Basso, G.; Persano, L. Annexin 2A sustains glioblastoma cell dissemination and proliferation. *Oncotarget* **2016**, *7*, 54632-49.

34. Jiang, X. C.; Zhou, T. F.; Wang, Z. C.; Bin, Q.; Xia, H. P. HSP47 promotes glioblastoma stemlike cell survival by modulating tumor microenvironment extracellular matrix through TGF-beta pathway. *ACS Chem Neurosci* **2017**, *8*, 128-34.

35. Xiong, Y. J.; Ji, W. J.; Fei, Y.; Zhao, Y. F.; Wang, L.; Wang, W. J.; Han, M. L.; Tan, C. H.; Fei, X. F.; Huang, Q.; Liang, Z. Q. Cathepsin L is involved in X-ray-induced invasion and migration of human glioma U251 cells. *Cell Signal* **2017**, *29*, 181-91.

36. Ono, Y.; Chiba, S.; Yano, H.; Nakayama, N.; Saio, M.; Tsuruma, K.; Shimazawa, M.; Iwama, T.; Hara, H. Glycoprotein nonmetastatic melanoma protein B (GPNMB) promotes the progression of brain glioblastoma via Na<sup>+</sup>/K<sup>+</sup>-ATPase. *Biochem Biophys Res Commun* **2016**, *481*, 7-12.

37. Godoy, P.; Montaldi, A. P. L.; Sakamoto-Hojo, E. T. HEB silencing induces anti-proliferative effects on U87MG cells cultured as neurospheres and monolayers. *Mol Med Rep* **2016**, *14*, 5253-60.
38. Gu, J. J.; Zhang, J. H.; Chen, H. J.; Wang, S. S. TPX2 promotes glioma cell proliferation and invasion via activation of the AKT signaling pathway. *Oncol Lett* **2016**, *12*, 5015-22.
39. Wu, J. H.; Li, L. F.; Jiang, G. Y.; Zhan, H.; Wang, N. N. B-cell CLL/lymphoma 3 promotes glioma cell proliferation and inhibits apoptosis through the oncogenic STAT3 pathway. *Int J Oncol* **2016**, *49*, 2471-9.
40. Petricoin, E. F.; Ardekani, A. M.; Hitt, B. A.; Levine, P. J.; Fusaro, V. A.; Steinberg, S. M.; Mills, G. B.; Simone, C.; Fishman, D. A.; Kohn, E. C.; Liotta, L. A. Use of proteomic patterns in serum to identify ovarian cancer. *Lancet* **2002**, *359*, 572-7.
41. Soltys, S. G.; Le, Q. T.; Shi, G. Y.; Tibshirani, R.; Giaccia, A. J.; Koong, A. C. The use of plasma surface-enhanced laser desorption/ionization time-of-flight mass spectrometry proteomic patterns for detection of head and neck squamous cell cancers. *Clin Cancer Res* **2004**, *10*, 4806-12.
42. Xiao, X. Y.; Liu, D. H.; Tang, Y.; Guo, F. H.; Xia, L.; Liu, J.; He, D. C. Development of proteomic patterns for detecting lung cancer. *Dis Markers* **2003**, *19*, 33-9.
43. Varnum, S. M.; Covington, C. C.; Woodbury, R. L.; Petritis, K.; Kangas, L. J.; Abdullah, M. S.; Pounds, J. G.; Smith, R. D.; Zangar, R. C. Proteomic characterization of nipple aspirate fluid: Identification of potential biomarkers of breast cancer. *Breast Cancer Res Treat* **2003**, *80*, 87-97.
44. Akers, J. C.; Ramakrishnan, V.; Kim, R.; Phillips, S.; Kaimal, V.; Mao, Y.; Hua, W.; Yang, I.; Fu, C. C.; Nolan, J.; Nakano, I.; Yang, Y.; Beaulieu, M.; Carter, B. S.; Chen, C. C. miRNA contents of cerebrospinal fluid extracellular vesicles in glioblastoma patients. *J Neurooncol* **2015**, *123*, 205-16.
45. Fathi, A. T.; Nahed, B. V.; Wander, S. A.; Iafrate, A. J.; Borger, D. R.; Hu, R. L.; Thabet, A.; Cahill, D. P.; Perry, A. M.; Joseph, C. P.; Muzikansky, A.; Chi, A. S. Elevation of urinary 2-hydroxyglutarate in IDH-mutant glioma. *Oncologist* **2016**, *21*, 214-9.
46. Patel, V.; Gokulrangan, G.; Chowdhury, S.; Chen, Y.; Sloan, A.; Koyuturk, M.; Barnholtz-Sloan, J.; Chance, M. Network signatures of survival in glioblastoma multiforme. *PLoS Comput Biol* **2013**, *9*, e1003237.
47. Di Meo, A.; Diamandis, E. P.; Rodriguez, H.; Hoofnagle, A. N.; Ioannidis, J.; Lopez, M. What is wrong with clinical proteomics? *Clin Chem* **2014**, *60*, 1258-66.

48. Broad Institute TCGA Genome Data Analysis Center. Firehose stddata\_\_2016\_01\_28 run. In Broad Institute of MIT Harvard: 2016.
49. Demeure, K.; Fack, F.; Duriez, E.; Tiemann, K.; Bernard, A.; Golebiewska, A.; Bougnaud, S.; Bjerkvig, R.; Domon, B.; Niclou, S. P. Targeted proteomics to assess the response to anti-angiogenic treatment in human glioblastoma (GBM). *Mol Cell Proteomics* **2016**, *15*, 481-92.
50. Freije, W. A.; Castro-Vargas, F. E.; Fang, Z.; Horvath, S.; Cloughesy, T.; Liao, L. M.; Mischel, P. S.; Nelson, S. F. Gene expression profiling of gliomas strongly predicts survival. *Cancer Res* **2004**, *64*, 6503-10.
51. Murat, A.; Migliavacca, E.; Gorlia, T.; Lambiv, W. L.; Shay, T.; Hamou, M. F.; de Tribolet, N.; Regli, L.; Wick, W.; Kouwenhoven, M. C.; Hainfellner, J. A.; Heppner, F. L.; Dietrich, P. Y.; Zimmer, Y.; Cairncross, J. G.; Janzer, R. C.; Domany, E.; Delorenzi, M.; Stupp, R.; Hegi, M. E. Stem cell-related "self-renewal" signature and high epidermal growth factor receptor expression associated with resistance to concomitant chemoradiotherapy in glioblastoma. *J Clin Oncol* **2008**, *26*, 3015-24.
52. Yu, F.; Fu, W. M. Identification of differential splicing genes in gliomas using exon expression profiling. *Mol Med Rep* **2015**, *11*, 843-50.
53. Nguyen, D. T.; Mathias, S.; Bologna, C.; Brunak, S.; Fernandez, N.; Gaulton, A.; Hersey, A.; Holmes, J.; Jensen, L. J.; Karlsson, A.; Liu, G.; Ma'ayan, A.; Mandava, G.; Mani, S.; Mehta, S.; Overington, J.; Patel, J.; Rouillard, A. D.; Schurer, S.; Sheils, T.; Simeonov, A.; Sklar, L. A.; Southall, N.; Ursu, O.; Vidovic, D.; Waller, A.; Yang, J.; Jadhav, A.; Oprea, T. I.; Guha, R. Pharos: Collating protein information to shed light on the druggable genome. *Nucleic Acids Res* **2017**, *45*, D995-D1002.
54. Tenzen, T.; Allen, B. L.; Cole, F.; Kang, J. S.; Krauss, R. S.; McMahon, A. P. The cell surface membrane proteins cdo and bloc are components and targets of the hedgehog signaling pathway and feedback network in mice. *Dev Cell* **2006**, *10*, 647-56.
55. Feng, Y. H.; Chen, W. Y.; Kuo, Y. H.; Tung, C. L.; Tsao, C. J.; Shiau, A. L.; Wu, C. L. Elov16 is a poor prognostic predictor in breast cancer. *Oncol Lett* **2016**, *12*, 207-12.
56. Riese, D. J.; Cullum, R. L. Epiregulin: Roles in normal physiology and cancer. *Semin Cell Dev Biol* **2014**, *28*, 49-56.
57. Batistatou, A.; Stefanou, D.; Goussia, A.; Arkoumani, E.; Papavassiliou, A. G.; Agnantis, N. J. Estrogen receptor beta (ER beta) is expressed in brain astrocytic tumors and declines with dedifferentiation of the neoplasm. *J Cancer Res Clin Oncol* **2004**, *130*, 405-10.
58. Sareddy, G. R.; Li, X. N.; Liu, J. Y.; Viswanadhapalli, S.; Garcia, L.; Gruslova, A.; Cavazos, D.; Garcia, M.; Strom, A. M.; Gustafsson, J. A.; Tekmal, R. R.; Brenner, A.; Vadlamudi,



- R. K. Selective estrogen receptor beta agonist LY500307 as a novel therapeutic agent for glioblastoma. *Sci Rep* **2016**, 6, 24185.
59. Hou, S.; Landego, I.; Jayachandran, N.; Miller, A.; Gibson, I. W.; Ambrose, C.; Marshall, A. J. Follicular dendritic cell secreted protein FDC-SP controls IgA production. *Mucosal Immunol* **2014**, 7, 948-57.
60. Wang, C. G.; Zhou, L.; Li, S. A.; Wei, J. C.; Wang, W.; Zhou, T.; Liao, S. J.; Weng, D. H.; Deng, D. R.; Weng, Y. J.; Wang, S. X.; Ma, D. C4orf7 contributes to ovarian cancer metastasis by promoting cancer cell migration and invasion. *Oncol Rep* **2010**, 24, 933-9.
61. Phillips-Mason, P. J.; Craig, S. E. L.; Brady-Kalnay, S. M. A protease storm cleaves a cell-cell adhesion molecule in cancer: Multiple proteases converge to regulate PTPmu in glioma cells. *J Cell Biochem* **2014**, 115, 1609-23.
62. Liu, Y. C.; Yen, H. Y.; Chen, C. Y.; Chen, C. H.; Cheng, P. F.; Juan, Y. H.; Khoo, K. H.; Yu, C. J.; Yang, P. C.; Hsu, T. L.; Wong, C. H. Sialylation and fucosylation of epidermal growth factor receptor suppress its dimerization and activation in lung cancer cells. *Proc Natl Acad Sci U S A* **2011**, 108, 11332-7.
63. Medema, J. P.; de Jong, J.; Peltenburg, L. T. C.; Verdegaal, E. M. E.; Gorter, A.; Bres, S. A.; Franken, K.; Hahne, M.; Albar, J. P.; Melief, C. J. M.; Offringa, R. Blockade of the granzyme B/perforin pathway through overexpression of the serine protease inhibitor PI-9/SPI-6 constitutes a mechanism for immune escape by tumors. *Proc Natl Acad Sci U S A* **2001**, 98, 11515-20.
64. Rousalova, I.; Krepela, E. Granzyme B-induced apoptosis in cancer cells and its regulation (Review). *Int J Oncol* **2010**, 37, 1361-78.
65. Seol, M. A.; Chu, I. S.; Lee, M. J.; Yu, G. R.; Cui, X. D.; Cho, B. H.; Ahn, E. K.; Leem, S. H.; Kim, I. H.; Kim, D. G. Genome-wide expression patterns associated with oncogenesis and sarcomatous transdifferentiation of cholangiocarcinoma. *BMC Cancer* **2011**, 11, 78.
66. Yang, Z. Q.; Liu, G.; Bollig-Fischer, A.; Giroux, C. N.; Ethier, S. P. Transforming properties of 8p11-12 amplified genes in human breast cancer. *Cancer Res* **2010**, 70, 8487-97.
67. Zou, J. R.; Guo, P.; Lv, N. H.; Huang, D. Q. Lipopolysaccharide-induced tumor necrosis factor-alpha factor enhances inflammation and is associated with cancer (Review). *Mol Med Rep* **2015**, 12, 6399-404.
68. Hong, J. H.; Kwak, Y.; Woo, Y.; Park, C.; Lee, S. A.; Lee, H.; Park, S. J.; Suh, Y.; Suh, B. K.; Goo, B. S.; Mun, D. J.; Sanada, K.; Nguyen, M. D.; Park, S. K. Regulation of the actin cytoskeleton by the Ndel1-Tara complex is critical for cell migration. *Sci Rep* **2016**, 6, 31827.

69. Bhatia-Gaur, R.; Donjacour, A. A.; Scivolino, P. J.; Kim, M.; Desai, N.; Young, P.; Norton, C. R.; Gridley, T.; Cardiff, R. D.; Cunha, G. R.; Abate-Shen, C.; Shen, M. M. Roles for Nkx3.1 in prostate development and cancer. *Genes Dev* **1999**, *13*, 966-77.
70. Heyn, H.; Moran, S.; Esteller, M. Aberrant DNA methylation profiles in the premature aging disorders Hutchinson-Gilford Progeria and Werner Syndrome. *Epigenetics* **2013**, *8*, 28-33.
71. Teng, C.; Zheng, H. Low expression of microRNA-1908 predicts a poor prognosis for patients with ovarian cancer. *Oncol Lett* **2017**, *14*, 4277-81.
72. Yan, Y.; Zhang, L.; Xu, T.; Zhou, J. X.; Qin, R.; Chen, C.; Zou, Y. X.; Fu, D.; Hu, G. H.; Chen, J. X.; Lu, Y. C. SAMS1 Is highly expressed and associated with a poor survival in glioblastoma multiforme. *Plos One* **2013**, *8*, e81905.
73. Bauerschlag, D. O.; Ammerpohl, O.; Bräutigam, K.; Schem, C.; Lin, Q.; Weigel, M. T.; Hilpert, F.; Arnold, N.; Maass, N.; Meinhold-Heerlein, I.; Wagner, W. Progression-free survival in ovarian cancer is reflected in epigenetic DNA methylation profiles. *Oncology* **2011**, *80*, 12-20.
74. Xie, H.; Notkins, A. L.; Lan, M. S. IA-2, a transmembrane protein tyrosine phosphatase, is expressed in human lung cancer cell lines with neuroendocrine phenotype. *Cancer Res* **1996**, *56*, 2742-4.
75. Katchman, B. A.; Antwi, K.; Hostetter, G.; Demeure, M. J.; Watanabe, A.; Decker, G. A.; Miller, L. J.; Von Hoff, D. D.; Lake, D. F. Quiescin sulfhydryl oxidase 1 promotes invasion of pancreatic tumor cells mediated by matrix metalloproteinases. *Mol Cancer Res* **2011**, *9*, 1621-31.
76. Parrinello, S.; Noon, L. A.; Harrisingh, M. C.; Digby, P. W.; Rosenberg, L. H.; Cremona, C. A.; Echave, P.; Flanagan, A. M.; Parada, L. F.; Lloyd, A. C. NF1 loss disrupts Schwann cell-axonal interactions: A novel role for semaphorin 4F. *Genes Dev* **2008**, *22*, 3335-48.
77. Tekin, I.; Roskoski, R.; Carkaci-Salli, N.; Vrana, K. E. Complex molecular regulation of tyrosine hydroxylase. *J Neural Transm* **2014**, *121*, 1451-81.
78. Denicolai, E.; Tabouret, E.; Colin, C.; Metellus, P.; Nanni, I.; Boucard, C.; Tchoghandjian, A.; Meyronet, D.; Baeza-Kallee, N.; Chinot, O.; Figarella-Branger, D. Molecular heterogeneity of glioblastomas: Does location matter? *Oncotarget* **2016**, *7*, 902-13.
79. Dufies, M.; Giuliano, S.; Ambrosetti, D.; Claren, A.; Ndiaye, P. D.; Mastri, M.; Moghrabi, W.; Cooley, L. S.; Ettaiche, M.; Chamorey, E.; Parola, J.; Vial, V.; Lupu-Plesu, M.; Bernhard, J. C.; Ravaud, A.; Borchielli, D.; Ferrero, J. M.; Bikfalvi, A.; Ebos, J. M.; Khabar, K. S.; Grépin, R.; Pagès, G. Sunitinib stimulates expression of VEGFC by tumor cells and promotes lymphangiogenesis in clear cell renal cell carcinomas. *Cancer Res* **2017**, *77*, 1212-26.
80. Hu, C. C.; Gan, P.; Zhang, R. Y.; Xue, J. X.; Ran, L. K. Identification of prostate cancer lncRNAs by RNA-seq. *Asian Pac J Cancer Prev* **2014**, *15*, 9439-44.

81. Robbins, D. J.; Fei, D. L.; Riobo, N. A. The Hedgehog signal transduction network. *Sci Signal* **2012**, *5*, re6.
82. Ho, D. W.; Kai, A. K.; Ng, I. O. TCGA whole-transcriptome sequencing data reveals significantly dysregulated genes and signaling pathways in hepatocellular carcinoma. *Front Med* **2015**, *9*, 322-30.
83. Edwards, D. K.; Jasny, E.; Yoon, H.; Horscroft, N.; Schanen, B.; Geter, T.; Fotin-Mleczek, M.; Petsch, B.; Wittman, V. Adjuvant effects of a sequence-engineered mRNA vaccine: Translational profiling demonstrates similar human and murine innate response. *J Transl Med* **2017**, *15*, 1.
84. Vyazunova, I.; Maklakova, V. I.; Berman, S.; De, I.; Steffen, M. D.; Hong, W.; Lincoln, H.; Morrissy, A. S.; Taylor, M. D.; Akagi, K.; Brennan, C. W.; Rodriguez, F. J.; Collier, L. S. Sleeping beauty mouse models identify candidate genes involved in gliomagenesis. *Plos One* **2014**, *9*, e113489.
85. Matsuzaka, T.; Shimano, H. Elovl6: A new player in fatty acid metabolism and insulin sensitivity. *J Mol Med* **2009**, *87*, 379-84.
86. Marien, E.; Meister, M.; Muley, T.; del Pulgar, T. G.; Derua, R.; Spraggins, J. M.; Van de Plas, R.; Vanderhoydonc, F.; Machiels, J.; Binda, M. M.; Dehairs, J.; Willette-Brown, J.; Hu, Y. L.; Dienemann, H.; Thomas, M.; Schnabel, P. A.; Caprioli, R. M.; Lacal, J. C.; Waelkens, E.; Swinnen, J. V. Phospholipid profiling identifies acyl chain elongation as a ubiquitous trait and potential target for the treatment of lung squamous cell carcinoma. *Oncotarget* **2016**, *7*, 12582-97.
87. Anelli, L.; Zagaria, A.; Coccaro, N.; Tota, G.; Impera, L.; Minervini, C. F.; Pastore, D.; Minervini, A.; Casieri, P.; Specchia, G.; Albano, F. A novel t(4;16)(q25;q23.1) associated with EGF and ELOVL6 deregulation in acute myeloid leukemia. *Gene* **2013**, *529*, 144-7.
88. Yamashita, Y.; Nishiumi, S.; Kono, S.; Takao, S.; Azuma, T.; Yoshida, M. Differences in elongation of very long chain fatty acids and fatty acid metabolism between triple-negative and hormone receptor-positive breast cancer. *BMC Cancer* **2017**, *17*, 589.
89. Muranaka, H.; Hayashi, A.; Minami, K.; Kitajima, S.; Kohno, S.; Nishimoto, Y.; Nagatani, N.; Suzuki, M.; Kulathunga, L. A. N.; Sasaki, N.; Okada, N.; Matsuzaka, T.; Shimano, H.; Tada, H.; Takahashi, C. A distinct function of the retinoblastoma protein in the control of lipid composition identified by lipidomic profiling. *Oncogenesis* **2017**, *6*, e350.
90. Wu, W. K. K.; Tse, T. T. M.; Sung, J. J. Y.; Li, Z. J.; Yu, L.; Ch, C. H. Expression of ErbB receptors and their cognate ligands in gastric and colon cancer cell lines. *Anticancer Res* **2009**, *29*, 229-34.
91. Sunaga, N.; Kaira, K.; Imai, H.; Shimizu, K.; Nakano, T.; Shames, D. S.; Girard, L.; Soh, J.; Sato, M.; Iwasaki, Y.; Ishizuka, T.; Gazdar, A. F.; Minna, J. D.; Mori, M. Oncogenic KRAS-

induced epiregulin overexpression contributes to aggressive phenotype and is a promising therapeutic target in non-small-cell lung cancer. *Oncogene* **2013**, 32, 4034-42.

92. Shigeishi, H.; Higashikawa, K.; Hiraoka, M.; Fujimoto, S.; Mitani, Y.; Ohta, K.; Takechi, M.; Kamata, N. Expression of epiregulin, a novel epidermal growth factor ligand associated with prognosis in human oral squamous cell carcinomas. *Oncol Rep* **2008**, 19, 1557-64.

93. Jacobs, B.; De Roock, W.; Piessevaux, H.; Van Oirbeek, R.; Biesmans, B.; De Schutter, J.; Fieuws, S.; Vandesompele, J.; Peeters, M.; Van Laethem, J. L.; Humblet, Y.; Penault-Llorca, F.; De Hertogh, G.; Laurent-Puig, P.; Van Cutsem, E.; Tejpar, S. Amphiregulin and epiregulin mRNA expression in primary tumors predicts outcome in metastatic colorectal cancer treated with cetuximab. *J Clin Oncol* **2009**, 27, 5068-74.

94. Li, X.; Massa, P. E.; Hanidu, A.; Peet, G. W.; Aro, P.; Savitt, A.; Mische, S.; Li, J.; Marcu, K. B. IKK alpha, IKK beta, and NEMO/IKK gamma are each required for the NF-kappa B-mediated inflammatory response program. *J Biol Chem* **2002**, 277, 45129-40.

95. Ornskov, D.; Nexø, E.; Sørensen, B. S. Insulin induces a transcriptional activation of epiregulin, HB-EGF and amphiregulin, by a PI3K-dependent mechanism: Identification of a specific insulin-responsive promoter element. *Biochem Biophys Res Commun* **2007**, 354, 885-91.

96. Orso, F.; Penna, E.; Cimino, D.; Astanina, E.; Maione, F.; Valdembri, D.; Giraud, E.; Serini, G.; Sismondi, P.; De Bortoli, M.; Taverna, D. AP-2 alpha and AP-2 gamma regulate tumor progression via specific genetic programs. *FASEB J* **2008**, 22, 2702-14.

97. Gupta, G. P.; Nguyen, D. X.; Chiang, A. C.; Bos, P. D.; Kim, J. Y.; Nadal, C.; Gomis, R. R.; Manova-Todorova, K.; Massague, J. Mediators of vascular remodelling co-opted for sequential steps in lung metastasis. *Nature* **2007**, 446, 765-70.

98. Freed, D. M.; Bessman, N. J.; Kiyatkin, A.; Salazar-Cavazos, E.; Byrne, P. O.; Moore, J. O.; Valley, C. C.; Ferguson, K. M.; Leahy, D. J.; Lidke, D. S.; Lemmon, M. A. EGFR ligands differentially stabilize receptor dimers to specify signaling kinetics. *Cell* **2017**, 171, 683-95.

99. Kohsaka, S.; Hinohara, K.; Wang, L.; Nishimura, T.; Urushido, M.; Yachi, K.; Tsuda, M.; Tanino, M.; Kimura, T.; Nishihara, H.; Gotoh, N.; Tanaka, S. Epiregulin enhances tumorigenicity by activating the ERK/MAPK pathway in glioblastoma. *Neuro Oncol* **2014**, 16, 960-70.

100. Paruthiyil, S.; Parmar, H.; Kerekatte, V.; Cunha, G. R.; Firestone, G. L.; Leitman, D. C. Estrogen receptor beta inhibits human breast cancer cell proliferation and tumor formation by causing a G(2) cell cycle arrest. *Cancer Res* **2004**, 64, 423-8.

101. Nikolos, F.; Thomas, C.; Bado, I.; Gustafsson, J. A. ERbeta sensitizes NSCLC to chemotherapy by regulating DNA damage response. *Mol Cancer Res* **2018**, 16, 233-42.

102. Lorenzi, L.; Doring, C.; Rausch, T.; Benes, V.; Lonardi, S.; Bugatti, M.; Campo, E.; Cabecadas, J.; Simonitsch-Klupp, I.; Borges, A.; Mehta, J.; Agostinelli, C.; Pileri, S. A.; Facchetti, F.; Hansmann, M. L.; Hartmann, S. Identification of novel follicular dendritic cell sarcoma markers, FDCSP and SRGN, by whole transcriptome sequencing. *Oncotarget* **2017**, *8*, 16463-72.
103. Marshall, A. J.; Du, Q. J.; Draves, K. E.; Shikishima, Y.; HayGlass, K. T.; Clark, E. A. FDC-SP, a novel secreted protein expressed by follicular dendritic cells. *J Immunol* **2002**, *169*, 2381-9.
104. Jaaks, P.; Bernasconi, M. The proprotein convertase furin in tumour progression. *Int J Cancer* **2017**, *141*, 654-63.
105. Mercapide, J.; De Cicco, R. L.; Bassi, D. E.; Castresana, J. S.; Thomas, G.; Klein-Szanto, A. J. P. Inhibition of furin-mediated processing results in suppression of astrocytoma cell growth and invasiveness. *Clin Cancer Res* **2002**, *8*, 1740-6.
106. Ventura, E.; Weller, M.; Burghardt, I. Cutting edge: ERK1 mediates the autocrine positive feedback loop of TGF-beta and furin in glioma-initiating cells. *J Immunol* **2017**, *198*, 4569-74.
107. Rucci, N.; Sanita, P.; Angelucci, A. Roles of metalloproteases in metastatic niche. *Curr Mol Med* **2011**, *11*, 609-22.
108. Dahms, S. O.; Jiao, G. S.; Than, M. E. Structural studies revealed active site distortions of human furin by a small molecule inhibitor. *ACS Chem Biol* **2017**, *12*, 2474.
109. Maluch, I.; Levesque, C.; Kwiatkowska, A.; Couture, F.; Ly, K.; Desjardins, R.; Neugebauer, W. A.; Prahl, A.; Day, R. Positional scanning identifies the molecular determinants of a high affinity multi-leucine inhibitor for furin and PACE4. *J Med Chem* **2017**, *60*, 2732-44.
110. Chen, C. Y.; Jan, Y. H.; Juan, Y. H.; Yang, C. J.; Huang, M. S.; Yu, C. J.; Yang, P. C.; Hsiao, M.; Hsu, T. L.; Wong, C. H. Fucosyltransferase 8 as a functional regulator of nonsmall cell lung cancer. *Proc Natl Acad Sci U S A* **2013**, *110*, 630-5.
111. Okeley, N. M.; Alley, S. C.; Anderson, M. E.; Boursalian, T. E.; Burke, P. J.; Emmerton, K. M.; Jeffrey, S. C.; Klussman, K.; Law, C. L.; Sussman, D.; Toki, B. E.; Westendorf, L.; Zeng, W. P.; Zhang, X. Q.; Benjamin, D. R.; Senter, P. D. Development of orally active inhibitors of protein and cellular fucosylation. *Proc Natl Acad Sci U S A* **2013**, *110*, 5404-9.
112. Choy, J. C. Granzymes and perforin in solid organ transplant rejection. *Cell Death Differ* **2010**, *17*, 567-76.
113. Cullen, S. P.; Brunet, M.; Martin, S. J. Granzymes in cancer and immunity. *Cell Death Differ* **2010**, *17*, 616-23.

114. Prizment, A. E.; Vierkant, R. A.; Smyrk, T. C.; Tillmans, L. S.; Nelson, H. H.; Lynch, C. F.; Pengo, T.; Thibodeau, S. N.; Church, T. R.; Cerhan, J. R.; Anderson, K. E.; Limburg, P. J. Cytotoxic T cells and granzyme B associated with improved colorectal cancer survival in a prospective cohort of older women. *Cancer Epidemiol Biomarkers Prev* **2017**, *26*, 622-31.
115. Wagnier, A.; Lafaurie, C.; Legros-Maida, S.; Bourge, J. F.; Sigaux, F.; Sasportes, M.; Paul, P. Down-regulation of human granzyme B expression by glucocorticoids - Dexamethasone inhibits binding to the Ikaros and AP-1 regulatory elements of the granzyme B promoter. *J Biol Chem* **1998**, *273*, 35326-31.
116. Huang, C. J.; Bi, E. G.; Hu, Y.; Deng, W. W.; Tian, Z. G.; Dong, C.; Hu, Y. J.; Sun, B. A novel NF-kappa B binding site controls human granzyme B gene transcription. *J Immunol* **2006**, *176*, 4173-81.
117. Jahrsdörfer, B.; Vollmer, A.; Blackwell, S. E.; Maier, J.; Sontheimer, K.; Beyer, T.; Mandel, B.; Lunov, O.; Tron, K.; Nienhaus, G. U.; Simmet, T.; Debatin, K. M.; Weiner, G. J.; Fabricius, D. Granzyme B produced by human plasmacytoid dendritic cells suppresses T-cell expansion. *Blood* **2010**, *115*, 1156-65.
118. Ordway, J. M.; Bedell, J. A.; Citek, R. W.; Nunberg, A.; Garrido, A.; Kendall, R.; Stevens, J. R.; Cao, D.; Doerge, R. W.; Korshunova, Y.; Holemon, H.; McPherson, J. D.; Lakey, N.; Leon, J.; Martienssen, R. A.; Jeddloh, J. A. Comprehensive DNA methylation profiling in a human cancer genome identifies novel epigenetic targets. *Carcinogenesis* **2006**, *27*, 2409-23.
119. Martorell, O.; Barriga, F. M.; Merlos-Suarez, A.; Attolini, C. S. O.; Casanova, J.; Batlle, E.; Sancho, E.; Casali, A. Iro/IRX transcription factors negatively regulate Dpp/TGF-beta pathway activity during intestinal tumorigenesis. *EMBO Rep* **2014**, *15*, 1210-8.
120. Tang, X. R.; Yang, Y.; Yuan, H. P.; You, J.; Burkatovskaya, M.; Amar, S. Novel transcriptional regulation of VEGF in inflammatory processes. *J Cell Mol Med* **2013**, *17*, 386-97.
121. Dreyfuss, J. M.; Johnson, M. D.; Park, P. J. Meta-analysis of glioblastoma multiforme versus anaplastic astrocytoma identifies robust gene markers. *Mol Cancer* **2009**, *8*, 71.
122. Zhou, Y.; Huang, J.; Yu, X.; Jiang, X.; Shi, Y.; Weng, Y.; Kuai, Y.; Lei, L.; Ren, G.; Feng, X.; Zhong, G.; Liu, Q.; Pan, H.; Zhang, X.; Zhou, R.; Lu, C. LITAF is a potential tumor suppressor in pancreatic cancer. *Oncotarget* **2018**, *9*, 3131-42.
123. Tang, X.; Molina, M.; Amar, S. p53 short peptide (p53pep164) regulates lipopolysaccharide-induced tumor necrosis factor-alpha factor/cytokine expression. *Cancer Res* **2007**, *67*, 1308-16.
124. Zhou, J.; Yang, Z.; Tsuji, T.; Gong, J.; Xie, J.; Chen, C.; Li, W.; Amar, S.; Luo, Z. LITAF and TNFSF15, two downstream targets of AMPK, exert inhibitory effects on tumor growth. *Oncogene* **2011**, *30*, 1892-900.

125. Toyo-Oka, K.; Sasaki, S.; Yano, Y.; Mori, D.; Kobayashi, T.; Toyoshima, Y. Y.; Tokuoka, S. M.; Ishii, S.; Shimizu, T.; Muramatsu, M.; Hiraiwa, N.; Yoshiki, A.; Wynshaw-Boris, A.; Hirotsune, S. Recruitment of katanin p60 by phosphorylated NDEL1, an LIS1 interacting protein, is essential for mitotic cell division and neuronal migration. *Hum Mol Genet* **2005**, *14*, 3113-28.
126. Hayashi, M. A.; Felicori, L. F.; Fresqui, M. A.; Yonamine, C. M. Protein-protein and peptide-protein interactions of NudE-like 1 (Ndel1): A protein involved in schizophrenia. *Curr Protein Pept Sci* **2015**, *16*, 754-67.
127. He, W. W.; Sciavolino, P. J.; Wing, J.; Augustus, M.; Hudson, P.; Meissner, P. S.; Curtis, R. T.; Shell, B. K.; Bostwick, D. G.; Tindall, D. J.; Gelmann, E. P.; Abate-Shen, C.; Carter, K. C. A novel human prostate-specific, androgen-regulated homeobox gene (NKX3.1) that maps to 8p21, a region frequently deleted in prostate cancer. *Genomics* **1997**, *43*, 69-77.
128. Abate-Shen, C.; Banach-Petrosky, W. A.; Sun, X. H.; Economides, K. D.; Desai, N.; Gregg, J. P.; Borowsky, A. D.; Cardiff, R. D.; Shen, M. M. Nkx3.1; Pten mutant mice develop invasive prostate adenocarcinoma and lymph node metastases. *Cancer Res* **2003**, *63*, 3886-90.
129. Jiang, Y.; Wang, X.; Liu, X.; Lv, W.; Zhang, H.; Zhang, M.; Li, X.; Xin, H.; Xu, Q. Enhanced antiglioma efficacy of ultrahigh loading capacity paclitaxel prodrug conjugate self-assembled targeted nanoparticles. *ACS Appl Mater Interfaces* **2017**, *9*, 211-7.
130. Schaefer, L.; Iozzo, R. V. Biological functions of the small leucine-rich proteoglycans: From genetics to signal transduction. *J Biol Chem* **2008**, *283*, 21305-9.
131. Shimizu-Hirota, R.; Sasamura, H.; Kuroda, M.; Kobayashi, E.; Saruta, T. Functional characterization of podocan, a member of a new class in the small leucine-rich repeat protein family. *FEBS Lett* **2004**, *563*, 69-74.
132. Ma, H.; Hueng, D.; Shui, H.; Han, J.; Wang, C.; Lai, Y.; Cheng, S.; Xiao, X.; Chen, M.; Yang, Y. Intratumoral decorin gene delivery by AAV vector inhibits brain glioblastomas and prolongs survival of animals by inducing cell differentiation. *Int J Mol Sci* **2014**, *15*, 4393-414.
133. Seidler, D. G.; Goldoni, S.; Agnew, C.; Cardi, C.; Thakur, M. L.; Owens, R. T.; McQuillan, D. J.; Iozzo, R. V. Decorin protein core inhibits in vivo cancer growth and metabolism by hindering epidermal growth factor receptor function and triggering apoptosis via caspase-3 activation. *J Biol Chem* **2006**, *281*, 26408-18.
134. Zhu, J. X.; Goldoni, S.; Bix, G.; Owens, R. T.; McQuillan, D. J.; Reed, C. C.; Iozzo, R. V. Decorin evokes protracted internalization and degradation of the epidermal growth factor receptor via caveolar endocytosis. *J Biol Chem* **2005**, *280*, 32468-79.
135. Xu, H.; Cai, T.; Carmona, G. N.; Abuhatzira, L.; Notkins, A. L. Small cell lung cancer growth is inhibited by miR-342 through its effect of the target gene IA-2. *J Transl Med* **2016**, *14*, 278.

136. Witt, D.; Burfeind, P.; von Hardenberg, S.; Opitz, L.; Salinas-Riester, G.; Bremmer, F.; Schweyer, S.; Thelen, P.; Neesen, J.; Kaulfuss, S. Valproic acid inhibits the proliferation of cancer cells by re-expressing cyclin D2. *Carcinogenesis* **2013**, 34, 1115-24.
137. Hooper, K. L.; Thorpe, C. Flavin-dependent sulfhydryl oxidases in protein disulfide bond formation. *Protein sensors and reactive oxygen species, Pt B, Thiol enzymes and proteins* **2002**, 348, 30-4.
138. Song, H.; Zhang, B.; Watson, M. A.; Humphrey, P. A.; Lim, H.; Milbrandt, J. Loss of Nkx3.1 leads to the activation of discrete downstream target genes during prostate tumorigenesis. *Oncogene* **2009**, 28, 3307-19.
139. Guo, J.; Jing, R.; Zhong, J. H.; Dong, X.; Li, Y. X.; Liu, Y. K.; Huang, T. R.; Zhang, C. Y. Identification of CD14 as a potential biomarker of hepatocellular carcinoma using iTRAQ quantitative proteomics. *Oncotarget* **2017**, 8, 62011-28.
140. Zhou, L.; Chen, H. M.; Qu, S.; Li, L.; Zhao, W.; Liang, Z. G.; Yu, B. B.; Chen, K. H.; Lu, Q. T.; Lin, G. X.; Zhu, X. D. Reduced QSOX1 enhances radioresistance in nasopharyngeal carcinoma. *Oncotarget* **2018**, 9, 3230-41.
141. Hanavan, P. D.; Borges, C. R.; Katchman, B. A.; Faigel, D. O.; Ho, T. H.; Ma, C. T.; Sergienko, E. A.; Meurice, N.; Petit, J. L.; Lake, D. F. Ebselen inhibits QSOX1 enzymatic activity and suppresses invasion of pancreatic and renal cancer cell lines. *Oncotarget* **2015**, 6, 18418-28.
142. Capparuccia, L.; Tamagnone, L. Semaphorin signaling in cancer cells and in cells of the tumor microenvironment - two sides of a coin. *J Cell Sci* **2009**, 122, 1723-36.
143. Rich, J. N.; Hans, C.; Jones, B.; Iversen, E. S.; McLendon, R. E.; Rasheed, B. A.; Dobra, A.; Dressman, H. K.; Bigner, D. D.; Nevins, J. R.; West, M. Gene expression profiling and genetic markers in glioblastoma survival. *Cancer Res* **2005**, 65, 4051-8.
144. Swiercz, J. M.; Worzfeld, T.; Offermanns, S. ErbB-2 and met reciprocally regulate cellular signaling via plexin-B1. *J Biol Chem* **2008**, 283, 1893-901.
145. Ayala, G. E.; Dai, H.; Powell, M.; Li, R.; Ding, Y.; Wheeler, T. M.; Shine, D.; Kadmon, D.; Thompson, T.; Miles, B. J.; Ittmann, M. M.; Rowley, D. Cancer-related axonogenesis and neurogenesis in prostate cancer. *Clin Cancer Res* **2008**, 14, 7593-603.
146. Gabrovskaja, P. N.; Smith, R. A.; Tiang, T.; Weinstein, S. R.; Haupt, L. M.; Griffiths, L. R. Semaphorin-plexin signalling genes associated with human breast tumourigenesis. *Gene* **2011**, 489, 63-9.
147. Mandriota, S. J.; Jussila, L.; Jeltsch, M.; Compagni, A.; Baetens, D.; Prevo, R.; Banerji, S.; Huarte, J.; Montesano, R.; Jackson, D. G.; Orci, L.; Alitalo, K.; Christofori, G.; Pepper, M. S.



Vascular endothelial growth factor-C-mediated lymphangiogenesis promotes tumour metastasis. *EMBO J* **2001**, 20, 672-82.

148. Jenny, B.; Harrison, J. A.; Baetens, D.; Tille, J. C.; Burkhardt, K.; Mottaz, H.; Kiss, J. Z.; Dietrich, P. Y.; De Tribolet, N.; Pizzolato, G. P.; Pepper, M. S. Expression and localization of VEGF-C and VEGFR-3 in glioblastomas and haemangioblastomas. *J Pathol* **2006**, 209, 34-43.

149. Xu, Y. M.; Zhong, Z. W.; Yuan, J.; Zhang, Z. H.; Wei, Q. T.; Song, W. Z.; Chen, H. W. Collaborative overexpression of matrix metalloproteinase-1 and vascular endothelial growth factor-C predicts adverse prognosis in patients with gliomas. *Cancer Epidemiol* **2013**, 37, 697-702.

150. Zhao, H. Q.; Hou, C. F.; Hou, A. W.; Zhu, D. Y. Concurrent expression of VEGF-C and neuropilin-2 is correlated with poor prognosis in glioblastoma. *Tohoku J Exp Med* **2016**, 238, 85-91.

151. Tao, P.; Wen, H.; Yang, B.; Zhang, A.; Wu, X.; Li, Q. miR-144 inhibits growth and metastasis of cervical cancer cells by targeting VEGFA and VEGFC. *Exp Ther Med* **2018**, 15, 562-68.

152. He, X.; Ping, J.; Wen, D. MicroRNA-186 regulates the invasion and metastasis of bladder cancer via vascular endothelial growth factor C. *Exp Ther Med* **2017**, 14, 3253-58.

153. Zhou, Y.; Shan, S.; Li, Z. B.; Xin, L. J.; Pan, D. S.; Yang, Q. J.; Liu, Y. P.; Yue, X. P.; Liu, X. R.; Gao, J. Z.; Zhang, J. W.; Ning, Z. Q.; Lu, X. P. CS2164, a novel multi-target inhibitor against tumor angiogenesis, mitosis and chronic inflammation with anti-tumor potency. *Cancer Sci* **2017**, 108, 469-77.

154. Hanash, S. M.; Bobek, M. P.; Rickman, D. S.; Williams, T.; Rouillard, J. M.; Kuick, R.; Puravs, E. Integrating cancer genomics and proteomics in the post-genome era. *Proteomics* **2002**, 2, 69-75.

155. Iwadate, Y.; Sakaida, T.; Hiwasa, T.; Nagai, Y.; Ishikura, H.; Takiguchi, M.; Yamaura, A. Molecular classification and survival prediction in human gliomas based on proteome analysis. *Cancer Res* **2004**, 64, 2496-501.

156. Yu, X.; Feng, L.; Liu, D.; Zhang, L.; Wu, B.; Jiang, W.; Han, Z.; Cheng, S. Quantitative proteomics reveals the novel co-expression signatures in early brain development for prognosis of glioblastoma multiforme. *Oncotarget* **2016**, 7, 14161-71.

157. Hajjar, K. A.; Krishnan, S. Annexin II: A mediator of the plasmin/plasminogen activator system. *Trends Cardiovas Med* **1999**, 9, 128-38.

158. Reddy, T. R. K.; Li, C.; Fischer, P. M.; Dekker, L. V. Three-dimensional pharmacophore design and biochemical screening identifies substituted 1,2,4-triazoles as inhibitors of the annexin A2-S100A10 protein interaction. *ChemMedChem* **2012**, *7*, 1435-46.
159. Woodham, A. W.; Taylor, J. R.; Jimenez, A. I.; Skeate, J. G.; Schmidt, T.; Brand, H. E.; Da Silva, D. M.; Kast, W. M. Small molecule inhibitors of the annexin A2 heterotetramer prevent human papillomavirus type 16 infection. *J Antimicrob Chemother* **2015**, *70*, 1686-90.
160. Stangeland, B.; Mughal, A. A.; Grieg, Z.; Sandberg, C. J.; Joel, M.; Nygard, S.; Meling, T.; Murrell, W.; Mo, E. O. V.; Langmoen, I. A. Combined expressional analysis, bioinformatics and targeted proteomics identify new potential therapeutic targets in glioblastoma stem cells. *Oncotarget* **2015**, *6*, 26192-215.
161. Behnan, J. G., Z.; Joel, M.; Ramsness, I.; Stangeland, B. Gene knockdown of CENPA reduces sphere forming ability and stemness of glioblastoma initiating cells. *Neuroepigenetics* **2016**, *7*, 6-18.
162. Ayllón, V.; O'Connor, R. PBK/TOPK promotes tumour cell proliferation through p38 MAPK activity and regulation of the DNA damage response. *Oncogene* **2007**, *26*, 3451-61.
163. Joel, M.; Mughal, A. A.; Grieg, Z.; Murrell, W.; Palmero, S.; Mikkelsen, B.; Fjerdingsstad, H. B.; Sandberg, C. J.; Behnan, J.; Glover, J. C.; Langmoen, I. A.; Stangeland, B. Targeting PBK/TOPK decreases growth and survival of glioma initiating cells in vitro and attenuates tumor growth in vivo. *Mol Cancer* **2015**, *14*, 121.
164. Grinshtein, N.; Rioseco, C. C.; Marcellus, R.; Uehling, D.; Aman, A.; Lun, X. Q.; Muto, O.; Podmore, L.; Lever, J.; Shen, Y. Q.; Blough, M. D.; Cairncross, G. J.; Robbins, S. M.; Jones, S. J.; Marra, M. A.; Al-Awar, R.; Senger, D. L.; Kaplan, D. R. Small molecule epigenetic screen identifies novel EZH2 and HDAC inhibitors that target glioblastoma brain tumor-initiating cells. *Oncotarget* **2016**, *7*, 59360-76.
165. Zhang, Y. Y.; Yu, X. G.; Chen, L.; Zhang, Z. B.; Feng, S. Y. EZH2 overexpression is associated with poor prognosis in patients with glioma. *Oncotarget* **2017**, *8*, 565-73.
166. Ferreira, W. A.; Araújo, M. D.; Anselmo, N. P.; de Oliveira, E. H.; Brito, J. R.; Burbano, R. R.; Harada, M. L.; Borges Bdo, D. Expression analysis of genes involved in the RB/E2F pathway in astrocytic tumors. *PloS One* **2015**, *10*, e0137259.
167. Tilghman, J.; Wu, H.; Sang, Y. Y.; Shi, X. H.; Guerrero-Cazares, H.; Quinones-Hinojosa, A.; Eberhart, C. G.; Latta, J.; Ying, M. Y. HMMR maintains the stemness and tumorigenicity of glioblastoma stem-like cells. *Cancer Res* **2014**, *74*, 3168-79.
168. Ghosh, D.; Funk, C. C.; Caballero, J.; Shah, N.; Rouleau, K.; Earls, J. C.; Soroceanu, L.; Foltz, G.; Cobbs, C. S.; Price, N. D.; Hood, L. A cell-surface membrane protein signature for glioblastoma. *Cell Syst* **2017**, *4*, 516-29.

169. Weidle, U. H.; Maisel, D.; Eick, D. Synthetic lethality-based targets for discovery of new cancer therapeutics. *Cancer Genom Proteom* **2011**, *8*, 159-71.
170. Szczurek, E.; Misra, N.; Vingron, M. Synthetic sickness or lethality points at candidate combination therapy targets in glioblastoma. *Int J Cancer* **2013**, *133*, 2123-32.
171. Kim, Y. W.; Liu, T. J.; Koul, D.; Tiao, N.; Feroze, A. H.; Wang, J.; Powis, G.; Yung, W. K. Identification of novel synergistic targets for rational drug combinations with PI3 kinase inhibitors using siRNA synthetic lethality screening against GBM. *Neuro Oncol* **2011**, *13*, 367-75.
172. Mai, W. X.; Gosa, L.; Daniels, V. W.; Ta, L.; Tsang, J. E.; Higgins, B.; Gilmore, W. B.; Bayley, N. A.; Harati, M. D.; Lee, J. T.; Yong, W. H.; Kornblum, H. I.; Bensinger, S. J.; Mischel, P. S.; Rao, P. N.; Clark, P. M.; Cloughesy, T. F.; Letai, A.; Nathanson, D. A. Cytoplasmic p53 couples oncogene-driven glucose metabolism to apoptosis and is a therapeutic target in glioblastoma. *Nat Med* **2017**, *23*, 1342-51.
173. Palanichamy, K.; Patel, D.; Jacob, J. R.; Litzenberg, K. T.; Gordon, N.; Acus, K.; Noda, S. E.; Chakravarti, A. Lack of constitutively active DNA repair sensitizes glioblastomas to Akt inhibition and induces synthetic lethality with radiation treatment in a p53-dependent manner. *Mol Cancer Ther* **2018**, *17*, 336-46.
174. Karpel-Massler, G.; Ishida, C. T.; Bianchetti, E.; Zhang, Y.; Shu, C.; Tsujiuchi, T.; Banu, M. A.; Garcia, F.; Roth, K. A.; Bruce, J. N.; Canoll, P.; Siegelin, M. D. Induction of synthetic lethality in IDH1-mutated gliomas through inhibition of Bcl-xL. *Nat Commun* **2017**, *8*, 1067.
175. Huszthy, P. C.; Daphu, I.; Niclou, S. P.; Stieber, D.; Nigro, J. M.; Sakariassen, P. O.; Miletic, H.; Thorsen, F.; Bjerkgvig, R. In vivo models of primary brain tumors: Pitfalls and perspectives. *Neuro Oncol* **2012**, *14*, 979-93.
176. Miyai, M.; Tomita, H.; Soeda, A.; Yano, H.; Iwama, T.; Hara, A. Current trends in mouse models of glioblastoma. *J Neurooncol* **2017**, *135*, 423-32.
177. Simeonova, I.; Huillard, E. In vivo models of brain tumors: Roles of genetically engineered mouse models in understanding tumor biology and use in preclinical studies. *Cell Mol Life Sci* **2014**, *71*, 4007-26.
178. Alcantara Llaguno, S.; Chen, J.; Kwon, C. H.; Jackson, E. L.; Li, Y.; Burns, D. K.; Alvarez-Buylla, A.; Parada, L. F. Malignant astrocytomas originate from neural stem/progenitor cells in a somatic tumor suppressor mouse model. *Cancer Cell* **2009**, *15*, 45-56.
179. William, D.; Mullins, C. S.; Schneider, B.; Orthmann, A.; Lamp, N.; Krohn, M.; Hoffmann, A.; Classen, C. F.; Linnebacher, M. Optimized creation of glioblastoma patient derived xenografts for use in preclinical studies. *J Transl Med* **2017**, *15*, 27.

180. Xie, Y.; Bergstrom, T.; Jiang, Y.; Johansson, P.; Marinescu, V. D.; Lindberg, N.; Segerman, A.; Wicher, G.; Niklasson, M.; Baskaran, S.; Sreedharan, S.; Everlien, I.; Kastemar, M.; Hermansson, A.; Elfineh, L.; Libard, S.; Holland, E. C.; Hesselager, G.; Alafuzoff, I.; Westermark, B.; Nelander, S.; Forsberg-Nilsson, K.; Uhrbom, L. The human glioblastoma cell culture resource: Validated cell models representing all molecular subtypes. *EBioMedicine* **2015**, *2*, 1351-63.
181. Malaney, P.; Nicosia, S. V.; Dave, V. One mouse, one patient paradigm: New avatars of personalized cancer therapy. *Cancer Lett* **2014**, *344*, 1-12.
182. Ben-David, U.; Ha, G.; Tseng, Y. Y.; Greenwald, N. F.; Oh, C.; Shih, J.; McFarland, J. M.; Wong, B.; Boehm, J. S.; Beroukhi, R.; Golub, T. R. Patient-derived xenografts undergo mouse-specific tumor evolution. *Nat Genet* **2017**, *49*, 1567-75.
183. Zuckermann, M.; Hovestadt, V.; Knobbe-Thomsen, C. B.; Zapatka, M.; Northcott, P. A.; Schramm, K.; Belic, J.; Jones, D. T.; Tschida, B.; Moriarity, B.; Largaespada, D.; Roussel, M. F.; Korshunov, A.; Reifenberger, G.; Pfister, S. M.; Lichter, P.; Kawauchi, D.; Gronych, J. Somatic CRISPR/Cas9-mediated tumour suppressor disruption enables versatile brain tumour modelling. *Nat Commun* **2015**, *6*, 7391.
184. Vorbrodt, A. W.; Dobrogowska, D. H. Molecular anatomy of intercellular junctions in brain endothelial and epithelial barriers: Electron microscopist's view. *Brain Res Rev* **2003**, *42*, 221-42.
185. Ebnet, K.; Suzuki, A.; Ohno, S.; Vestweber, D. Junctional adhesion molecules (JAMs): More molecules with dual functions? *J Cell Sci* **2004**, *117*, 19-29.
186. Banks, W. A. Characteristics of compounds that cross the blood-brain barrier. *BMC Neurol* **2009**, *9*, S3.
187. Christensen, H. N. Role of amino-acid-transport and countertransport in nutrition and metabolism. *Physiol Rev* **1990**, *70*, 43-77.
188. Nutt, J. G.; Woodward, W. R.; Hammerstad, J. P.; Carter, J. H.; Anderson, J. L. The on off phenomenon in Parkinsons-disease - relation to levodopa absorption and transport. *N Eng J Med* **1984**, *310*, 483-8.
189. Duffy, K. R.; Pardridge, W. M. Blood-brain-barrier transcytosis of insulin in developing rabbits. *Brain Res* **1987**, *420*, 32-8.
190. Henthorn, T. K.; Liu, Y.; Mahapatro, M.; Ng, K. Y. Active transport of fentanyl by the blood-brain barrier. *J Pharmacol Exp Ther* **1999**, *289*, 1084-9.

191. Fletcher, J. I.; Williams, R. T.; Henderson, M. J.; Norris, M. D.; Haber, M. ABC transporters as mediators of drug resistance and contributors to cancer cell biology. *Drug Resist Updat* **2016**, 26, 1-9.
192. Chacko, A. M.; Li, C. S.; Pryma, D. A.; Brem, S.; Coukos, G.; Muzykantov, V. Targeted delivery of antibody-based therapeutic and imaging agents to CNS tumors: Crossing the blood-brain barrier divide. *Expert Opin Drug Deliv* **2013**, 10, 907-26.
193. van Tellingen, O.; Yetkin-Arik, B.; de Gooijer, M. C.; Wesseling, P.; Wurdinger, T.; de Vries, H. E. Overcoming the blood-brain tumor barrier for effective glioblastoma treatment. *Drug Resist Updat* **2015**, 19, 1-12.
194. Banks, W. A. From blood-brain barrier to blood-brain interface: New opportunities for CNS drug delivery. *Nat Rev Drug Discov* **2016**, 15, 275-92.
195. Wajner, M.; Coelho, D. M.; Barschak, A. G.; Araujo, P. R.; Pires, R. F.; Lulhier, F. L.; Vargas, C. R. Reduction of large neutral amino acid concentrations in plasma and CSF of patients with maple syrup urine disease during crises. *J Inherit Metab Dis* **2000**, 23, 505-12.
196. Leinenga, G.; Langton, C.; Nisbet, R.; Gotz, J. Ultrasound treatment of neurological diseases - current and emerging applications. *Nat Rev Neurol* **2016**, 12, 161-74.
197. Lipinski, C. A.; Lombardo, F.; Dominy, B. W.; Feeney, P. J. Experimental and computational approaches to estimate solubility and permeability in drug discovery and development settings. *Adv Drug Deliv Rev* **2001**, 23, 3-25.
198. Ghose, A. K.; Herbertz, T.; Hudkins, R. L.; Dorsey, B. D.; Mallamo, J. P. Knowledge-based, central nervous system (CNS) lead selection and lead optimization for CNS drug discovery. *ACS Chem Neurosci* **2012**, 3, 50-68.
199. Wager, T. T.; Hou, X.; Verhoest, P. R.; Villalobos, A. Moving beyond rules: The development of a central nervous system multiparameter optimization (CNS MPO) approach to enable alignment of druglike properties. *ACS Chem Neurosci* **2010**, 1, 435-49.
200. Rankovic, Z. CNS physicochemical property space shaped by a diverse set of molecules with experimentally determined exposure in the mouse brain. *J Med Chem* **2017**, 60, 5943-54.
201. Kola, I.; Landis, J. Can the pharmaceutical industry reduce attrition rates? *Nat Rev Drug Discov* **2004**, 3, 711-5.
202. Kesselheim, A. S.; Hwang, T. J.; Franklin, J. M. Two decades of new drug development for central nervous system disorders. *Nat Rev Drug Discov* **2015**, 14, 815-6.
203. Batchelor, T. T.; Mulholland, P.; Neyns, B.; Nabors, L. B.; Campone, M.; Wick, A.; Mason, W.; Mikkelsen, T.; Phuphanich, S.; Ashby, L. S.; DeGroot, J.; Gattamaneni, R.; Cher, L.;

Rosenthal, M.; Payer, F.; Jurgensmeier, J. M.; Jain, R. K.; Sorensen, A. G.; Xu, J.; Liu, Q.; van den Bent, M. Phase III randomized trial comparing the efficacy of cediranib as monotherapy, and in combination with lomustine, versus lomustine alone in patients with recurrent glioblastoma. *J Clin Oncol* **2013**, 31, 3212-8.

204. Swartz, A. M.; Li, Q. J.; Sampson, J. H. Rindopepimut: A promising immunotherapeutic for the treatment of glioblastoma multiforme. *Immunotherapy* **2014**, 6, 679-90.

205. Inman, S. Rindopepimut misses OS endpoint in phase III glioblastoma trial. In OncLive: 2016.

206. Miller, T. E.; Liau, B. B.; Wallace, L. C.; Morton, A. R.; Xie, Q.; Dixit, D.; Factor, D. C.; Kim, L. J. Y.; Morrow, J. J.; Wu, Q.; Mack, S. C.; Hubert, C. G.; Gillespie, S. M.; Flavahan, W. A.; Hoffmann, T.; Thummalapalli, R.; Hemann, M. T.; Paddison, P. J.; Horbinski, C. M.; Zuber, J.; Scacheri, P. C.; Bernstein, B. E.; Tesar, P. J.; Rich, J. N. Transcription elongation factors represent in vivo cancer dependencies in glioblastoma. *Nature* **2017**, 547, 355-9.

207. Reardon, D. A.; Groves, M. D.; Wen, P. Y.; Nabors, L.; Mikkelsen, T.; Rosenfeld, S.; Raizer, J.; Barriuso, J.; McLendon, R. E.; Suttle, A. B.; Ma, B.; Curtis, C. M.; Dar, M. M.; de Bono, J. A phase I/II trial of pazopanib in combination with lapatinib in adult patients with relapsed malignant glioma. *Clin Cancer Res* **2013**, 19, 900-8.

208. Rankovic, Z. CNS drug design: Balancing physicochemical properties for optimal brain exposure. *J Med Chem* **2015**, 58, 2584-608.

209. Poduslo, J. F.; Curran, G. L.; Berg, C. T. Macromolecular permeability across the blood-nerve and blood-brain barriers. *Proc Natl Acad Sci U S A* **1994**, 91, 5705-9.

210. Lang, F. F.; Conrad, C.; Gomez-Manzano, C.; Yung, W. K. A.; Sawaya, R.; Weinberg, J. S.; Prabhu, S. S.; Rao, G.; Fuller, G. N.; Aldape, K. D.; Gumin, J.; Vence, L. M.; Wistuba, I.; Rodriguez-Canales, J.; Villalobos, P. A.; Dirven, C. M. F.; Tejada, S.; Valle, R. D.; Alonso, M. M.; Ewald, B.; Peterkin, J. J.; Tufaro, F.; Fueyo, J. Phase I study of DNX-2401 (Delta-24-RGD) oncolytic adenovirus: Replication and immunotherapeutic effects in recurrent malignant glioma. *J Clin Oncol* **2018**, 36, 1419-27.

211. Bart, J.; Groen, H. J.; Hendrikse, N. H.; van der Graaf, W. T.; Vaalburg, W.; de Vries, E. G. The blood-brain barrier and oncology: New insights into function and modulation. *Cancer Treat Rev* **2000**, 26, 449-62.

212. Marie, Y.; Carpentier, A. F.; Omuro, A. M.; Sanson, M.; Thillet, J.; Hoang-Xuan, K.; Delattre, J. Y. EGFR tyrosine kinase domain mutations in human gliomas. *Neurology* **2005**, 64, 1444-5.

213. Ballard, P.; Yates, J. W.; Yang, Z.; Kim, D. W.; Yang, J. C.; Cantarini, M.; Pickup, K.; Jordan, A.; Hickey, M.; Grist, M.; Box, M.; Johnstrom, P.; Varnas, K.; Malmquist, J.; Thress, K.

S.; Janne, P. A.; Cross, D. Preclinical comparison of osimertinib with other EGFR-TKIs in EGFR-mutant NSCLC brain metastases models, and early evidence of clinical brain metastases activity. *Clin Cancer Res* **2016**, *22*, 5130-40.

214. Wen, P. Y.; Cloughesy, T. F.; Olivero, A.; Lu, X.; Mueller, L.; Coimbra, A. F.; Gerstner, E. R.; Ahnert, J. R. A first-in-human phase 1 study to evaluate the brain-penetrant PI3K/mTOR inhibitor GDC-0084 in patients with progressive or recurrent high-grade glioma. *J Clin Oncol* **2016**, *34*, 2012-2012.

215. Heffron, T. P.; Ndubaku, C. O.; Salphati, L.; Alicke, B.; Cheong, J.; Drobnick, J.; Edgar, K.; Gould, S. E.; Lee, L. B.; Lesnick, J. D.; Lewis, C.; Nonomiya, J.; Pang, J.; Plise, E. G.; Sideris, S.; Wallin, J.; Wang, L.; Zhang, X.; Olivero, A. G. Discovery of clinical development candidate GDC-0084, a brain penetrant inhibitor of PI3K and mTOR. *ACS Med Chem Lett* **2016**, *7*, 351-6.

216. Reardon, D. A.; Galanis, E.; DeGroot, J. F.; Cloughesy, T. F.; Wefel, J. S.; Lamborn, K. R.; Lassman, A. B.; Gilbert, M. R.; Sampson, J. H.; Wick, W.; Chamberlain, M. C.; Macdonald, D. R.; Mehta, M. P.; Vogelbaum, M. A.; Chang, S. M.; Van den Bent, M. J.; Wen, P. Y. Clinical trial end points for high-grade glioma: The evolving landscape. *Neuro Oncol* **2011**, *13*, 353-61.

217. Rankovic, Z. Retraction of "CNS physicochemical property space shaped by a diverse set of molecules with experimentally determined exposure in the mouse brain". *J Med Chem* **2019**, *62*, 1699.

## CHAPTER II

### Protein Disulfide Isomerase

#### Historical background<sup>2</sup>

The dithiol-disulfide oxidoreductase protein disulfide isomerase (PDI) was discovered in 1963 as the first protein folding chaperone. Research groups led by Brunó Straub<sup>1</sup> and Christian B. Anfinsen<sup>2</sup> independently made pivotal discoveries about an enzyme that reactivated reduced ribonuclease. Straub and co-workers purified the reactivating system from chicken pancreas. Anfinsen studied the system in conjunction with his Nobel-prize-winning work on ribonuclease and purified a system with similar activity from rat liver microsomes. In 1972, the enzyme was given the name protein disulfide isomerase and its official classification number, EC 5.3.4.1. The newly purified protein was identified as the “ribonuclease-reactivating enzyme,” and was nearly identical to glutathione-insulin transhydrogenase, causing confusion in the field.<sup>3</sup> Both enzymes catalyze disulfide exchanges, require a thiol for activity, and inactivate insulin. Confusion was cleared with key experiments using covalent chromatography to demonstrate that PDI is more sensitive to reducing conditions than glutathione-insulin transhydrogenase.<sup>4</sup> The official name was first used in a publication on conformational barriers to disulfide bond formation in 1975.<sup>5</sup> Challenges in monitoring disulfide bond formation and isomerization slowed research on the

---

<sup>2</sup> This work has been published and is being reprinted with permission from Shergalis, A., & Neamati, N. (2017). Protein Disulfide Isomerase. *Encyclopedia of Signaling Molecules*, 1-12.

**Author contributions:** Andrea Shergalis was the primary author. Nouri Neamati is the corresponding author.



enzyme until a pivotal review on PDI was published in 1984.<sup>6</sup> Then, in 1985, Edman and colleagues identified the sequence of rat PDI, which led to the discovery that PDI contains sequences highly homologous to the cytoplasmic redox signaling enzyme thioredoxin.<sup>7</sup> This discovery provided valuable insight into the mechanism of redox reactions catalyzed by PDI and indicated the active sites of PDI contained the critical WCGHC sequence.

PDI has gained much attention in the following years due to its role in cancer, cardiovascular diseases, diabetes, and neurodegenerative diseases such as Huntington's disease. In addition to its role as an oxidoreductase and molecular chaperone, PDI is important for several other physiological processes, including collagen biosynthesis, antigen presentation, and lipoprotein synthesis. PDI is the beta subunit of prolyl 4-hydroxylase, an essential collagen biosynthesis enzyme, and mutations in PDI lead to bone fragility disorders.<sup>8</sup> In recent years, it was discovered that PDI is overexpressed in several cancers. Following this discovery, researchers have found that PDI contributes to tumor growth, progression, and chemotherapeutic resistance. In addition to its role in cancer, PDI has a pro-apoptotic function in Huntington's disease and other brain dysfunction diseases.<sup>9</sup> Targeting PDI function may be a promising therapeutic approach for multiple human diseases. The structure and function, as well as the role of PDI in various disease states, will be reviewed in detail in the subsequent paragraphs.

Since there are numerous PDI family members, this chapter will focus on PDIA1, as it has been proven to be most relevant to several disease states. However, the other PDI family members will also be discussed in brief. The acronym PDI is often used to refer to PDIA1, but for clarity in this text, PDI will be used when making general statements about the protein family, and specific isoform nomenclature will be used when necessary. Several comprehensive reviews covering a variety of aspects of PDI have been published in recent years.<sup>10-13</sup>

## Domain structure and isoforms

The PDI family consists of at least 22 members (Figure II-1) that share at least one thioredoxin-like fold domain ( $\beta\alpha\beta\alpha\beta\alpha\beta\alpha$ ).<sup>10</sup> PDI family members primarily reside in the endoplasmic reticulum (ER), but have also been found in the nucleus, cytoplasm, and on the plasma membrane (Table II-1). The full-length founding member of the PDI family, PDIA1, contains 508 amino acids, 17 of which form an ER signal peptide that is cleaved from the N-terminal tail in the mature form. Most PDI family members contain the catalytic **a** and **a'** domains that are structurally similar to thioredoxin, with the conserved CXXC active site surrounded by hydrophobic regions. The **b** and **b'** domains are homologous to the **a** and **a'** domains and also contain the thioredoxin-like fold, despite lacking sequence similarity to the **a** and **a'** domains and the CXXC active site. The structures of several domains of mammalian,<sup>14</sup> yeast,<sup>15</sup> and fungal<sup>16</sup> PDI have been solved with X-ray crystallography and NMR; however, the full-length structure has yet to be resolved, likely due to its size and flexibility. The complete oxidized and reduced crystallized PDI structure with the exception of the C-terminal extension (i.e. containing **abb'xa'** domains) demonstrated that the active site of the **a'** domain shifts closer to the **a** domain active site upon reduction, shielding access to the hydrophobic pocket (Figure II-2).<sup>14</sup> The **b** and **b'** domains are non-catalytic; the **b'** domain is primarily responsible for substrate recognition with help from the **a'** domain, and to date, the function of the **b** domain is unclear. It has been suggested that the **b** domain in Pdip, a yeast paralog of PDI, plays a role in substrate recognition.<sup>15</sup> PDI also contains a flexible **x** linker 19 amino acids long that spans between the **a'** and **b'** domains. The **x** region can move to obstruct the substrate binding site in the **b'** domain, and therefore this conformational change may regulate the substrate binding cycle of PDI.<sup>15</sup> PDI also contains an acidic C-terminal extension in which the ER retention signal resides. While the C-terminal region

is important for catalytic activity of the a' domain in yeast PDI,<sup>15</sup> truncating the C-terminal region of mammalian PDI has little effect.<sup>14</sup>

Table II-1 Function and subcellular localization of 22 PDI isoforms

<b>Isoform</b>	<b>Subcellular Localization</b>	<b>Function</b>
<b>PDIA1</b>	Endoplasmic reticulum, extracellular space, plasma membrane	Oxidoreductase, chaperone
<b>PDIA2</b>	Endoplasmic reticulum, extracellular space	Oxidoreductase, chaperone, estrogen-binding
<b>PDIA3</b>	Endoplasmic reticulum, extracellular space, nucleus	Oxidoreductase
<b>PDIA4</b>	Endoplasmic reticulum, extracellular space	Oxidoreductase
<b>PDIA5</b>	Endoplasmic reticulum, extracellular space	Oxidoreductase
<b>PDIA6</b>	Endoplasmic reticulum, extracellular space, plasma membrane	Oxidoreductase, chaperone, platelet aggregation and activation
<b>PDIA7</b>	Endoplasmic reticulum	Chaperone, spermatogenesis
<b>PDIA8</b>	Endoplasmic reticulum	Function unknown
<b>PDIA9 (ERp29)</b>	Endoplasmic reticulum, extracellular space	Processes and transports secretory proteins
<b>PDIA10 (ERp44)</b>	Endoplasmic reticulum, extracellular space	Mediator of ER retention of proteins such as ERO1
<b>PDIA11 (TMX1)</b>	Endoplasmic reticulum, extracellular space, nucleus	Oxidoreductase
<b>PDIA12 (TMX2)</b>	Endoplasmic reticulum	Function unknown
<b>PDIA13 (TMX3)</b>	Endoplasmic reticulum	Oxidoreductase
<b>PDIA14 (TMX4)</b>	Endoplasmic reticulum	Function unknown
<b>(TMX5)</b>	Unknown	Potential chaperone

<b>PDIA15 (ERp46)</b>	Endoplasmic reticulum, extracellular space, lysosome, vacuole	Thioredoxin activity
<b>PDIA16 (ERp19, AGR1)</b>	Endoplasmic reticulum	Protein oxidase
<b>PDIA17 (AGR2, HAG-2)</b>	Endoplasmic reticulum, extracellular space	Mucus production and secretion
<b>PDIA18 (AGR3, HAG-3)</b>	Endoplasmic reticulum	Calcium-mediated regulation of ciliary beat frequency
<b>PDIA19 (ERdj5)</b>	Endoplasmic reticulum	Oxidoreductase
<b>PDIB1 (CASQ1)</b>	Endoplasmic reticulum, mitochondrion, plasma membrane	Calcium storage
<b>PDIB2 (CASQ2)</b>	Endoplasmic reticulum, cytosol	Calcium storage

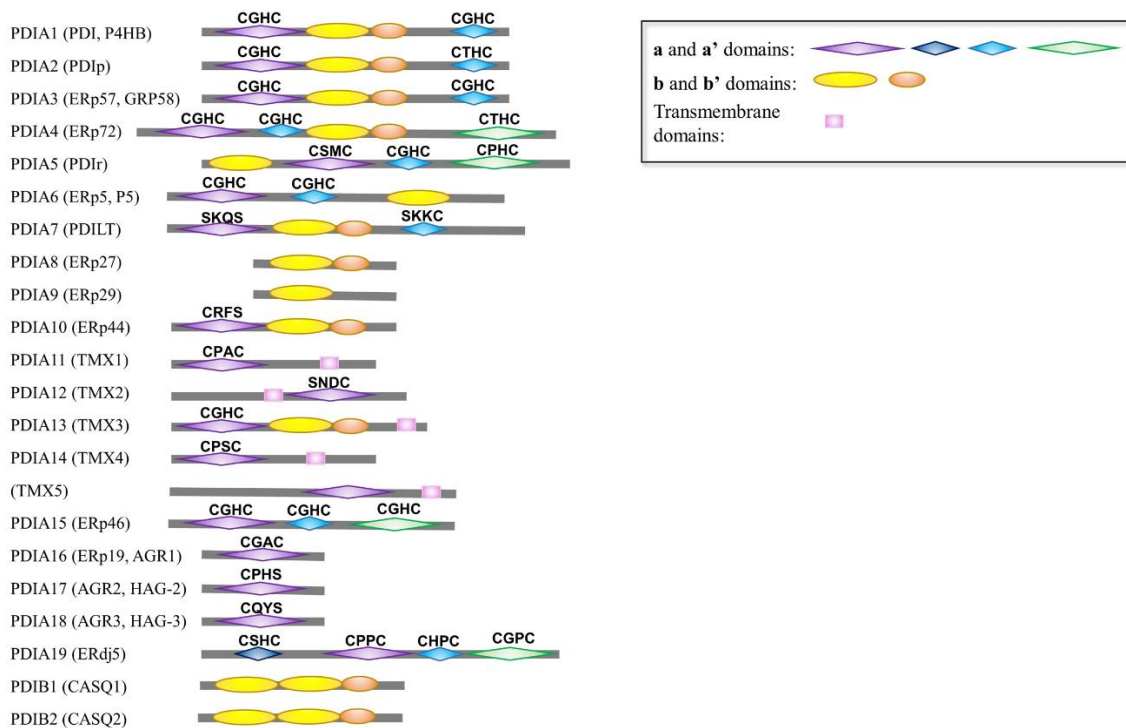


Figure II-1 Domain structure of PDI family members. Active site amino acids are shown.

The PDI active sites are located on the **a** and **a'** domains, which share 33.6% identity in PDIA1 and contain the four conserved amino acids Cys-Gly-His-Cys. The cysteine thiols on each domain sit about 30 Å apart when PDI is oxidized, and 15 Å apart when PDI is reduced.<sup>14</sup> The cysteines are responsible for disulfide exchange on PDI and the kinetics of the reactions catalyzed by this enzyme rely on the conformation and pK<sub>a</sub> of the cysteines. For example, PDI catalyzes both the reduction and oxidation of various substrates, and the more favorable of the two reactions depends on the conformational state and pK<sub>a</sub> of the active site cysteine residues. The pK<sub>a</sub> of the N-terminal active-site cysteine is in the range of 4.4 to 6.7, lower than the pK<sub>a</sub> (8.3) of a typical cysteine thiol, allowing it to be more reactive. The pK<sub>a</sub> of the C-terminal active site cysteine is much higher than normal at 12.8, allowing it to attack the N-terminal cysteine after it forms a

disulfide with the substrate. The inner histidine and glycine amino acids in the active site also affect the  $pK_a$  of the thiols and the stability of the disulfide state.<sup>10</sup>

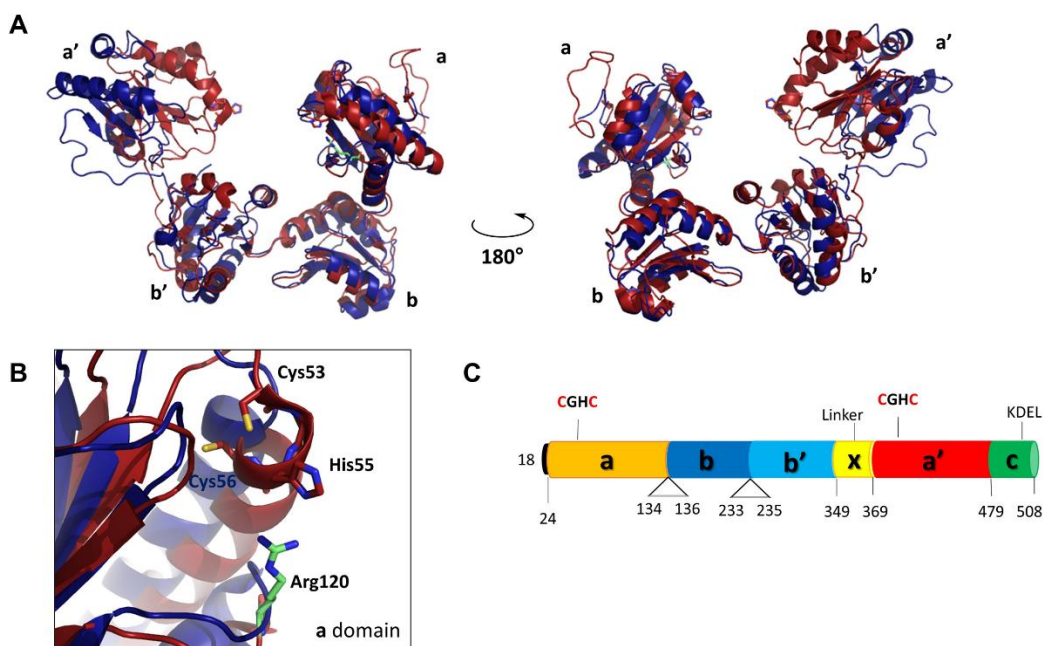


Figure II-2 PDI structure (A) Crystal structures of reduced (4EKZ, red) and oxidized (4EL1, blue) PDIA1. (B) Close up of the CGHC active site of the a domain of reduced PDIA1 and associated arginine residue (green).

Even though the **b** and **b'** domains contain the thioredoxin fold of the **a** and **a'** domains, they are enzymatically inactive and do not contain the CGHC active site. The function of the **b** domain is still up for debate, however, the **b'** domain is responsible for substrate interactions via a hydrophobic pocket. Exposed hydrophobic regions in unfolded or partially folded proteins associate with the hydrophobic region spanning the **b'xa'** domain, thus allowing PDI to form disulfide bridges necessary for proper protein folding. Interestingly, small molecules binding in the substrate binding pocket can enhance PDI activity.<sup>17</sup>

### Function and regulation

PDI catalyzes the reduction, oxidation, and rearrangement of disulfide bonds in nascent polypeptides. PDI is highly abundant in the ER and accounts for up to 0.8% of total cellular

protein.<sup>6</sup> It is also synthesized downstream of the unfolded protein response (UPR).<sup>18</sup> PDI family members are also found on the cell surface and in the nucleus, suggesting PDI has multiple functions. Cell-surface PDI is involved in multiple biological processes, including glioma cell migration,<sup>19</sup> T cell migration,<sup>20</sup> and injury response.<sup>21</sup> PDI family members that lack the ER retention sequence localize to other compartments such as the nucleus to influence gene transcription. For example, ERp57 mainly resides in the ER, but contains a nuclear localization signal that shuttles the enzyme to the nucleus in response to stress signals. In addition to its oxidoreductase activity, PDI is also involved in complex formation, substrate recognition, and molecular chaperone function. It is also a necessary component of the microsomal triglyceride transfer protein complex.<sup>22</sup> Knockout experiments have not been reported for a whole-body PDIA1 knockout model.

PDI activity is regulated by the redox state of its active site cysteine thiols. In the oxidizing environment of the ER, the enzyme is primed to reduce free thiols on other proteins. ER oxidoreductin 1 (ERO1), a FAD-cofactor-containing enzyme, recycles PDI for reuse (Figure II-3). PDI expression is also regulated by ER stress and the unfolded protein response.<sup>18</sup> Three central proteins are activated in response to the UPR, which is an overloading burden of unfolded proteins on the ER, to maintain homeostatic balance. One of these central effectors, PERK, is a kinase that phosphorylates eIF2 $\alpha$ , a transcription factor that translocates to the nucleus and attenuates translation. eIF2 $\alpha$  activates the transcription of several genes, including PDI and GRP78.

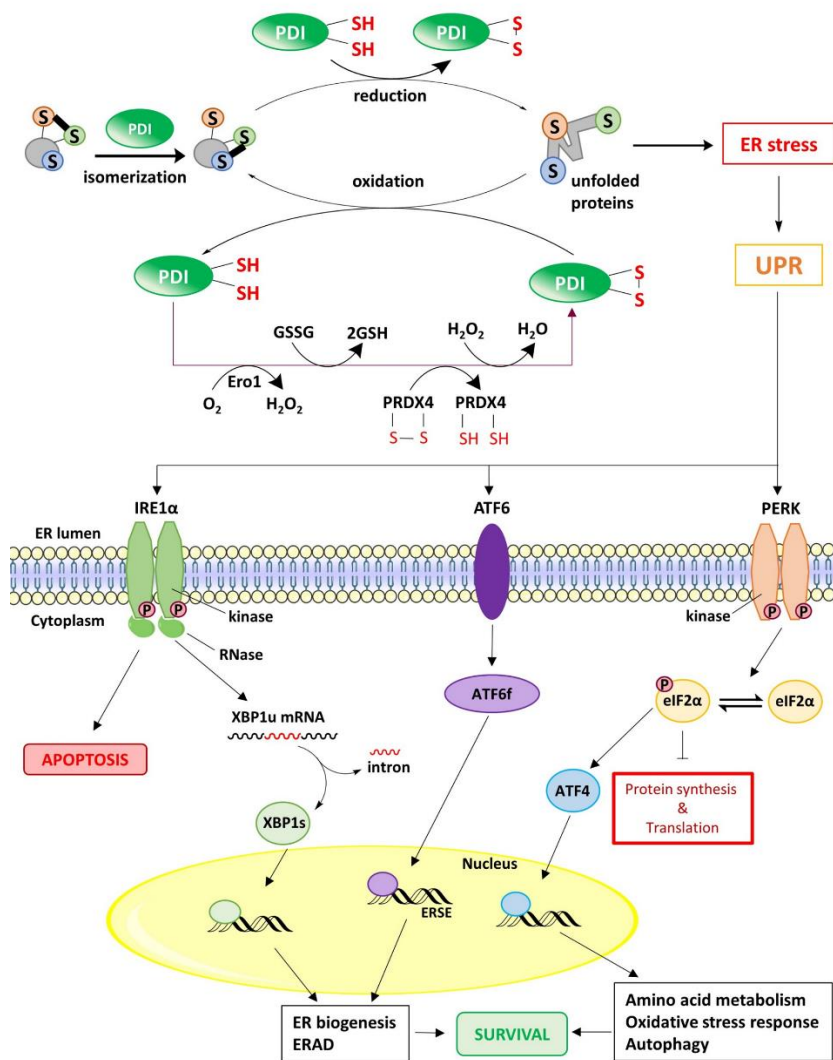


Figure II-3 Role of PDI in the endoplasmic reticulum. PDI catalyzes the oxidation and isomerization of misfolded proteins in the ER. PDI is reoxidized by ERO1, or PRDX4 in the presence of oxidized glutathione. Impairment of PDI activity leads to the unfolded protein response, which activates IRE1, PERK, and ATF6. IRE1 splices XBP1 mRNA, which causes it to translocate to the nucleus and promote gene expression. PERK phosphorylates eIF2 $\alpha$  to inhibit translation and activate ATF4. ATF4 translocates to the nucleus and promotes autophagy and cell survival. ATF6 is also modified in the Golgi apparatus and translocated to the nucleus to impact ER biogenesis and ERAD to promote cell survival. ERSE: Endoplasmic reticulum stress element. XBP1u: X-box protein 1 unspliced variant. XBP1s: X-box protein 1 spliced variant.

PDI catalyzes three different types of reactions (Figure II-4). The first is the oxidation of a protein or peptide substrate to the disulfide state. The second is the reduction of a protein or peptide disulfide bond. The third reaction PDI is able to catalyze is an isomerization of a mixed disulfide bond in a protein or peptide substrate. The oxidoreductase activity of PDI depends on the reduction potential and  $pK_a$  of its active-site cysteine thiols. The N-terminal Cys active site has a low  $pK_a$  to



maintain a sufficiently high reduction potential to form intermediate disulfide species with a protein substrate. The transient heterodimer is attacked by the low-pK<sub>a</sub> C-terminal thiol in the “escape pathway,” forming an intramolecular bridge and displacing the thiol. A model substrate peptide consisting of 12 amino acids bound PDI with an apparent K<sub>M</sub> value less than 3 μM in an experiment analyzing disulfide bond formation.<sup>23</sup> While PDI is generally understood to have several folding protein and peptide substrates, only a handful have been experimentally determined. These include bovine pancreatic trypsin inhibitor, Δ-somatostatin, mastoparan, insulin, and RNase. Interestingly, while PDI does exhibit flexibility in its a' domain through the x linker, substrate binding studies reveal that the protein and peptide substrates of PDI are more likely to change conformation to fit into the hydrophobic binding pocket.<sup>10</sup> After the reaction takes place, oxidized or reduced PDI can be recycled by a number of agents, including glutathione and ERO1.

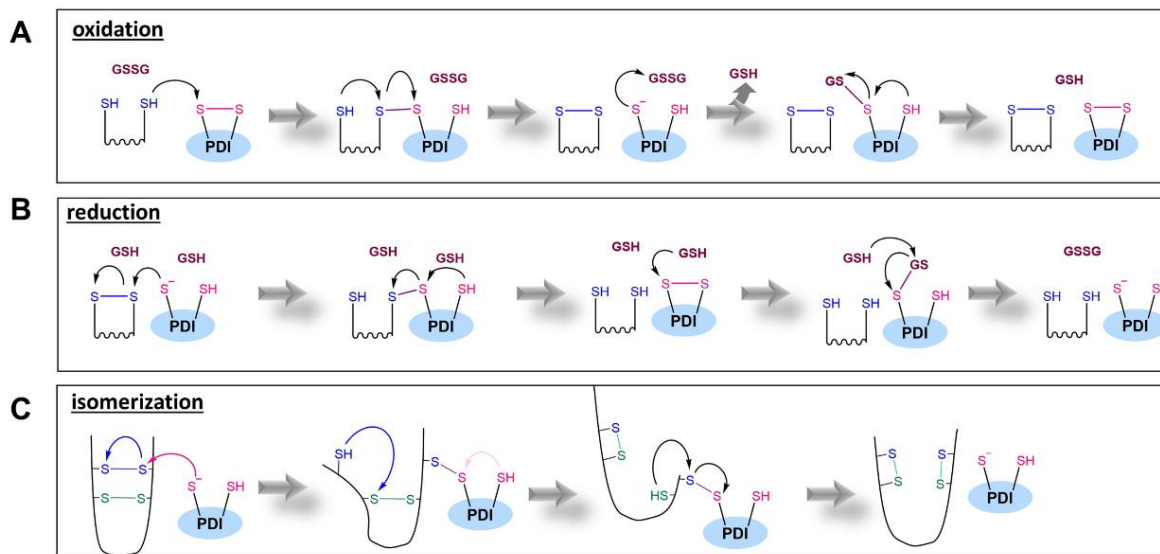


Figure II-4 Multifunctional roles of the PDI family. PDI catalyzes the oxidation (A), reduction (B), and isomerization (C) of cysteine thiols on substrate peptides and proteins.

Before ERO1 was discovered in 1998, the consensus was that glutathione, the primary redox buffer in the ER, was the primary oxidizing agent for PDI. However, it is now understood

that in its reduced state, PDI is predominantly reoxidized by ERO1. There are two mammalian isoforms of ERO1: ERO1 $\alpha$  and ERO1 $\beta$ . ERO1 $\alpha$  is well-characterized and its activity is tightly regulated by the redox environment. The activity of ERO1 $\beta$  is less well-characterized, but it is less tightly regulated than ERO1 $\alpha$ . The ERO1 enzymes rely on molecular oxygen as the electron acceptor and in return for each disulfide bond formed, produce one molecule of H<sub>2</sub>O<sub>2</sub>. ERO1 primarily oxidizes PDIA1, and, to a lesser extent, ERp46.<sup>24, 25</sup> Other PDI isoforms are selectively recycled by enzymes such as peroxiredoxin 4 (PRDX4) and vitamin K epoxide reductase (VKOR).

In addition to ERO1 reoxidation, H<sub>2</sub>O<sub>2</sub>, PRDX4, docosahexaenoic acid (DHA), and vitamin K can reoxidize PDI.<sup>10</sup> Moreover, several members of the PDI family can undergo disulfide exchanges with each other, without the need for an outside oxidant or reductant.<sup>26</sup> The cysteine thiols in the active site of PDI are common in other redox-sensing proteins. The low pK<sub>a</sub> value of the active site thiols (around 4.4 to 6.7) means that at physiological pH, the residue is deprotonated as a thiolate anion (R-S<sup>-</sup>). The thiol group of typical cysteines is protonated (R-SH) and renders the group unreactive at physiological pH. The charge on the thiolate anion in PDI is stabilized by a charge–charge interaction with the nearby positively charged Arg120.<sup>27</sup> The substrate binding/release cycle of PDI may be dependent on the redox state of the CXXC active sites. Oxidized PDI takes on an open conformation, promoting accessibility of the hydrophobic binding pocket. After PDI transfers a disulfide bond to its substrate, the conformational shift shuts off accessibility to the binding pocket. In addition to redox regulation, PDI can be regulated by other post-translational modifications, such as S-nitrosylation.

Cell-surface PDI is regulated by S-nitrosylation on the thiol active sites, which has been shown to contribute to neurological diseases such as Alzheimer's disease.<sup>28</sup> S-nitrosylation can change protein conformation, regulate protein activity, and alter protein–protein interactions,

among other functions. Aberrant S-nitrosylation leads to protein misfolding that can stimulate synaptic loss and contribute to the pathogenesis of Alzheimer's disease.

PDI also plays a role as the noncatalytic  $\beta$  subunit of prolyl 4-hydroxylase (P4H).<sup>29</sup> The P4H complex consists of two non-catalytic PDI subunits and two catalytic  $\alpha$  subunits. P4H resides in the ER and catalyzes the proline hydroxylation of procollagens, crucial for mature collagen function. Hydroxylation of collagen is critical for the stability of the collagen triple helix. PDI is necessary to prevent the  $\alpha$  subunit from aggregation and is likely responsible for maintaining ER localization of the complex.<sup>30</sup>

Another well-established function of PDI is as a critical component of the microsomal triglyceride transfer protein (MTP) complex.<sup>22</sup> MTP is composed of an  $\alpha\beta$  heterodimeric complex in which PDI makes up the smaller  $\beta$  subunit. MTP is a lipid transporter necessary for the biosynthesis of apolipoprotein B (apoB)-containing triglyceride-rich lipoproteins, regulation of cholesterol ester synthesis, and propagation of hepatitis C virus. The reduction, oxidation, and isomerization functions of PDI are not necessary for MTP to function properly; therefore, PDI likely plays a role in structural stability and solubilization of the complex.<sup>31</sup>

PDI also aids peptide loading onto major histocompatibility complex class 1 (MHC-1).<sup>16</sup> The MHC-1 complex binds antigenic peptides as they are synthesized through the ER and presents the synthesized peptides to cytotoxic T lymphocyte cells.

### **Functions in disease**

Proper protein folding is essential for cellular homeostasis and signaling. Aberrant PDI expression leads to several types of diseases caused by misfolded proteins (Figure II-5). Therefore, PDI inhibitors may be important for preventing and curing a wide range of diseases. For example, in cancer, PDI is overexpressed to combat the increasing ER load of protein synthesis,<sup>11</sup> and

knockdown of PDI in breast cancer cells leads to cell death via apoptosis.<sup>32</sup> In models of Huntington's disease, PDI induces apoptosis via mitochondrial membrane permeabilization (MOMP), and inhibition of PDI suppresses cell toxicity.<sup>9</sup> Protein folding malfunctions also play an important role in diabetes due to the link between diabetes, misfolding of proinsulin, and the UPR. Malfunctions in PDI caused by mutations in PDIA1 and ERp57 contribute to abnormal motor control and dendritic morphology.<sup>33</sup>

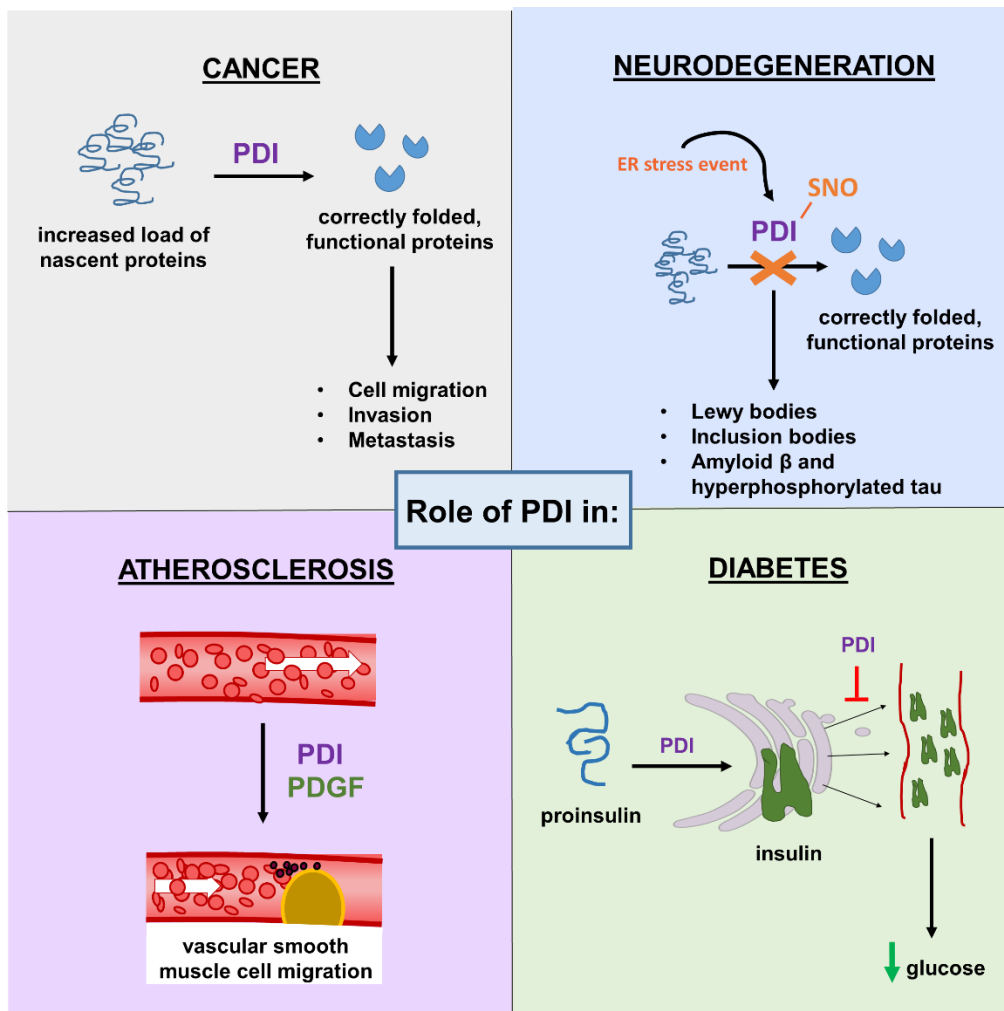


Figure II-5 PDI plays an important role in various disease states. In cancer, PDI folds nascent proteins to contribute to cell migration, invasion, and metastasis. In neurodegenerative diseases, SNO modification of PDI renders the enzyme incapable of protein folding, leading to the formation of Lewy bodies, inclusion bodies, amyloid  $\beta$  and hyperphosphorylated tau. In diabetes, PDI contributes to the production of insulin from proinsulin, but it also inhibits insulin secretion into the bloodstream, preventing insulin from lowering blood glucose levels. In cardiovascular diseases, in particular atherosclerosis, PDI is required for the PDGF-catalyzed vascular smooth muscle cell migration that causes plaque buildup. SNO (S-nitrosylation); PDGF (platelet-derived growth factor)

## **Cancer**

The connection between cancer and several PDI family members has been the subject of intense study for over a decade. In most cases, higher expression of PDI is protective for the cancer cells and correlates with poor patient survival. Inhibition of PDIA1 is cytotoxic to ovarian cancer cells.<sup>34</sup> In breast cancer mammospheres, knockdown of PDIA1, ERp44, or ERp57 inhibits cell growth.<sup>35</sup> Increased PDIA3 and PDIA6 gene expression correlates with aggressiveness of primary ductal breast cancer,<sup>36</sup> and high AGR2 expression is inversely correlated with survival in lung cancer patients.<sup>37</sup>

Although PDI inhibitors have yet to reach clinical trials, for the past several years, PDI has been actively pursued as a small molecule drug target. Several PDI inhibitors that interact with the reactive cysteine thiol active site have been identified for ovarian cancer,<sup>34</sup> multiple myeloma,<sup>38</sup> and other cancers. A propynoic acid carbamoyl methyl amide, PACMA31 was demonstrated to be an orally bioavailable PDI inhibitor with anti-cancer properties against ovarian cancer.<sup>34</sup> Small molecule inhibitors of PDI will be efficacious as cancer treatments, and research is actively being pursued in this area.

## **Neurodegenerative diseases**

A common pathological characteristic of neurodegenerative diseases such as Alzheimer's, Parkinson's, and amyotrophic lateral sclerosis (ALS) is the misfolding of proteins. Changes in redox homeostasis in such cases can lead to impairments in PDI function. PDI malfunction is involved in protein misfolding in Alzheimer's, Parkinson's, and Huntington's disease, as well as ALS and prion diseases. Increased levels of reactive oxygen species (ROS) and reactive nitrogen species (RNS) can modify target proteins. For example, the reactive thiol group on the CGHC active site of PDI can be modified with a nitric oxide moiety, in a reaction called S-nitrosylation.

S-nitrosylation is a post-translational modification in which nitric oxide species attach to a thiol to form an S-nitrosothiol. It can occur as a form of redox signaling, but has also been implicated in disease states. In the case of Alzheimer's disease, disruption of normal PDI function by S-nitrosylation triggers an important signaling event that leads to  $\alpha$ -synuclein oligomerization.<sup>11</sup> Interestingly, normally-functioning PDI inhibits tau fibrillization, a possible contributor to the pathogenesis of Alzheimer's disease.

Similarly, under normal physiological conditions, PDI forms a complex with  $\alpha$ -synuclein, which are protein aggregates common in Lewy bodies. PDI prevents protein aggregation in Parkinson's disease.<sup>11</sup> Patients with Parkinson's disease also exhibit upregulated levels of brain PDIp.<sup>39</sup> This suggests that PDI is upregulated in response to increased levels of ER stress; however, heightened levels of RNS lead to S-nitrosylation of PDI and prevent the enzyme from halting aggregate formation.

PDI inhibitors are also effective in models of Huntington's disease.<sup>9</sup> Huntington's disease is caused by a mutation in the huntingtin gene that causes the huntingtin protein to fold incorrectly. As a response to the mutant huntingtin protein, PDI localizes to the mitochondrial membrane and induces MOMP, an event in the intrinsic apoptotic pathway. Inhibitors of PDI are in pre-clinical development as a treatment for Huntington's disease and may be applicable to a wide range of neurodegenerative diseases.

### **Diabetes**

Dysfunction of human islet amyloid polypeptide (hIAPP) leads to misfolding events in diabetes similar to those contributing to the pathogenesis of Alzheimer's disease.<sup>40</sup> In addition, the hyperglycemic and hyperlipidemic conditions that occur with diabetes lead to a disruption in ER homeostasis and consequently upregulate the UPR. PDI interacts with hIAPP to prevent protein

aggregation. Therefore PDI plays an important role in diabetes, but this role varies depending on several conditions.<sup>41</sup> PDI also interacts with proinsulin in the ER of pancreatic  $\beta$ -cells, and blocks insulin export.<sup>42</sup> PDI acts as a retention factor for proinsulin in  $\beta$ -cells, and PDI represents an attractive potential target in Type II diabetes.

### **Other diseases**

The importance of PDI as an ER chaperone and oxidoreductase is realized under pathological conditions. PDI has also been implicated in several other protein conformation diseases, including liver disease, atherosclerosis, viral infection,<sup>43</sup> and prion diseases.<sup>12</sup> Atherosclerosis is the hardening or thickening of the arteries, caused by plaque formation due to high cholesterol levels and other factors. In atherosclerosis, PDI is required for platelet derived growth factor (PDGF)-induced vascular smooth muscle cell migration that causes platelet accumulation.<sup>44</sup> In platelets, PDI is localized in storage granules and on the extracellular surface of cells within the dense tubular system. UPR activation is involved in liver disease onset and progression.<sup>45</sup> In viral infections, thiol-disulfide exchange is important for HIV-1 entry in primary T-lymphocytes and human monocyte-derived macrophages. Both PDI and thioredoxin play essential roles in this process.

### **Summary**

Over 30% of secreted proteins rely on disulfide bond formation to both stabilize their tertiary structure and function properly. Thus, PDI is a crucial protein for the maintenance of cellular protein homeostasis. As a multifunctional protein with oxidoreductase and chaperone activity, PDI can be found not only in the ER, but also at the cell surface and in other locations in the cell. PDI overexpression is involved in various cancers, and PDI inhibitors are crucial tools for exploring disease models of cancer, Huntington's disease, HIV-1 infection, and cardiovascular

diseases. Both inhibitors of PDI function and inducers of PDI expression would be beneficial to combat PDI activity in different scenarios. For example, PDI inhibitors would be beneficial against cancer and viral infection; however, PDI oxidizers may prove useful against certain neurological diseases. PDI inhibitors are currently under pre-clinical development for many of these diseases and compelling research is under way to fully comprehend the involvement of PDI in various disease states.



## References

1. Venetianer, P.; Straub, F. Enzymic reactivation of reduced ribonuclease. *Biochim Biophys Acta* **1963**, 67, 166-8.
2. Goldberger, R. F.; Epstein, C. J.; Anfinsen, C. B. Acceleration of reactivation of reduced bovine pancreatic ribonuclease by a microsomal system from rat liver. *J Biol Chem* **1963**, 238, 628-35.
3. Bjelland, S.; Wallevik, K.; Kroll, J.; Dixon, J. E.; Morin, J. E.; Freedman, R. B.; Lambert, N.; Varandani, P. T.; Nafz, M. A. Immunological identity between bovine preparations of thiol - protein-disulfide oxidoreductase, glutathione-insulin transhydrogenase and protein-disulfide isomerase. *Biochim Biophys Acta* **1983**, 747, 197-9.
4. Hillson, D. A.; Freedman, R. B. Resolution of protein disulfide-isomerase and glutathione-insulin transhydrogenase activities by covalent chromatography - properties of the purified protein disulfide-isomerase. *Biochem J* **1980**, 191, 373-88.
5. Hawkins, H. C.; Freedman, R. B. Randomly reoxidized soybean trypsin-inhibitor and possibility of conformational barriers to disulfide isomerization in proteins. *FEBS Lett* **1975**, 58, 7-11.
6. Freedman, R. B. Native disulfide band formation in protein-biosynthesis - Evidence for the role of protein disulfide isomerase. *Trends Biochem Sci* **1984**, 9, 438-41.
7. Edman, J. C.; Ellis, L.; Blacher, R. W.; Roth, R. A.; Rutter, W. J. Sequence of protein disulfide isomerase and implications of its relationship to thioredoxin. *Nature* **1985**, 317, 267-70.
8. Rauch, F.; Fahiminiya, S.; Majewski, J.; Carrot-Zhang, J.; Boudko, S.; Glorieux, F.; Mort, J. S.; Bachinger, H. P.; Moffatt, P. Cole-Carpenter syndrome is caused by a heterozygous missense mutation in P4HB. *Am J Hum Genet* **2015**, 96, 425-31.
9. Hoffstrom, B. G.; Kaplan, A.; Letso, R.; Schmid, R. S.; Turmel, G. J.; Lo, D. C.; Stockwell, B. R. Inhibitors of protein disulfide isomerase suppress apoptosis induced by misfolded proteins. *Nat Chem Biol* **2010**, 6, 900-6.
10. Hatahet, F.; Ruddock, L. W. Protein disulfide isomerase: A critical evaluation of its function in disulfide bond formation. *Antioxid Redox Signal* **2009**, 11, 2807-50.
11. Xu, S.; Sankar, S.; Neamati, N. Protein disulfide isomerase: A promising target for cancer therapy. *Drug Discov Today* **2014**, 19, 222-40.
12. Benham, A. M. The protein disulfide isomerase family: Key players in health and disease. *Antioxid Redox Signal* **2012**, 16, 781-9.

13. Wang, L.; Wang, X.; Wang, C. C. Protein disulfide-isomerase, a folding catalyst and a redox-regulated chaperone. *Free Radic Biol Med* **2015**, 83, 305-13.
14. Wang, C.; Li, W.; Ren, J.; Fang, J.; Ke, H.; Gong, W.; Feng, W.; Wang, C. C. Structural insights into the redox-regulated dynamic conformations of human protein disulfide isomerase. *Antioxid Redox Signal* **2013**, 19, 36-45.
15. Tian, G.; Xiang, S.; Noiva, R.; Lennarz, W. J.; Schindelin, H. The crystal structure of yeast protein disulfide isomerase suggests cooperativity between its active sites. *Cell* **2006**, 124, 61-73.
16. Yagi-Utsumi, M.; Satoh, T.; Kato, K. Structural basis of redox-dependent substrate binding of protein disulfide isomerase. *Sci Rep* **2015**, 5, 13909.
17. Bekendam, R. H.; Bendapudi, P. K.; Lin, L.; Nag, P. P.; Pu, J.; Kennedy, D. R.; Feldenzer, A.; Chiu, J.; Cook, K. M.; Furie, B.; Huang, M.; Hogg, P. J.; Flaumenhaft, R. A substrate-driven allosteric switch that enhances PDI catalytic activity. *Nat Commun* **2016**, 7, 12579.
18. Hetz, C. The biological meaning of the UPR. *Nat Rev Mol Cell Biol* **2013**, 14, 404.
19. Goplen, D.; Wang, J.; Enger, P. O.; Tysnes, B. B.; Terzis, A. J.; Laerum, O. D.; Bjerkvig, R. Protein disulfide isomerase expression is related to the invasive properties of malignant glioma. *Cancer Res* **2006**, 66, 9895-902.
20. Bi, S.; Hong, P. W.; Lee, B.; Baum, L. G. Galectin-9 binding to cell surface protein disulfide isomerase regulates the redox environment to enhance T-cell migration and HIV entry. *Proc Natl Acad Sci U S A* **2011**, 108, 10650-5.
21. Reinhardt, C.; von Bruhl, M. L.; Manukyan, D.; Grahl, L.; Lorenz, M.; Altmann, B.; Dlugai, S.; Hess, S.; Konrad, I.; Orschiedt, L.; Mackman, N.; Ruddock, L.; Massberg, S.; Engelmann, B. Protein disulfide isomerase acts as an injury response signal that enhances fibrin generation via tissue factor activation. *J Clin Invest* **2008**, 118, 1110-22.
22. Wetterau, J. R.; Combs, K. A.; Spinner, S. N.; Joiner, B. J. Protein disulfide isomerase is a component of the microsomal triglyceride transfer protein complex. *J Biol Chem* **1990**, 265, 9800-7.
23. Darby, N. J.; Freedman, R. B.; Creighton, T. E. Dissecting the mechanism of protein disulfide isomerase: catalysis of disulfide bond formation in a model peptide. *Biochemistry* **1994**, 33, 7937-47.
24. Appenzeller-Herzog, C.; Riemer, J.; Zito, E.; Chin, K. T.; Ron, D.; Spiess, M.; Ellgaard, L. Disulphide production by Ero1alpha-PDI relay is rapid and effectively regulated. *EMBO J* **2010**, 29, 3318-29.
25. Araki, K.; Iemura, S.; Kamiya, Y.; Ron, D.; Kato, K.; Natsume, T.; Nagata, K. Ero1-alpha and PDIs constitute a hierarchical electron transfer network of endoplasmic reticulum oxidoreductases. *J Cell Biol* **2013**, 202, 861-74.

26. Oka, O. B.; Yeoh, H. Y.; Bulleid, N. J. Thiol-disulfide exchange between the PDI family of oxidoreductases negates the requirement for an oxidase or reductase for each enzyme. *Biochem J* **2015**, 469, 279-88.
27. Lappi, A. K.; Lensink, M. F.; Alanen, H. I.; Salo, K. E.; Lobell, M.; Juffer, A. H.; Ruddock, L. W. A conserved arginine plays a role in the catalytic cycle of the protein disulfide isomerases. *J Mol Biol* **2004**, 335, 283-95.
28. Kim, H. T.; Russell, R. L.; Raina, A. K.; Harris, P. L.; Siedlak, S. L.; Zhu, X.; Petersen, R. B.; Shimohama, S.; Smith, M. A.; Perry, G. Protein disulfide isomerase in Alzheimer disease. *Antioxid Redox Signal* **2000**, 2, 485-9.
29. Koivu, J.; Myllyla, R.; Helaakoski, T.; Pihlajaniemi, T.; Tasanen, K.; Kivirikko, K. I. A single polypeptide acts both as the beta subunit of prolyl 4-hydroxylase and as a protein disulfide-isomerase. *J Biol Chem* **1987**, 262, 6447-9.
30. Vuori, K.; Pihlajaniemi, T.; Marttila, M.; Kivirikko, K. I. Characterization of the human prolyl 4-hydroxylase tetramer and its multifunctional protein disulfide-isomerase subunit synthesized in a baculovirus expression system. *Proc Natl Acad Sci U S A* **1992**, 89, 7467-70.
31. Hussain, M. M.; Rava, P.; Walsh, M.; Rana, M.; Iqbal, J. Multiple functions of microsomal triglyceride transfer protein. *Nutr Metab (Lond)* **2012**, 9, 14.
32. Hashida, T.; Kotake, Y.; Ohta, S. Protein disulfide isomerase knockdown-induced cell death is cell-line-dependent and involves apoptosis in MCF-7 cells. *J Toxicol Sci* **2011**, 36, 1-7.
33. Woehlbier, U.; Colombo, A.; Saaranen, M. J.; Perez, V.; Ojeda, J.; Bustos, F. J.; Andreu, C. I.; Torres, M.; Valenzuela, V.; Medinas, D. B.; Rozas, P.; Vidal, R. L.; Lopez-Gonzalez, R.; Salameh, J.; Fernandez-Collemani, S.; Munoz, N.; Matus, S.; Armisen, R.; Sagredo, A.; Palma, K.; Irrazabal, T.; Almeida, S.; Gonzalez-Perez, P.; Campero, M.; Gao, F. B.; Henny, P.; van Zundert, B.; Ruddock, L. W.; Concha, M. L.; Henriquez, J. P.; Brown, R. H.; Hetz, C. ALS-linked protein disulfide isomerase variants cause motor dysfunction. *EMBO J* **2016**, 35, 845-65.
34. Xu, S.; Butkevich, A. N.; Yamada, R.; Zhou, Y.; Debnath, B.; Duncan, R.; Zandi, E.; Petasis, N. A.; Neamati, N. Discovery of an orally active small-molecule irreversible inhibitor of protein disulfide isomerase for ovarian cancer treatment. *Proc Natl Acad Sci U S A* **2012**, 109, 16348-53.
35. Wise, R.; Duhachek-Muggy, S.; Qi, Y.; Zolkiewski, M.; Zolkiewska, A. Protein disulfide isomerases in the endoplasmic reticulum promote anchorage-independent growth of breast cancer cells. *Breast Cancer Res Treat* **2016**, 157, 241-52.
36. Ramos, F. S.; Serino, L. T. R.; Carvalho, C. M. S.; Lima, R. S.; Urban, C. A.; Cavalli, I. J.; Ribeiro, E. PDIA3 and PDIA6 gene expression as an aggressiveness marker in primary ductal breast cancer. *Genet Mol Res* **2015**, 14, 6960-7.

37. Alavi, M.; Mah, V.; Maresh, E. L.; Bagryanova, L.; Horvath, S.; Chia, D.; Goodglick, L.; Liu, A. Y. High expression of AGR2 in lung cancer is predictive of poor survival. *BMC Cancer* **2015**, *15*, 655.
38. Vatolin, S.; Phillips, J. G.; Jha, B. K.; Govindgari, S.; Hu, J.; Grabowski, D.; Parker, Y.; Lindner, D. J.; Zhong, F.; Distelhorst, C. W.; Smith, M. R.; Cotta, C.; Xu, Y.; Chilakala, S.; Kuang, R. R.; Tall, S.; Reu, F. J. Novel protein disulfide isomerase inhibitor with anticancer activity in multiple myeloma. *Cancer Res* **2016**, *76*, 3340-50.
39. Conn, K. J.; Gao, W.; McKee, A.; Lan, M. S.; Ullman, M. D.; Eisenhauer, P. B.; Fine, R. E.; Wells, J. M. Identification of the protein disulfide isomerase family member PDIP in experimental Parkinson's disease and Lewy body pathology. *Brain Res* **2004**, *1022*, 164-72.
40. Montane, J.; de Pablo, S.; Obach, M.; Cadavez, L.; Castano, C.; Alcarraz-Vizan, G.; Visa, M.; Rodriguez-Comas, J.; Parrizas, M.; Servitja, J. M.; Novials, A. Protein disulfide isomerase ameliorates beta-cell dysfunction in pancreatic islets overexpressing human islet amyloid polypeptide. *Mol Cell Endocrinol* **2016**, *420*, 57-65.
41. Sun, J. H.; Cui, J. Q.; He, Q.; Chen, Z.; Arvan, P.; Liu, M. Proinsulin misfolding and endoplasmic reticulum stress during the development and progression of diabetes. *Mol Aspects Med* **2015**, *42*, 105-18.
42. Rajpal, G.; Schuiki, I.; Liu, M.; Volchuk, A.; Arvan, P. Action of protein disulfide isomerase on proinsulin exit from endoplasmic reticulum of pancreatic  $\beta$ -cells. *J Biol Chem* **2012**, *287*, 43-7.
43. Khan, M. M.; Simizu, S.; Lai, N. S.; Kawatani, M.; Shimizu, T.; Osada, H. Discovery of a small molecule PDI inhibitor that inhibits reduction of HIV-1 envelope glycoprotein gp120. *ACS Chem Biol* **2011**, *6*, 245-51.
44. Primm, T. P.; Gilbert, H. F. Hormone binding by protein disulfide isomerase, a high capacity hormone reservoir of the endoplasmic reticulum. *J Biol Chem* **2001**, *276*, 281-6.
45. Zhang, L. C.; Wang, H. H. The essential functions of endoplasmic reticulum chaperones in hepatic lipid metabolism. *Dig Liver Dis* **2016**, *48*, 709-16.

## CHAPTER III

### Discovery and Mechanistic Elucidation of a Class of PDI Inhibitors for the Treatment of Glioblastoma

#### Introduction<sup>3</sup>

Glioblastoma is the most common type of malignant central nervous system (CNS) tumor. Prevalence increases with age with peak incidence in individuals aged 60-79 years.<sup>1</sup> Despite the treatment options available – surgical resection followed by chemoradiotherapy and adjuvant chemotherapy (temozolomide) – the five-year survival rate of patients diagnosed with glioblastoma is only 5.0 %.<sup>1,2</sup> Current treatments are marginally effective and the number of cases is expected to grow with the aging population, emphasizing the urgent need for the development of novel and effective therapies for glioblastoma. Disease recurrence and drug resistance remain the major challenges for a successful cure.

Protein disulfide isomerase (PDI; EC 5.3.4.1) is a 57-kDa endoplasmic reticulum (ER) oxidoreductase of the thioredoxin superfamily that assists protein folding in the ER by catalyzing

---

<sup>3</sup> This work has been published and is being reprinted with permission from Kyani, A., Tamura, S., Yang, S., Shergalis, A., Samanta, S., Kuang, Y., Ljungman, M., & Neamati, N. (2018). Discovery and Mechanistic Elucidation of a Class of Protein Disulfide Isomerase Inhibitors for the Treatment of Glioblastoma. *ChemMedChem*, 13(2), 164-177.

**Author contributions:** Anahita Kyani, Shuzo Tamara, Suhui Yang, and Andrea Shergalis were the primary authors. Anahita Kyani generated figure III-4 and performed docking studies. Shuzo Tamara generated figure III-1 and cytotoxicity data. Soma Somanta generated figure III-2, I-5, I-6, and I-7. Yuting Kuang performed experiments to generate figure III-6. Suhui Yang synthesized all compounds. Mats Ljungman generated figure III-5. Nouri Neamati is the corresponding author.

disulfide rearrangements (isomerase activity), disulfide formation (oxidase activity), and disulfide reduction (reductase activity).<sup>3</sup> PDI is overexpressed in several cancers but most significantly in glioblastoma.<sup>3</sup> Previously, we demonstrated that PDI knockdown by siRNA leads to substantial cytotoxicity in ovarian cancer cells.<sup>4</sup> PDI inhibitors and modulators are being developed to combat cancer and neurological diseases. The PDI inhibitor bacitracin inhibits migration and invasion of glioblastoma cells<sup>5</sup> and enhances apoptosis caused by ER stress-inducing agents in melanoma cells.<sup>6</sup> Another class of compounds, including **PS89**, are weak reversible inhibitors of PDI and, at moderately high concentrations, sensitize several cancer cell lines to etoposide treatment.<sup>7</sup> Interestingly, after further characterization, BAP31 (B-cell receptor-associated protein 31) was identified as the major target of **PS89**, instead of PDI.<sup>8</sup> A reversible, selective, non-toxic PDI inhibitor, **ML359**, was developed as a probe to study thrombosis-related diseases.<sup>9</sup> Modulators of PDI have also been shown to be neuroprotective. A reversible PDI modulator, **LOC14** ( $EC_{50} = 500$  nM), has neuroprotective effects in cellular and rat models of Huntington's disease.<sup>10</sup> Furthermore, PDI inhibitor **CCF642** was demonstrated to be effective in a mouse xenograft model of multiple myeloma.<sup>11</sup> Mounting evidence highlights PDI as an important target against several diseases including cancer, emphasizing the need for potent, clinically relevant PDI inhibitors for cancer treatment.

Herein, we report on the development of **35G8** as a novel and potent PDI inhibitor that demonstrates activity in brain cancer cells and has drug-like properties. The activity of **35G8** in a diverse set of robust assays confirmed that the initial observation of activity was not a consequence of its redox-cycling status. Results from nascent RNA Bru-seq<sup>12</sup> analysis showed that the transcription of 498 genes increased and 238 genes decreased at least 2-fold following a 4-hour incubation with **35G8** in U87MG glioblastoma cells. Gene set enrichment analysis demonstrated

the upregulated genes to be involved in the Nrf2 antioxidant response and the unfolded protein response (UPR). Genes with decreased transcription involved histone and DNA repair pathways. In addition, **35G8** upregulates two key genes, SLC7A11 and HMOX1, and may kill cells through an iron-dependent form of cell death independent of apoptosis and necrosis, called ferroptosis.<sup>13</sup> The alterations in the transcriptional landscape induced by **35G8** provide a more comprehensive understanding of the mechanisms of PDI inhibition in brain cancer therapy.

## Results and discussion

### **35G8 is a nanomolar inhibitor of PDI**

To identify cytotoxic small molecules, we screened a highly diverse library of 20,000 compounds, representing over one million compounds, in the colon cancer cell line HCT116 (Figure III-1). From the initial screen, we identified 443 cytotoxic compounds with  $IC_{50}$  values under 10  $\mu$ M. These 443 compounds were tested for PDI inhibition in an insulin turbidity assay.<sup>14</sup> Eight compounds demonstrated potent inhibition ( $IC_{50} < 1.0 \mu$ M), and after confirming the activity with re-purchased compound stocks and verifying a dose-dependent response, the most potent compound, 1,3,6-trimethylpyrimido[5,4-e] [1,2,4] triazine-5,7(1H,6H)-dione (**35G8**), was selected for further analysis and optimization.

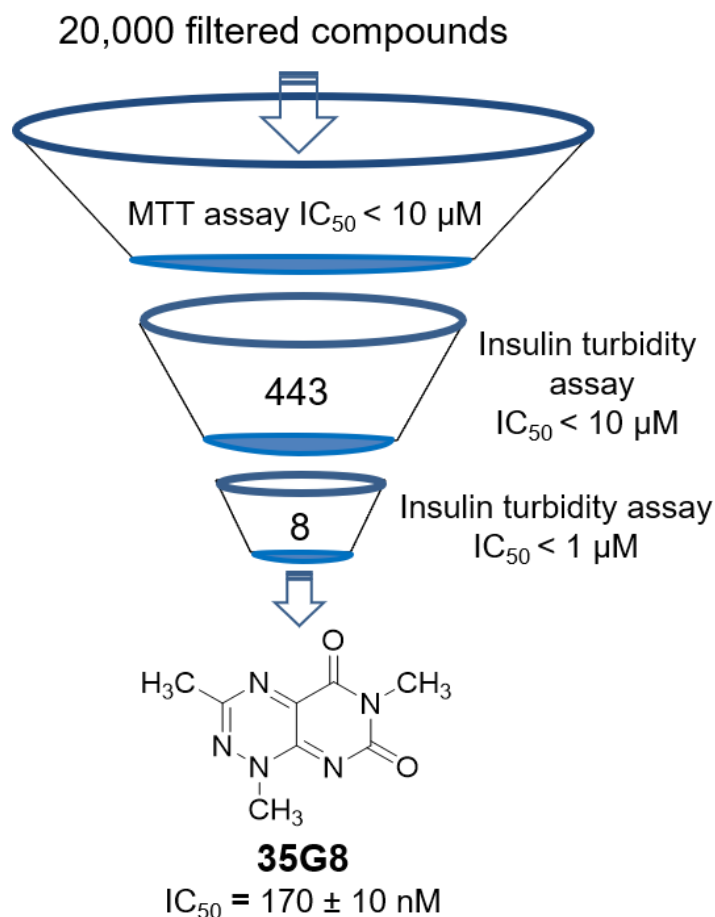


Figure III-1 Discovery of **35G8**. Workflow summarizing the screening process that identified **35G8** as a potent PDI inhibitor. 20,000 compounds were screened in an MTT assay with HCT116 cells and 443 compounds were cytotoxic in these cells. The 443 compounds were tested further in an insulin turbidity assay; **35G8** had the most potent  $IC_{50}$  value and was taken for further biochemical analysis and optimization.

We next used the thermal shift assay<sup>15</sup> to validate whether **35G8** stabilizes its presumed target, PDI. Intriguingly, **35G8** destabilized PDI, indicated by the decrease in melting temperature of the protein (Figure III-2). The dose-dependence of the negative thermal shifts at all concentrations tested ( $\Delta T_m$ :  $-3.64 \text{ }^\circ\text{C}$  at  $100 \mu\text{M}$ ;  $-2.94 \text{ }^\circ\text{C}$  at  $10 \mu\text{M}$ ;  $-1.43 \text{ }^\circ\text{C}$  at  $1 \mu\text{M}$ ) provides further evidence that **35G8** associates with and destabilizes PDI. The melting temperature of a protein shifts positively or negatively in the presence of a ligand, and this change in melting temperature parallels the stability of the protein.<sup>16</sup> These results suggest **35G8** interacts with PDI at a unique site compared to known stabilizing ligands, such as estradiol.<sup>17</sup> To further validate **35G8** binding to



PDI, we performed the cellular thermal shift assay (CETSA) and drug affinity responsive target stability (DARTS) assay. **35G8** also destabilized PDI via CETSA (Figure III-2). **35G8** had little effect on a related molecular chaperone, GRP78, but did seem to stabilize the cysteine-containing glutathione-transferase Omega 1 (GSTO1). In the DARTS assay, U87MG cell lysates were subjected to pronase degradation in the presence or absence of **PACMA31** or **35G8**. Both compounds protected PDI from proteolysis, but had no effect on the degradation of GRP78 or GSTO1. These results established **35G8** as a potent, selective inhibitor of PDI.

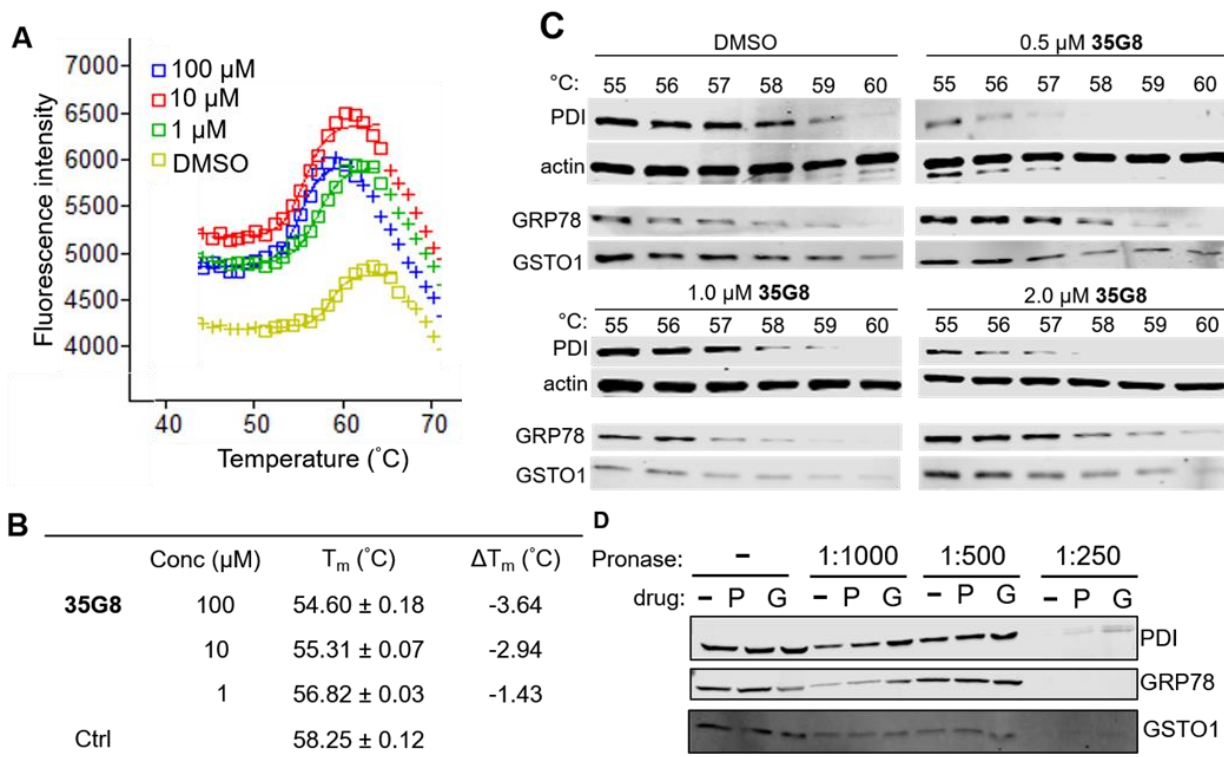
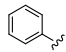
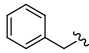
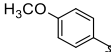
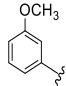
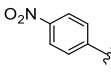
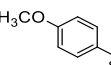


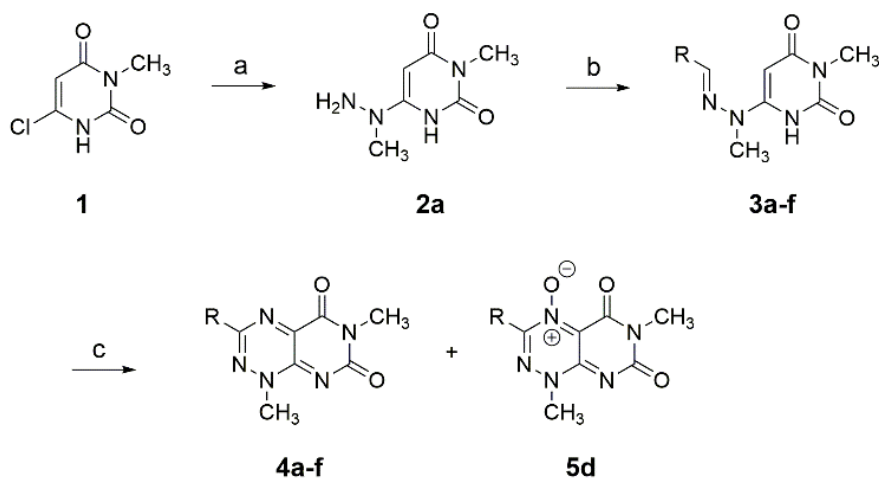
Figure III-2 **35G8** destabilizes PDI. (A) Thermal shifts observed for recombinant PDI (0.3 mg/ml) with various concentrations of **35G8**. DMSO was used as a control. (B) Apparent melting temperatures (T<sub>m</sub>) and change in melting temperature derived from ThermoFluor assay (C) Protein expression of PDI, GRP78, GSTO1, and actin (loading control) in the absence or presence of **35G8** at varying temperatures in the cellular thermal shift assay (D) Western blot analysis of DARTS assay with PDI, GRP78, and GSTO1 subjected to 100 μM **PACMA31** (P), 100 μM **35G8** (G), or DMSO (-). Samples were subjected to varying concentrations of pronase. Data are means from three independent experiments.

Table III-1 PDI inhibitory activity of **35G8** analogues. IC<sub>50</sub> values obtained in insulin turbidity assay. Data are means ± standard deviation from three independent experiments.

Compound	Basic Module	R1	R2	IC <sub>50</sub> (μM)
<b>35G8 (4a)</b> <sup>[a]</sup>	A	CH <sub>3</sub>	CH <sub>3</sub>	0.17 ± 0.01
<b>4b</b> <sup>[b]</sup>	A		CH <sub>3</sub>	0.39 ± 0.03
<b>4c</b> <sup>[c]</sup>	A		CH <sub>3</sub>	0.33 ± 0.04
<b>4d</b> <sup>[d]</sup>	A		CH <sub>3</sub>	0.36 ± 0.05
<b>4e</b> <sup>[e]</sup>	A		CH <sub>3</sub>	0.32 ± 0.01
<b>4f</b> <sup>[f]</sup>	A		CH <sub>3</sub>	0.24 ± 0.04
<b>5d</b> <sup>[g]</sup>	B		CH <sub>3</sub>	0.42 ± 0.07
<b>NC72 (NSC67078)</b>	A	H	CH <sub>3</sub>	0.105 ± 0.004
<b>NC75 (NSC99733)</b>	A	H	H	> 120
<b>NC79 (NSC280172)</b>	B	CH <sub>3</sub>	CH <sub>3</sub>	6.55 ± 1.19
<b>PACMA31</b>	-	-	-	5.81 ± 1.23

[a] 1,3,6-Trimethylpyrimido[5,4-e][1,2,4]triazine-5,7(1H,6H)-dione. [b] 1,6-Dimethyl-3-phenylpyrimido[5,4-e][1,2,4]triazine-5,7(1H,6H)-dione. [c] 3-Benzyl-1,6-dimethylpyrimido[5,4-e][1,2,4]triazine-5,7(1H,6H)-dione. [d] 3-(4-Methoxyphenyl)-1,6-dimethylpyrimido[5,4-e][1,2,4]triazine-5,7(1H,6H)-dione. [e] 3-(3-Methoxyphenyl)-1,6-dimethylpyrimido[5,4-e][1,2,4]triazine-5,7(1H,6H)-dione. [f] 1,6-Dimethyl-3-(4-nitrophenyl)pyrimido[5,4-e][1,2,4]triazine-5,7(1H,6H)-dione. [g] 3-(4-Methoxyphenyl)-1,6-dimethyl-5,7-dioxo-1,5,6,7-tetrahydropyrimido[5,4-e][1,2,4]triazine 4-oxide.

We also synthesized several analogues of **35G8** to validate the above findings. The lead compound, **35G8**, contains methyl substituents at the three N1, C3, and N6 positions (Figure III-1). We incorporated various substituents at the C3 position while maintaining the methyl groups at N1 and N6 due to the efficient introduction of the N1 and N6 methyl groups early in the synthesis (Scheme III-1). Nucleophilic attack of methylhydrazine on 6-chloro-3-methyl uracil (**1**) led to hydrazinylpyrimidine-2,4(1H,3H)-dione (**2a**).<sup>18</sup> Further condensation with aldehydes furnished the corresponding hydrazones (**3a-f**). Each hydrazone was cyclized by treatment with sodium nitrite in acetic acid/water to afford a mixture of pyrimidotriazinediones (**4a-f**) and the corresponding N-oxide derivative (**5d**).



Scheme III-1 Synthesis of 3-substituted **35G8** analogues. Reagents and conditions: (a) methylhydrazine, EtOH, reflux; (b) aldehyde (R-CHO), anhydrous EtOH, room temperature; (c) NaNO<sub>2</sub>, AcOH/H<sub>2</sub>O, room temperature.

All **35G8** analogues had strong PDI inhibitory activity with submicromolar IC<sub>50</sub> values, except **NC75** (> 120 μM) and **NC79** (6.55 ± 1.19 μM) in the insulin turbidity assay (Table III-1). The pyrimidotriazinedione compound (**35G8**, IC<sub>50</sub>: 0.17 ± 0.01 μM) was more potent than the corresponding N-oxide compound (**NC79**). A similar trend was observed between **4d** (IC<sub>50</sub>: 0.36 ± 0.05 μM) and **5d** (IC<sub>50</sub>: 0.42 ± 0.07 μM). Among the pyrimidotriazinediones, the compounds

containing a methyl group (**4a**) or no substituent (**NC72**) at R1 had enhanced activity compared to those with an aromatic moiety (**4b-f**), likely due to steric effects. Interestingly, the PDI inhibitory activity was abolished upon removal of the methyl substituent at R2 (**NC75**:  $IC_{50} > 120 \mu\text{M}$ ) compared to **NC72** ( $IC_{50}$ :  $0.11 \mu\text{M}$ ), indicating that the methyl group at R2 may be necessary to retain PDI inhibitory activity. Furthermore, the removal of PDI inhibitory activity abolished the cytotoxicity of the compound.

### **35G8 analogues inhibit glioblastoma cell proliferation**

All synthesized compounds demonstrated potent cytotoxicity in four glioblastoma cell lines, U87MG, U118MG, A172 and NU04, with  $IC_{50}$  values under  $10 \mu\text{M}$ , except **4c** (Table III-2). The  $IC_{50}$  value of **35G8** in U87MG cells is  $1.1 \pm 0.2 \mu\text{M}$ . **NC72** demonstrated the most potent cytotoxicity ( $IC_{50} = 0.5 \pm 0.1 \mu\text{M}$ ), complementing its potency in the PDI assay. **NC75** and **NC79** had little effect on cell growth. Interestingly, this suggests that the methyl substituent is important for both PDI activity (as seen in the dramatic  $IC_{50}$  value increase from **NC72** to **NC75**) and cytotoxicity.

Table III-2 *In vitro* cytotoxicity of **35G8** analogues in a panel of human glioblastoma cell lines. Cytotoxicity measured in the MTT assay. Data are means from at least three independent experiments.

Compound	IC <sub>50</sub> (μM)			
	U87MG	U118MG	NU04	A172
<b>35G8</b>	1.1 ± 0.2	3.9 ± 0.1	0.8 ± 0.2	2.0 ± 0.6
<b>4b</b>	3.0 ± 0.3	4.6 ± 0.5	3.7 ± 1.2	1.8 ± 0.4
<b>4c</b>	12.7 ± 3.7	24.0 ± 7.4	> 30	8.2 ± 2.5
<b>4d</b>	1.2 ± 0.2	3.9 ± 0.6	0.86 ± 0.04	1.5 ± 0.4
<b>4e</b>	1.1 ± 0.2	2.4 ± 0.6	0.76 ± 0.22	1.5 ± 0.1
<b>4f</b>	1.8 ± 0.7	6.2 ± 1.6	4.9 ± 1.2	1.1 ± 0.2
<b>5d</b>	1.9 ± 0.7	4.3 ± 0.1	1.5 ± 0.7	1.7 ± 0.1
<b>NC72</b>	0.5 ± 0.1	-	-	-
<b>NC75</b>	> 100	-	-	-
<b>NC79</b>	> 100	-	-	-
<b>PACMA31</b>	0.13 ± 0.07	0.28 ± 0.04	0.4 ± 0.1	0.12 ± 0.10

Pretreatment with Z-VAD-FMK, an irreversible caspase inhibitor,<sup>19</sup> and necrostatin-1, a necroptosis inhibitor,<sup>20</sup> did not protect the cells from **35G8**-induced cell death (Table III-3). These results indicate that neither necrosis nor apoptosis are the main pathways responsible and another pathway may be implicated in cell death. To assess the role of ferroptosis upon **35G8** treatment, we treated the cells with deferoxamine (DFO), an iron chelator (Figure III-3). **35G8**-induced cell death was rescued in the presence of DFO, suggesting ferroptosis may play a role in **35G8**-induced cell death.

Table III-3 Cell death rescue from **35G8** treatment in U87MG cells

IC <sub>50</sub> (μM)		
<b>35G8</b>	<b>35G8+ZVAD</b>	<b>35G8+Necrostatin</b>
1.12 ± 0.04	1.22 ± 0.11	1.06 ± 0.01

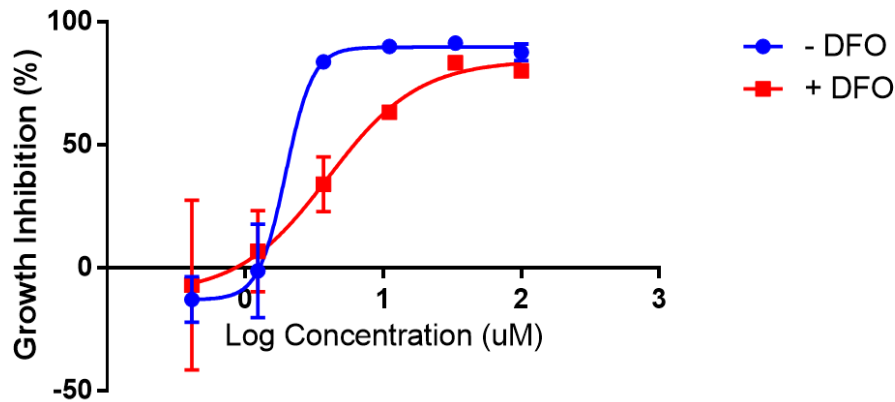


Figure III-3 DFO decreases the potency of **35G8**. U87MG cells were subjected to 100 μM DFO at increasing concentrations of 35G8. Results are means from three independent experiments; error bars show s.d.

### **35G8 induces the Nrf2 antioxidant pathway and ER stress response**

To better elucidate the cellular response to the pyrimidotriazinediones, we performed nascent RNA sequencing using the Bru-seq<sup>21</sup> method and analyzed changes in gene transcription rates in response to **35G8** in U87MG cells. Four hours after **35G8** treatment, 498 genes were upregulated at least two-fold and 238 genes were downregulated at least two-fold. Many of the top upregulated genes are implicated in the Nrf2 antioxidant response, ER stress response, and autophagy. We identified the top 20 upregulated and downregulated gene sets and analyzed the genes that were upregulated or downregulated at least two-fold with IPA (Ingenuity Pathway Analysis) (Figure III-4) and GSEA (Gene Set Enrichment Analysis). GSEA revealed enrichment of the Nrf2-mediated oxidative stress response upon **35G8** treatment (Figure III-4). Treatment also

correlates with KOBAYASHI\_EGFR\_SIGNALING\_24HR\_DN gene set, suggesting **35G8** may inhibit EGFR signaling. DAVID (the Database for Annotation, Visualization and Integrated Discovery) analysis and GSEA identified functional terms related to ER and redox-active disulfide, providing further evidence for PDI inhibition by **35G8** (Figure III-4).

The upregulation of Nrf2 response genes, including HMOX1 (19-fold increase), SLC7A11 (63-fold increase), AKR1C1 (59-fold increase), and LOC344887 (23-fold increase), is likely a protective response to the insults caused by **35G8**.

We also confirmed parallel increases in HMOX1 and SLC7A11 protein expression (Figure III-4). The Nrf2 antioxidant pathway mitigates oxidative stress by inducing antioxidant response elements.<sup>22</sup> PDI is vital in the UPR, and inhibiting this key protein disrupts proteostasis, ultimately leading to ER stress and cell death when the cell cannot cope with the accumulation of misfolded proteins. ER stress target genes downstream the PERK-ATF4 ER stress response pathway, CHAC1 (46-fold increase), DDIT3 (4-fold increase), and HSPA5 (8-fold increase) increased as a result of **35G8** treatment. Protein expression of GRP78 (HSPA5) and DDIT3 increased upon 24-hour treatment of 2  $\mu$ M **35G8**; however, CHAC1 protein was undetectable, likely because the CHAC1 protein is rapidly degraded by the proteasome.<sup>23</sup> mRNA expression of other downstream targets of the PERK-ATF4 ER stress response pathway, including TRIB3 and ASNS,<sup>24, 25</sup> also increased in response to **35G8**. These results suggest that brain cancer cells rely on PDI to maintain redox homeostasis, and when PDI is inhibited, cells undergo irremediable ER stress that leads to cell death.

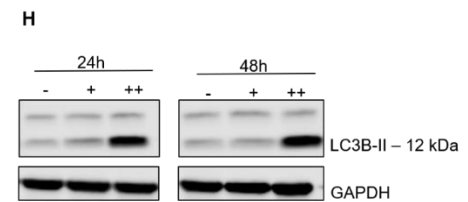
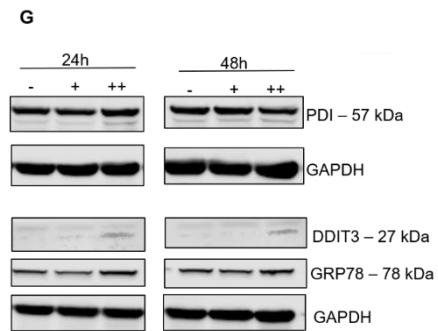
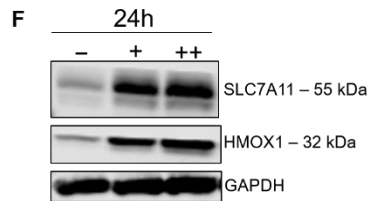
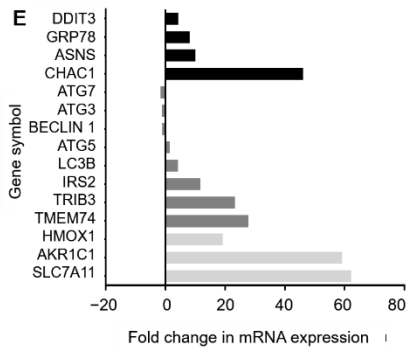
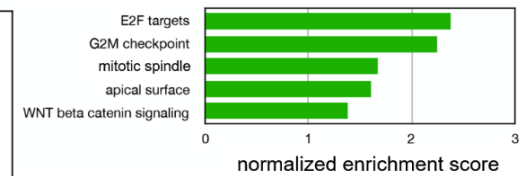
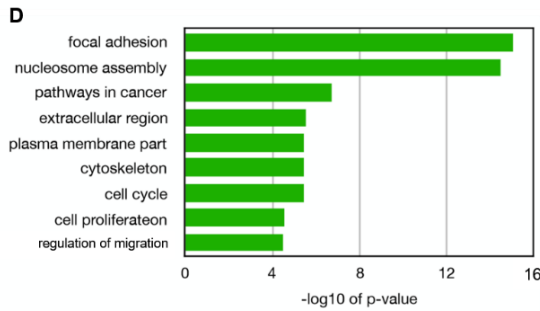
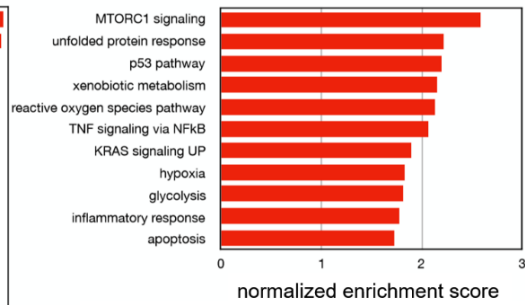
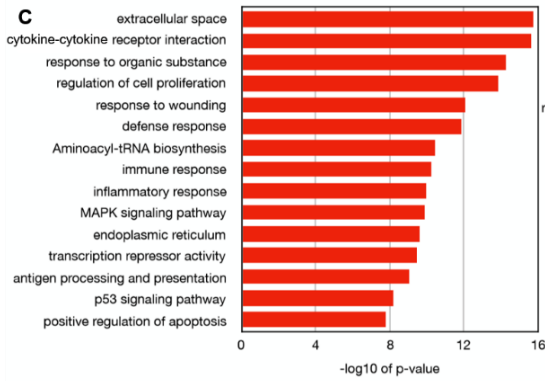
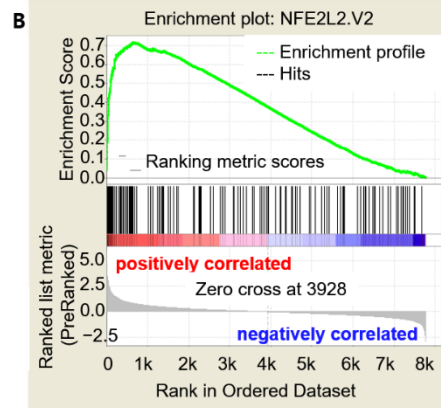
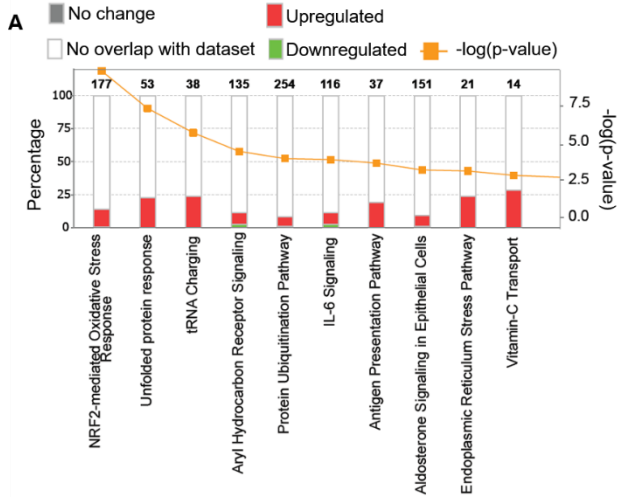




Figure III-4 Effects of **35G8** treatment on cellular pathways. (A) Pathways from the Bru-seq analysis of **35G8**-treated cells. (B) GSEA for “NFE2L2.V2,” the top gene set matched with upregulated genes from Bru-seq results. Functional terms represented by genes upregulated (C) and downregulated (D) at least 2-fold by **35G8** treatment. Pathway analysis was performed using DAVID (left) and GSEA (right). (E) Histograms of differentially expressed proteins between **35G8**-treated and DMSO-treated U87MG cells. Fold change bars are in black for UPR genes, dark grey for autophagy-related genes, and light grey for Nrf2-related genes. (F) Western blot showing Nrf2-regulated proteins SLC7A11 and HMOX1 expression upon 24-hour treatment of U87MG cells with 1 or 2  $\mu\text{M}$  **35G8**. (G) Western blot of ER stress-induced proteins DDIT3 and GRP78 expression upon 24-hour treatment of U87MG cells with 1 and 2  $\mu\text{M}$  **35G8**. (H) Western blot of autophagy-related proteins LC3B, beclin 1, ATG3, ATG5, and ATG7 expression upon 24-hour treatment of U87MG cells with 1 (+) and 2 (++)  $\mu\text{M}$  **35G8**. -: vehicle-treated control. GAPDH used as a loading control. Experiments repeated in triplicate.

We also identified several autophagic signaling genes that respond to ER stress triggered by **35G8**, including *TRIB3*, *IRS2*, and *TMEM74*. *TRIB3* (23-fold increase), as a downstream target of ATF4, mediates autophagy by inhibiting the mTORC1 pathway.<sup>26</sup> *IRS2* (12-fold increase) activation induces protective autophagy to clear unwanted protein aggregates<sup>27</sup> and may also help remove damaged cells. *TMEM74* (28-fold increase), a transmembrane protein localized to the lysosome and autophagosome, regulates autophagy.<sup>28</sup> The increased transcription of these autophagy-related genes prompted us to measure protein expression of several autophagy markers. Cleaved LC3B expression increased significantly after 24-hour treatment with 2  $\mu\text{M}$  **35G8**, however expression levels of other autophagy markers, including ATG3, ATG5, ATG7, and beclin 1, did not change, suggesting that autophagy may play a more protective role in this case. These results indicate that **35G8** induces the ER stress and Nrf2 response in brain cancer cells to contribute to cell death.

### **Bru-seq analysis identifies novel glioblastoma markers**

*AKR1C1*, *IL-6*, *CHAC1* and *TNFSF9* are among the top 20 upregulated genes with significantly decreased expression in brain cancer compared to normal brain tissues (Figure III-5). Conversely, genes that were downregulated upon **35G8** treatment, including *TXNIP* (-7.40-fold change), *EGR1* (-5.65-fold change), and *ITGA3* (-3.89-fold change) are often overexpressed in brain cancer (Figure III-5). Additional genes affected include *HMOX1*, *IRS2*, *SLC7A11*, and

*mir181A2HG* (**Figure S6**). These data suggest **35G8** inhibits transcription of these mRNA or inhibits an upstream regulator of *ITGA3* and *EGR1*. The results also indicate a gene such as *IL6* may be used as a biomarker of **35G8** inhibition in future studies and *EGR1* may be a novel glioblastoma marker.

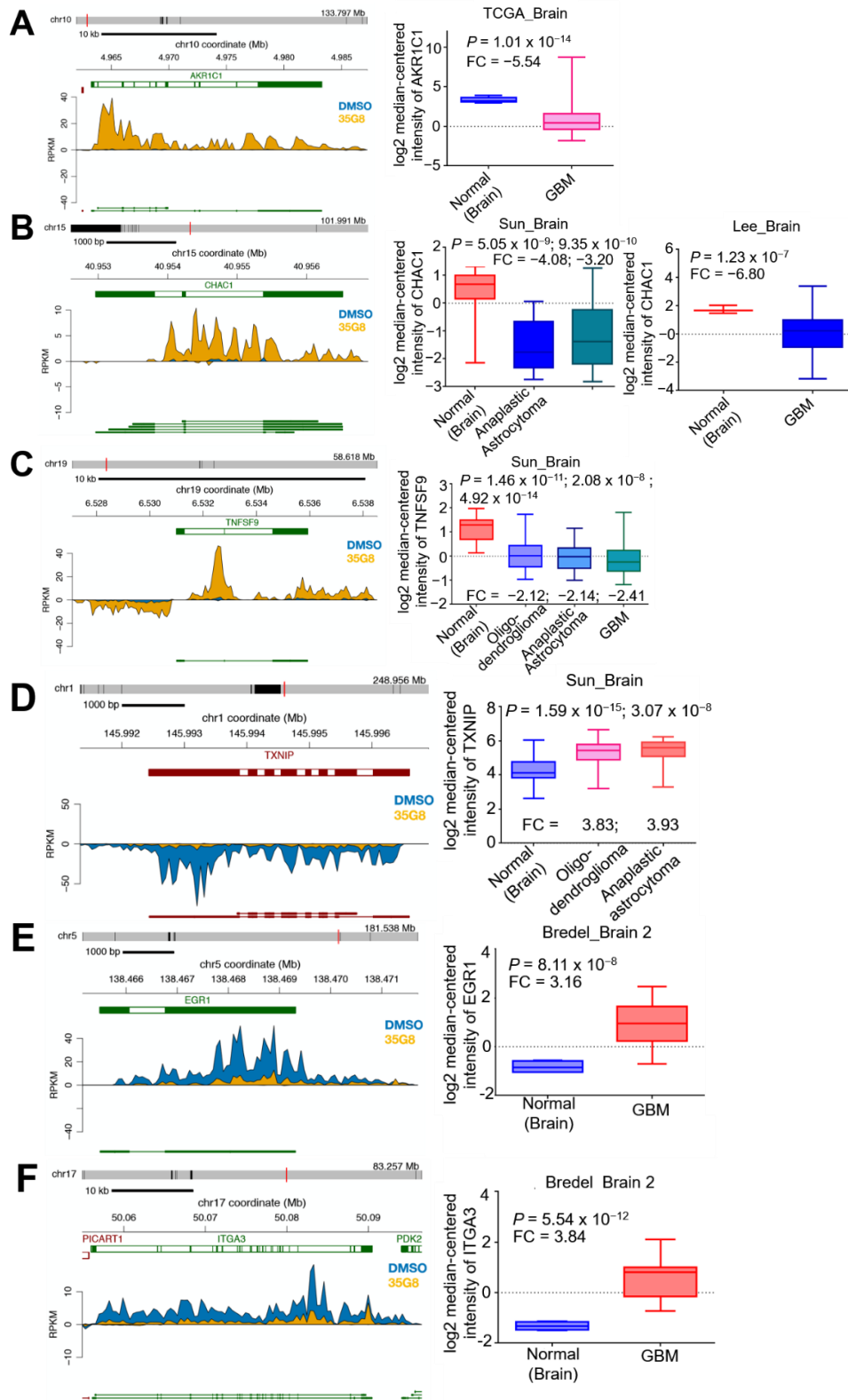


Figure III-5 Effect of **35G8** treatment on RNA synthesis in U87MG cells. **35G8** induces transcription of (A) *AKR1C1*, (B) *CHAC1* and (C) *TNFSF9* while corresponding box plots show downregulation of these genes in brain cancer. **35G8** inhibits the transcription of (D) *TXNIP*, (E) *EGR1* and (F) *ITGA3* while corresponding box plots show upregulation of these genes in brain cancer. FC: fold change; GBM: glioblastoma

### 35G8 induces ROS formation

Because the cells responded to **35G8** by upregulating the Nrf2-mediated oxidative stress response, we investigated the production of reactive oxygen species (ROS) by **35G8** and its analogues to determine whether the cytotoxicity of these compounds is dependent on ROS induction. We observed significant ROS induction by all **35G8** analogues tested at 5  $\mu\text{M}$  as early as four hours after treatment, except for **4c** (Figure III-6). ROS accumulation with these compounds was time-dependent. At 24 hours, 5  $\mu\text{M}$  **35G8** treatment achieved maximal ROS induction, comparable to 100  $\mu\text{M}$   $\text{H}_2\text{O}_2$  treatment. No change in the fluorescent signal in the samples containing **35G8** without  $\text{H}_2\text{DCFDA}$  dye was observed, eliminating the possibility of

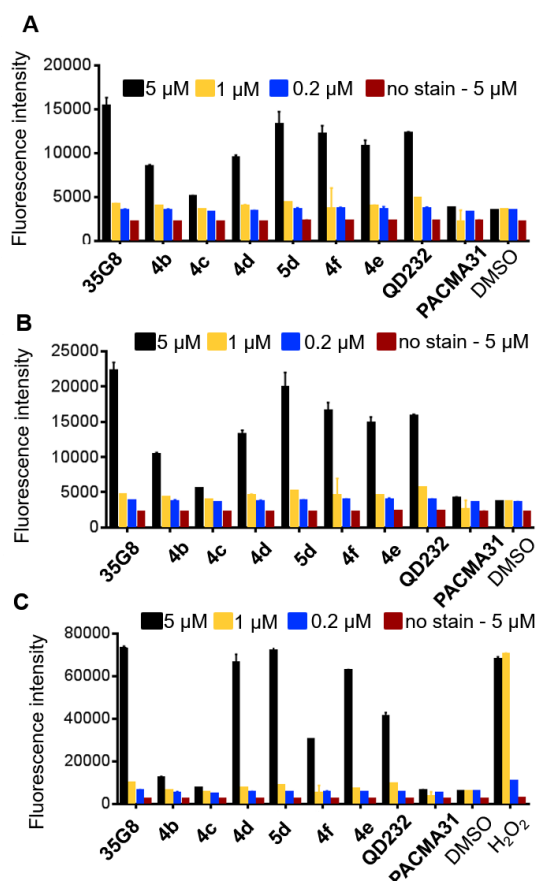


Figure III-6 ROS induction of **35G8** analogues at (A) 4 hours, (B) 6 hours, and (C) 24 hours. In (C),  $\text{H}_2\text{O}_2$  concentration is 500, 100, and 20  $\mu\text{M}$ , from left to right. Data are means from three independent experiments; error bars show standard deviation.

endogenous fluorescence affecting the assay. N-acetyl cysteine (NAC) did not affect the cytotoxicity of **35G8** significantly. This suggests **35G8**-induced cell death is not solely dependent on ROS induction.

### 35G8 induces ferroptosis

Both transcription and protein expression of HMOX1 and SLC7A11 are highly upregulated by **35G8**. These proteins have been implicated in the non-apoptotic cell death mechanism, ferroptosis. HMOX1 is necessary for ferroptosis and is a major source of iron in the body.<sup>29</sup> Inhibition of cysteine-glutamate exchange through system  $x^c$ , of which SLC7A11 is a component, induces iron-dependent cell death.<sup>30</sup> To determine whether **35G8** induces

ferroptosis in U87MG cells, we treated the cells in the presence or absence of deferoxamine (DFO), an iron chelator.<sup>31</sup> In the presence of DFO, **35G8** is almost three times less potent ( $IC_{50} = 5.8 \pm 1.0 \mu\text{M}$ ) than when used alone ( $IC_{50} = 2.2 \pm 0.7 \mu\text{M}$ ). These data suggest that PDI may play an important role in preventing ferroptosis in brain cancer.

### **35G8 is expected to cross the blood-brain barrier**

The likelihood of blood-brain barrier (BBB) permeation, AlogP, water solubility, polar surface area, and number of rotatable bonds of **35G8** and its synthesized analogues were determined with a qualitative model in the ADMET predictor (Version 7.0). The AlogP of the compounds is between -1.1 and 1.1 and the likelihood of BBB permeation is high. The polar surface area of **35G8** is less than  $90 \text{ \AA}^2$ , the cutoff for predicted CNS penetration.<sup>32</sup> The average molecular weight of marketed CNS compounds is 310, and the **35G8** analogues range in molecular weight from 207 – 315. Similarly, TMZ has a molecular weight of 194 Da, ClogP of -0.82, and a polar surface area of  $108 \text{ \AA}^2$ . These data demonstrate that **35G8** will be able to cross the blood-brain barrier.

## **Discussion**

The screen of 20,000 diverse compounds in a growth inhibition assay produced **35G8** as the most potent inhibitor of proliferation of the colon cancer cell line HCT116. **35G8** destabilizes PDI and blocks its reductase activity. As a consequence, **35G8** likely causes cell death via continuous activation of ER stress and disruption of homeostatic balance, among other factors. **35G8** was validated in orthogonal assays to rule out that activity was not a consequence of its redox-cycling status. **35G8** generates  $\text{H}_2\text{O}_2$  in the presence of DTT at the concentrations used in the PDI assay (Figure III-7), however,  $\text{H}_2\text{O}_2$  does not interfere with insulin reduction catalyzed by

PDI (Figure III-7). The reactive nature of the pyrimidotriazinedione class underlines the importance of testing activity in a wide variety of assays, including non-fluorescent methods, in order to eliminate false positive results. Therefore, we performed several assays with various output methods to test our novel compounds.

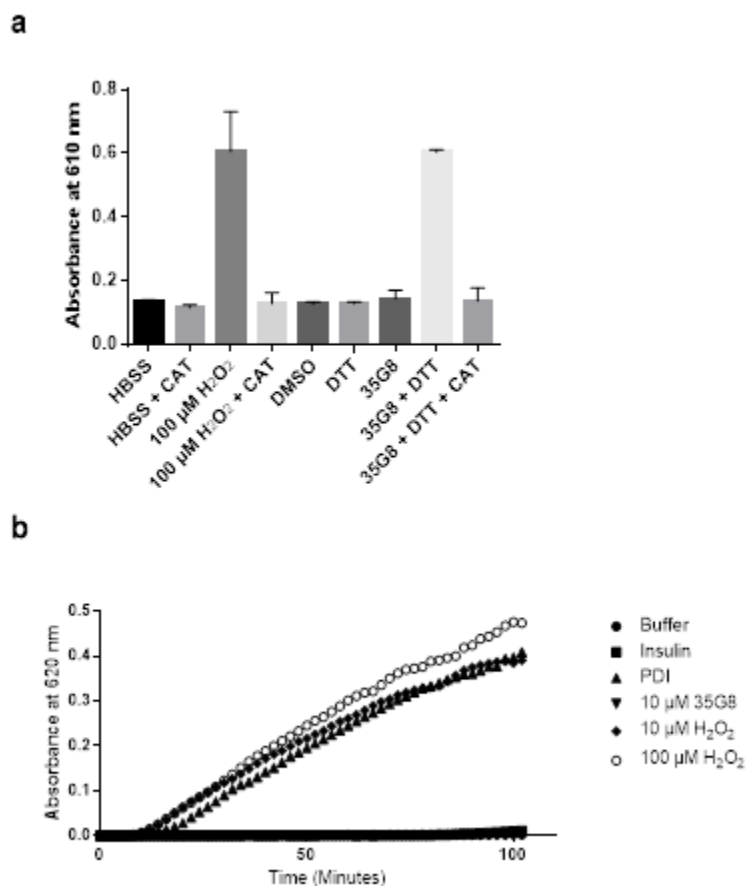


Figure III-7 PAINS characteristics of **35G8** do not interfere with PDI activity in the insulin turbidity assay. (A) Redox cycling assay measuring absorbance at 610 nm. Data are presented as mean  $\pm$  standard deviation of three independent experiments. (B) H<sub>2</sub>O<sub>2</sub> in insulin turbidity assay. Ability of PDI to reduce insulin measured in the presence of 10  $\mu$ M and 100  $\mu$ M H<sub>2</sub>O<sub>2</sub>, and 10  $\mu$ M **35G8**. ● Sodium phosphate buffer only. ■ 130  $\mu$ M insulin in buffer and DTT ▲ 1  $\mu$ M PDI + 130  $\mu$ M insulin + DTT ▼ 10  $\mu$ M **35G8** in 1  $\mu$ M PDI + 130  $\mu$ M insulin + DTT ◆ 10  $\mu$ M H<sub>2</sub>O<sub>2</sub> in 1  $\mu$ M PDI + 130  $\mu$ M insulin + DTT ○ 100  $\mu$ M H<sub>2</sub>O<sub>2</sub> in 1  $\mu$ M PDI + 130  $\mu$ M insulin + DTT.

The Bru-seq results revealed that **35G8** promoted the activation of the Nrf2 pathway. Of the top 20 upregulated genes following a 4-hour **35G8** treatment, four are implicated in the Nrf2 pathway (SLC7A11, HMOX1, AKR1C1, and LOC344887). Nrf2 is a transcription factor that

normally is kept at low levels due to degradation mediated by Keap1.<sup>33</sup> Following exposure to ROS, Keap1 is inactivated and Nrf2 induces transcription of genes to counteract the oxidative insult.<sup>34</sup> SLC7A11 is part of a cysteine-glutamate transporter (system x<sup>c-</sup>) that is regulated by Nrf2 as well as ATF4.<sup>35</sup> HMOX1, another Nrf2-regulated gene, increased over 19-fold upon **35G8** treatment. We also found that transcription of the *AKR1C1* gene, which is induced by ROS but expressed at low levels in gliomas, increased significantly following **35G8** treatment. Furthermore, the lncRNA *LOC344887* has been shown to be activated by Nrf2.<sup>36</sup> Nrf2-regulated genes may be responsible for treatment resistance in glioblastoma, providing further evidence that inhibiting PDI could be a sound strategy to treat glioblastoma.<sup>37, 38</sup>

Several ER stress markers were induced in response to **35G8** treatment, including CHAC1, DDIT3, ASNS, and ATF3. Due to the strong upregulation of *CHAC1*, a pro-apoptotic marker regulated by ATF4, we hypothesize that the PERK-ATF4-DDIT3 branch of the UPR is likely activated upon PDI inhibition by **35G8** treatment. The ER stress response and autophagy are closely linked, and ER stress may induce autophagy in **35G8**-treated cells.

Autophagy is the process of protein and organelle degradation by lysosomes, used as a survival mechanism to provide energy for the cell.<sup>39</sup> The ER stress response protein ATF4 promotes autophagy<sup>40</sup> by upregulating genes like *TRIB3*.<sup>41</sup> While autophagy can be protective as a survival mechanism, increased autophagic signaling causes cell death. It is still unclear whether *TMEM74* is regulated by ATF4, but upregulation of *TMEM74* mRNA may lead to autophagic PI3K signaling. The increase of *ARG2* expression upon **35G8** treatment may be a result of the activation of the UPR and lower cellular levels of arginine, leading to autophagy.<sup>42</sup> IRS2, a key insulin signaling protein regulated by the UPR and silenced by JNK, is expressed to remove damaged cells.<sup>43</sup> **35G8** treatment initiates a protective response by upregulating the UPR and

inducing autophagy to combat ER stress. Ultimately, unbalanced homeostatic mechanisms overwhelm the cellular machinery, and this leads to cell death.

ROS induction is likely responsible for the increased expression levels of *TXNRD1* (9-fold increase) and *TXN* (2-fold increase). *TXNIP* inhibits *TXN* activity, and *TXNIP* expression is significantly inhibited by **35G8** treatment (7.4-fold decrease). ER stress activates the ERK1/2 MAP kinase signaling pathway, repressing *TXNIP* expression leading to thioredoxin nuclear translocation.<sup>44</sup> Interestingly, *TXNIP* is overexpressed in brain cancer patients. Furthermore, *TXNIP* can bind *PDI* and increase its activity. Lower *TXNIP* levels allow *TRX* to bind *ASK1* and prevent apoptosis.<sup>45</sup> Therefore, decreased expression of *TXNIP* may contribute to the absence of apoptosis signaling observed upon **35G8** treatment.

Another class of genes that were repressed by **35G8** are involved in DNA repair. GSEA analysis showed that several genes involved in mismatch repair, homologous recombination, base excision repair and nucleotide excision repair had reduced transcription following **35G8** treatment. It is possible that these genes share a common transcription factor that requires *PDI*-assisted protein folding for optimal function. Importantly, these findings suggest that **35G8** may be used in combination with DNA damaging agents or *PARP1* inhibitors to augment their therapeutic effectiveness.

The key *Nrf2*-regulated genes *SLC7A11* and *HMOX1* are essential markers for iron-dependent, erastin-induced ferroptosis. *SLC7A11* is a negative regulator of ferroptosis and upregulation of *SLC7A11* occurs as a response to system *xc<sup>-</sup>* inhibition. Efforts to treat glioma patients by inhibiting system *xc<sup>-</sup>* have failed;<sup>46</sup> however, combining *SLC7A11* inhibition with a *PDI* inhibitor may be a promising new strategy.



System  $xc^-$  imports cystine for glutathione synthesis to maintain intracellular redox balance, and the expression of this system is often elevated in several cancers, including gliomas.<sup>47</sup> System  $xc^-$  inhibitors, in particular sulfasalazine, as single agents for the treatment of gliomas have been unsuccessful,<sup>48</sup> but have been shown to sensitize glioma cells to radiation therapy.<sup>49</sup> Similarly, the ferroptosis inducer erastin sensitizes glioblastoma cells to temozolomide by inhibiting system  $xc^-$ .<sup>50</sup> These studies provide evidence that system  $xc^-$  is an important target for combating resistance in brain cancer. Importantly, **35G8**-induced cell death can be rescued by deferoxamine, suggesting that ferroptosis is occurring. Interestingly, Bru-seq analysis of **35G8**-treated cells revealed a pattern of gene expression similar to that of erastin-treated cells (Figure III-8), including induction of the ER stress response, unfolded protein response, and expression of the erastin-exposure pharmacodynamic marker, CHAC1.<sup>30</sup>

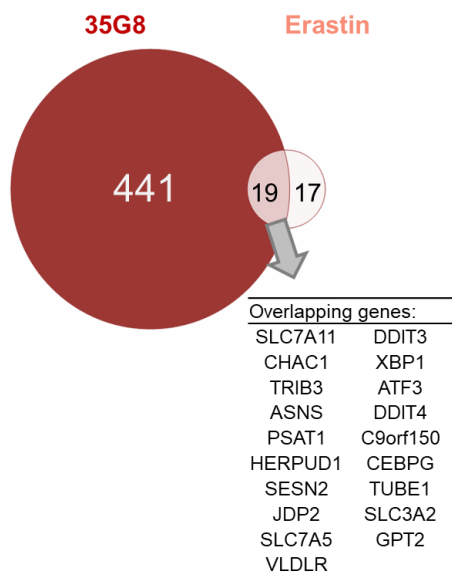


Figure III-8 Venn diagram for the genes with greater than two-fold change in **35G8** and erastin treatments.

This indicates that as a consequence of PDI inhibition, **35G8** blocks transport via system  $xc^-$ . However, a link between PDI and SLC7A11 expression has not yet been established and further investigation is warranted.

## Conclusions

We identified **35G8** as a markedly potent PDI inhibitor that may have therapeutic potential as a single agent and in combination with SLC7A11 inhibitors or DNA-damaging agents. **35G8** and its analogues demonstrate activity in human brain cancer cells likely through upregulation of ER stress and UPR that leads to autophagy-mediated ferroptosis. Taken together, our data suggest **35G8** is a useful investigational PDI inhibitor, expected to easily cross the blood brain barrier, that can be optimized to develop novel therapeutic agents to treat malignant glioma.

## Experimental Section

**Reagents.** 3-(4,5-dimethylthiazol-2-yl)-2, 5-diphenyltetrazolium bromide (MTT) was purchased from Amresco (Solon, OH). N-acetylcysteine (NAC) was purchased from Sigma-Aldrich (St. Louis, MO). Methyl (3S)-5-fluoro-3-[[[(2S)-2-[[[(2S)-3-methyl-2-(phenylmethoxycarbonylamino)butanoyl] amino] propanoyl] amino]-4-oxopentanoate (Z-VAD-FMK) was purchased from Tocris Bioscience (Bristol, UK). 5-(1H-indol-3-ylmethyl)-3-methyl-2-sulfanylideneimidazolidin-4-one (Necrostatin-1) was purchased from Cayman Chemical Company (Ann Arbor, MI). Phenol red, H<sub>2</sub>O<sub>2</sub>, and horseradish peroxidase (HRP) were purchased from Sigma-Aldrich (St. Louis, MO). Hank's Balanced Salt Solution (HBSS) was purchased from Hyclone (Logan, UT), and sodium hydroxide was purchased from EMD (Gibbstown, NJ).

**Cell Culture.** The human glioblastoma cells, U87MG, U118MG, NU04 and A172 (ATCC, Manassas, VA), were obtained in 2013 and were maintained in RPMI-1640 (Thermo Fisher Scientific, Waltham, MA) supplemented with 10 % fetal bovine serum (Thermo Fisher Scientific). Cells were grown as monolayer cultures at 37 °C in a humidified atmosphere of 5 % CO<sub>2</sub> and

tested for *Mycoplasma* contamination with the *Mycoplasma* detection kit, PlasmoTest (InvivoGen, San Diego, California).

**Growth Inhibition Assay.** Cell growth inhibition was assessed by MTT assay as previously described.<sup>51</sup> Cells were seeded in duplicate in 96-well plates at 7000 - 10000 cells/well. After overnight incubation at 37 °C and 5 % CO<sub>2</sub>, cells were treated with indicated compounds for 72 hours. For the combination therapies, NAC was added to the well at the same time as **35G8** (24 hours after plates were seeded), and Z-VAD-FMK and Necrostatin-1 were added to the well 1 hour prior to **35G8** addition. The plates were incubated with drug or vehicle control for 72 hours at 37 °C and 5 % CO<sub>2</sub>. MTT solution (20 µL, 3 mg/mL) was added to the wells, and the cells were incubated for 4 hours at 37 °C. Supernatant was removed and DMSO (100 µl) was added to each well. The plates were shaken for 15 min at room temperature, and absorbance of the formazan crystals was measured at 570 nm. Cell growth inhibition was assessed by the cell viability rate as  $[1-(A_t-A_b)/(A_c-A_b)] \times 100$  ( $A_t$ ,  $A_c$  and  $A_b$  were the absorbance values from cells treated with compound, cells not treated with compound, and blank, respectively). Cell viability was determined with the MTT assay. U87MG cells were seeded at 5000 cells per well in 96-well plates. Deferoxamine (Sigma Aldrich) was added to cells in a five-point, three-fold dilution series from 400 µM. **35G8** was added immediately after in a five-point, three-fold dilution series from 100 µM. Cells were incubated with compounds for 12 hours at 37 °C, and MTT assay was performed as stated above.

**PDI Protein Purification.** The expression vector of recombinant human PDI protein with N-terminal His tag was a gift from Dr. Lloyd W. Ruddock (University of Oulu, Oulu, Finland). PDI expression and purification were performed as previously described with slight modifications.<sup>4</sup> In brief, protein production was carried out in *Escherichia Coli* strain BL21 (DE3) grown in LB

medium with 200 µg/ml ampicillin (EMD Biosciences, La Jolla, CA) at 37 °C and incubated at an A<sub>600</sub> of 0.5 for 4 hours with 1 mM isopropyl β-D-1-thiogalactopyranoside (GoldBio, St. Louis, MO). Cells were harvested by centrifugation (4000g for 15 min) and were re-suspended in one-tenth volume Buffer A (20 mM sodium phosphate, pH 7.3). Cells were lysed by sonication and the cell debris was removed by centrifugation (17000g for 45 min). The supernatant was applied to a bed of Ni-nitrilotriacetic acid in a histidine-binding column (Qiagen, Hilden, Germany), equilibrated with 10 ml of Buffer A and incubated at 4 °C, overnight. After incubation, the column was washed in Buffer A and then in Buffer B (20 mM sodium phosphate, 0.5 M sodium chloride and 50 mM imidazole, pH 7.3). His-tagged proteins were eluted using Buffer C (20 mM sodium phosphate and 50 mM EDTA, pH 7.3) and eluent was dialyzed in 100 mM sodium phosphate buffer (pH 7.0) with 2 mM EDTA.

**Measurement of PDI Activity.** PDI activity was assessed by measuring the PDI-catalyzed reduction of insulin as described previously.<sup>14</sup> In brief, recombinant PDI protein (0.4 µM) was incubated with indicated compounds at 37 °C for 1 hour in sodium phosphate buffer (100 mM sodium phosphate, 2 mM EDTA, 8 µM DTT, pH 7.0). A mixture of sodium phosphate buffer, DTT (500 µM), and bovine insulin (130 µM; Gemini BioProducts, West Sacramento, CA) was added to the incubated PDI protein. The reduction reaction was catalyzed by PDI at room temperature, and the resulting aggregation of reduced insulin B chains was measured at 620 nm. PDI activity was calculated with the formula, PDI activity (%) = [(ODT<sub>80</sub>[PDI+DTT+compound] - ODT<sub>0</sub>[PDI+DTT+compound]) - (ODT<sub>80</sub>[DTT] - ODT<sub>0</sub>[DTT])] / [(ODT<sub>80</sub>[PDI+DTT] - ODT<sub>0</sub>[PDI+DTT]) - (ODT<sub>80</sub>[DTT] - ODT<sub>0</sub>[DTT])] × 100 (ODT<sub>0</sub> and ODT<sub>80</sub> were the absorbance values at 0 min and 80 min after the reduction reaction, respectively).

**Thermal Shift Assay.** Thermal shift of purified PDI (0.3 mg/ml in 100 mM NaPO<sub>4</sub>, pH 7.0) in the presence or absence of **35G8** was determined as described.<sup>15</sup> Briefly, 5 µl protein-dye (1,8-ANS, 0.3 mM; Sigma Aldrich) solutions were dispensed in each well of a 384-well microplate (Thermo Scientific, AB1384K) and equal volumes of the test compound solutions were dispensed to each well. Then, 3 µl of silicone oil (Sigma Aldrich) was added to each well to prevent evaporation. DMSO (2 % in buffer) was used as control. Fluorescence emission was detected by measuring light intensity using a CCD camera. The plate was heated at a temperature range from 25 to 90 °C at 1°C/minute in the ThermoFluor instrument (Johnson & Johnson, New Brunswick, NJ). Compounds were replicated three times in a 384-well plate.

**Cellular Thermal Shift Assay.** The cellular thermal shift assay was performed following previously established procedure.<sup>52</sup> U87MG cells were seeded at 2 x 10<sup>6</sup> cells/100 mm dish and allowed to attach overnight. Cells were treated with 0.5, 1.0, or 2.0 µM **35G8**, or DMSO as the negative control, for 2 hours at 37 °C, 5 % CO<sub>2</sub>. After treatment, cells were trypsinized, washed with DPBS twice, and suspended in 600 µL DPBS. The cells were split into 100 µL aliquots, heated at indicated temperatures for 3 min in the Veriti Thermal Cycler (Applied Biosystems), and incubated for 3 min at room temperature. The cells were flash-frozen twice and spun at 14000g for 20 min at 4 °C. Supernatants were collected and loaded onto a 10 % polyacrylamide gel at a volume of 16 µL, with 4 µL 4X SDS loading dye. Subsequently, Western blotting was run following the procedure reported herein.

**Drug Affinity Responsive Target Stability.** The DARTS assay was performed following previously established procedure.<sup>53</sup> U87MG cells were grown to approximately 80-85% confluence, washed with ice-cold DPBS, and lysed with lysis buffer (150 mM NaCl, 1.0% NP-40, 0.5% sodium deoxycholate, 50 mM Tris, pH 8.0). Cells were collected, and lysis was allowed to

occur for 10 min on ice. Cells were spun at 18000g for 20 min at 4 °C to collect the supernatant. Protein concentration was determined via BCA assay. 100 μM **PACMA31** or **35G8** or 1% DMSO were incubated with aliquots of cell lysate at 5 mg/ml for 30 min with shaking at room temperature. Pronase (Sigma Aldrich) was added to 20 μL aliquots of cell lysates at 0, 1:1000 (0.005 μg/μL), 1:500 (0.01 μg/μL), or 1:250 (0.02 μg/μL) for 30 min at room temperature. Digestion was stopped by adding 1X protease inhibitor cocktail (Sigma Aldrich) and incubating the reactions on ice for 10 min. SDS-PAGE loading buffer (6 μL of 5X) was added to the samples, and samples were heated for 10 min at 70 °C. Samples were spun down briefly and 20 μg of protein was loaded into acrylamide gels (10 %) for Western blot analysis.

**Bru-seq Analysis.** Bru-seq experiments<sup>12</sup> and analysis were performed as previously reported. Briefly, U87MG cells were placed in dishes on Day 1. Cells were changed to fresh media on Day 5 and treated with DMSO or **35G8** at 1 μM for 4 hours. Bromouridine was added into the media to a final concentration of 2 mM to label newly synthesized nascent RNA in the last 30 min of treatment. Cells were then collected in TRIzol (Thermo Fisher Scientific) and total RNA was isolated. The bromouridine-containing RNA population was further isolated and sequenced. Sequencing reads were mapped to a reference genome.

**Bioinformatic Analysis.** Bru-seq data of **35G8** treatment was filtered using the cut off value of gene size > 300 bp and mean (RPKM) > 0.5 and a total of 7,770 genes were ranked based on the fold change values versus control (DMSO). DAVID functional annotation analysis<sup>54, 55</sup> was performed on 460 upregulated and 220 downregulated genes with fold change  $\geq 2$  and  $\leq -2$ . IPA of Bru-seq data was performed using the IPA web-based application (Ingenuity Systems, Inc.) on the list of 680 up- and downregulated genes (fold change  $\geq 2$  and  $\leq -2$ ). Top canonical pathways were ranked based on the P-value of significance and maximum number of genes in the pathway.

GSEA of Bru-seq data was done on a pre-ranked gene list of 7,770 genes of **35G8** treatment based on the Kolmogorov–Smirnov statistic.<sup>56</sup>

**ROS Detection Assay.** U87MG cells were detached with 0.05% trypsin-EDTA, neutralized, centrifuged and resuspended in cell culture media. Suspension was treated with 20  $\mu$ M cell-permeable H<sub>2</sub>DCFDA for 30 min at 37 °C. Cells were centrifuged again and washed with cell culture media to remove excess probe. After washing, cells were placed in a black-wall 384-well plate at 20,000 cells/well, incubated for 30 min and treated with compounds at designated conditions. Fluorescent signals were read at 493 nm/523 nm for ROS detection at designated time points (4, 6, and 24 hours).

**Western Blot.** Primary antibodies for GRP78, HMOX1, CHAC1, CHOP, LC3B, GSTO1, and SLC7A11 and secondary antibodies were purchased from Cell Signaling (Danvers, MA). Primary antibody for P4HB was purchased from Protein Tech (Rosemont, IL). U87MG cells were treated with DMSO or 2  $\mu$ M **35G8** for 1, 3, 6, 12, or 24 hours. Cells were harvested with a lysis buffer (25 mM tris(hydroxymethyl)aminomethane, 150 mM sodium chloride, 17 mM Triton X-100, 3.5 mM sodium dodecyl sulfate, pH 7.4), lysed via sonication, and spun in a centrifuge at 13500g at 4 °C for 10 min. Supernatant was collected and protein concentration determined with the BCA assay (Thermo Fisher Scientific, Waltham, MO). Samples were prepared with 50  $\mu$ g protein and loaded onto 10 % (or 12 % for LC3B and DDIT3) acrylamide (Bio-Rad, Hercules, CA) gels. Protein from gels was electrotransferred to methanol-activated immobilon-FL PVDF membranes (EMD Millipore, La Jolla, CA). Membranes were blocked for 1 hour with Odyssey blocking buffer (LI-COR Biosciences, Lincoln, NE). Membranes were probed for proteins using primary antibodies (P4HB, 1:1000; GRP78, 1:1000; GSTO1, 1:1000; HMOX1, 1:1000; CHAC1, 1:1000; CHOP, 1:500; LC3B, 1:2000; SLC7A11, 1:2000) overnight at 4 °C. Membranes were incubated

with secondary antibodies (anti-rabbit, 1:7500, or anti-mouse, 1:7500) and fluorescence was imaged by Odyssey imaging system (LI-COR Biosciences).

**Redox Cycling Assay.** The redox cycling assay was adapted from a previously published experiment.<sup>57</sup> In duplicate in a 384-well plate, 20  $\mu\text{L}$  of HBSS buffer, 100 U of catalase, 100  $\mu\text{M}$   $\text{H}_2\text{O}_2$ , 100  $\mu\text{M}$   $\text{H}_2\text{O}_2$  + 100 U catalase, 0.5% DMSO, 500  $\mu\text{M}$  DTT, 10  $\mu\text{M}$  **35G8**, 10  $\mu\text{M}$  **35G8** + 500  $\mu\text{M}$  DTT, or 10  $\mu\text{M}$  **35G8** + 500  $\mu\text{M}$  DTT + 100 U of catalase was added to a reaction mixture with HBSS to a final volume of 60  $\mu\text{L}$ . The reaction was incubated at room temperature for 30 min, and phenol red-HRP detection reagent was added to a final concentration of 100  $\mu\text{g}/\text{ml}$  phenol red and 60  $\mu\text{g}/\text{ml}$  HRP in each well. The reaction was incubated for an hour at room temperature. Sodium hydroxide (10  $\mu\text{L}$ , 1 N) was added to wells and absorbance was measured at 610 nm.

**Statistical Analysis.**  $\text{IC}_{50}$  values were calculated using GraphPad Prism 7 software (GraphPad Software, Inc.). The error bars indicate mean  $\pm$  standard deviation.



### **Notes to Chapter IV**

All synthesis was performed by Suhui Yang. The authors would like to thank Michelle Paulsen for running the Bru-seq experiments. The expression vector of recombinant human PDI was a generous gift from Dr. Lloyd W. Ruddock (University of Oulu, Oulu, Finland). This work was supported in part by a grant from NIH (CA193690).

This includes reprints of a journal article that the student has authored or co-authored and is being submitted as part of the dissertation, for which the authors have transferred copyright to the publisher.

## References

1. Ostrom, Q. T.; Gittleman, H.; Liao, P.; Rouse, C.; Chen, Y. W.; Dowling, J.; Wolinsky, Y. L.; Kruchko, C.; Barnholtz-Sloan, J. CBTRUS statistical report: Primary brain and central nervous system tumors diagnosed in the United States in 2007-2011. *Neuro Oncol* **2014**, *16*, 1-63.
2. Stupp, R.; Mason, W. P.; van den Bent, M. J.; Weller, M.; Fisher, B.; Taphoorn, M. J.; Belanger, K.; Brandes, A. A.; Marosi, C.; Bogdahn, U.; Curschmann, J.; Janzer, R. C.; Ludwin, S. K.; Gorlia, T.; Allgeier, A.; Lacombe, D.; Cairncross, J. G.; Eisenhauer, E.; Mirimanoff, R. O. European Organisation for Research and Treatment of Cancer Brain Tumor and Radiotherapy Groups; National Cancer Institute of Canada Clinical Trials Group. Radiotherapy plus concomitant and adjuvant temozolomide for glioblastoma. *N Engl J Med* **2005**, *352*, 987-96.
3. Xu, S.; Sankar, S.; Neamati, N. Protein disulfide isomerase: A promising target for cancer therapy. *Drug Discov Today* **2014**, *19*, 222-40.
4. Xu, S.; Butkevich, A. N.; Yamada, R.; Zhou, Y.; Debnath, B.; Duncan, R.; Zandi, E.; Petasis, N. A.; Neamati, N. Discovery of an orally active small-molecule irreversible inhibitor of protein disulfide isomerase for ovarian cancer treatment. *Proc Natl Acad Sci U S A* **2012**, *109*, 16348-53.
5. Goplen, D.; Wang, J.; Enger, P. O.; Tysnes, B. B.; Terzis, A. J.; Laerum, O. D.; Bjerkvig, R. Protein disulfide isomerase expression is related to the invasive properties of malignant glioma. *Cancer Res* **2006**, *66*, 9895-902.
6. Lovat, P. E.; Corazzari, M.; Armstrong, J. L.; Martin, S.; Pagliarini, V.; Hill, D.; Brown, A. M.; Piacentini, M.; Birch-Machin, M. A.; Redfern, C. P. Increasing melanoma cell death using inhibitors of protein disulfide isomerases to abrogate survival responses to endoplasmic reticulum stress. *Cancer Res* **2008**, *68*, 5363-9.
7. Eirich, J.; Braig, S.; Schyschka, L.; Servatius, P.; Hoffmann, J.; Hecht, S.; Fulda, S.; Zahler, S.; Antes, I.; Kazmaier, U.; Sieber, S. A.; Vollmar, A. M. A small molecule inhibits protein disulfide isomerase and triggers the chemosensitization of cancer cells. *Angew Chem Intl Ed Engl* **2014**, *53*, 12960-5.
8. Koczian, F.; Naglo, O.; Vomacka, J.; Vick, B.; Servatius, P.; Zisis, T.; Hettich, B.; Kazmaier, U.; Sieber, S. A.; Jeremias, I.; Zahler, S.; Braig, S. Targeting the endoplasmic reticulum-mitochondria interface sensitizes leukemia cells to cytostatics. *Haematologica* **2019**, *104*, 546-55.
9. Khodier, C.; VerPlank, L.; Nag, P. P.; Pu, J.; Wurst, J.; Pilyugina, T.; Dockendorff, C.; Galinski, C. N.; Scalise, A. A.; Passam, F.; van Hessem, L.; Dilks, J.; Kennedy, D. R.; Flaumenhaft, R.; Palmer, M. A. J.; Dandapani, S.; Munoz, B.; Schrieber, S. L. Identification of

ML359 as a small molecule inhibitor of protein disulfide isomerase. In *Probe Reports from the NIH Molecular Libraries Program*, Bethesda (MD), 2010.

10. Kaplan, A.; Gaschler, M. M.; Dunn, D. E.; Colligan, R.; Brown, L. M.; Palmer, A. G.; Lo, D. C.; Stockwell, B. R. Small molecule-induced oxidation of protein disulfide isomerase is neuroprotective. *Proc Natl Acad Sci U S A* **2015**, 112, E2245-52.
11. Vatolin, S.; Phillips, J. G.; Jha, B. K.; Govindgari, S.; Hu, J.; Grabowski, D.; Parker, Y.; Lindner, D. J.; Zhong, F.; Distelhorst, C. W.; Smith, M. R.; Cotta, C.; Xu, Y.; Chilakala, S.; Kuang, R. R.; Tall, S.; Reu, F. J. Novel protein disulfide isomerase inhibitor with anticancer activity in multiple myeloma. *Cancer Res* **2016**, 76, 3340-50.
12. Paulsen, M. T.; Veloso, A.; Prasad, J.; Bedi, K.; Ljungman, E. A.; Magnuson, B.; Wilson, T. E.; Ljungman, M. Use of Bru-Seq and BruChase-Seq for genome-wide assessment of the synthesis and stability of RNA. *Methods* **2014**, 67, 45-54.
13. Dixon, S. J.; Lemberg, K. M.; Lamprecht, M. R.; Skouta, R.; Zaitsev, E. M.; Gleason, C. E.; Patel, D. N.; Bauer, A. J.; Cantley, A. M.; Yang, W. S.; Morrison, B., III; Stockwell, B. R. Ferroptosis: An iron-dependent form of nonapoptotic cell death. *Cell* **2012**, 149, 1060-72.
14. Khan, M. M.; Simizu, S.; Lai, N. S.; Kawatani, M.; Shimizu, T.; Osada, H. Discovery of a small molecule PDI inhibitor that inhibits reduction of HIV-1 envelope glycoprotein gp120. *ACS Chem Biol* **2011**, 6, 245-51.
15. Pantoliano, M. W.; Petrella, E. C.; Kwasnoski, J. D.; Lobanov, V. S.; Myslik, J.; Graf, E.; Carver, T.; Asel, E.; Springer, B. A.; Lane, P.; Salemme, F. R. High-density miniaturized thermal shift assays as a general strategy for drug discovery. *J Biomol Screen* **2001**, 6, 429-40.
16. Cimperman, P.; Baranauskienė, L.; Jachimovičiūtė, S.; Jachno, J.; Torresan, J.; Michailovienė, V.; Matulienė, J.; Sereikaitė, J.; Bumelis, V.; Matulis, D. A quantitative model of thermal stabilization and destabilization of proteins by ligands. *Biophys J* **2008**, 95, 3222-31.
17. Primm, T. P.; Gilbert, H. F. Hormone binding by protein disulfide isomerase, a high capacity hormone reservoir of the endoplasmic reticulum. *J Biol Chem* **2001**, 276, 281-6.
18. Daves, G. D.; Cheng, C. C.; Robins, R. K. Total synthesis of toxoflavin. *J Am Chem Soc* **1961**, 83, 3904-5.
19. Degterev, A.; Huang, Z. H.; Boyce, M.; Li, Y. Q.; Jagtap, P.; Mizushima, N.; Cuny, G. D.; Mitchison, T. J.; Moskowitz, M. A.; Yuan, J. Y. Chemical inhibitor of nonapoptotic cell death with therapeutic potential for ischemic brain injury. *Nat Chem Biol* **2005**, 1, 112-9.
20. Degterev, A.; Hitomi, J.; Gemscheid, M.; Ch'en, I. L.; Korkina, O.; Teng, X.; Abbott, D.; Cuny, G. D.; Yuan, C.; Wagner, G.; Hedrick, S. M.; Gerber, S. A.; Lugovskoy, A.; Yuan, J. Identification of RIP1 kinase as a specific cellular target of necrostatins. *Nat Chem Biol* **2008**, 4, 313-21.

21. Paulsen, M. T.; Veloso, A.; Prasad, J.; Bedi, K.; Ljungman, E. A.; Tsan, Y. C.; Chang, C. W.; Tarrier, B.; Washburn, J. G.; Lyons, R.; Robinson, D. R.; Kumar-Sinha, C.; Wilson, T. E.; Ljungman, M. Coordinated regulation of synthesis and stability of RNA during the acute TNF-induced proinflammatory response. *Proc Natl Acad Sci U S A* **2013**, 110, 2240-5.
22. Itoh, K.; Chiba, T.; Takahashi, S.; Ishii, T.; Igarashi, K.; Katoh, Y.; Oyake, T.; Hayashi, N.; Satoh, K.; Hatayama, I.; Yamamoto, M.; Nabeshima, Y. An Nrf2 small Maf heterodimer mediates the induction of phase II detoxifying enzyme genes through antioxidant response elements. *Biochem Biophys Res Commun* **1997**, 236, 313-22.
23. Oh-hashi, K.; Nomura, Y.; Shimada, K.; Koga, H.; Hirata, Y.; Kiuchi, K. Transcriptional and post-translational regulation of mouse cation transport regulator homolog 1. *Mol Cell Biochem* **2013**, 380, 97-106.
24. Shang, Y. Y.; Zhong, M.; Zhang, L. P.; Guo, Z. X.; Wang, Z. H.; Zhang, Y.; Deng, J. T.; Zhang, W. Tribble 3, a novel oxidized low-density lipoprotein-inducible gene, is induced via the activating transcription factor 4-C/EBP homologous protein pathway. *Clin Exp Pharmacol Physio* **2010**, 37, 51-5.
25. Siu, F.; Bain, P. J.; LeBlanc-Chaffin, R.; Chen, H.; Kilberg, M. S. ATF4 is a mediator of the nutrient-sensing response pathway that activates the human asparagine synthetase gene. *J Biol Chem* **2002**, 277, 24120-7.
26. Salazar, M.; Carracedo, A.; Salanueva, I. J.; Hernandez-Tiedra, S.; Lorente, M.; Egia, A.; Vazquez, P.; Blazquez, C.; Torres, S.; Garcia, S.; Nowak, J.; Fimia, G. M.; Piacentini, M.; Cecconi, F.; Pandolfi, P. P.; Gonzalez-Feria, L.; Iovanna, J. L.; Guzman, M.; Boya, P.; Velasco, G. Cannabinoid action induces autophagy-mediated cell death through stimulation of ER stress in human glioma cells. *J Clin Invest* **2009**, 119, 1359-72.
27. Yamamoto, A.; Cremona, M. L.; Rothman, J. E. Autophagy-mediated clearance of huntingtin aggregates triggered by the insulin-signaling pathway. *J Cell Biol* **2006**, 172, 719-31.
28. Yu, C. F.; Wang, L.; Lv, B. F.; Lu, Y.; Zeng, L.; Chen, Y. Y.; Ma, D. L.; Shi, T. P. TMEM74, a lysosome and autophagosome protein, regulates autophagy. *Biochem Biophys Res Commun* **2008**, 369, 622-9.
29. Kwon, M.-Y.; Park, E.; Lee, S.-J.; Chung, S. W. Heme oxygenase-1 accelerates erastin-induced ferroptotic cell death. *Oncotarget* **2015**, 6, 24393-403.
30. Dixon, S. J.; Patel, D. N.; Welsch, M.; Skouta, R.; Lee, E. D.; Hayano, M.; Thomas, A. G.; Gleason, C. E.; Tatonetti, N. P.; Slusher, B. S.; Stockwell, B. R. Pharmacological inhibition of cystine-glutamate exchange induces endoplasmic reticulum stress and ferroptosis. *Elife* **2014**, 3, e02523.
31. Gutteridge, J. M.; Richmond, R.; Halliwell, B. Inhibition of the iron-catalyzed formation of hydroxyl radicals from superoxide and of lipid peroxidation by desferrioxamine. *Biochem J* **1979**, 184, 469-72.

32. van de Waterbeemd, H.; Camenisch, G.; Folkers, G.; Chretien, J. R.; Raevsky, O. A. Estimation of blood-brain barrier crossing of drugs using molecular size and shape, and H-bonding descriptors. *J Drug Target* **1998**, *6*, 151-65.
33. Itoh, K.; Wakabayashi, N.; Katoh, Y.; Ishii, T.; Igarashi, K.; Engel, J. D.; Yamamoto, M. Keap1 represses nuclear activation of antioxidant responsive elements by Nrf2 through binding to the amino-terminal Neh2 domain. *Genes Dev* **1999**, *13*, 76-86.
34. Wondrak, G. T. Redox-directed cancer therapeutics: Molecular mechanisms and opportunities. *Antioxid Redox Signal* **2009**, *11*, 3013-69.
35. Bridges, R. J.; Natale, N. R.; Patel, S. A. System xc- cystine/glutamate antiporter: An update on molecular pharmacology and roles within the CNS. *Br J Pharmacol* **2012**, *165*, 20-34.
36. Johnson, G.; Beaver, L.; Williams, D. E.; Ho, E.; Dashwood, R. H. In *Regulation and function of Nrf2-associated long noncoding RNA*, Thirteenth Annual AACR International Conference on Frontiers in Cancer Prevention Research, New Orleans, LA, 2015; *Can. Prev. Res.* : New Orleans, LA, 2015.
37. Zhu, J. H.; Wang, H. D.; Sun, Q.; Ji, X. J.; Zhu, L.; Cong, Z. X.; Zhou, Y.; Liu, H. D.; Zhou, M. L. Nrf2 is required to maintain the self-renewal of glioma stem cells. *BMC Cancer* **2013**, *13*, 380.
38. Zhu, J. H.; Wang, H. D.; Fan, Y. W.; Lin, Y. X.; Zhang, L.; Ji, X. J.; Zhou, M. L. Targeting the NF-E2-related factor 2 pathway: A novel strategy for glioblastoma (Review). *Oncol Rep* **2014**, *32*, 443-50.
39. Levine, B. Cell biology - Autophagy and cancer. *Nature* **2007**, *446*, 745-7.
40. B'chir, W.; Maurin, A. C.; Carraro, V.; Averous, J.; Jousse, C.; Muranishi, Y.; Parry, L.; Stepien, G.; Fafournoux, P.; Bruhat, A. The eIF2 $\alpha$ /ATF4 pathway is essential for stress-induced autophagy gene expression. *Nucleic Acids Res* **2013**, *41*, 7683-99.
41. Salazar, M.; Lorente, M.; Orea-Soufi, A.; Dávila, D.; Erazo, T.; Lizcano, J.; Carracedo, A.; Kiss-Toth, E.; Velasco, G. Oncosuppressive functions of tribbles pseudokinase 3. *Biochem Soc Trans* **2015**, *43*, 1122-6.
42. García-Navas, R.; Munder, M.; Mollinedo, F. Depletion of L-arginine induces autophagy as a cytoprotective response to endoplasmic reticulum stress in human T lymphocytes. *Autophagy* **2012**, *8*, 1557-76.
43. Xu, L.; Spinas, G. A.; Niessen, M. ER stress in adipocytes inhibits insulin signaling, represses lipolysis, and alters the secretion of adipokines without inhibiting glucose transport. *Horm Metab Res* **2010**, *42*, 643-51.
44. Ogata, F. T.; Batista, W. L.; Sartori, A.; Gesteira, T. F.; Masutani, H.; Arai, R. J.; Yodoi, J.; Stern, A.; Monteiro, H. P. Nitrosative/oxidative stress conditions regulate thioredoxin-

interacting protein (TXNIP) expression and thioredoxin-1 (TRX-1) nuclear localization. *PLoS One* **2013**, 8, e84588.

45. Lee, S.; Kim, S. M.; Lee, R. T. Thioredoxin and thioredoxin target proteins: From molecular mechanisms to functional significance. *Antioxid Redox Signal* **2013**, 18, 1165-207.

46. Robe, P. A.; Martin, D. H.; Nguyen-Khac, M. T.; Artesi, M.; Deprez, M.; Albert, A.; Vanbelle, S.; Califice, S.; Bredel, M.; Bours, V. Early termination of ISRCTN45828668, a phase 1/2 prospective, randomized study of Sulfasalazine for the treatment of progressing malignant gliomas in adults. *BMC Cancer* **2009**, 9, 372.

47. Chung, W. J.; Lyons, S. A.; Nelson, G. M.; Hamza, H.; Gladson, C. L.; Gillespie, G. Y.; Sontheimer, H. Inhibition of cystine uptake disrupts the growth of primary brain tumors. *J Neurosci* **2005**, 25, 7101-10.

48. Gout, P. W.; Buckley, A. R.; Simms, C. R.; Bruchovsky, N. Sulfasalazine, a potent suppressor of lymphoma growth by inhibition of the x(c)(-) cystine transporter: A new action for an old drug. *Leukemia* **2001**, 15, 1633-40.

49. Sleire, L.; Skeie, B. S.; Netland, I. A.; Forde, H. E.; Dodoo, E.; Selheim, F.; Leiss, L.; Heggdal, J. I.; Pedersen, P. H.; Wang, J.; Enger, P. O. Drug repurposing: Sulfasalazine sensitizes gliomas to gamma knife radiosurgery by blocking cystine uptake through system Xc(-), leading to glutathione depletion. *Oncogene* **2015**, 34, 5951-9.

50. Chen, L.; Li, X.; Liu, L.; Yu, B.; Xue, Y.; Liu, Y. Erastin sensitizes glioblastoma cells to temozolomide by restraining xCT and cystathionine-gamma-lyase function. *Oncol Rep* **2015**, 33, 1465-74.

51. Carmichael, J.; DeGraff, W. G.; Gazdar, A. F.; Minna, J. D.; Mitchell, J. B. Evaluation of a tetrazolium-based semiautomated colorimetric assay: Assessment of chemosensitivity testing. *Cancer Res* **1987**, 47, 936-42.

52. Jafari, R.; Almqvist, H.; Axelsson, H.; Ignatushchenko, M.; Lundback, T.; Nordlund, P.; Martinez Molina, D. The cellular thermal shift assay for evaluating drug target interactions in cells. *Nat Protoc* **2014**, 9, 2100-22.

53. Lomenick, B.; Jung, G.; Wohlschlegel, J. A.; Huang, J. Target identification using drug affinity responsive target stability (DARTS). *Curr Protoc Chem Biol* **2011**, 3, 163-80.

54. Dennis, G. J.; Sherman, B. T.; Hosack, D. A.; Yang, J.; Gao, W.; Lane, H. C.; Lempicki, R. A. DAVID: Database for annotation, visualization, and integrated discovery. *Genome Biol* **2003**, 4, 3.

55. Huang, d. W.; Sherman, B. T.; Lempicki, R. A. Systematic and integrative analysis of large gene lists using DAVID bioinformatics resources. *Nat Protoc* **2009**, 4, 44-57.

56. Subramanian, A.; Tamayo, P.; Mootha, V. K.; Mukherjee, S.; Ebert, B. L.; Gillette, M. A.; Paulovich, A.; Pomeroy, S. L.; Golub, T. R.; Lander, E. S.; Mesirov, J. P. Gene set enrichment

analysis: A knowledge based approach for interpreting genome-wide expression profiles. *Proc Natl Acad Sci U S A* **2005**, 102, 15545-50.

57. Johnston, P. A.; Soares, K. M.; Shinde, S. N.; Foster, C. A.; Shun, T. Y.; Takyi, H. K.; Wipf, P.; Lazo, J. S. Development of a 384-well colorimetric assay to quantify hydrogen peroxide generated by the redox cycling of compounds in the presence of reducing agents. *Assay Drug Dev Technol* **2008**, 6, 505-18.

## CHAPTER IV

### Design, Synthesis, and Biological Evaluation of Novel Allosteric Protein Disulfide

#### Isomerase Inhibitors

##### Introduction<sup>4</sup>

Cancer cells require increased protein synthesis and respond to endoplasmic reticulum (ER) stress by activating the unfolded protein response (UPR) which is mediated by ER chaperones.<sup>1-3</sup> ER chaperones such as protein disulfide isomerase (PDI) have emerged as interesting targets for cancer research. PDI is an oxidoreductase chaperone, located in the ER, that assists protein folding by catalyzing disulfide-bond formation (oxidation), breakage (reduction), and rearrangement (isomerization).<sup>4, 5</sup> PDI is composed of four thioredoxin-like domains (a, a', b, and b'), a linker between the a' and b' domains (x), and a C terminal acidic tail. Both the a and a' domains contain structurally similar active sites, including a CGHC motif, and are responsible for the oxidoreductase activity.<sup>6</sup> The b' domain possesses a large hydrophobic pocket for substrate binding and recognition. The C-terminal domain functions in chaperone activity.<sup>7</sup> All these domains are attached in a U-shaped structure that is open in the oxidized state and closed in the

---

<sup>4</sup> This work has been published and is being reprinted with permission from Yang, S., Shergalis, A., Lu, D., Kyani, A., Liu, Z., Ljungman, M., & Neamati, N. (2019). Design, synthesis, and biological evaluation of novel allosteric protein disulfide isomerase inhibitors. *Journal of medicinal chemistry*, 62(7), 3447-3474.

**Author contributions:** Suhui Yang and Andrea Shergalis were the primary authors. Suhui Yang, Dan Lu, and Ziwei Liu synthesized and characterized all compounds. Andrea Shergalis evaluated compounds in biochemical and cell-based assays. Suhui Yang generated figures IV-1 and IV-2. Anahita Kyani generated figure IV-16 and performed docking studies. Mats Ljungman generated figure IV-7. Nouri Neamati is the corresponding author.



reduced state. In addition to the vital roles in protein folding, PDI is overexpressed in a variety of cancers but more significantly in GBM.<sup>4</sup> Furthermore, upregulation of PDI is associated with acquired temozolomide resistance in GBM, thus inhibition of PDI enhances temozolomide-mediated cell death through apoptosis via the ER stress response pathway.<sup>8</sup> Selective PDI inhibitors can sensitize several cancer cell lines to chemotherapeutic agents such as etoposide, fenretinide, and velcade.<sup>9, 10</sup> PDI inhibition induces acute ER stress in multiple myeloma cells accompanied by apoptosis-inducing calcium release.<sup>11</sup> In addition, PDI is strongly expressed in invasive glioma cells, in both xenografts and at the invasive front of human GBMs, and PDI inhibition leads to reduced glioma cell migration and invasion by interfering with the integrin outside-in signaling pathway.<sup>12, 13</sup> All these findings suggest that PDI is an important target for cancer therapy, especially for brain cancers, thus emphasizing the need for the development of novel and potent PDI inhibitors.

Recently, we discovered the PDI inhibitor **BAP2**, a benzylidene acetophenone, with an  $IC_{50}$  value of  $930 \pm 90$  nM, via a combination of high-throughput screening and experimental analysis.<sup>14</sup> **BAP2** shows *in vitro* and *in vivo* antiproliferative activities in human brain cancer models as a single agent. A simple chalcone is a 1,3-diaryl-2-propen-1-one in which the two aromatic rings are connected by a three-carbon  $\alpha,\beta$  unsaturated carbonyl bridge. Chalcone is considered a valuable scaffold due to its simple chemistry, ease of synthesis, and wide biological activity, including anti-oxidant, anti-inflammatory, anti-bacterial, and antitumor properties.<sup>15</sup> Several chalcones, such as metochalcone, sofalcone,<sup>16, 17</sup> PD-156707, licochalcone A, and Elafibranor, have been marketed or clinically tested for various diseases, indicating that chalcones

are well-tolerated and non-toxic to humans, and they have reasonable pharmacokinetic properties (Figure IV-1).<sup>18</sup> Herein, we report the synthesis of 67 novel **BAP2** derivatives, a structure-activity relationship (SAR) analysis, and evaluation of PDI inhibitory activity and cytotoxicity against brain cancer cells. The most potent **BAP2** analogues inhibited GBM migration and cell growth, lowered MMP9 expression, and blocked MMP2 secretion. Furthermore, extensive transcriptomic and proteomic analysis of analogue treatment in a brain cancer cell line demonstrated that **BAP2** and analogues induced ER stress, increased expression of G2M checkpoint proteins, and reduced expression of ribosomal and DNA replication proteins. While **BAP2** and **59** have some thiol reactivity, we provide evidence that PDI inhibition by **BAP2** analogues is dependent on allosteric binding in the b' domain.

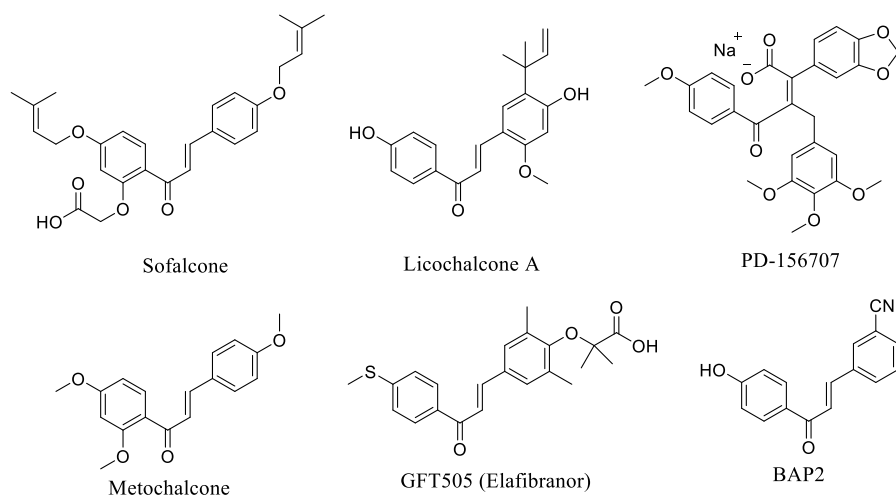


Figure IV-1 Chemical structures of chalcones that have been marketed or clinically tested, and the hit compound **BAP2** as a PDI inhibitor.

## Results

### Synthesis of BAP2 derivatives and their structure-activity relationship

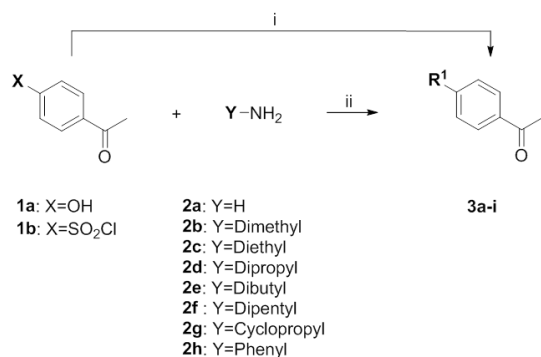
To investigate the structural aspects of the lead **BAP2** for ability to inhibit PDI reductase activity, a series of derivatives were designed and prepared. For the synthesis of chalcones, the most commonly used method is the base-catalyzed Claisen-Schmidt condensation reaction between a methyl ketone and an aldehyde in the presence of sodium hydroxide (NaOH),<sup>19, 20</sup> potassium hydroxide (KOH),<sup>21</sup> or lithium hydroxide (LiOH·H<sub>2</sub>O).<sup>22</sup> However, the base-mediated reactions sometimes require longer reaction times (several days), give low chemical yields, and have a high possibility of side reactions such as the Cannizzaro reaction of an aldehyde, aldol condensation, or Michael addition reaction.<sup>23</sup> On the other hand, the acid-catalyzed method involves the use of aluminum trichloride (AlCl<sub>3</sub>)<sup>24</sup> or dry HCl,<sup>25</sup> and recently boron trifluoride etherate (BF<sub>3</sub>·Et<sub>2</sub>O) has been used as a condensing agent.<sup>26, 27</sup> This new BF<sub>3</sub>·Et<sub>2</sub>O-assisted method is advantageous over existing methods because it produces higher yields, requires shorter reaction times, and has minimal side reactions.<sup>26, 28, 29</sup> Therefore, we applied the BF<sub>3</sub>·Et<sub>2</sub>O method for the synthesis of most **BAP2** derivatives in this study.

Several 4-substituted acetophenones (**3a-n**) and benzaldehydes (**4a-b**) were prepared *via* typical methylation (**3a**),<sup>30</sup> nucleophilic substitution reactions with amines (**3b-i**, **4b**), activation of acid with thionyl chloride and the subsequent substitution reaction with nucleophiles (**3j-m**), hydroxylation at an aliphatic carbon of 3'-bromo-4'-methyl acetophenone (**3n**), and esterification of 3-carboxybenzaldehyde (**4a**) (Scheme IV-1). With the acetophenones (**3**) and benzaldehydes (**4**), most **BAP2** derivatives were prepared by a modified procedure of the BF<sub>3</sub>·Et<sub>2</sub>O-assisted

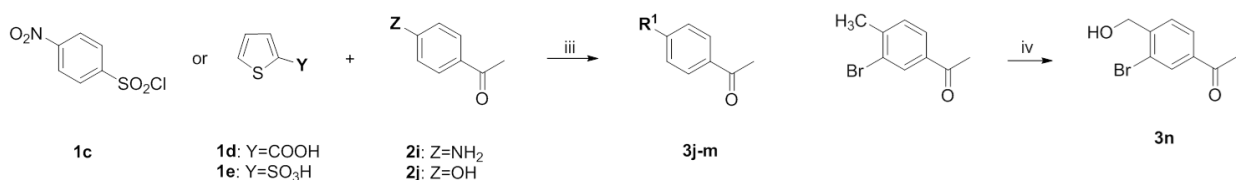
Claisen-Schmidt reaction (Scheme IV-2).<sup>26</sup> Some **BAP2** derivatives were synthesized by applying the base-catalyzed condensation reaction (**8-9**, **39**),<sup>19</sup> and pyrazine-containing derivatives were obtained in the presence of diethylamine in pyridine at 80-120 °C (**29** and **56**). Microwave-assisted one-pot reaction of a Sonogashira coupling of an aryl halide with an aryl alcohol and the subsequent base-catalyzed isomerization were carried out to provide the boronate-containing chalcone **71**,<sup>31</sup> and further oxidative cleavage of the boronate afforded the boronic acid chalcone **72**.<sup>32</sup> Another boronic acid chalcone **31** was prepared by Miyaura borylation of aryl halide **10** and subsequent oxidative cleavage. Microwave-assisted Suzuki coupling of aryl halide **67** afforded chalcones **68** and **69**. In addition, methylation of compounds **5** and **25**, demethylation of **8**, esterification of **37**, and base-promoted hydrolysis of **53** afforded corresponding **BAP2** derivatives **7**, **27**, **6**, **46**, and **45**, respectively.

Scheme IV-1 Synthesis of 4-substituted acetophenones (**3a-n**) and benzaldehydes (**4a-b**)<sup>a</sup>

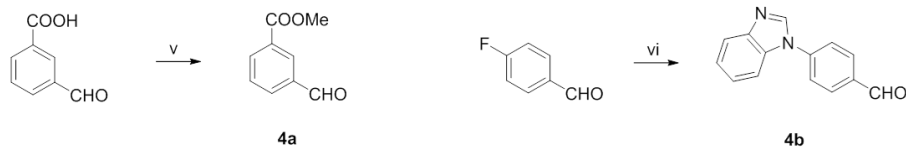
A. Synthesis of acetophenones



No.	R <sup>1</sup>	No.	R <sup>1</sup>	No.	R <sup>1</sup>
<b>3a</b>		<b>3f</b>		<b>3j</b>	
<b>3b</b>		<b>3g</b>		<b>3k</b>	
<b>3c</b>		<b>3h</b>		<b>3l</b>	
<b>3d</b>		<b>3i</b>		<b>3m</b>	
<b>3e</b>					

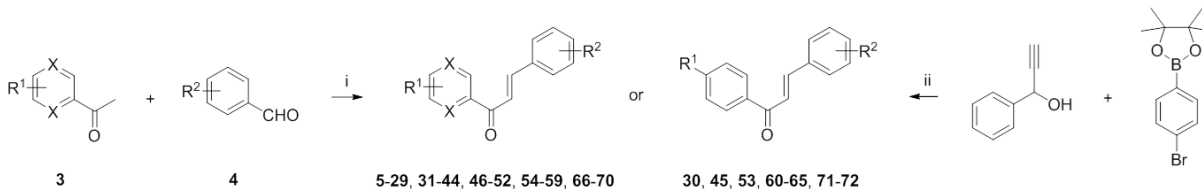


B. Synthesis of benzaldehyde



<sup>a</sup>Reagents and conditions: (i) **3a**: K<sub>2</sub>CO<sub>3</sub>, MeI, acetone, reflux; (ii) **3b**: THF, rt; **3c-i**: Et<sub>3</sub>N, anh THF, rt; (iii) **3j**: (1) pyridine, anh DCM, rt; (2) 1 N HCl. **3k-m**: (1) SOCl<sub>2</sub>, rt; (2) pyridine, DCM; (iv) **3n**: (1) NBS, AIBN, MeCN, reflux; (2) CaCO<sub>3</sub>, dioxane, H<sub>2</sub>O, reflux; (v) (1) Cs<sub>2</sub>CO<sub>3</sub>, MeOH/H<sub>2</sub>O (10:1), rt; (2) MeI, DMF, rt; (vi) benzimidazole, K<sub>2</sub>CO<sub>3</sub>, DMF, 100 °C.

Scheme IV-2 Synthesis of **BAP2** analogues **5-72**<sup>a</sup>



	X	R <sup>1</sup>	R <sup>2</sup>
5:	C	3-OH	3-CN
6:	C	4-OH	3-CN
7:	C	3-OMe	3-CN
8:	C	4-OMe	3-CN
9:	C	4-NH <sub>2</sub>	3-CN
10:	C	4-Br	3-CN
11:	C	4-Morpholine	3-CN
12:	C	4-Piperidine	3-CN
13:	C	4-SO <sub>2</sub> NH <sub>2</sub>	3-CN
14:	C	4-SO <sub>2</sub> NMe <sub>2</sub>	3-CN
15:	C	4-SO <sub>2</sub> NEt <sub>2</sub>	3-CN
16:	C	4-SO <sub>2</sub> NPr <sub>2</sub>	3-CN
17:	C	4-SO <sub>2</sub> NBu <sub>2</sub>	3-CN
18:	C	4-SO <sub>2</sub> NPe <sub>2</sub>	3-CN
19:	C	4-SO <sub>2</sub> NHCP	3-CN
20:	C	4-SO <sub>2</sub> NHPh	3-CN
21:	C	2-OH, 4-F	3-CN
22:	C	3-OH, 4-F	3-CN
23:	C	4-OH, 4-F	3-CN
24:	C	3-CF <sub>3</sub> , 4-OH	3-CN
25:	C	3-OH, 4-OMe	3-CN
26:	C	3-OMe, 4-OH	3-CN
27:	C	3,4-OMe	3-CN
28:	C	3-F, 4-Cl	3-CN
29:	N	H	3-CN
30:		<i>N</i> -Methyl-4-nitrobenzenesulfonamide	3-CN
31:	C	4-B(OH) <sub>2</sub>	3-CN
32:	C	4-OH	4-CN
33:	C	2-OH, 4-F	4-CN
34:	C	3-OH, 4-F	4-CN
35:	C	3-F, 4-OH	4-CN
36:	C	3-CF <sub>3</sub> , 4-OH	4-CN
37:	C	3-OH	3-COOH
38:	C	4-NO <sub>2</sub>	3-COOH
39:	C	4-NH <sub>2</sub>	3-COOH

	X	R <sup>1</sup>	R <sup>2</sup>
40:	C	4-Morpholine	3-COOH
41:	C	4-Piperidine	3-COOH
42:	C	3-OH, 4-OMe	3-COOH
43:	C	3-F, 4-OH	3-COOH
44:	C	3-CF <sub>3</sub> , 4-OH	3-COOH
45:		<i>N</i> -Methyl-4-nitrobenzenesulfonamide	3-COOH
46:	C	3-OH	3-COOMe
47:	C	4-OH	3-COOMe
48:	C	3-OH, 4-OMe	3-COOMe
49:	C	3-CF <sub>3</sub> , 4-OH	3-COOMe
50:	C	3-Br, 4-CH <sub>2</sub> OH	3-COOMe
51:	C	4-SO <sub>2</sub> NPr <sub>2</sub>	3-COOMe
52:	C	4-SO <sub>2</sub> NBu <sub>2</sub>	3-COOMe
53:		<i>N</i> -Methyl-4-nitrobenzenesulfonamide	3-COOMe
54:	C	4-OH	2-CF <sub>3</sub>
55:	C	4-OH	3-CF <sub>3</sub>
56:	N	H	3-CF <sub>3</sub>
57:	C	4-OH	4-CF <sub>3</sub>
58:	C	4-SO <sub>2</sub> NEt <sub>2</sub>	3-OH
59:	C	4-SO <sub>2</sub> NPe <sub>2</sub>	3-OH
60:		<i>N</i> -Methylthiophene-2-carboxamide	3-OH
61:		<i>N</i> -Methylthiophene-2-sulfonamide	3-OH
62:		Methyl thiophene-2-carboxylate	3-OH
63:		<i>N</i> -Methylthiophene-2-carboxamide	4-OMe
64:		<i>N</i> -Methylthiophene-2-sulfonamide	4-OMe
65:		Methyl thiophene-2-carboxylate	4-OMe
66:	C	4-OH	4-OMe
67:	C	3-OH	4-Br
68:	C	3-OH	3-Methylpyridine
69:	C	3-OH	4-Methylpyridine
70:	C	3-OH	1-Methyl benzimidazole
71:		H	4-Boronic acid pinacol ester
72:		H	4-B(OH) <sub>2</sub>

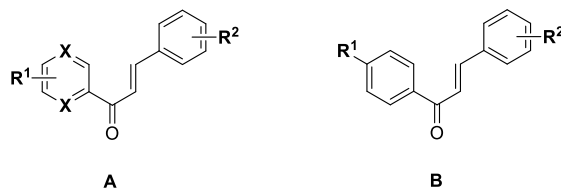
<sup>a</sup>Reagents and conditions: (i) **5**, **10-26**, **28**, **30-38**, **40-44**, **47-55**, **57-67**, **70**: BF<sub>3</sub>·Et<sub>2</sub>O, 1,4-dioxane, 80 °C. **8-9**, **39**: 60% NaOH, EtOH, 0 °C → rt. **29**, **56**: (1) Et<sub>2</sub>NH, pyridine, 80-120 °C; (2) acetic acid; (ii) **71**: DBU, PPh<sub>3</sub>, PdCl<sub>2</sub>(PPh<sub>3</sub>)<sub>2</sub>, THF, MW 120 °C, 40 min; (iii) **6**: (1) Py·HCl, 210 °C; (2) NaHCO<sub>3</sub>, pH 7-8; (iv) **7**, **27**: K<sub>2</sub>CO<sub>3</sub>, MeI, acetone, reflux; (v) **31**: (1) Bis(pinacolato)diboron, PdCl<sub>2</sub>(dppf), KOAc, dioxane, reflux; (2) NaIO<sub>4</sub>, THF, H<sub>2</sub>O, rt; (3) HCl, H<sub>2</sub>O, rt; (vi) **45**: (1) NaOH, H<sub>2</sub>O, THF, rt; (2) HCl, H<sub>2</sub>O;

(vii) **46**: cat H<sub>2</sub>SO<sub>4</sub>, anh MeOH, reflux; (viii) **68**: Pyridine-3-boronic acid, 10 mol% Pd(OAc)<sub>2</sub>, KF, PEG/EtOH, MW 110 °C, 30 min; (ix) **69**: Cs<sub>2</sub>CO<sub>3</sub>, Pd(PPh<sub>3</sub>)<sub>4</sub>, DMF, MW 130 °C, 20 min; (x) **72**: (1) NaIO<sub>4</sub>, H<sub>2</sub>O, THF, rt; (2) HCl, H<sub>2</sub>O, rt.

A total of 68 synthetic chalcone compounds were prepared and tested for the inhibitory effect against PDI using the PDI reductase assay.<sup>33, 34</sup> Their structure-activity relationship (SAR) was analyzed by categorizing the derivatives into three clusters based on the substituent of ring **B**. In the first series of analogues (Table IV-1), we maintained the nitrile group of the lead **BAP2** at R<sup>2</sup> and made modifications at R<sup>1</sup>. Replacement of the hydroxyl group (**6**, IC<sub>50</sub> of 0.85 μM) with bromine (**10**) led to a 2-fold decrease in the inhibition of PDI activity. Activity dropped substantially upon replacement of the hydroxyl group (**5**, IC<sub>50</sub> of 1.87 μM and **6**) with a methoxy group (**7** and **8**), amine (**9**), or heterocycle (**11**, **12**), and upon the introduction of a pyrazine moiety to replace the phenyl ring (**29**). Similarly, the compounds containing at least one hydroxyl group retained activity or showed stronger activity depending on the additional substituent (**21-24**, **32-36**, IC<sub>50</sub> range of 0.21 – 2.37 μM), regardless of the position of the nitrile at *meta* or *para* of R<sup>2</sup>. However, introduction of a methoxy group (**25**, **26**) seemed to be unfavorable for activity even with the hydroxyl group maintained (IC<sub>50</sub> of 10.9 and 2.72 μM, respectively). Analogue activity decreased with dimethoxy groups (**27**) or dihalogen atoms (**28**) in place of the hydroxyl group, indicating the importance of the hydroxyl group for potency. Interestingly, several **BAP2** analogues lacking a hydroxyl group retained or even improved PDI inhibitory activity (**13-20**). These compounds contain a sulfonamide moiety in place of the hydroxyl group and increase in hydrophobic character with increasing alkyl chain. As hydrophobicity increased, the PDI inhibitory activity of the analogues improved, and the derivatives with 3 < ClogP < 5 were the

most potent with  $IC_{50}$  values of 0.82 – 1.23  $\mu\text{M}$  (**15**, **16**, **19**, **20**). On the other hand, another type of sulfonamide-containing chalcone derivative (e.g. **30**,  $IC_{50}$  of 8.51  $\mu\text{M}$ ) was not as potent as **20** ( $IC_{50}$  of 1.11  $\mu\text{M}$ ) although they both have a bulky hydrophobic moiety, suggesting that electron withdrawing group such as  $-\text{SO}_2\text{NHR}$  prepare the olefin for nucleophilic attack by the thiol in the active site. Potentially, the hydrophobic region would interact with a pocket near the active site to stabilize binding. These findings suggest that both active site and hydrophobic interactions play important roles in the activity of this series.

Table IV-1 PDI inhibitory activity of the synthesized **BAP2** derivatives **5-36**<sup>a</sup>



Compd	Scaffold	X	R <sup>1</sup>	R <sup>2</sup>	$IC_{50}$ ( $\mu\text{M}$ ) <sup>b</sup>
<b>6</b> ( <b>BAP2</b> )	A	C	4-OH	3-CN	0.85 ± 0.14
<b>5</b>	A	C	3-OH	3-CN	1.87 ± 0.58
<b>7</b>	A	C	3-OMe	3-CN	8.13 ± 1.53
<b>8</b>	A	C	4-OMe	3-CN	> 500
<b>9</b>	A	C	4-NH <sub>2</sub>	3-CN	> 500
<b>10</b>	A	C	4-Br	3-CN	1.66 ± 0.42
<b>11</b>	A	C	4-Morpholine	3-CN	> 500
<b>12</b>	A	C	4-Piperidine	3-CN	> 500
<b>13</b>	A	C	4-SO <sub>2</sub> NH <sub>2</sub>	3-CN	6.64 ± 0.11
<b>14</b>	A	C	4-SO <sub>2</sub> NMe <sub>2</sub>	3-CN	6.23 ± 0.67

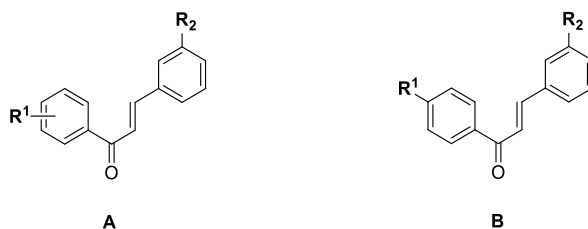


15	A	C	4-SO <sub>2</sub> NEt <sub>2</sub>	3-CN	1.23 ± 0.06
16	A	C	4-SO <sub>2</sub> NPr <sub>2</sub>	3-CN	0.82 ± 0.34
17	A	C	4-SO <sub>2</sub> NBu <sub>2</sub>	3-CN	1.34 ± 0.19
18	A	C	4-SO <sub>2</sub> NPe <sub>2</sub>	3-CN	0.16 ± 0.06
19	A	C	4-SO <sub>2</sub> NHCPH	3-CN	1.05 ± 0.76
20	A	C	4-SO <sub>2</sub> NHPh	3-CN	1.11 ± 0.14
21	A	C	2-OH, 4-F	3-CN	2.37 ± 1.22
22	A	C	3-OH, 4-F	3-CN	1.15 ± 0.08
23	A	C	3-F, 4-OH	3-CN	1.14 ± 0.17
24	A	C	3-CF <sub>3</sub> , 4-OH	3-CN	2.00 ± 0.37
25	A	C	3-OH, 4-OMe	3-CN	10.93 ± 0.73
26	A	C	3-OMe, 4-OH	3-CN	2.72 ± 0.74
27	A	C	3,4-OMe	3-CN	>100
28	A	C	3-F, 4-Cl	3-CN	>500
29	A	N	H	3-CN	>500
30	B		<i>N</i> -methyl-4-nitrobenzenesulfonamide	3-CN	8.51 ± 3.51
31	B		B(OH) <sub>2</sub>	3-CN	0.83 ± 0.38
32	A	C	4-OH	4-CN	0.74 ± 0.09
33	A	C	2-OH, 4-F	4-CN	1.80 ± 0.60
34	A	C	3-OH, 4-F	4-CN	1.83 ± 0.49
35	A	C	3-F, 4-OH	4-CN	0.21 ± 0.08
36	A	C	3-CF <sub>3</sub> , 4-OH	4-CN	1.11 ± 0.33

<sup>a</sup>Inhibition of PDI was assessed by PDI reductase assay. <sup>b</sup>IC<sub>50</sub> values are indicated as the mean ± SD (standard error) of at least three independent experiments.

Next, we investigated PDI inhibitory activity of the derivatives containing a carboxylic acid or carboxymethyl ester in place of the nitrile group at *meta* position of R<sup>2</sup> (Table IV-2). The introduction of carboxylic acid at R<sup>2</sup> (**37-45**) generally reduced potency, regardless of the presence of a hydroxyl group at R<sup>1</sup>. However, a carboxymethyl ester (**46, 47, 49**) increased potency with an IC<sub>50</sub> range of 0.12 – 0.49 μM compared to compounds containing a nitrile group (**5, 6, 24**, IC<sub>50</sub> range of 0.85 – 2.0 μM), and we obtained the most potent analogue **46** with a carboxymethyl ester (IC<sub>50</sub> = 120 ± 10 nM) at R<sup>2</sup>. These results indicate that the carboxymethyl ester facilitates stronger binding affinity for PDI than chalcones containing other electron-withdrawing groups such as a nitrile group or carboxylic acid. Intriguingly, the activity was lost when the carboxymethyl ester at R<sup>2</sup> was added to the sulfonamide-containing chalcones (**51-53**), suggesting that the chalcones with a hydroxyl group or a sulfonamide moiety at R<sup>1</sup> may have different binding modes.

Table IV-2 PDI inhibitory activity of the synthesized **BAP2** derivatives **37-53**<sup>a</sup>



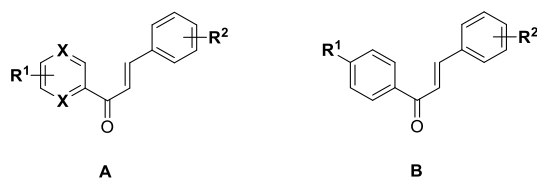
Compd	Scaffold	X	R <sup>1</sup>	R <sup>2</sup>	IC <sub>50</sub> (μM) <sup>b</sup>
<b>6</b> ( <b>BAP2</b> )	A	C	4-OH	3-CN	0.85 ± 0.14
<b>37</b>	A	C	3-OH	3-COOH	10.19 ± 1.41
<b>38</b>	A	C	4-NO <sub>2</sub>	3-COOH	40 < IC <sub>50</sub> < 500
<b>39</b>	A	C	4-NH <sub>2</sub>	3-COOH	> 100

40	A	C	4-Morpholine	3-COOH	> 100
41	A	C	4-Piperidine	3-COOH	40 < IC <sub>50</sub> < 500
42	A	C	3-OH, 4-OMe	3-COOH	> 100
43	A	C	3-F, 4-OH	3-COOH	9.10 ± 2.10
44	A	C	3-CF <sub>3</sub> , 4-OH	3-COOH	4.09 ± 1.31
45	B		<i>N</i> -methyl-4-nitrobenzenesulfonamide	3-COOH	4.00 ± 0.60
46	A	C	3-OH	3-COOMe	0.12 ± 0.01
47	A	C	4-OH	3-COOMe	0.40 ± 0.16
48	A	C	3-OH, 4-OMe	3-COOMe	47.8 ± 11.0
49	A	C	3-CF <sub>3</sub> , 4-OH	3-COOMe	0.49 ± 0.13
50	A	C	3-Br, 4-CH <sub>2</sub> OH	3-COOMe	0.13 ± 0.03
51	A	C	4-SO <sub>2</sub> NPr <sub>2</sub>	3-COOMe	> 100
52	A	C	4-SO <sub>2</sub> NBu <sub>2</sub>	3-COOMe	> 100
53	B		<i>N</i> -methyl-4-nitrobenzenesulfonamide	3-COOMe	> 100

<sup>a</sup>Inhibition of PDI was assessed by PDI reductase assay. <sup>b</sup>IC<sub>50</sub> values are indicated as the mean ± SD (standard error) of at least three independent experiments.

We also examined the potency of **BAP2** derivatives containing different functional groups such as trifluoromethyl, hydroxy, methoxy, bromo, boronate, or boronic acid moieties at R<sup>2</sup> (Table IV-3). Replacing the nitrile in **BAP2** (**6**) and **32** with a trifluoromethyl group reduced the potency about 2 to 4-fold (**55**, **57**), suggesting the electron-withdrawing properties at R<sup>2</sup> are not driving inhibition. But interestingly, replacement with a heterocycle increased analogue activity with IC<sub>50</sub> values of 0.21 – 0.35 μM (**68-70**). In a series of carboxamide-, sulfonamide-, or carboxylate-containing analogues (**60-65**), the compounds with a hydroxyl group at R<sup>2</sup> afforded PDI inhibition with an IC<sub>50</sub> range of 1.7 – 11 μM (**60-62**), but the potency was abolished upon replacement with a methoxy group (**63-65**), suggesting that the analogues with a hydrophobic moiety at R<sup>1</sup> may require the hydroxyl anchor at R<sup>2</sup> to position them for hydrophobic interactions around the binding pocket. In addition, the analogues containing -SO<sub>2</sub>NHR at R<sup>1</sup> and hydroxyl group at R<sup>2</sup> (**58**, **59**) tolerated the activity compared to the ones containing nitrile group at R<sup>2</sup> (**15**, **16**).

Table IV-3 PDI inhibitory activity of the synthesized **BAP2** derivatives **54-72**<sup>a</sup>



Compd	Scaffold	X	R <sup>1</sup>	R <sup>2</sup>	IC <sub>50</sub> (μM) <sup>b</sup>
<b>6</b> ( <b>BAP2</b> )	A	C	4-OH	3-CN	0.85 ± 0.14
<b>54</b>	A	C	4-OH	2-CF <sub>3</sub>	1.67 ± 0.29
<b>55</b>	A	C	4-OH	3-CF <sub>3</sub>	1.56 ± 0.36
<b>56</b>	A	N	H	3-CF <sub>3</sub>	9.57 ± 0.52
<b>57</b>	A	C	4-OH	4-CF <sub>3</sub>	2.56 ± 1.01
<b>58</b>	A	C	4-SO <sub>2</sub> NEt <sub>2</sub>	3-OH	1.29 ± 0.31
<b>59</b>	A	C	4-SO <sub>2</sub> NPe <sub>2</sub>	3-OH	0.81 ± 0.56
<b>60</b>	B		<i>N</i> -methylthiophene-2-carboxamide	3-OH	5.74 ± 0.10
<b>61</b>	B		<i>N</i> -methylthiophene-2-sulfonamide	3-OH	11.13 ± 0.50
<b>62</b>	B		Methyl thiophene-2-carboxylate	3-OH	1.75 ± 0.27
<b>63</b>	B		<i>N</i> -methylthiophene-2-carboxamide	4-OMe	> 500
<b>64</b>	B		<i>N</i> -methylthiophene-2-sulfonamide	4-OMe	40 < IC <sub>50</sub> < 500
<b>65</b>	B		Methyl thiophene-2-carboxylate	4-OMe	40 < IC <sub>50</sub> < 500
<b>66</b>	A	C	4-OH	4-OMe	1.74 ± 0.50
<b>67</b>	A	C	3-OH	4-Br	0.40 ± 0.04
<b>68</b>	A	C	3-OH	4-(Pyridin-3-yl)	0.35 ± 0.20
<b>69</b>	A	C	3-OH	3-(Pyridin-4-yl)	0.21 ± 0.19
<b>70</b>	A	C	3-OH	4-(Benzoimidazol-1-yl)	0.23 ± 0.09
<b>71</b>	B		H		2.20 ± 0.79

<sup>a</sup>Inhibition of PDI was assessed by PDI reductase assay. <sup>b</sup>IC<sub>50</sub> values are indicated as the mean ± SD (standard error) of at least three independent experiments.

The SAR of all derivatives are summarized in Figure IV-2, and the results indicate there are two different series of active chalcone derivatives. The first series contains a hydroxyl group at *meta* or *para* position of ring A, and the potency of compounds decreases based on the functional group on ring B as follows: COOMe ≈ Br, pyridine, benzimidazole > CN > CF<sub>3</sub> ≫ COOH. The second series contains a sulfonamide moiety or aromatic ring with linkers such as carboxamide, carboxylate, or sulfonamide at *para* position on ring A, and the potency of compounds decreased based on the functional group of ring B as follows: CN ≈ OH > OMe ≈ COOMe.

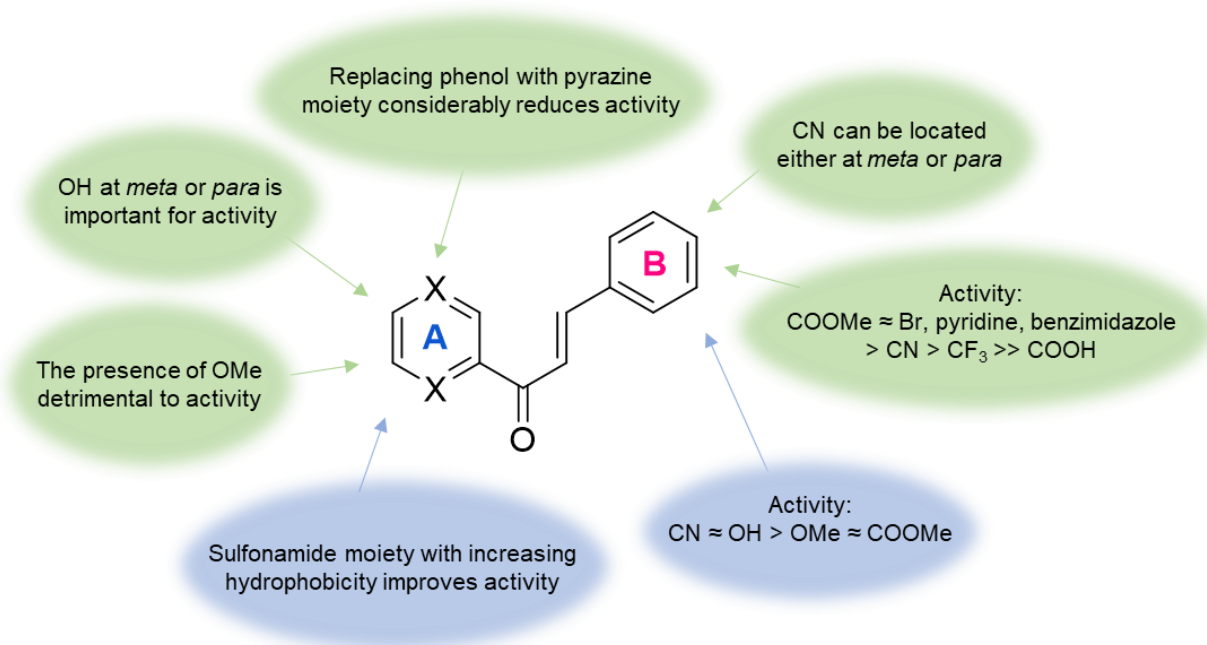


Figure IV-2 Summarized SAR of synthesized **BAP2** analogues.

### **BAP2 analogues selectively reduce brain cancer cell viability**

We selected 23 **BAP2** analogues with  $IC_{50}$  values lower than 1.5  $\mu\text{M}$  against PDI and tested for cytotoxicity in a panel of brain cancer cell lines (U87MG, A172, and NU04) (Table IV-4). Compound **19** was not soluble in DMSO and therefore not considered further in this study. The **BAP2** analogues were moderately cytotoxic to U87MG cells, with  $IC_{50}$  values from 10 to 30  $\mu\text{M}$  for most of the analogues. In general, the NU04 cells were more sensitive than the U87MG cells to treatment. Compounds more potent than **BAP2** (**6**) in both A172 and NU04 cells included **18**, **59**, **68**, **69**, and **70**. Among the compounds, compound **18** was the most potent in both U87MG and A172 cells ( $IC_{50} = 5.6 \pm 2.1 \mu\text{M}$  and  $9.0 \pm 3.4 \mu\text{M}$ , respectively). Compound **69** was the most potent in the NU04 cell line, with an  $IC_{50}$  value of  $3.8 \pm 0.1 \mu\text{M}$ . These chalcone derivatives also inhibited PDI activity more potently compared to **PACMA31**<sup>33</sup>, a previously reported PDI inhibitor (Figure IV-3). Next, we investigated the effect of five **BAP2** derivatives on GBM cell proliferation. All compounds generally showed a dose-dependent inhibition of colony formation in U87MG cells. **BAP2** was less potent in the colony formation assay than in the MTT assay as it inhibited less than 40 % of cell proliferation at 10  $\mu\text{M}$ , whereas the  $IC_{50}$  value of **BAP2** in U87MG cells was  $10.7 \pm 1.8 \mu\text{M}$  (Table IV-4). Interestingly, unlike **BAP2**, all other analogues except **59** inhibited more than 50% of cell proliferation at a lower dose than their  $IC_{50}$  values in U87MG cells, indicating that these analogues can inhibit the clonogenic properties of the cells.

Table IV-4 Cytotoxicity of the 23 selected **BAP2** analogues in a panel of human GBM cell lines<sup>a</sup>

Compd	IC <sub>50</sub> (μM)		
	U87MG	A172	NU04
<b>6 (BAP2)</b>	10.3 ± 2.3	16.8 ± 3.5	15.7 ± 3.4
<b>15</b>	17.7 ± 4.6	26.4 ± 4.1	19.9 ± 8.3
<b>16</b>	25.6 ± 5.0	35.0 ± 13.1	26.6 ± 0.7
<b>17</b>	17.0 ± 3.3	67.3 ± 46.8	15.5 ± 4.2
<b>18</b>	5.6 ± 2.1	9.0 ± 3.4	5.0 ± 1.8
<b>19</b>	NS	NS	NS
<b>20</b>	48.5 ± 37.5	28.9 ± 3.0	18.7 ± 11.4
<b>22</b>	22.9 ± 8.1	16.8 ± 3.3	10.6 ± 3.8
<b>23</b>	29.1 ± 6.9	21.9 ± 7.1	9.8 ± 1.3
<b>31</b>	24.3 ± 11.0	20.2 ± 11.0	13.0 ± 2.2
<b>32</b>	15.1 ± 5.6	20.0 ± 8.6	12.8 ± 2.7
<b>35</b>	29.0 ± 9.3	28.4 ± 8.4	15.8 ± 10.3
<b>36</b>	26.4 ± 8.2	33.7 ± 13.5	10.4 ± 1.3
<b>46</b>	16.5 ± 7.6	19.5 ± 6.9	22.7 ± 8.2
<b>47</b>	28.8 ± 2.3	32.3 ± 1.6	30.6 ± 4.4
<b>49</b>	11.6 ± 0.6	35.0 ± 35.7	10.3 ± 0.7
<b>50</b>	13.6 ± 1.8	20.6 ± 10.4	17.2 ± 10.2
<b>58</b>	40.7 ± 14.5	31.2 ± 8.0	19.2 ± 10.1
<b>59</b>	15.0 ± 3.5	11.3 ± 0.3	7.6 ± 3.1
<b>67</b>	76.3 ± 23.8	67.8 ± 6.4	26.2 ± 8.3
<b>68</b>	10.7 ± 0.8	11.0 ± 0.8	4.9 ± 1.0
<b>69</b>	24.9 ± 12.1	11.3 ± 0.1	3.8 ± 0.1
<b>70</b>	10.8 ± 1.2	10.7 ± 0.6	9.9 ± 1.5



72

31.2 ± 2.1

32.1 ± 1.1

22.9 ± 6.5

---

<sup>a</sup>Cytotoxicity was assessed by MTT assay. IC<sub>50</sub> values are indicated as the mean ± SD (standard error) of at least three independent experiments for active compounds (IC<sub>50</sub> < 20 μM). NS: not soluble in DMSO.

Next, we tested the five **BAP2** derivatives in HFF-1 normal human fibroblast cells to determine the therapeutic window of this series (Table IV-5). Interestingly, **BAP2** had the largest therapeutic window, with a 5.8-fold difference in potency in NU04 (15.7 ± 3.4 μM) versus HFF-1 cells (91.2 ± 13.1 μM). Compounds **59** and **68** demonstrated a 3.8-fold and 4.6-fold difference in potency, respectively, between cancer cells and normal cells. In the case of compound **18**, potency was greater against the HFF-1 cells (3.4 ± 1.1 μM) than the NU04 cells (5.0 ± 1.8 μM). These results suggest that **BAP2** and analogues may be effective in combination therapy because they may cause less off-target toxicity.

Table IV-5 Cytotoxicity of 6 **BAP2** analogues in a human fibroblast cell line HFF-1 and comparison to NU04<sup>a</sup>

ID	IC <sub>50</sub> (μM)		Fold Difference
	NU04 (μM)	HFF-1 (μM)	
<b>BAP2</b>	15.7 ± 3.4	91.2 ± 13.1	5.80
<b>18</b>	5.0 ± 1.8	3.4 ± 1.1	0.67
<b>46</b>	22.7 ± 8.2	17.4 ± 3.5	0.77
<b>59</b>	7.6 ± 3.1	29.2 ± 4.5	3.85
<b>68</b>	4.9 ± 1.0	22.5 ± 8.0	4.57
<b>69</b>	3.8 ± 0.1	31.8 ± 13.2	8.39

<sup>a</sup>Cytotoxicity was assessed by MTT assay. IC<sub>50</sub> values are indicated as the mean ± SD (standard error) of at least three independent experiments.

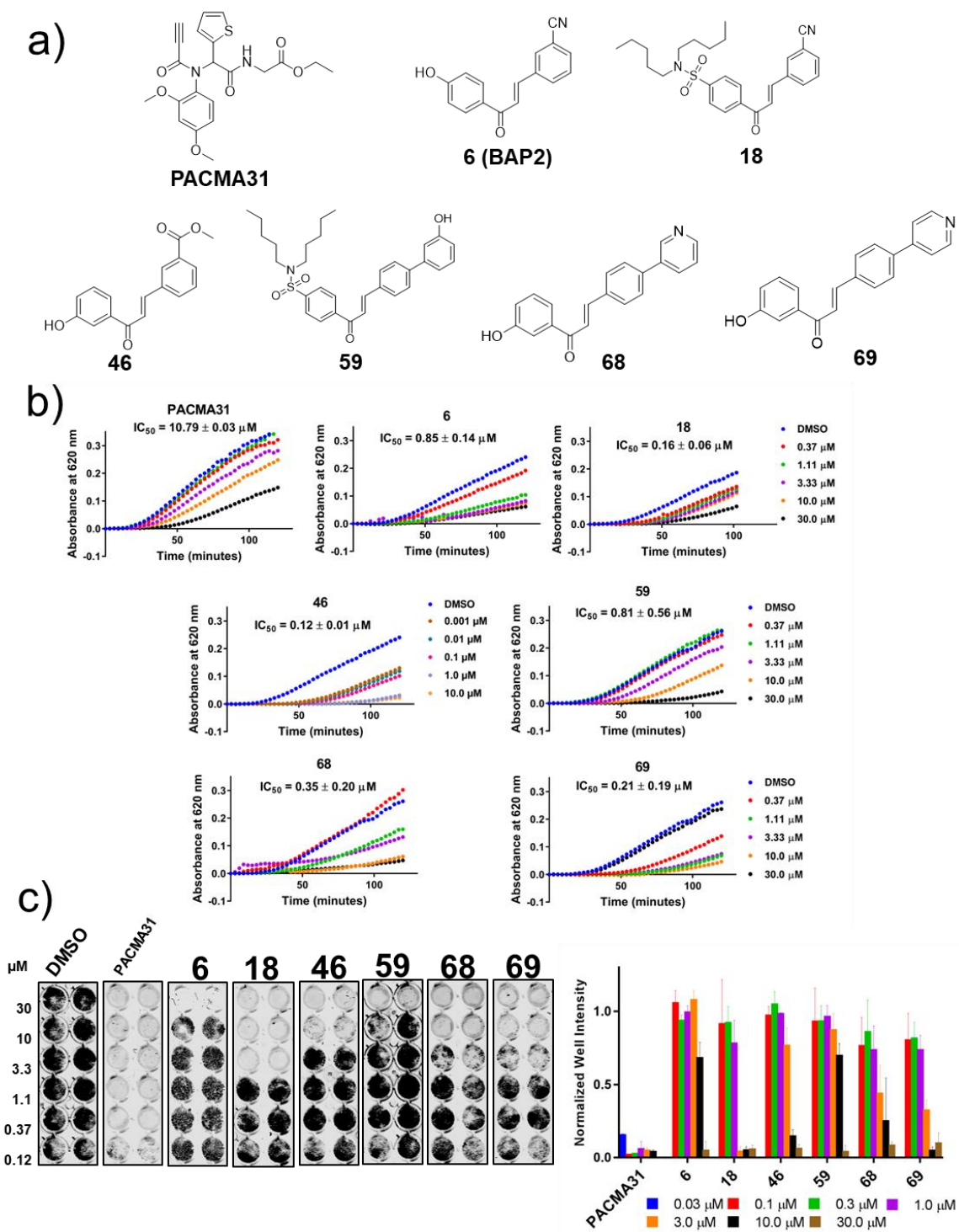


Figure IV-3 Optimized **BAP2** analogues inhibit colony formation and PDI activity. (A) Chemical structures of five optimized **BAP2** (**6**) analogues. (B) PDI reductase inhibition activity of **PACMA31**, **6**, **18**, **46**, **59**, **68**, and **69**. Recombinant PDI at 400 nM

was incubated at 37 °C for 1 h in the presence or absence of indicated compounds. Reduction of insulin was followed by an increase in absorbance at 620 nm for 120 min. IC<sub>50</sub> values were calculated at 80 min. (C) Colony formation ability of U87MG cells was determined in the presence of DMSO, or PDI inhibitors. Normalized well intensity from three independent experiments is shown in the right panel.

### **BAP2 analogues stabilize PDI to thermal degradation**

In order to validate that our compounds interact with PDI and stabilize the protein to thermal denaturation, we further tested the compounds in the biochemical thermal shift assay. Compounds **18**, **46**, **59**, **68**, and **69** were tested at 100 μM against recombinant PDI, and an inactive compound **8** was used as a negative control in addition to DMSO. Typically, compounds that bind to a protein stabilize its secondary structure and increase the melting temperature; however, **PACMA31**, a validated PDI inhibitor, does not stabilize PDI. This may be explained by the irreversible covalent nature of binding to the reactive site cysteines. Because the bond is irreversibly covalent, it may not require additional interaction to inhibit PDI activity. On the other hand, estradiol, known to bind in the b' domain of PDI and form critical interactions with His256,<sup>35</sup> stabilizes PDI to thermal denaturation.

Similar to estradiol and **BAP2**, the analogues **46**, **59**, and **68** increased the melting temperature by more than 1 °C in a dose-dependent manner, suggesting that these compounds form important stabilizing interactions with PDI (Figure IV-4). However, compounds **18** and **69** did not stabilize PDI in the thermal shift assay, despite being potent inhibitors of PDI activity; these results suggest that these compounds may interact in the active site of PDI, instead of the hydrophobic pocket of the b' domain. This suggests that **BAP2** analogues **46**, **59**, and **68** may form critical interactions with PDI that **PACMA31** does not form. To provide additional evidence to support

our hypothesis, we prepared two mutants of PDI: H256A and C53S/C397S. The H256A mutant contains a point mutation from histidine to alanine at the key residue 256 where estradiol was proposed to bind. The C53S/C397S mutant contains serine residues replacing one cysteine from each of the CGHC active sites. In the thermal shift assay, the stabilization by estradiol and **BAP2** was abolished in the H256A mutant, but not the C53S/C397S mutant (Figure IV-4). Interestingly, the shift caused by analogues **46**, **59**, and **68** was not abolished by either mutation. This suggests that the histidine may be crucial for **BAP2** binding, but other hydrophobic interactions are important for analogue binding and activity. Specifically, **46**, **59**, and **68** may react with the active site thiols. These results ultimately suggest that **46**, **59**, and **68** may be interacting with both the active site and b' domain of PDI.

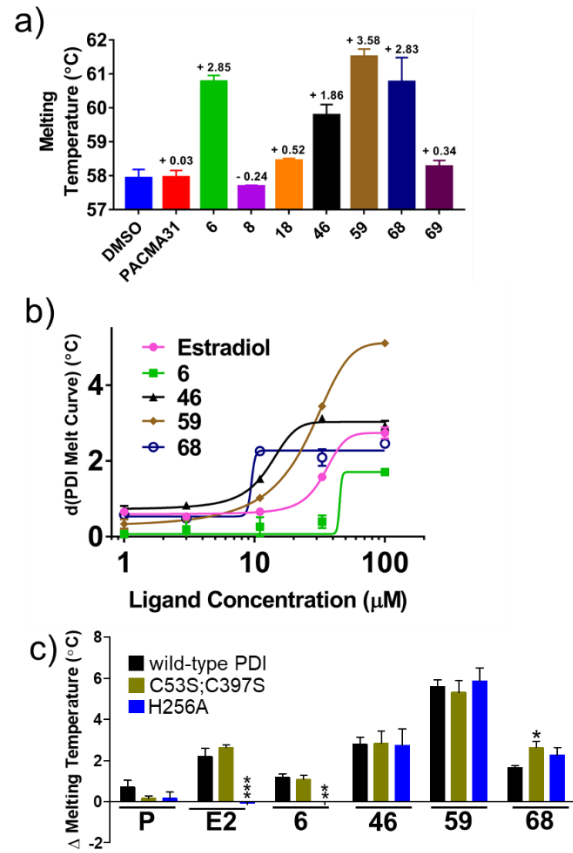


Figure IV-4 Optimized **BAP2** analogues stabilize PDI. (A) Boltzmann melting temperatures calculated for PDI (0.5 µg/µl) in the presence of 100 µM **PACMA31**, **6**, **8**, **18**, **46**, **59**, **68**, **69**, or DMSO. The change in melting temperature compared to DMSO is reported above each bar. (B) Dose-response effects of estradiol, **6**, **46**, **59**, and **68** in the presence of PDI. Results are reported as the change in the melting temperature of the curve compared to the vehicle control. (C) Change in melting temperature of 0.5 µg/µl wild-type, C53S/C397S, and H256A PDI in the presence of indicated compounds at 100 µM (DMSO used as vehicle control.) P: **PACMA31**; E2: estradiol. Results are reported as mean ± standard deviation of three experiments. \*:  $p < 0.05$ ; \*\*:  $p < 0.01$ ; \*\*\*:  $p < 0.001$ , compared to wild-type PDI values. Statistical significance was measured using 2-way analysis of variance (ANOVA).

### BAP2 analogues induce ER stress in GBM cells

PDI plays an important role in regulating the ER stress response, a mechanism that triggers the UPR and ultimately balances ER homeostasis.<sup>36</sup> In this study, we hypothesized that inhibition of PDI by **BAP2** analogues would exacerbate ER stress mechanisms by disrupting homeostatic balance, ultimately leading to cell death. We first investigated their effect on phosphorylation of

eukaryotic translation initiation factor 2 $\alpha$  (EIF2 $\alpha$ ) in U87MG and A172 cells (Figure IV-5). EIF2 $\alpha$  is a translation initiation factor downstream of the PERK arm of the UPR, and phosphorylation of EIF2 $\alpha$  in response to ER stress leads to inhibition of protein synthesis.<sup>36</sup> Like tunicamycin, a protein glycosylation inhibitor, treatment with **BAP2** analogues increased phosphorylation of EIF2 $\alpha$  above basal levels in both GBM cell lines. Unexpectedly, **PACMA31** did not induce phosphorylation of EIF2 $\alpha$ . **PACMA31**, **BAP2**, and analogues also increased expression of GRP78 (Figure IV-5). These results indicate that treatment of GBM cells with **BAP2** analogues promotes ER stress, upregulates the UPR, and inhibits protein synthesis. Compound **46** significantly promotes the ER stress response in GBM cells.

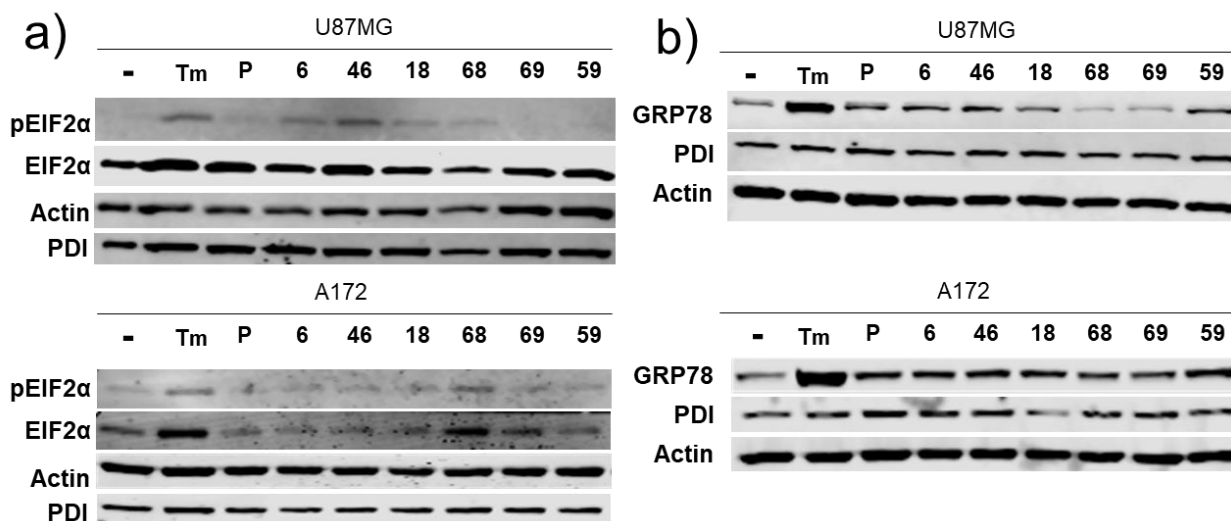


Figure IV-5 **BAP2** analogues inhibit protein synthesis via EIF2 $\alpha$  pathway. (A) U87MG cells were treated with tunicamycin (10  $\mu$ g/mL), 1.0  $\mu$ M **PACMA31**, or 20  $\mu$ M **6**, **46**, **18**, **68**, **69**, or **59** for 2 hours and Western blots were performed as described in the Experimental Section. (B) U87MG cells treated with tunicamycin (10  $\mu$ g/mL), 1.0  $\mu$ M **PACMA31**, or indicated compounds at 20  $\mu$ M for 24 hours. Abbreviations: P – **PACMA31**; TM – tunicamycin

## **BAP2 analogues inhibit GBM cell migration**

PDI is involved in the migratory capabilities of glioma cells via the integrin outside-in pathway.<sup>37</sup> Therefore inhibiting PDI may prevent GBM cell invasion and metastasis. In order to determine whether the **BAP2** analogues could inhibit cell migration, we performed the wound healing assay in A172 cells. **BAP2** inhibited wound healing at 10  $\mu$ M, and all analogues, except **69**, inhibited cell migration in a dose-dependent manner, similar to **PACMA31** (Figure IV-6).

An additional transwell migration assay was performed to validate the migration of A172 cells in the presence of selected compounds, **PACMA31**, **6**, **18**, and **59** at subtoxic concentrations (Figure IV-6). Cells were treated with the compounds for 4 hours. All compounds inhibited migration at 30  $\mu$ M, and **18** inhibited migration at 10  $\mu$ M. We further examined the effect of the compounds on the expression level of migration markers including MMP2, MMP9 and p-FAK in U87MG cells at 10  $\mu$ M for 48 hours. Gelatin zymography and Western blot analysis of the conditioned media confirmed that **PACMA31** and **68** inhibit MMP2 activity and secretion. MMP2 expression in cells did not change upon **BAP2** analogue treatment; however, MMP9 expression decreased in the presence of **PACMA31**, **18**, **59**, and **68**. FAK phosphorylation did not change with **BAP2** analogue treatment. These results demonstrate that **BAP2** analogues inhibit GBM cell migration via downregulation of MMP9 and decreased secretion of MMP2.



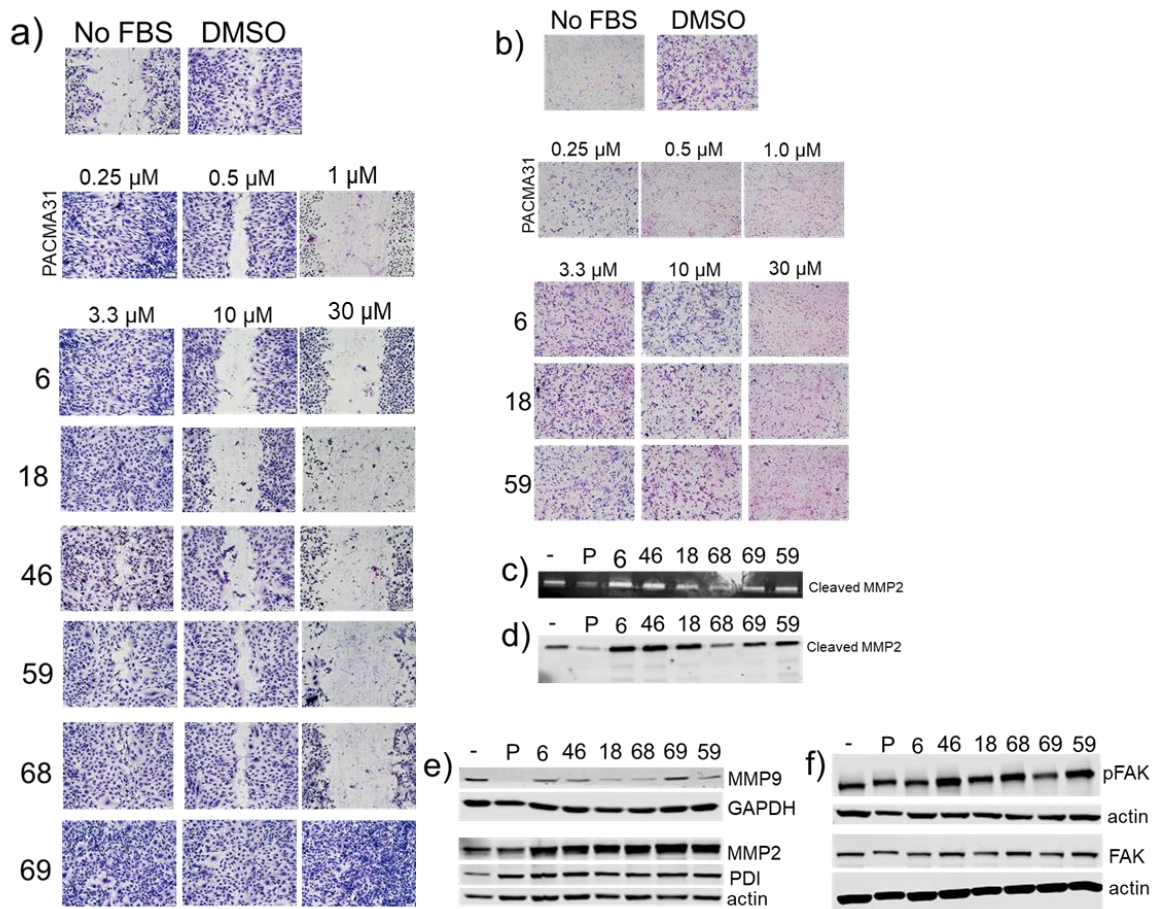


Figure IV-6 **BAP2** analogues inhibit cell migration in a dose-dependent manner. (A) Compounds tested in the wound healing assay for 24 hours. Cells were stained with Giemsa stain and images were taken at 10X magnification. (B) A172 cells migrated through an 8.0  $\mu\text{m}$  membrane in the transwell migration assay, in the presence of **6**, **18**, **59**, **PACMA31**, at indicated concentrations, or DMSO as a vehicle control. Wells without FBS were used as a control. Images are representative of 5 fields per well. (C) U87 cells were treated for 48 hours with 10  $\mu\text{M}$  **BAP2** analogues (or 0.25  $\mu\text{M}$  **PACMA31**). The activity of MMP2 was assessed by gelatin zymography. (D) Western blot was performed on the conditioned media of the chalcone-treated cells to determine the expression of cleaved MMP2. (E) Western blot was performed on the cell lysates of the chalcone-treated U87MG cells to determine expression of MMP2 and MMP9. (F) Western blot was performed on chalcone-treated U87MG cells to assess changes in the phosphorylation of FAK.

### **BAP2 and analogue 46 induce ER stress and downregulate DNA damage response genes**

Previously, with nascent RNA sequencing (Bru-seq), we demonstrated that **BAP2** treatment of U87MG cells upregulated ER stress and UPR genes and decreased expression of DNA repair and DNA damage response (DDR) genes.<sup>38</sup> We performed Bru-seq on analogues **18** and **46**

and found they had a similar effect on the cells. The transcription of ER stress response genes including *DDIT3*, *CHAC1*, *ASNS*, and *XBPI* increased upon treatment with both compounds, though **18** increased transcription to a greater extent (Figure IV-7). Furthermore, both compounds also decreased transcription of *RAD51* and *E2F1* (Figure IV-7). Additionally, Gene Set Enrichment Analysis (GSEA) was performed on the log 2-fold changes of the abundance ratios of protein expression between DMSO- and compound-treated U87MG cells. GSEA confirmed that both **18** and **46** treatment resulted in profiles that positively correlated with UPR and negatively correlated with E2F signaling (Figure IV-8, Figure IV-9, Figure IV-10, Figure IV-11). We applied Hallmark pathway analysis via GSEA and identified that genes with decreased transcription upon **46** treatment also correlated with epithelial-to-mesenchymal transition, TNF $\alpha$  signaling, and KRAS signaling.

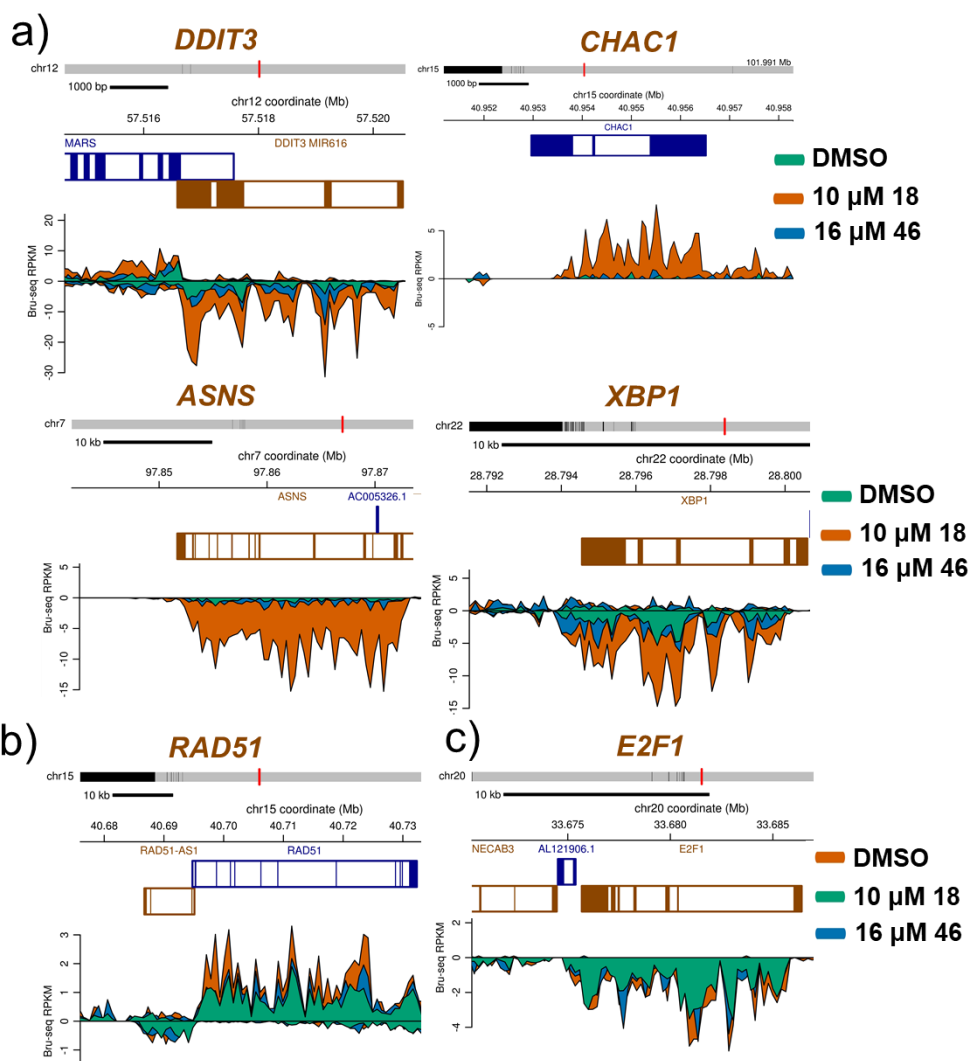


Figure IV-7 **BAP2** analogues induce transcription of ER stress genes and downregulate DNA damage response genes *RAD51* and *E2F1*. Traces of RNA transcripts derived from (A) ER stress genes, (B) *RAD51*, or (C) *E2F1* loci in U87MG cells treated with 10  $\mu\text{M}$  **18** or 16  $\mu\text{M}$  **46** for 4 hours. Traces represent RNA abundance following treatment. RPKM: reads/kilobase of transcript/million mapped reads.

To further validate the GSEA results, proteomics with tandem mass tag multiplexing was performed in U87MG cells treated for 24 hours with DMSO, 20  $\mu\text{M}$  of **BAP2** or **18**. GSEA revealed that **BAP2** treatment was positively correlated with the G2M DNA damage checkpoint and negatively correlated with ribosomes and associated proteins. Furthermore, **18** treatment was

positively correlated with an arsenic oxide signature and negatively correlated with DNA replication (Figure IV-12). These results suggest the analogues are targeting PDI and promoting a similar transcriptional profile in the cells as **BAP2**. Long, non-coding RNAs (lncRNA) can act as transcriptional regulators<sup>39</sup> and impact glioma initiation and progression.<sup>40</sup> GSEA of the Bru-seq transcription profiles of **18** and **46** also revealed non-coding genes with increased or decreased transcription. Transcription of *NMRAL2P*, a transcribed unprocessed pseudogene and target of Nrf2,<sup>41</sup> increased upon both **18** (+ 2.72 log2 fold change) and **46** (+ 4.10 log2 fold change) treatment of U87MG cells.

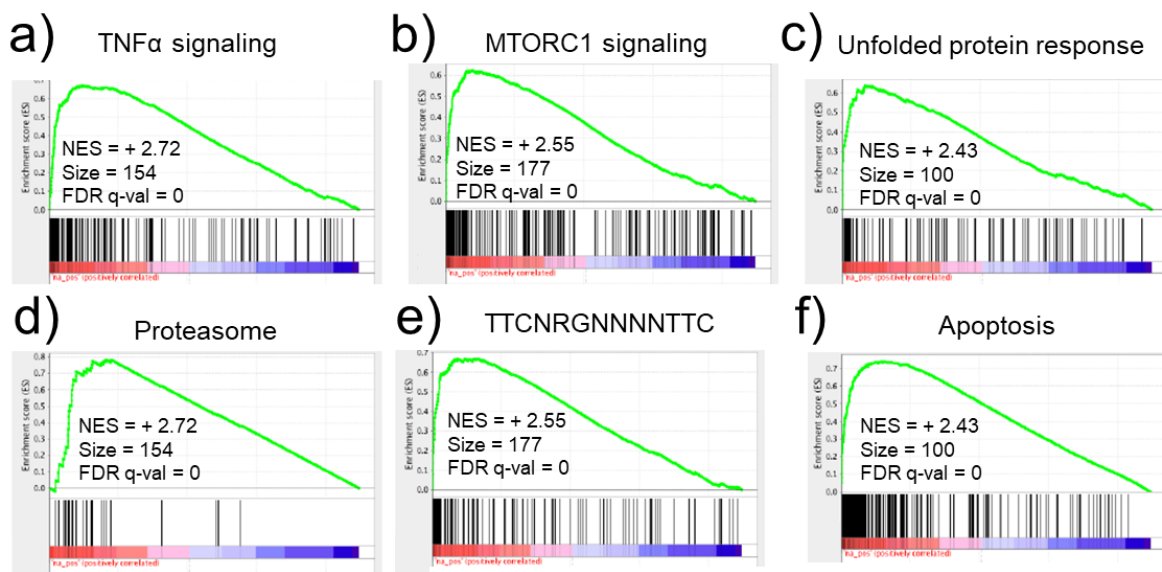


Figure IV-8 Upregulated GSEA of **18** treatment. Compound **18** treatment (10  $\mu$ M in U87MG cells) positively correlates with enrichment of (A) HALLMARK\_TNFA\_SIGNALING\_VIA\_NFKB, (B) HALLMARK\_MTORC1\_SIGNALING, (C) HALLMARK\_UNFOLDED\_PROTEIN\_RESPONSE, (D) KEGG\_PROTEASOME, (E) TTCNRGNNNTTC\_HSF\_Q6, and (F) CONCANNON\_APOPTOSIS\_BY\_EPOXOMICIN\_UP. NES: normalized enrichment score; FDR q-val: false discovery rate q-value

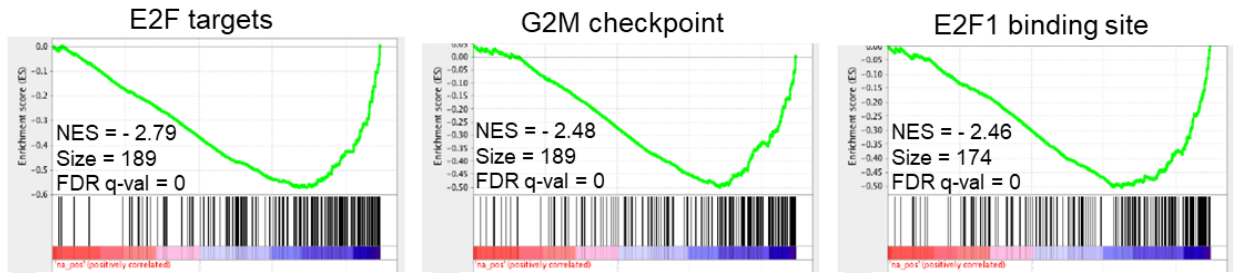


Figure IV-9 Downregulated GSEA of **18** treatment. Compound **18** treatment (10 μM in U87MG cells) negatively correlates with enrichment of (A) HALLMARK\_E2F\_TARGETS, (B) HALLMARK\_G2M\_CHECKPOINT, and (C) E2F1\_Q6. NES: normalized enrichment score; FDR q-val: false discovery rate q-value

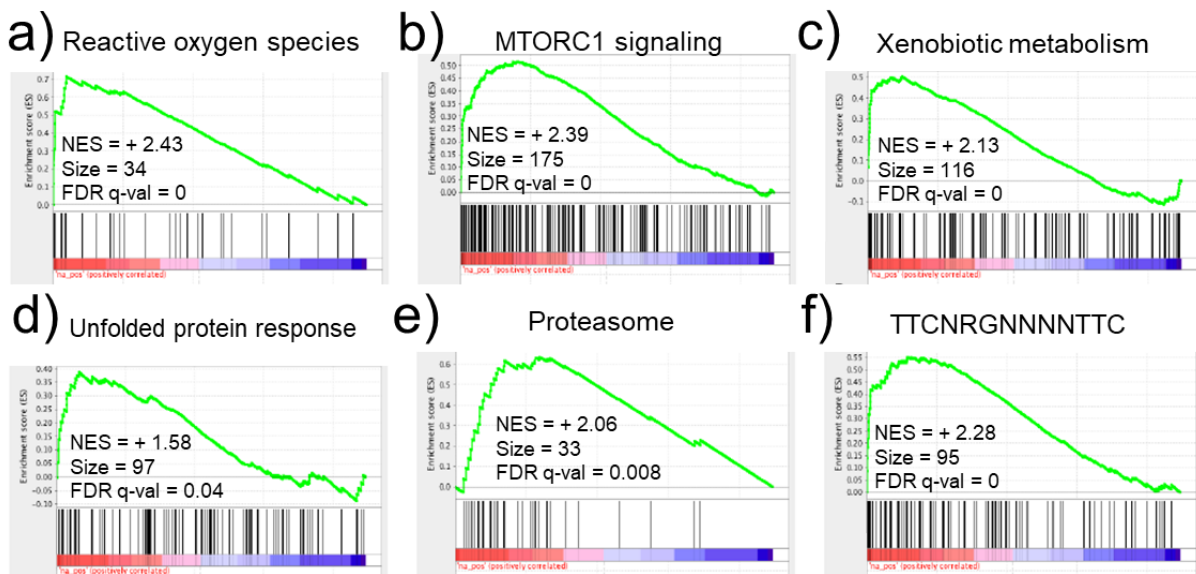


Figure IV-10 Upregulated GSEA of **46** treatment. Compound **46** treatment (16 μM in U87MG cells) positively correlates with enrichment of (A) HALLMARK\_REACTIVE\_OXYGEN\_SPECIES\_PATHWAY, (B) HALLMARK\_MTORC1\_SIGNALING, (C) HALLMARK\_XENOBIOTIC\_METABOLISM, (D) HALLMARK\_UNFOLDED\_PROTEIN\_RESPONSE, (E) KEGG\_PROTEASOME, and (F) TTCNRGNNNTTC\_HSF\_Q6. NES: normalized enrichment score; FDR q-val: false discovery rate q-value

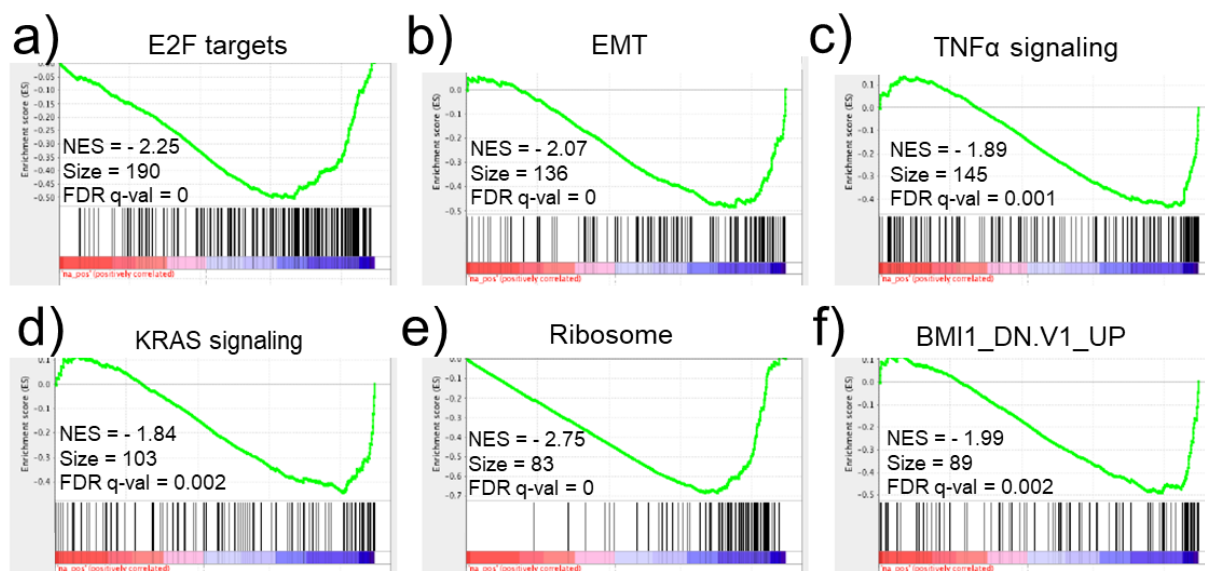


Figure IV-11 Downregulated GSEA of **46** treatment. Compound **46** treatment (16  $\mu$ M in U87MG cells) negatively correlates with enrichment of (A) HALLMARK\_E2F\_TARGETS, (B) HALLMARK\_EPITHELIAL\_MESENCHYMAL\_TRANSITION, (C) HALLMARK\_TNFA\_SIGNALING\_VIA\_NFKB, (D) HALLMARK\_KRAS\_SIGNALING\_UP, (E) KEGG\_RIBOSOME, and (F) BMI1\_DN.V1\_UP. NES: normalized enrichment score; FDR q-val: false discovery rate q-value

Additionally, PDI inhibition by **18** and **46** induces an immune response. Treatment of U87MG cells with **18** increases transcription of genes involved in the GO\_ANTIGEN\_PROCESSING\_AND\_PRESENTATION\_OF\_EXOGENOUS\_PEPTIDE\_ANTIGEN\_VIA\_MHC\_CLASS\_I gene set (NES = +2.37; FDR q-val = 0), and treatment with **46** correlates with the REACTOME\_CLASS\_I\_MHC\_MEDIATED\_ANTIGEN\_PROCESSING\_PRESENTATION gene set (NES = + 1.47; FDR q-val = 0.24). Furthermore, treatment with compound **18** correlates with both an inflammatory and immune response. PDI has been demonstrated to play a role in the immune response, and PDI is required for the degradation of major histocompatibility complex (MHC) class I, a protein responsible for antigen presentation that is essential for adaptive immunity.<sup>42, 43</sup> On the other hand, another study demonstrated that

PDI forms a key disulfide bond with the  $\alpha_2$  domain of the MHC class I heavy chain to aid early folding of the complex,<sup>44</sup> and another PDI family member, ERp57, may also aid stabilization of the MHC class I heavy chain via disulfide bond formation.<sup>45</sup> Thus, the role of PDI in the immune response is complex and the upregulation of transcription in these pathways in response to PDI inhibition may be a feedback response to pathway inhibition.

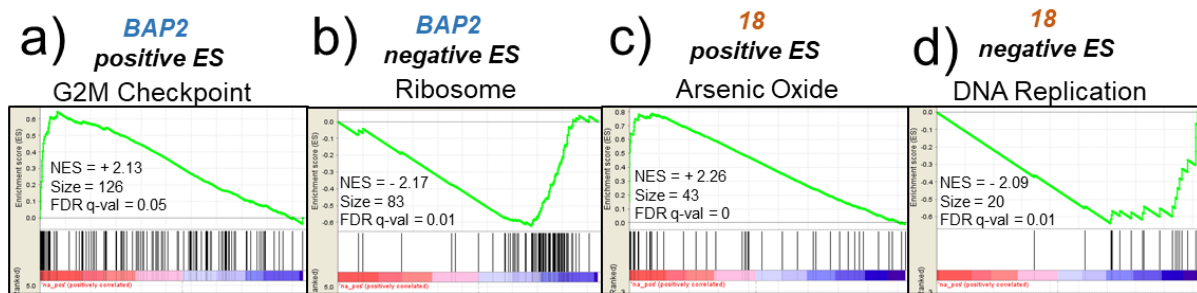


Figure IV-12 GSEA analysis of proteome perturbation by **BAP2** and **18** reveals increased expression of G2M checkpoint and arsenic trioxide response and reduced expression of proteins involved in ribosome and DNA replication. Gene set enrichment analysis was used to assess the effect of PDI inhibitors **BAP2** and **18** on the proteome of U87MG cells. GSEA plots of (A) upregulated and (B) downregulated pathways upon 20  $\mu$ M **BAP2** treatment: G2M Checkpoint and Ribosome, respectively. GSEA plots of (C) upregulated and (D) downregulated pathways upon 20  $\mu$ M **18** treatment: Response to Arsenic Trioxide and DNA replication, respectively.

### **BAP2 analogue treatment is synergistic with arsenic trioxide**

Previously, we demonstrated that **BAP2** treatment induces transcription of genes similar to that of arsenite treatment.<sup>38</sup> Furthermore, we observed increased expression of proteins involved in the response to arsenic oxide upon treatment with compound **18**. Arsenic oxide has been used to treat patients with acute promyelocytic leukemia<sup>46</sup> and synergy between tetra-arsenic oxide and paclitaxel in cancer cells has been observed.<sup>47</sup> **BAP2** and derivatives **13**, **14**, and **45** inhibit GBM cell proliferation synergistically with  $As_2O_3$  (Figure IV-13). Synergistic combinations had a



combination index value below 1 using the Chou-Talalay method.<sup>48</sup> Our results suggest that these **BAP2** analogues may best function in combination with other drugs.

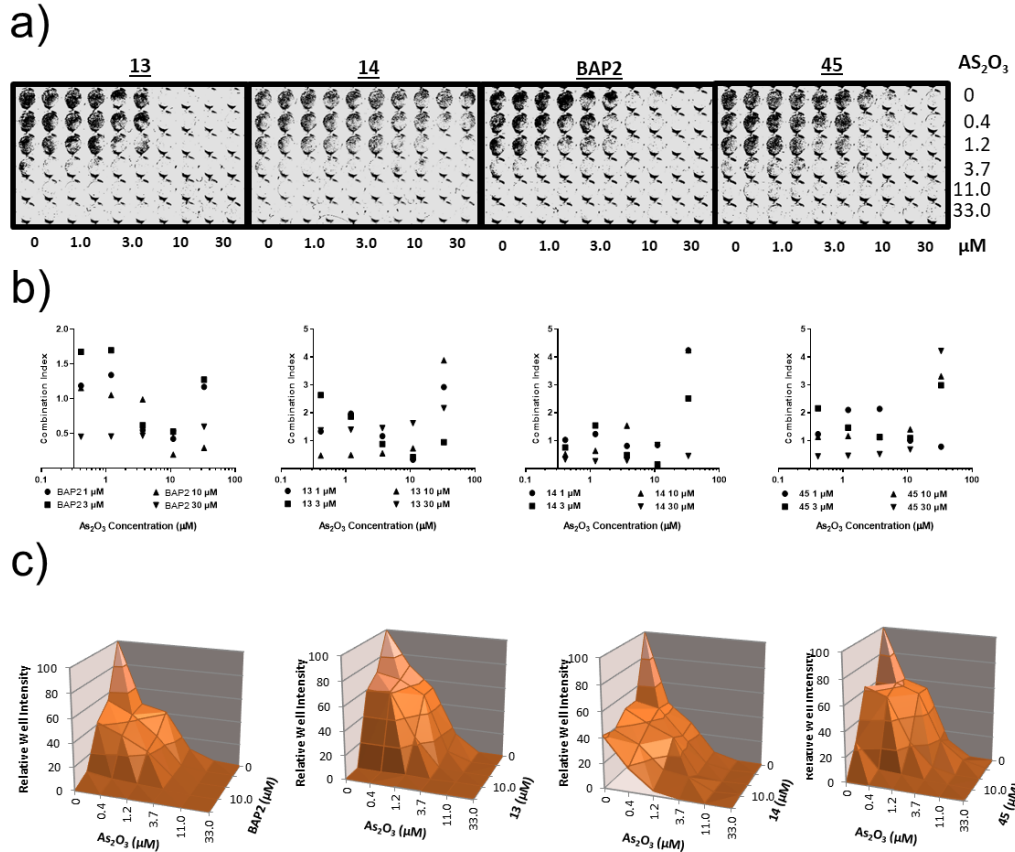


Figure IV-13 **BAP2** analogues synergize with As<sub>2</sub>O<sub>3</sub>. (A) U87MG cells were treated with indicated compounds and As<sub>2</sub>O<sub>3</sub> for 24 hours and the ability of cells to form colonies was measured. (B) Combination index of the concentration response in Panel A, calculated with the Chao Talalay method. Points below the 1.0 indicate synergistic combinations. Points above the line indicate antagonistic combinations. (C) Surface representation of the concentration response in Panel A.

### BAP2 analogue treatment synergizes with radiation

Since PDI inhibition and **BAP2** treatment cause global downregulation of DNA damage repair genes, we next determined whether **BAP2** analogues would synergize with radiation to decrease GBM cell viability. PDI inhibition radiosensitizes GBM cells.<sup>38</sup> The clonogenic survival



assay demonstrated synergy upon combination of PDI inhibitors and ionizing radiation (IR) compared to either modality alone (Figure IV-14). Both **BAP2** and **68** treatment synergized with IR; however, **PACMA31** at 0.05  $\mu\text{M}$  did not. It is likely that the dose of **PACMA31** was too low to demonstrate synergy, because the enzymatic  $\text{IC}_{50}$  value of **PACMA31** inhibition of PDI is around 10  $\mu\text{M}$ . Therefore, the more potent **BAP2** analogues likely synergize with IR by inhibiting PDI. These findings provide a strong rationale for the development of PDI inhibitors as agents to combine with DNA damage-inducing therapies such as IR.

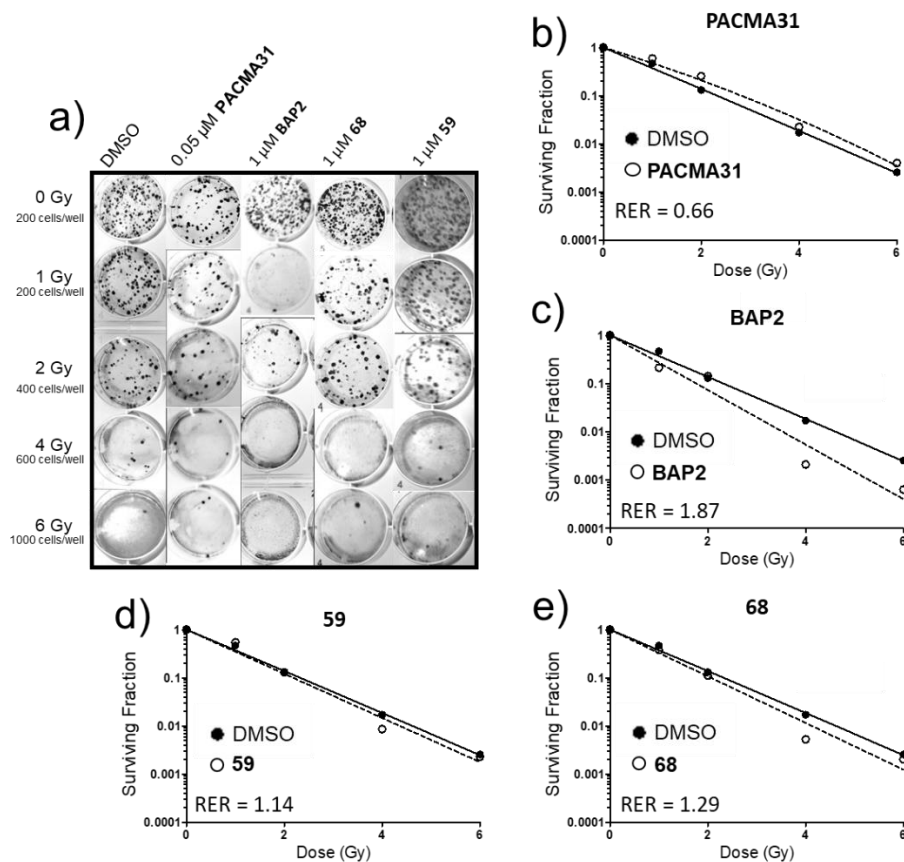


Figure IV-14 **BAP2** and analogue **68** synergize with radiation to inhibit clonogenic growth. (A) D54 cells were treated with indicated compounds after exposure to 0, 1, 2, 4, or 6 Gy of radiation. Cells were allowed to form colonies for ten days before staining and imaging. Survival curves were generated and radiation enhancement ratio (RER) was calculated for **PACMA31** (B), **BAP2** (C), **59** (D), and **68** (E).

### **BAP2 analogue activity varies against H256A mutant PDI**

As we previously demonstrated that **BAP2** requires His256 in the b' domain for activity, similar to estradiol binding, we also tested the **BAP2** analogues in the PDI reductase assay against H256A PDI (Figure IV-15). The activity of **BAP2** analogues, except **59**, was reduced upon mutation of His256 to Ala similar to **BAP2**, suggesting the analogues also bind in the b' domain of PDI and require His256 for activity. To further confirm their binding, we used the fluorescent dye, 1-anilinonaphthalene-8-sulfonic acid (ANS), which is known to bind and fluoresce selectively in the b' domain of PDI.<sup>49</sup> As expected, **BAP2** and active analogues hindered the ability of ANS to fluoresce at 370 nm, whereas **PACMA31**, which binds in the active site of PDI, and inactive **BAP2** analogues (**8** and **29**) did not hinder dye fluorescence (Figure IV-15). Compound **59** is active against the H256A mutant, but competes with ANS for the b' domain, further suggesting a complex binding mode. It is possible that **59** inhibits PDI by binding in between the a' and b' domains or binds in both sites. To address the potential role of thiol-dependent inhibition, we tested the **BAP2** analogues after competition with N-acetyl cysteine (NAC). As a positive control, the activity of **PACMA31** was significantly abolished after competition with NAC (Figure IV-15). Activity of **BAP2** and **68** were unaffected by up to 5 mM NAC. Activity of **46** and **59** was abolished by 5 mM NAC, but not by lower concentrations, suggesting they may be attacked by the thiol groups on the cysteine active sites. For compound **59**, this is further confirmed by the fact that activity is not dependent on His256. These results, in combination with the alanine mutation of His256, suggest that analogue **68** binds in the b' domain of PDI to inhibit activity.

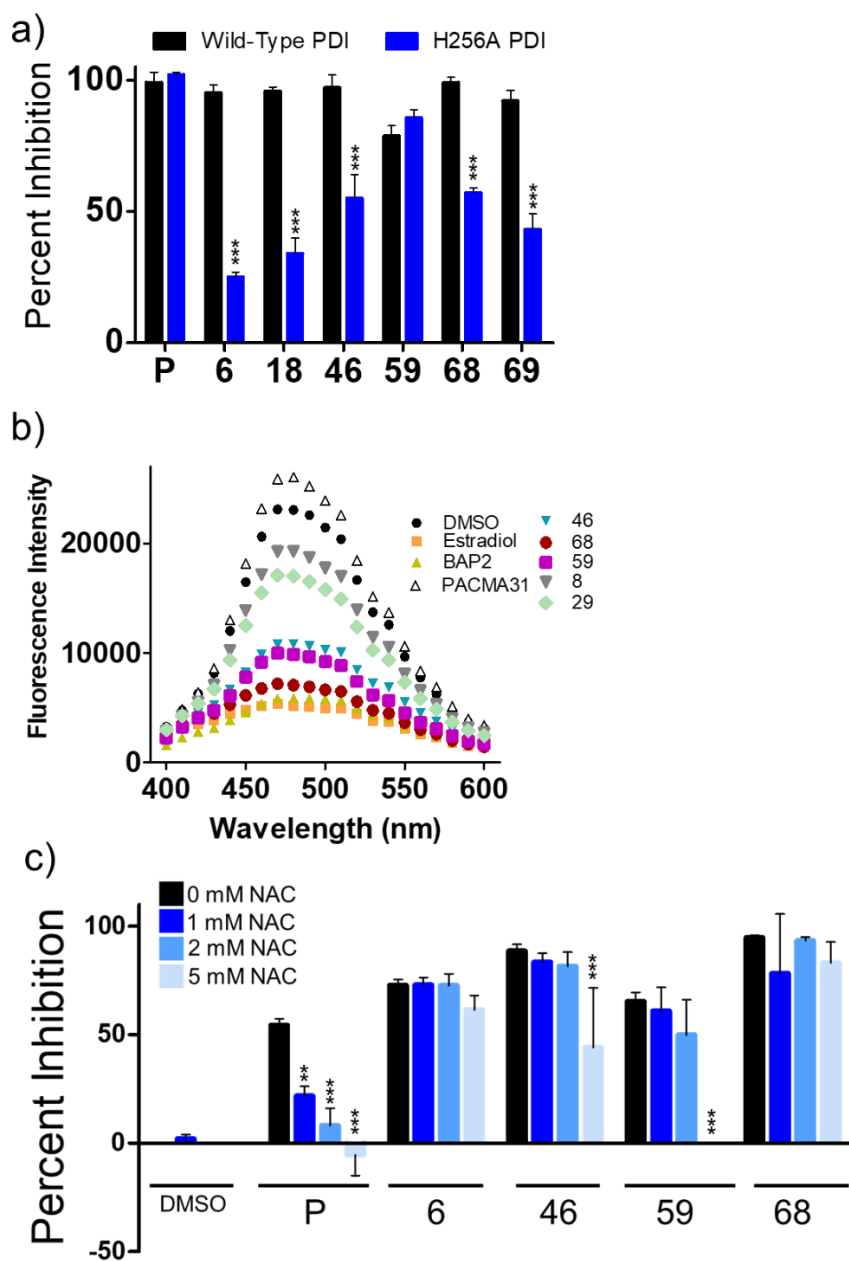


Figure IV-15 **BAP2** analogues interact with the b' domain of PDI. (A) Activity of PDI inhibitors at 10  $\mu$ M (**PACMA31** tested at 30  $\mu$ M) against wild-type and H256A PDI, measured with the PDI reductase assay. Results are reported as mean  $\pm$  standard deviation of three independent experiments. (B) ANS spectral scan with 5  $\mu$ M PDI and 100  $\mu$ M PDI inhibitors (estradiol, **BAP2**, **PACMA31**, **46**, **68**, and **59**) or inactive **BAP2** analogues (**8** and **29**). (C) Activity of PDI inhibitors at 40  $\mu$ M in the presence of indicated concentrations of N-acetyl cysteine (NAC). P: **PACMA31**. DMSO used as a negative control. \*\*:  $p < 0.01$ ; \*\*\*:  $p < 0.001$  compared to wild-type PDI result in the same treatment group. Statistical significance was measured using 2-way analysis of variance (ANOVA).

## BAP2 analogues interact with hydrophobic residues in the b' domain

We hypothesized that **BAP2** derivatives may interact with the b' domain to enhance binding to PDI. This hypothesis is supported by the observation that the replacement of residue His256 with Ala abolishes the activity of **BAP2** and its analogues. Using a computational approach, we docked all **BAP2** analogues into three PDI ligand binding sites, including two catalytic sites as well as the hydrophobic pocket in the b' domain (Figure IV-16). The catalytic sites contain reactive Cys56 and Cys397, where **PACMA31** binds<sup>33</sup>, and the b' domain contains a hydrophobic pocket for substrate recognition. Molecular docking demonstrated that **BAP2** analogues preferentially interact with the b' domain of PDI compared to catalytic sites, supporting the mutagenesis results (Figure IV-16).

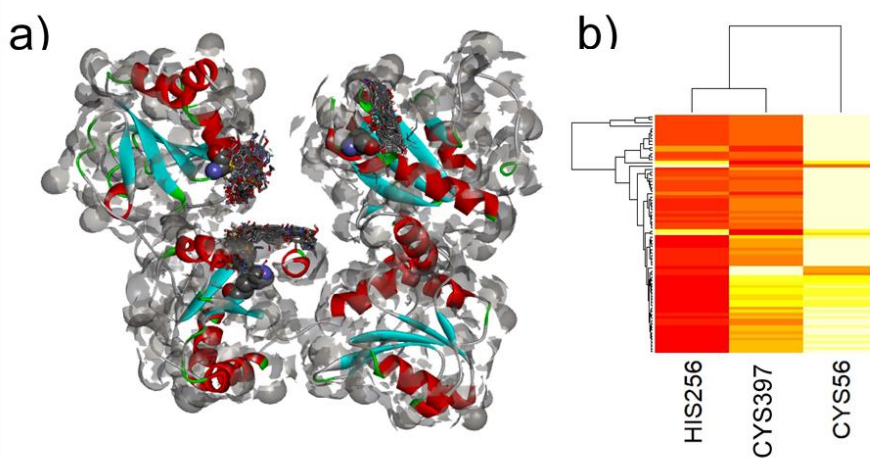


Figure IV-16 **BAP2** analogues interact with the b' domain of PDI. (A) Molecular docking of 68 **BAP2** derivatives into three binding sites of PDIA1 (PDB ID: 4EKZ): Cys56 (Top right), His256 (middle) and Cys397 (top left). (B) Heat map plot for binding affinities of **BAP2** derivatives in three potential binding pockets.

## Discussion

In this study, we report a novel target, PDI, for a series of chalcones, perform an extensive SAR study, determine their activity on human glioblastoma cell lines, and propose their mechanism of action as allosteric inhibitors of the b' domain of PDI. Electron-deficient olefins such as Michael acceptors are susceptible to reactions with nucleophiles, resulting in a covalent bond with threonine and cysteine residues of proteins.<sup>50, 51</sup> For example, **PACMA31**, which was previously discovered as PDI inhibitor, irreversibly inhibits PDI through its propynoic acid amide moiety by covalently binding to cysteine residues in the active site<sup>33</sup>, and this is further supported by the results herein that demonstrate that **PACMA31** inhibition of PDI is challenged by N-acetyl cysteine. We would expect chalcone analogues would also inhibit PDI via Michael addition reaction with the nucleophilic cysteines in the PDI active site because of their olefin structure. However, the activity of **BAP2** and its analogues **46** and **68** is unaffected by NAC. Instead, their ability to inhibit PDI is abolished upon mutation of the key residue, His256, that is responsible for substrate-binding interactions in the b' domain.<sup>35, 52</sup> Furthermore, the stabilizing shift caused by **BAP2** and analogues in the thermal shift assay is also abolished upon H256A mutation, and **BAP2** and analogues compete with ANS for the b' hydrophobic binding pocket of PDI. These results suggest that the b' domain is at least critical for **BAP2** analogue binding. It should be noted that the activity of some **BAP2** analogues, such as **59**, is not His256-dependent, and the electron-withdrawing sulfonamide may activate the olefin for nucleophilic attack., These findings indicate that **BAP2** and analogues primarily use the hydrophobic pocket in the b' domain to inhibit PDI.

When the substituent on ring A is an electron-withdrawing group such as a sulfonamide, the carbonyl may be activated for a Michael addition with the thiols in the PDI active sites. Without an electron-withdrawing group on ring A, the carbonyl is a weak electrophile, and other hydrophobic interactions, such as the hydrogen bond with His256, may play a more important role instead. It remains to be determined whether b' domain-binding analogues such as **BAP2** and **46** also interact reversibly with the active site cysteines. As a whole, the mutagenesis evidence suggests that **BAP2** and analogue **46** inhibit PDI not by attack on the weak Michael acceptor, but by interaction with the hydrophobic binding pocket of PDI. This agrees with the recent findings that chalcones without any substituents on the olefin do not induce Nrf2, possibly because no effective alkylation reaction occurs between the electrophilic chalcone compound and the distinct cysteine residues in Keap1.<sup>53</sup> Finally, although all the tested chalcones contain the Michael accepting site, only few are potent PDI inhibitors. Additionally, the SAR profile of the analogues was not flat, demonstrating that these compounds do not all bind the active site cysteines, but have a more complex binding mode.

Nascent RNA transcription analysis of **BAP2** analogue treatment provided a blueprint of their effect on GBM cell transcription. Cells treated with **BAP2** analogues **18** and **46** demonstrated increased transcription of genes related to the UPR after four hours of treatment. The increased transcription of UPR genes suggests the compounds inhibit PDI in the cells, leading to an increase in the unfolded protein load. This result is consistent with the findings of another research group that treatment with 2'-hydroxy-2,3,5'-trimethoxychalcone induces the UPR in MDA-MB-231 breast cancer cells.<sup>54</sup> Additionally, **BAP2** analogues **18** and **46** decreased transcription of E2F targets. **BAP2** downregulated protein expression of E2F1, and PDI knockdown was linked to

reduced E2F expression.<sup>38</sup> These results provide further target engagement validation and suggest **BAP2** analogues inhibit PDI activity in the cells.

In addition to their role in tumor proliferation, PDI family members are involved in tumor immune recognition. Immune response proteins, such as antibodies, are secretory molecules and require maturation through the ER to be prepared for secretion. Tumors evade immune recognition by “shedding” key immune signal proteins from the tumor cell surface. Neutrophil L-selectin adhesion to lymphocytes is dependent on disulfide bonds. PDI inhibition promotes neutrophil L-selectin shedding, suggesting that PDI promotes signaling for immune pathways to eliminate tumor cells.<sup>55</sup> Furthermore, PDI has been shown to promote antibody production and the humoral immune response in GM-CSF-secreting cancer cells.<sup>56</sup> However, ERp5 is necessary for shedding of the soluble major histocompatibility complex class-I-related ligand MICA, and thus allows the tumor to evade the immune response.<sup>57</sup> ERp5, along with ADAM10 (a disintegrin and metalloproteinase 10), were also found to block the anti-tumor immune response in classic Hodgkin’s lymphoma by shedding NKG2D (natural killer group 2D) receptor ligands.<sup>58</sup> Thus, the increase in transcription of MHC-related genes that we observe upon treatment with **BAP2** analogues may be a response to MHC complex degradation. Clearly, thiol-based redox reactions play a key role in regulating the humoral immune response; however, the precise role of PDI in each pathway remains to be defined.

In summary, we explored the structure of **BAP2** by modifying the substituents around ring A and ring B and identified potent analogues that may be promising treatment strategies for GBM. We identified five compounds that were more potent and cytotoxic than the lead **BAP2**, as well as

compounds that induced ER stress and inhibited GBM cell migration and MMP9 expression. Especially, the analogues **18** and **46** induced genes involved in the UPR and decreased expression of E2F target genes, validating PDI inhibition in the cells. Additionally, we demonstrated the therapeutic window afforded with the derivatives and the potential for combination with As<sub>2</sub>O<sub>3</sub>. Furthermore, preliminary results suggest that the interaction between the compounds and PDI may rely on more than a nucleophilic attack with the Michael acceptor region of the compound, and hydrophobic interaction in the b' domain of PDI may play the most significant role. Further structural studies are needed to confirm the binding pose of the **BAP2** analogues. Our data demonstrate that PDI inhibitors should be tested in combination with other targeted agents as well as cytotoxic chemotherapy to deliver significant beneficial effects.

### Experimental section

**Cell Culture.** The human cell lines, U87MG, A172, and NU04 (ATCC, Manassas, VA), were obtained in 2013 and were maintained in RPMI-1640 or DMEM (Thermo Fisher Scientific, Waltham, MA) with 10 % fetal bovine serum (Thermo Fisher Scientific, Waltham, MA). Cells were grown as monolayer cultures at 37 °C in a humidified atmosphere of 5 % CO<sub>2</sub> and tested for *Mycoplasma* contamination with the *Mycoplasma* detection kit, Plasmotest (InvivoGen, San Diego, California). All cell lines were authenticated with STR DNA profiling (University of Michigan, Michigan) and matched to reference profiles from the ATCC database.

**PDI Protein Purification.** PDI for this project was purified as reported in **Chapter 3**. PDI wild-type, C53S/C397S, and H256A expression and purification were performed as previously described with slight modifications.<sup>9,14</sup>



**Measurement of PDI Activity and Competition With N-Acetyl Cysteine.** PDI activity was assessed by measuring the PDI-catalyzed reduction of insulin as previously described.<sup>17</sup> In brief, recombinant PDI protein (0.4  $\mu$ M) was incubated with indicated compounds at 37 °C for 1 hour in sodium phosphate buffer (100 mM sodium phosphate, 2 mM EDTA, 8  $\mu$ M DTT, pH 7.0). For the PDI reductase assay containing H256A PDI, the compounds were tested at 10  $\mu$ M. A mixture of sodium phosphate buffer, DTT (500  $\mu$ M), and bovine insulin (130  $\mu$ M; Gemini BioProducts, West Sacramento, CA) was added to the incubated PDI protein. The reduction reaction was catalyzed by PDI at room temperature, and the resulting aggregation of reduced insulin B chains was measured at 620 nm. PDI activity was calculated with the formula, PDI activity (%) =  $[(OD_{T80[PDI+DTT+compound]} - OD_{T0[PDI+DTT+compound]}) - (OD_{T80[DTT]} - OD_{T0[DTT]})] / [(OD_{T80[PDI+DTT]} - OD_{T0[PDI+DTT]}) - (OD_{T80[DTT]} - OD_{T0[DTT]})] \times 100$  ( $OD_{T0}$  and  $OD_{T80}$  were the absorbance values at 0 min and 80 min after the reduction reaction, respectively).

To assess the effect of NAC on compound activity, compounds were pre-treated with NAC for 30 min at 37 °C. The compound:NAC complexes were added to the PDI reductase assay as described above to a final concentration of 40  $\mu$ M and 0, 1, 2, or 5 mM NAC.

**Thermal Shift Assay.** Thermal shift of purified PDI (0.5 mg/mL in 50 mM Tris, pH 7.0) in the presence or absence of 100  $\mu$ M compound was determined as described.<sup>18</sup> Briefly, 5  $\mu$ l PBS, 2  $\mu$ L PDI, 1  $\mu$ L ligand in 100% DMSO, 2.5  $\mu$ L 8X ROX dye (from Protein Thermal Shift Dye Kit, Thermo Fisher Scientific), and water to 20  $\mu$ L, were dispensed in each well of a 384-well microplate. DMSO (5 % in buffer) was used as control. The plate was heated at a temperature range from 25 to 99 °C at 1°C/minute in the QuantStudio 6 Flex Real-Time PCR System (Thermo

Fisher Scientific), and melt curves were analyzed with the Protein Thermal Shift software (Thermo Fisher Scientific).

**Growth Inhibition Assay.** Cell growth inhibition was assessed by MTT assay as previously described in **Chapter 3**.<sup>61</sup> Cells were seeded in 96-well plates at 4000 cells/well (A172, NU04) or 5000 cells/well (U87MG).

**Colony Formation Assay.** U87MG cells were seeded in 96-well plates at 200 cells/well. After overnight incubation at 37 °C and 5 % CO<sub>2</sub>, cells were treated with indicated compounds for 24 hours. The media was removed and replaced with fresh media, and the cells were incubated ten days at 37 °C and 5 % CO<sub>2</sub>. Media was then removed, and crystal violet solution was added (50 µL) for 30 min. Crystal violet was removed, and cells were washed twice with water and imaged with the Odyssey imaging system (LI-COR Biosciences).

**Western Blot Analysis.** For ER stress analysis, 0.5 x 10<sup>6</sup> U87MG cells/well in 6-well plates were treated with 20 µM chalcone analogues, 1 µM **PACMA31**, or DMSO for 24 hours to assess changes in GRP78 expression. As a positive control, cells were treated with 10 µg/mL tunicamycin for 2 or 24 hours before cells were harvested. For EIF2α phosphorylation analysis, cells were treated with 1 µM **PACMA31** or 20 µM **6, 18, 46, 59, 68, or 69** for 2 hours. Cells were harvested with a lysis buffer (25 mM tris(hydroxymethyl)aminomethane, 150 mM NaCl, 17 mM Triton X-100, 3.5 mM SDS, pH 7.4), lysed via sonication, and spun in a centrifuge at 13,500g at 4 °C for 10 min. Supernatant was collected, and protein concentration determined with the BCA assay (Thermo Fisher Scientific). Samples were prepared with 30 µg protein and loaded onto 10 % acrylamide (Bio-Rad, Hercules, CA) gels. Protein was electrotransferred to methanol-activated

immobilon-FL PVDF membranes (EMD Millipore, La Jolla, CA). Membranes were blocked for 1 hour with Odyssey blocking buffer (LI-COR Biosciences). Membranes were probed for proteins using primary antibodies (PDI, Cell Signaling, Danvers, MA, 1:4000; GRP78, Cell Signaling, Danvers, MA, 1:2000; pEIF2 $\alpha$ , Cell Signaling, 1:200; EIF2 $\alpha$ , Cell Signaling, 1:200; actin, Santa Cruz, 1:3000; MMP2, Cell Signaling, 1:1000; MMP9, Cell Signaling, 1:1000; p-FAK, Cell Signaling, 1:1000; FAK, Cell Signaling, 1:1000) overnight at 4 °C. Membranes were incubated with secondary antibodies (anti-rabbit, Cell Signaling, 1:7500, or anti-mouse, Cell Signaling, 1:5000) and fluorescence was imaged with the Odyssey imaging system (LI-COR Biosciences).

**Gelatin Zymography.** U87MG cells were seeded at  $0.5 \times 10^6$  cells/well in 6-well plates and allowed to attach overnight. Cells were serum-starved for 12 hours prior to designated treatment with chalcone analogues for 24 hours. Conditioned media was collected, cleared, and mixed with 5X SDS loading buffer, and 5  $\mu$ g of protein was subjected to electrophoresis on a 10% SDS-PAGE gel containing 0.1% gelatin. After electrophoresis, the gels were washed in washing buffer (50 mM Tris HCl, 5 mM CaCl<sub>2</sub>, 1  $\mu$ M ZnCl<sub>2</sub>, 2.5 % Triton X-100) twice for 30 min each time, then washed for 5 min in incubation buffer (50 mM Tris HCl, 5 mM CaCl<sub>2</sub>, 1  $\mu$ M ZnCl<sub>2</sub>, 1.0 % Triton X-100). Incubation buffer was replaced, and the gels were incubated overnight at 37 °C to allow for digestion of the gelatin. The gelatinolytic activity of MMPs was visualized by staining the gels with 0.5% Coomassie blue R-250 in 45 % methanol and 10 % acetic acid for 1 hour. The gels were destained with 45 % methanol and 10 % acetic acid until clear bands appeared. Gels were imaged with the Odyssey imaging system (LI-COR Biosciences).

**Wound Healing Assay.** A172 cells were seeded in 12-well plates at 50,000 cells/well. After overnight incubation at 37 °C and 5 % CO<sub>2</sub>, media was replaced with serum-free DMEM and the cells were incubated another 24 hours. A scratch was made in each well, and compounds were added at indicated concentrations in media containing 10 % FBS. Cells were allowed to grow for 24 hours, until the scratch in the negative control wells containing DMSO closed. Cells were stained with Giemsa stain (Sigma Aldrich) and imaged with the Olympus IX83 inverted microscope at 10X magnification.

**Transwell Migration Assay.** The transwell migration assay was performed with BioCoat Control Inserts with 8.0 µm PET membrane (Corning, Corning, NY). 1 x 10<sup>5</sup> A172 cells were treated with indicated compounds and seeded into inserts containing serum-free medium. 500 µL DMEM with 10 % FBS was added to the bottom of each well. The cells were incubated for 4 hours and stained with the Giemsa stain. The stained cells were imaged with the Olympus IX83 inverted microscope at 10X magnification.

**Bromouridine RNA Sequencing (Bru-seq).** Bru-seq was performed as previously described.<sup>59</sup> U87MG cells were treated with DMSO, **18** (10 µM), or **46** (16 µM) for 4 hours. 2 mM Bru was added in the last 30 min of treatment. Cells were collected, and total RNA was isolated with TRIzol reagent. Bru-labeled RNA was captured from total RNA by incubation with anti-BrdU antibodies (BD Biosciences) conjugated to magnetic beads (Dynabeads, goat anti-mouse IgG; Invitrogen). Bru-containing RNA population was isolated and sequenced. Sequencing reads were mapped to the hg19 reference genome. Pre-ranked gene lists were generated for each treatment ranking genes

by fold change in transcription compared to control. Sequencing results were filtered using cutoff value of gene size > 300 bp and mean RPKM > 0.5.

The datasets were interrogated with Gene Set Enrichment Analysis (GSEA).<sup>60</sup> A pre-ranked gene list of 7,749 genes was analyzed for gene enrichment using GSEA gene sets based on the Kolmogorov-Smirnov statistic. For each gene set, an enrichment score (ES) was normalized to account for the difference in gene set size, and a false discovery rate (FDR) was calculated based on the normalized enrichment score (NES) values.

The datasets were also interrogated with Connectivity Map (CMap, <https://www.broadinstitute.org/connectivity-map-cmap>). Bru-seq gene sets were used with a cutoff of  $\geq 2$ -fold change in transcription. Some genes were omitted from analysis because they had no connection in CMap.

**Proteomics with Tandem Mass Tag Multiplexing.** U87MG cells were seeded and allowed to attach overnight. Cells were treated with DMSO, 20  $\mu$ M **BAP2** or 20  $\mu$ M **18**. Cells were washed three times in DPBS and suspended in RIPA buffer. Proteomics experiment and analysis performed by the Mass Spectrometry-Based Proteomics Resource Facility in the Department of Pathology at the University of Michigan with the TMTsixplex™ Isobaric Label Reagent Set (Thermo Fisher). The abundance ratio datasets were transformed to  $\log_2(\text{fold change})$  values and interrogated with GSEA.

**Protein Identification and Relative Quantitation by TMT labeling and LC-Tandem MS.** Tandem Mass Tag (TMT) labeling was performed using the TMT-6plex™ isobaric labeling kit (ThermoFisher Scientific, catalogue no. 90061) according to the manufacturer's protocol with

minor modifications. Briefly, 75 µg of protein from each sample was reduced with DTT (5 mM) at 45 °C for 1 h followed by alkylation with 2-chloroacetamide (15 mM) at room temperature for 30 min. Proteins were precipitated by adding 6 volumes of ice cold acetone and incubating overnight at -20 °C. Precipitated proteins were pelleted by centrifuging at 8000g for 10 min at 4 °C and supernatant was discarded. The pellet was resuspended in 100 µL of 100 mM TEAB and digested overnight at 37 °C by adding 1.5 µg of sequencing grade, modified porcine trypsin (Promega, V5113). TMT reagents were reconstituted in 41 µL of anhydrous acetonitrile and digested peptides were transferred to the TMT reagent vial and incubated at room temperature for 1 h. The reaction was quenched by adding 8 µL of 5 % hydroxylamine and incubating it for further 15 min. The samples were combined and dried.

Prior to MS analysis, two-dimensional separation of the samples was performed. For the first dimension, an offline fractionation of an aliquot each sample mix (200 µg) using high pH reverse phase fractionation kit into 10 fractions was performed following the manufacturer's protocol (Pierce, catalogue no. 84868). Fractions were dried and reconstituted in 12 µL of loading buffer (0.1 % formic acid and 2 % acetonitrile).

**Liquid chromatography-mass spectrometry analysis (LC-MultiNotch MS3).** The MultiNotch-MS3 method was employed.<sup>61</sup> Orbitrap Fusion (Thermo Fisher Scientific) and RSLC Ultimate 3000 Nano-UPLC (Dionex) were used to acquire the data. Two µM of each fraction was resolved in the second dimension on a nano-capillary reverse phase column (Acclaim PepMap C18, 2 µm, 75 µm i.d. x 50 cm, ThermoScientific) using a 0.1% formic/acetonitrile gradient at 300 nl/min (2-22% acetonitrile in 150 min; 22-32% acetonitrile in 40 min; 20 min wash at 90% followed by 50 min re-equilibration) and directly sprayed on to Orbitrap Fusion using EasySpray

source (ThermoFisher Scientific). Mass spectrometer was set to collect one MS1 scan (Orbitrap; 120K resolution; AGC target  $2 \times 10^5$ ; max IT 100 ms) followed by data-dependent, “Top Speed” (3 seconds) MS2 scans (collision induced dissociation; ion trap; NCD 35; AGC  $5 \times 10^3$ ; max IT 100 ms). For multinotch-MS3, top 10 precursors from each MS2 were fragmented by HCD followed by Orbitrap analysis (NCE 55; 60K resolution; AGC  $5 \times 10^4$ ; max IT 120 ms, 100-500 m/z scan range).

Proteome Discoverer (v2.1; Thermo Fisher) was used for data analysis. MS2 spectra were searched against SwissProt human protein database (release 2015-11-11; 42084 sequences) using the following search parameters: MS1 and MS2 tolerance were set to 10 ppm and 0.6 Da, respectively; carbamidomethylation of cysteines (57.02146 Da) and TMT labeling of lysine and N-termini of peptides (229.16293 Da) were considered static modifications; oxidation of methionine (15.9949 Da) and deamidation of asparagine and glutamine (0.98401 Da) were considered variable. Identified proteins and peptides were filtered to retain only those that passed  $\leq 1\%$  FDR threshold. Quantitation was performed using high-quality MS3 spectra (average signal-to-noise ratio of 6 and  $< 40\%$  isolation interference).

**1-Anilinonaphthalene-8-sulfonic Acid (ANS) Spectral Scan.** The ANS spectral scan was performed as previously described.<sup>49</sup> Briefly, 5  $\mu\text{M}$  PDI was incubated in the presence 100  $\mu\text{M}$  compounds or equivalent DMSO concentration in 50  $\mu\text{L}$  of TBS at 37 °C for 1 hour. Subsequently, 50 mM ANS was added and the mixture was incubated in the dark at 25 °C for 20 min. Fluorescence spectrum (Ex, 370 nm, Em, 400–700 nm) was measured in a 384-well plate.

**Clonogenic Assay.** D54 cells were irradiated with 0, 1, 2, 4, or 6 Gy and immediately plated in 6-well plates at 200, 200, 400, 600, and 1000 cells/well, respectively. Cells were treated with DMSO, 0.05  $\mu\text{M}$  **PACMA31**, 1  $\mu\text{M}$  **BAP2**, 1  $\mu\text{M}$  **59**, or 1  $\mu\text{M}$  **68** and incubated for 10-12 days before colonies were stained using 0.1% crystal violet solution.

**Molecular Docking.** Molecular docking of **BAP2** derivatives on PDI was performed in the two catalytic sites and the hydrophobic binding site using a crystal structure of PDI (Protein Data Bank 4EKZ). In three separate docking studies, all analogues were docked into the three binding sites using Autodock Vina.<sup>62</sup> The structures of the **BAP2** derivatives were optimized using steepest descent geometry optimization with the MMFF94 force field and PyRx tool.

AutoDock (version 1.5.6; Molecular Graphics Laboratory, La Jolla, CA, USA) was used to prepare the input pdbqt file by merging nonpolar hydrogen atoms of PDI and calculating Gasteiger charges. Docking was conducted by defining the SG atom in Cys56 and Cys397 and NE1 in His256 as the center of the grid box for the catalytic and hydrophobic sites, respectively. The grid cavity size was set to  $15 \times 15 \times 15$  in the dimensions of x, y and z using 0.375 Å spacing. The 2D and 3D diagrams for receptor-ligand interactions were plotted using Discovery Studio Visualizer v17.2.0.16349.

**Statistics.** The 50 % inhibitory concentration values ( $\text{IC}_{50}$ ) were determined by analyzing the log of the concentration–response curves by nonlinear regression analysis using GraphPad Prism (version 5). Biochemical and cell culture experiments were performed at least three separate times unless otherwise noted. Bru-seq and proteomics experiments were performed once.





## **Notes to Chapter V**

All synthesis was performed by Suhui Yang, Dan Lu, and Ziwei Liu. I would like to acknowledge the following people who contributed to the work presented in this chapter. Kirin Cromer, Kelly Torolski, Amina Tanweer, Fah Koranant, Pantira Khonlumb, Trey Feldstein, Hannah Driks, and Ding Xue helped generating data for the manuscript, and their help is greatly appreciated. The expression vector of recombinant human PDI was a generous gift from Dr. Lloyd W. Ruddock (University of Oulu, Oulu, Finland). We are grateful for the University of Michigan Proteomics & Peptide Synthesis Core for performing the proteomics experiments and analyzing the results. We would also like to thank the University of Michigan DNA Sequencing Core. This work was supported in part by a grant from the NIH (CA193690).

## References

1. Larsson, O.; Zetterberg, A.; Engstrom, W. Cell-cycle-specific induction of quiescence achieved by limited inhibition of protein synthesis: Counteractive effect of addition of purified growth factors. *J Cell Sci* **1985**, *73*, 375-87.
2. Kim, I.; Xu, W.; Reed, J. C. Cell death and endoplasmic reticulum stress: Disease relevance and therapeutic opportunities. *Nat Rev Drug Discov* **2008**, *7*, 1013-30.
3. Luo, B.; Lee, A. S. The critical roles of endoplasmic reticulum chaperones and unfolded protein response in tumorigenesis and anticancer therapies. *Oncogene* **2013**, *32*, 805-18.
4. Xu, S. L.; Sankar, S.; Neamati, N. Protein disulfide isomerase: A promising target for cancer therapy. *Drug Discov Today* **2014**, *19*, 222-40.
5. Shergalis, A.; Neamati, N. Protein disulfide isomerase. In *Encyclopedia of Signaling Molecules*, Choi, S., Ed. Springer New York: 2016; pp 1-12.
6. Wang, C.; Li, W.; Ren, J.; Fang, J.; Ke, H.; Gong, W.; Feng, W.; Wang, C. C. Structural insights into the redox-regulated dynamic conformations of human protein disulfide isomerase. *Antioxid Redox Signal* **2013**, *19*, 36-45.
7. Tian, R.; Li, S. J.; Wang, D. L.; Zhao, Z.; Liu, Y.; He, R. Q. The acidic C-terminal domain stabilizes the chaperone function of protein disulfide isomerase. *J Biol Chem* **2004**, *279*, 48830-5.
8. Sun, S.; Lee, D.; Ho, A. S.; Pu, J. K.; Zhang, X. Q.; Lee, N. P.; Day, P. J.; Lui, W. M.; Fung, C. F.; Leung, G. K. Inhibition of prolyl 4-hydroxylase, beta polypeptide (P4HB) attenuates temozolomide resistance in malignant glioma via the endoplasmic reticulum stress response (ERSR) pathways. *Neuro Oncol* **2013**, *15*, 562-77.
9. Eirich, J.; Braig, S.; Schyschka, L.; Servatius, P.; Hoffmann, J.; Hecht, S.; Fulda, S.; Zahler, S.; Antes, I.; Kazmaier, U.; Sieber, S. A.; Vollmar, A. M. A small molecule inhibits protein disulfide isomerase and triggers the chemosensitization of cancer cells. *Angew Chem Intl Ed Engl* **2014**, *53*, 12960-5.
10. Lovat, P. E.; Corazzari, M.; Armstrong, J. L.; Martin, S.; Pagliarini, V.; Hill, D.; Brown, A. M.; Piacentini, M.; Birch-Machin, M. A.; Redfern, C. P. Increasing melanoma cell death using inhibitors of protein disulfide isomerases to abrogate survival responses to endoplasmic reticulum stress. *Cancer Res* **2008**, *68*, 5363-9.

11. Vatolin, S.; Phillips, J. G.; Jha, B. K.; Govindgari, S.; Hu, J.; Grabowski, D.; Parker, Y.; Lindner, D. J.; Zhong, F.; Distelhorst, C. W.; Smith, M. R.; Cotta, C.; Xu, Y.; Chilakala, S.; Kuang, R. R.; Tall, S.; Reu, F. J. Novel protein disulfide isomerase inhibitor with anticancer activity in multiple myeloma. *Cancer Res* **2016**, *76*, 3340-50.
12. Goplen, D.; Wang, J.; Enger, P. O.; Tysnes, B. B.; Terzis, A. J.; Laerum, O. D.; Bjerkvig, R. Protein disulfide isomerase expression is related to the invasive properties of malignant glioma. *Cancer Res* **2006**, *66*, 9895-902.
13. Wen, P. Y.; Cloughesy, T. F.; Olivero, A.; Lu, X.; Mueller, L.; Coimbra, A. F.; Gerstner, E. R.; Ahnert, J. R. A first-in-human phase 1 study to evaluate the brain-penetrant PI3K/mTOR inhibitor GDC-0084 in patients with progressive or recurrent high-grade glioma. *J Clin Oncol* **2016**, *34*, 2012-2012.
14. Xu, S.; Liu, Y.; Yang, K.; Wang, H.; Shergalis, A.; Kyani, A.; Bankhead, A., 3rd; Tamura, S.; Yang, S.; Wang, X.; Wang, C. C.; Rehemtulla, A.; Ljungman, M.; Neamati, N. Inhibition of protein disulfide isomerase in glioblastoma causes marked downregulation of DNA repair and DNA damage response genes. *Theranostics* **2019**, *9*, 2282-98.
15. Zhuang, C.; Zhang, W.; Sheng, C.; Zhang, W.; Xing, C.; Miao, Z. Chalcone: A privileged structure in medicinal chemistry. *Chem Rev* **2017**, *117*, 7762-810.
16. Higuchi, K.; Watanabe, T.; Tanigawa, T.; Tominaga, K.; Fujiwara, Y.; Arakawa, T. Sofalcone, a gastroprotective drug, promotes gastric ulcer healing following eradication therapy for *Helicobacter pylori*: A randomized controlled comparative trial with cimetidine, an H<sub>2</sub>-receptor antagonist. *J Gastroenterol Hepatol* **2010**, *25* Suppl 1, S155-160.
17. Shibuya, A.; Onda, K.; Kawahara, H.; Uchiyama, Y.; Nakayama, H.; Omi, T.; Nagaoka, M.; Matsui, H.; Hirano, T. Sofalcone, a gastric mucosa protective agent, increases vascular endothelial growth factor via the Nrf2-heme-oxygenase-1 dependent pathway in gastric epithelial cells. *Biochem Biophys Res Commun* **2010**, *398*, 581-4.
18. Yang, Z.; Yang, J.; Jia, Y.; Tian, Y.; Wen, A. Pharmacokinetic properties of hydroxysafflor yellow A in healthy Chinese female volunteers. *J Ethnopharmacol* **2009**, *124*, 635-8.
19. Syam, S.; Abdelwahab, S. I.; Al-Mamary, M. A.; Mohan, S. Synthesis of chalcones with anticancer activities. *Molecules* **2012**, *17*, 6179-95.
20. Nielsen, S. F.; Christensen, S. B.; Cruciani, G.; Kharazmi, A.; Liljefors, T. Antileishmanial chalcones: Statistical design, synthesis, and three-dimensional quantitative structure-activity relationship analysis. *J Med Chem* **1998**, *41*, 4819-32.
21. Bu, X. Y.; Li, Y. L. Synthesis of exiguaflavanone K and (+/-)-leachianone G. *J Nat Prod* **1996**, *59*, 968-9.

22. Choi, J. W.; Jang, B. K.; Cho, N. C.; Park, J. H.; Yeon, S. K.; Ju, E. J.; Lee, Y. S.; Han, G.; Pae, A. N.; Kim, D. J.; Park, K. D. Synthesis of a series of unsaturated ketone derivatives as selective and reversible monoamine oxidase inhibitors. *Bioorg Med Chem* **2015**, *23*, 6486-96.
23. Palleros, D. R. Solvent-free synthesis of chalcones. *J Chem Educ* **2004**, *81*, 1345-7.
24. Calloway, N. O.; Green, L. D. Reactions in the presence of metallic halides I beta-unsaturated ketone formation as a side reaction in Friedel-Crafts acylations. *J Am Chem Soc* **1937**, *59*, 809-11.
25. Sipos, G.; Sirokman, F. Chalcon formation of different substituted acetophenones and *p*-hydroxy-benzaldehyde. *Nature* **1964**, *202*, 489.
26. Narender, T.; Reddy, K. P. A simple and highly efficient method for the synthesis of chalcones by using borontrifluoride-etherate. *Tetrahedron Lett* **2007**, *48*, 3177-80.
27. Hara, H.; Ikeda, R.; Ninomiya, M.; Kamiya, T.; Koketsu, M.; Adachi, T. Newly synthesized 'hidabeni' chalcone derivatives potently suppress LPS-induced NO production via inhibition of STAT1, but not NF-kappaB, JNK, and p38, pathways in microglia. *Biol Pharm Bull* **2014**, *37*, 1042-9.
28. Hara, H.; Nakamura, Y.; Ninomiya, M.; Mochizuki, R.; Kamiya, T.; Aizenman, E.; Koketsu, M.; Adachi, T. Inhibitory effects of chalcone glycosides isolated from *Brassica rapa* L. 'hidabeni' and their synthetic derivatives on LPS-induced NO production in microglia. *Bioorg Med Chem* **2011**, *19*, 5559-68.
29. Narender, T.; Venkateswarlu, K.; Nayak, B. V.; Sarkar, S. A new chemical access for 3'-acetyl-4'-hydroxychalcones using borontrifluoride-etherate via a regioselective Claisen-Schmidt condensation and its application in the synthesis of chalcone hybrids. *Tetrahedron Lett* **2011**, *52*, 5794-8.
30. Meltzer, P. C.; Butler, D.; Deschamps, J. R.; Madras, B. K. 1-(4-Methylphenyl)-2-pyrrolidin-1-yl-pentan-1-one (Pyrovalerone) analogues: A promising class of monoamine uptake inhibitors. *J Med Chem* **2006**, *49*, 1420-32.
31. Liao, W. W.; Muller, T. J. J. Sequential coupling-isomerization-coupling reactions - A novel three-component synthesis of aryl chalcones. *Synlett* **2006**, 3469-73.
32. Mazzotti, A. R.; Campbell, M. G.; Tang, P.; Murphy, J. M.; Ritter, T. Palladium(III)-catalyzed fluorination of arylboronic acid derivatives. *J Am Chem Soc* **2013**, *135*, 14012-5.
33. Xu, S.; Butkevich, A. N.; Yamada, R.; Zhou, Y.; Debnath, B.; Duncan, R.; Zandi, E.; Petasis, N. A.; Neamati, N. Discovery of an orally active small-molecule irreversible inhibitor of protein disulfide isomerase for ovarian cancer treatment. *Proc Natl Acad Sci U S A* **2012**, *109*, 16348-53.

34. Khan, M. M.; Simizu, S.; Lai, N. S.; Kawatani, M.; Shimizu, T.; Osada, H. Discovery of a small molecule PDI inhibitor that inhibits reduction of HIV-1 envelope glycoprotein gp120. *ACS Chem Biol* **2011**, *6*, 245-51.
35. Fu, X. M.; Wang, P.; Zhu, B. T. Characterization of the estradiol-binding site structure of human pancreas-specific protein disulfide isomerase: Indispensable role of the hydrogen bond between His278 and the estradiol 3-hydroxyl group. *Biochemistry* **2011**, *50*, 106-15.
36. Hetz, C.; Chevet, E.; Harding, H. P. Targeting the unfolded protein response in disease. *Nat Rev Drug Discov* **2013**, *12*, 703-19.
37. Li, S.; Li, C.; Ryu, H. H.; Lim, S. H.; Jang, W. Y.; Jung, S. Bacitracin inhibits the migration of U87-MG glioma cells via interferences of the integrin outside-in signaling pathway. *J Korean Neurosurg Soc* **2016**, *59*, 106-16.
38. Liu, Y.; Ji, W.; Shergalis, A.; Xu, J.; Delaney, A. M.; Calcaterra, A.; Pal, A.; Ljungman, M.; Neamati, N.; Rehemtulla, A. Activation of the unfolded protein response via inhibition of protein disulfide isomerase decreases the capacity for DNA repair to sensitize glioblastoma to radiotherapy. *Cancer Res* **2019**, *79*, 2923-32.
39. Martianov, I.; Ramadass, A.; Serra Barros, A.; Chow, N.; Akoulitchev, A. Repression of the human dihydrofolate reductase gene by a non-coding interfering transcript. *Nature* **2007**, *445*, 666-70.
40. Liu, S.; Mitra, R.; Zhao, M. M.; Fan, W.; Eischen, C. M.; Yin, F.; Zhao, Z. The potential roles of long noncoding RNAs (lncRNA) in glioblastoma development. *Molecular Cancer Therapeutics* **2016**, *15*, 2977-86.
41. Johnson, G. S.; Li, J.; Beaver, L. M.; Dashwood, W. M.; Sun, D.; Rajendran, P.; Williams, D. E.; Ho, E.; Dashwood, R. H. A functional pseudogene, NMRAL2P, is regulated by Nrf2 and serves as a coactivator of NQO1 in sulforaphane-treated colon cancer cells. *Molecular Nutrition & Food Research* **2017**, *61*, 1600769.
42. Lee, S. O.; Cho, K.; Cho, S.; Kim, I.; Oh, C.; Ahn, K. Protein disulphide isomerase is required for signal peptide peptidase-mediated protein degradation. *EMBO J* **2010**, *29*, 363-75.
43. Kim, Y.; Kang, K.; Kim, I.; Lee, Y. J.; Oh, C.; Ryoo, J.; Jeong, E.; Ahn, K. Molecular mechanisms of MHC class I-antigen processing: Redox considerations. *Antioxid Redox Signal* **2009**, *11*, 907-36.
44. Park, B.; Lee, S.; Kim, E.; Cho, K.; Riddell, S. R.; Cho, S.; Ahn, K. Redox regulation facilitates optimal peptide selection by MHC class I during antigen processing. *Cell* **2006**, *127*, 369-82.

45. Farmery, M. R.; Allen, S.; Allen, A. J.; Bulleid, N. J. The role of ERp57 in disulfide bond formation during the assembly of major histocompatibility complex class I in a synchronized semipermeabilized cell translation system. *J Biol Chem* **2000**, *275*, 14933-8.
46. Larochette, N.; Decaudin, D.; Jacotot, E.; Brenner, C.; Marzo, I.; Susin, S. A.; Zamzami, N.; Xie, Z. H.; Reed, J.; Kroemer, G. Arsenite induces apoptosis via a direct effect on the mitochondrial permeability transition pore. *Experimental Cell Research* **1999**, *249*, 413-421.
47. Chung, W. H.; Sung, B. H.; Kim, S. S.; Rhim, H.; Kuh, H. J. Synergistic interaction between tetra-arsenic oxide and paclitaxel in human cancer cells in vitro. *Int J Oncol* **2009**, *34*, 1669-79.
48. Ashton, J. C. Drug combination studies and their synergy quantification using the Chou-Talalay method-Letter. *Cancer Res* **2015**, *75*, 2400.
49. Bekendam, R. H.; Bendapudi, P. K.; Lin, L.; Nag, P. P.; Pu, J.; Kennedy, D. R.; Feldenzer, A.; Chiu, J.; Cook, K. M.; Furie, B.; Huang, M.; Hogg, P. J.; Flaumenhaft, R. A substrate-driven allosteric switch that enhances PDI catalytic activity. *Nat Commun* **2016**, *7*, 12579.
50. Lee, C. U.; Grossmann, T. N. Reversible covalent inhibition of a protein target. *Angew Chem Intl Ed Engl* **2012**, *51*, 8699-700.
51. Gersch, M.; Kreuzer, J.; Sieber, S. A. Electrophilic natural products and their biological targets. *Natural Product Reports* **2012**, *29*, 659-82.
52. Yagi-Utsumi, M.; Satoh, T.; Kato, K. Structural basis of redox-dependent substrate binding of protein disulfide isomerase. *Sci Rep* **2015**, *5*, 13909.
53. Rucker, H.; Al-Rifai, N.; Rasche, A.; Gottfried, E.; Brodziak-Jarosz, L.; Gerhauser, C.; Dick, T. P.; Amslinger, S. Enhancing the anti-inflammatory activity of chalcones by tuning the Michael acceptor site. *Organic & biomolecular chemistry* **2015**, *13*, 3040-7.
54. Lee, D. H.; Jung, Y. J.; Koh, D.; Lim, Y.; Lee, Y. H.; Shin, S. Y. A synthetic chalcone, 2'-hydroxy-2,3,5'-trimethoxychalcone triggers unfolded protein response-mediated apoptosis in breast cancer cells. *Cancer Letters* **2016**, *372*, 1-9.
55. Bennett, T. A.; Edwards, B. S.; Sklar, L. A.; Rogelj, S. Sulfhydryl regulation of L-selectin shedding: Phenylarsine oxide promotes activation-independent L-selectin shedding from leukocytes. *J Immunol* **2000**, *164*, 4120-9.
56. Fonseca, C.; Soiffer, R.; Ho, V.; Vanneman, M.; Jinushi, M.; Ritz, J.; Neuberg, D.; Stone, R.; DeAngelo, D.; Dranoff, G. Protein disulfide isomerases are antibody targets during immune-mediated tumor destruction. *Blood* **2009**, *113*, 1681-8.

57. Kaiser, B. K.; Yim, D.; Chow, I. T.; Gonzalez, S.; Dai, Z.; Mann, H. H.; Strong, R. K.; Groh, V.; Spies, T. Disulphide-isomerase-enabled shedding of tumour-associated NKG2D ligands. *Nature* **2007**, 447, 482-6.
58. Zocchi, M. R.; Catellani, S.; Canevali, P.; Tavella, S.; Garuti, A.; Villaggio, B.; Zunino, A.; Gobbi, M.; Fraternali-Orcioni, G.; Kunkl, A.; Ravetti, J. L.; Boero, S.; Musso, A.; Poggi, A. High ERp5/ADAM10 expression in lymph node microenvironment and impaired NKG2D ligands recognition in Hodgkin lymphomas. *Blood* **2012**, 119, 1479-89.
59. Paulsen, M. T.; Veloso, A.; Prasad, J.; Bedi, K.; Ljungman, E. A.; Tsan, Y. C.; Chang, C. W.; Tarrier, B.; Washburn, J. G.; Lyons, R.; Robinson, D. R.; Kumar-Sinha, C.; Wilson, T. E.; Ljungman, M. Coordinated regulation of synthesis and stability of RNA during the acute TNF-induced proinflammatory response. *Proc Natl Acad Sci U S A* **2013**, 110, 2240-5.
60. Subramanian, A.; Tamayo, P.; Mootha, V. K.; Mukherjee, S.; Ebert, B. L.; Gillette, M. A.; Paulovich, A.; Pomeroy, S. L.; Golub, T. R.; Lander, E. S.; Mesirov, J. P. Gene set enrichment analysis: A knowledge-based approach for interpreting genome-wide expression profiles. *Proc Natl Acad Sci U S A* **2005**, 102, 15545-50.
61. McAlister, G. C.; Nusinow, D. P.; Jedrychowski, M. P.; Wuhr, M.; Huttlin, E. L.; Erickson, B. K.; Rad, R.; Haas, W.; Gygi, S. P. MultiNotch MS3 enables accurate, sensitive, and multiplexed detection of differential expression across cancer cell line proteomes. *Analytical Chemistry* **2014**, 86, 7150-8.
62. Trott, O.; Olson, A. J. AutoDock Vina: Improving the speed and accuracy of docking with a new scoring function, efficient optimization, and multithreading. *J Comput Chem* **2010**, 31, 455-61.



## CHAPTER V

### Characterization of Alpha-Aminobenzylphenol Analogues in Glioblastoma Cell Lines

#### Introduction<sup>5</sup>

GBM cells survive by upregulating the protein folding oxidoreductase protein disulfide isomerase (PDIA1, also known as PDI). PDI reduces, oxidizes, and isomerizes disulfide bonds in nascent polypeptides and other substrates via two catalytic CGHC active sites that sit 15-30 Å apart in two homogenous domains.<sup>1</sup> PDI is overexpressed in several cancers to meet the increased demands in protein synthesis.<sup>2-4</sup> **PACMA31**, an irreversible inhibitor of PDI, demonstrated *in vivo* efficacy in a mouse model of ovarian cancer.<sup>5</sup> Furthermore, **PACMA31** exhibited synergy with the multi-kinase inhibitor sorafenib in a mouse model of hepatocellular carcinoma.<sup>6</sup>

The **a** and **a'** domains of PDI are connected by **b** and **b'** domains, which share identity with the **a** and **a'** domains, but do not contain the CGHC active sites. As evidenced by the pK<sub>a</sub> values, the N-terminal cysteine in each **a** and **a'** domain active site (Cys53 and Cys397) is stabilized in the thiolate form, while the C-terminal cysteine thiolate is destabilized. This allows the nucleophilic N-terminal cysteines to attack substrates and form mixed disulfides. The C-terminal cysteines

---

<sup>5</sup> **Author contributions:** Ding Xue synthesized all compounds and prepared Tables V-6, V-7, and V-8. Hannah Driks generated data for Figure V-6F, Figure V-8, and Figure V-10. Kirin Cromer generated data for Figure V-10, V-11, and V-14A. Amina Tanweer helped generate IC<sub>50</sub> values for **AS15** analogues and data for Figure V-6G and V-15.

more selectively react with the N-terminal cysteines, mediated in the **a** domain by the pK<sub>a</sub> of Cys56 that is lowered by the local environment, containing a conserved Arg120.<sup>7</sup> This reaction generates a reduced substrate and oxidized state of PDI.

The thiolate form of the redox active N-terminal cysteines reacts with electrophilic compounds. Thus, many electrophilic compounds have been identified as covalent PDI inhibitors, including **PACMA31**<sup>5</sup>, **KSC-34**<sup>8</sup>, 3,4-methylenedioxy- $\beta$ -nitrostyrene (MNS)<sup>9</sup>, and **16F16**<sup>10</sup> (Figure V-1). One of the main challenges of characterizing the many PDI inhibitors identified to date, only recently emphasized by Foster, et al., is competition with endogenous levels of glutathione.<sup>11</sup> Active site PDI inhibitors, especially reactive electrophiles such as **PACMA31**, may compete with glutathione for binding the cysteine thiols of PDI. This strategy is further confounded by the fact that numerous PDI family members share similar active site motifs, and although the CGHC active site is one of the most reactive of the thioredoxin superfamily, electrophiles that bind this site may also bind to other CxxC-containing PDI family members. To address this characteristic, we assessed whether the PDI inhibitors retained activity in the presence of competing glutathione and used BODIPY-labeled probes to validate target engagement.

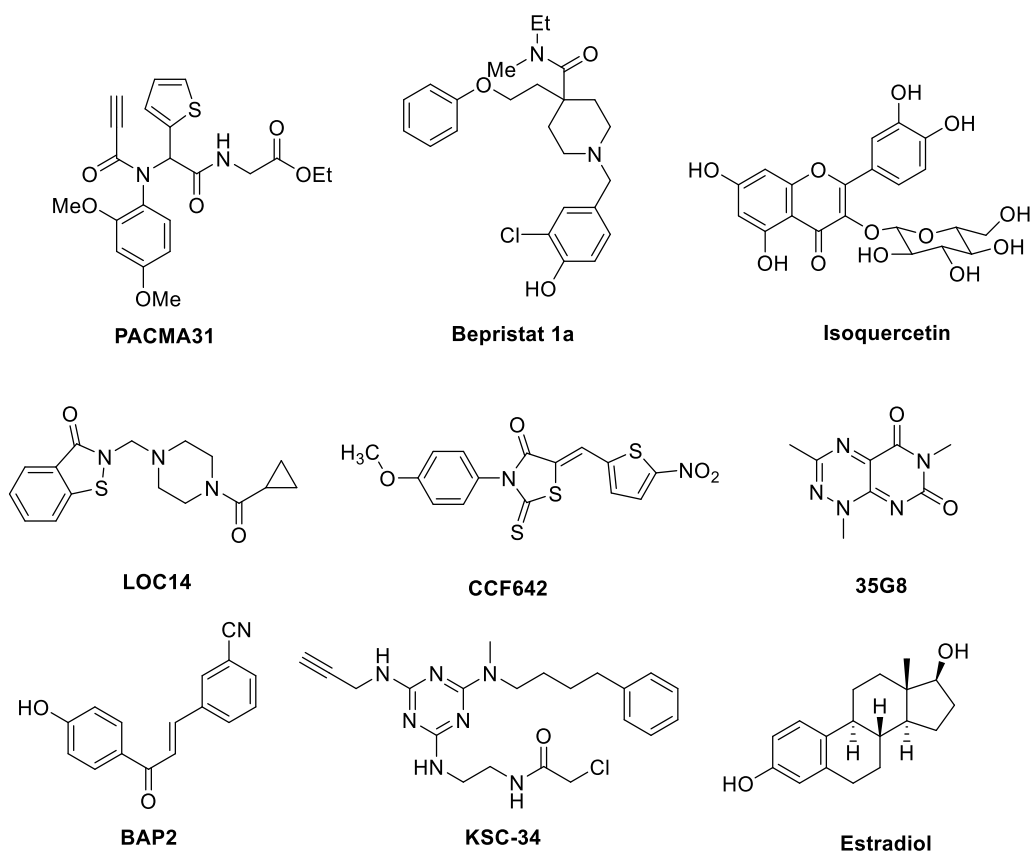


Figure V-1 Previously reported PDI inhibitors studied in the context of ovarian cancer (**PACMA31**), Huntington's disease (**LOC14**), brain cancer (**BAP2** and **35G8**), thrombosis (**Bepristat 1a** and **isoquercetin**), and multiple myeloma (**CCF642**). **KSC-34** is an a-site selective probe and estradiol is an endogenous ligand of PDIA1.

In addition to upregulated PDI expression, glioblastoma cells upregulate the antioxidant defense system and are increasingly dependent on glutathione as the tumor grows.<sup>12</sup> Glutathione is one of the most abundant molecules in the cell, with concentrations of reduced glutathione (GSH) estimated to reach up to 10 mM in cellular compartments. The tripeptide composed of glutamic acid, glycine, and cysteine is a key redox buffer and antioxidant molecule involved in many cellular processes including reactive oxygen species removal, signal transduction, and protein synthesis.<sup>13</sup> Although the total glutathione concentration is similar in the cytosol and

endoplasmic reticulum, the ratio of reduced to oxidized glutathione dictates its role in each compartment. In the cytosol, glutathione is present mainly in its reduced form, with a ratio of GSH:GSSG of ~50,000:1; the ER is a more oxidizing compartment, with an estimated GSH:GSSG ratio of less than 7:1.<sup>14</sup> The oxidizing environment of the ER aids in protein folding and specifically disulfide bond formation.

The initial goal of this study was to characterize a new class of PDI inhibitors in the context of glioblastoma. Via a medium-throughput biochemical screen, we identified a series of  $\alpha$ -aminobenzylphenols as inhibitors of PDI that likely target the active site cysteines of PDI via a retro-Michael addition reaction. Similar compounds have been reported for multiple targets, including HDACs<sup>15</sup>, MIF tautomerase<sup>16-19</sup>, STAT3/5<sup>20</sup>, and frataxin<sup>21</sup>, among others. Furthermore, we synthesized two BODIPY-labeled analogues that covalently bound at least two proteins in the cell lysate. In addition, cytotoxicity was enhanced when the cells were pre-treated with BSO. Thus, the compounds are cell-permeable; however, they may target other thiol-containing proteins in the cell. Further optimization to consider these compounds as selective PDI inhibitors in the cells is warranted. In all, this study represents the importance of validating in-cell target engagement early in the drug discovery process and provides extensive characterization of a class of cysteine-reactive small molecules.

## Results

**Lead Compound AS15 Is a Nanomolar Inhibitor of PDI.** A screening campaign of 1000 highly diverse compounds from the National Cancer Institute at 40  $\mu$ M in the PDI reductase assay

afforded almost 200 compounds that inhibited 50% of PDI activity (Figure V-2). Those compounds were screened for cytotoxicity in U87MG and MiaPaCa-2 cell lines, and compounds with > 40% inhibition of cell growth at 30  $\mu$ M were subjected to dose response assays in both the MTT assay and PDI reductase assays. **AS15** and **CD343** emerged as lead scaffolds with  $IC_{50}$  values in the PDI reductase assay of  $300 \pm 90$  nM and  $150 \pm 40$  nM, respectively (Figure V-2). When a residue in the **b'** domain of PDI important for substrate binding, Histidine 256, was mutated to an alanine residue, both **AS15** and **CD343** retained their activity (Figure V-3). **AS15** inhibited activity of PDIp and ERp57 (Figure V-3). Interestingly, **CD343** demonstrated selectivity for PDI, was relatively inactive against PDIp, and inactive up to 40  $\mu$ M against ERp57. The lead compounds decreased viability of U87MG cells with  $IC_{50}$  values of  $18.3 \pm 9.2$   $\mu$ M for **AS15** and  $10.6 \pm 0.7$   $\mu$ M for **CD343** (Figure V-3). Interaction with PDI was further probed with the thermal shift assay; however, **AS15** and **CD343** did not stabilize PDI to thermal degradation, similar to **PACMA31**. These initial results suggested that the compounds inhibit PDI by binding to the active site cysteines, and not in the substrate-binding domain like estradiol or **BAP2**.<sup>22, 23</sup>

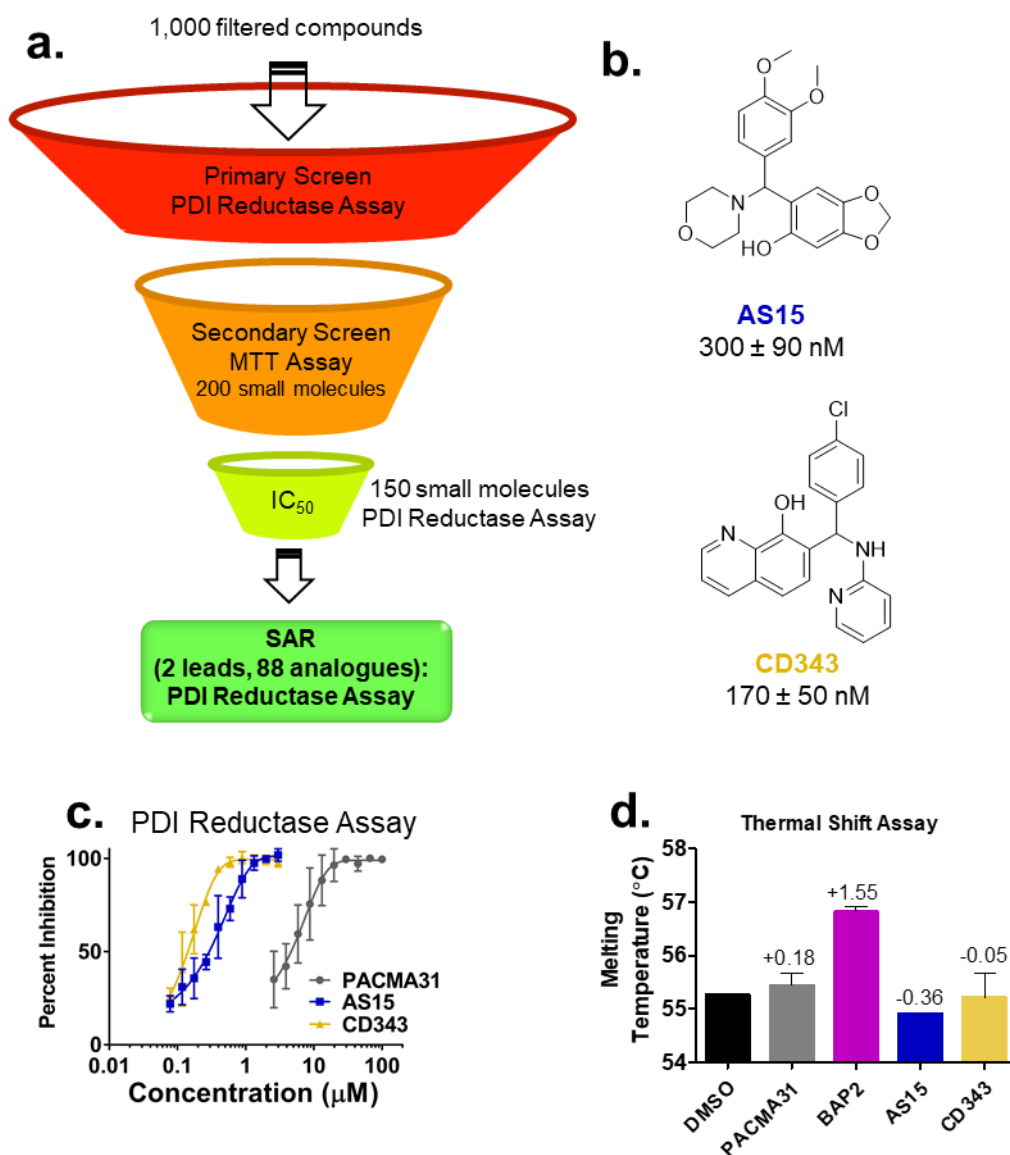


Figure V-2 Discovery and characterization of **AS15** and **CD343**. (A) Discovery funnel. (B) Structures of **AS15** and **CD343**, and IC<sub>50</sub> values calculated in the PDI reductase assay. (C) Dose-response curves of **PACMA31**, **AS15**, and **CD343** in the PDI reductase assay. (D) Thermal melt curves of **PACMA31**, **AS15**, and **CD343** in the thermal shift assay. SAR: structure-activity relationship.

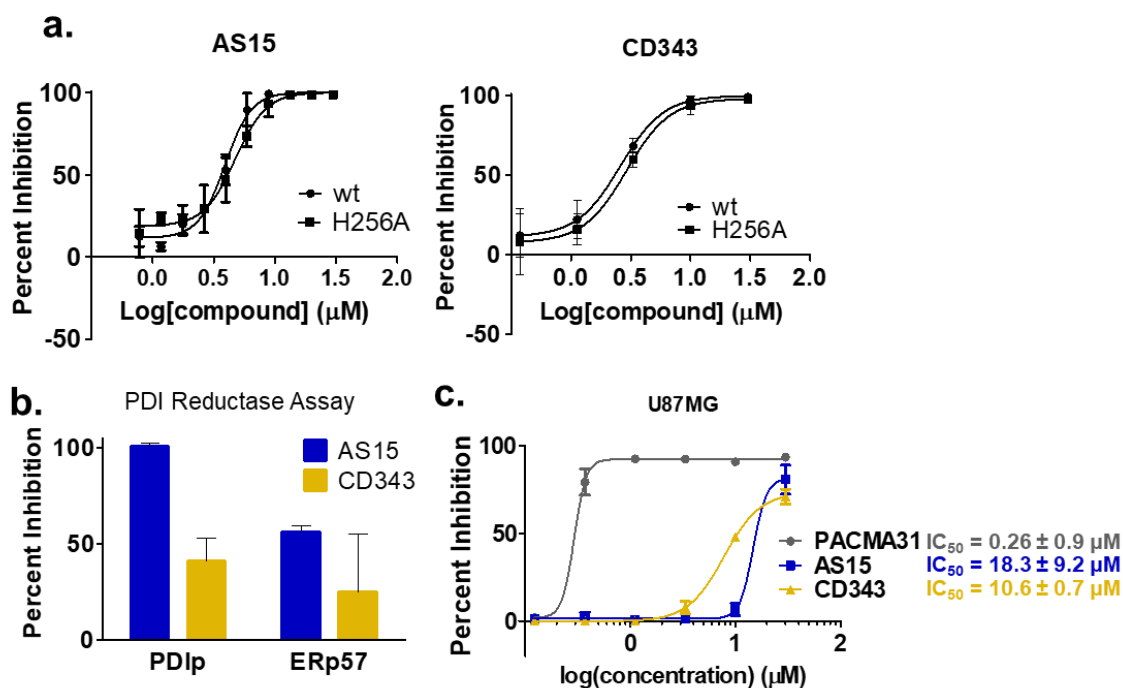


Figure V-3 **AS15** selectivity for PDIA1 (A) Activity of **AS15** and **CD343** against wild-type PDIA1 (wt) and H256A mutant PDIA1 (H256A) in the PDI reductase assay (B) Activity of **AS15** and **CD343** at 40  $\mu\text{M}$  against PDIp and ERp57 in the PDI reductase assay (C) Dose response curves of PDI inhibitors in the MTT assay against U87MG cells. Cells were treated with compounds for 72 hours before cell viability was measured.

**Structure-Activity Relationships Reveal AS15 Analogues Are Not Substrate-Binding Domain Inhibitors.** To further assess the mechanism of inhibition of **AS15** and **CD343** and determine the structural requirements for their activity, we obtained 89 analogues from Chem Div libraries and the NCI Cancer Therapeutics program and tested their potency in the PDI reductase assay (Table V-1; Table V-2; Table V-3; Table V-4). Compounds were tested for purity, and only compounds with purity > 95 % were used for structure-activity relationship analysis. Generally, all **AS15** and **CD343** analogues possess an  $\alpha$ -aminobenzylphenol core that has a 2-phenol, amino and phenyl moiety attached to a center tertiary carbon (Figure V-4). We kept the 5-

hydroxybenzo[*d*][1,3]dioxole (**AS15** analogues) or 8-hydroxyquinoline (**CD343** analogues) moiety consistent as the phenolic moiety and explored more diverse structures in the amino and phenyl moieties. For compounds with 5-hydroxybenzo[*d*][1,3]dioxole moiety, a variety of cyclic amines like morpholine, piperidine, piperazine and pyrrolidine were incorporated. Most of the compounds inhibited PDI with IC<sub>50</sub> values below 1 μM, and different halogens and electron donating groups such as chloro, fluoro, methoxy, amino and hydroxy were well-tolerated. Some of those compounds showed moderate cytotoxicity with IC<sub>50</sub> values of 10-30 μM; however, correlation with PDI inhibition was not well observed (Table V-1). Aromatic amines such as aminopyridine, aminopyrimidine and imidazole were generally accepted, and PDI inhibition was comparable to those with saturated cyclic amines. Ureas were not tolerated, and lead to a complete loss of activity, possibly because the basicity contributes to PDI binding (Table V-2). Compounds without the bicyclic aromatic core or hydroxy group were inactive against PDI and non-toxic (Figure V-5). Furthermore, compounds without the tertiary amine were inactive against PDI and were non-toxic, with the exception of compounds containing the tri-methoxy substituent on the aromatic ring (Table V-5). The **CD** series compounds possess the 8-hydroxyquinoline core along with aromatic amines such as 2-aminopyridines and anilines, and inhibition of PDI was comparable to the **AS15** analogues, except that the 4-methyl substitution of the pyridine was not compatible when methyl or chloro was present on the phenyl moiety. Interestingly, many of these compounds showed stronger cytotoxicity with IC<sub>50</sub> values as low as 2.1 ± 0.1 μM.



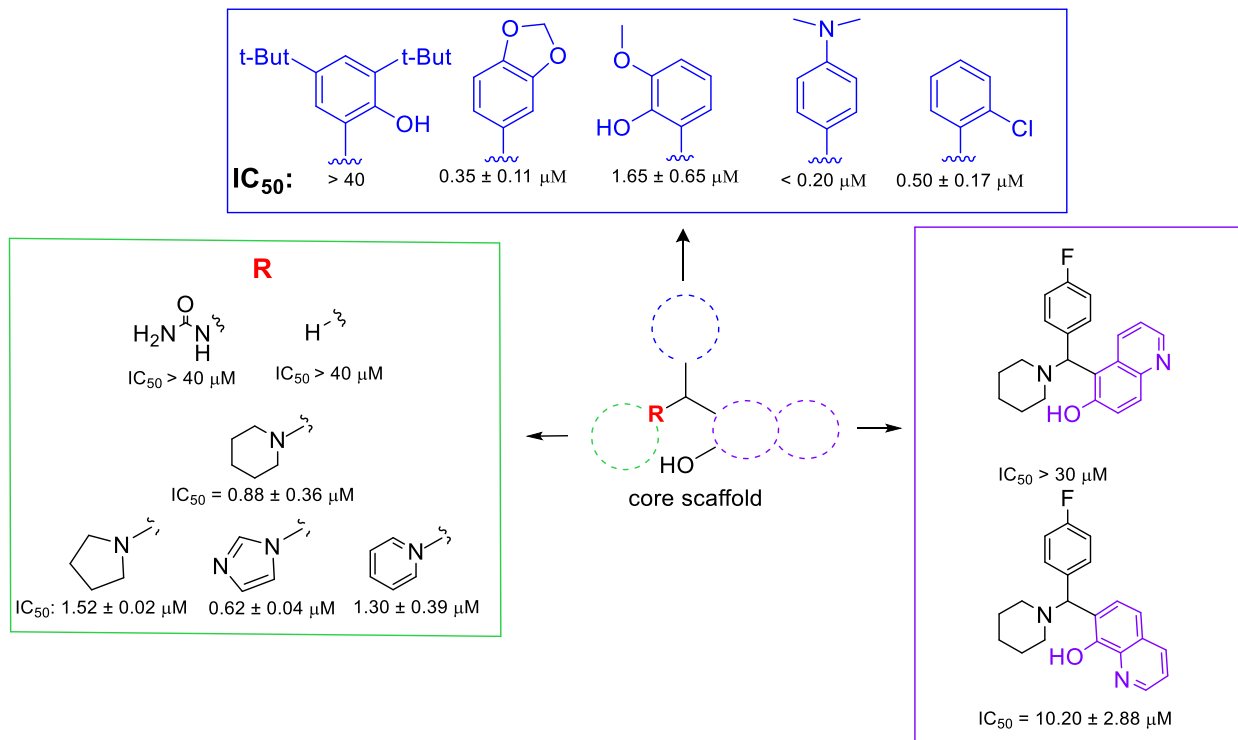
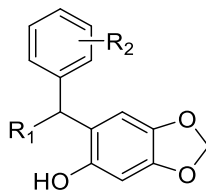

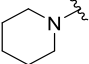
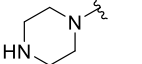
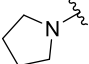


Figure V-4 Structure-activity relationship analysis of AS15 analogues in the PDI reductase assay.

Table V-1 SAR of compounds with 5-hydroxybenzo[d][1,3]dioxole and saturated cyclic amine moieties

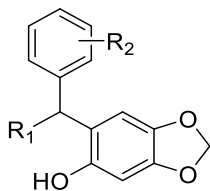


Compound	NSC Number	R <sub>1</sub>	R <sub>2</sub>	PDI IC <sub>50</sub>	MTT IC <sub>50</sub>
				( $\mu$ M) <sup>a</sup>	( $\mu$ M) <sup>b</sup>
AS15/NC014	368252		3,4-di-OCH <sub>3</sub>	0.30 ± 0.09	18.3 ± 9.2
NC016	368260		3,4,5-tri-OCH <sub>3</sub>	0.64 ± 0.31	> 10
NC133	381577		2,4,6-tri-OCH <sub>3</sub>	0.98 ± 0.30	13.6 ± 1.7
NC107	368248		3,4-OCH <sub>2</sub> O-	< 0.2	> 30
NC108	368256		2-OH, 3-OCH <sub>3</sub>	0.90 ± 0.75	> 10
NC110	368261		3-OCH <sub>3</sub> , 4-OH	0.23 ± 0.11	27.1 ± 2.4
NC161	364724		4-OCH <sub>3</sub>	0.13 ± 0.06	> 10
NC134	381579		2-OCH <sub>3</sub>	0.33 ± 0.05	27.7 ± 2.7
NC115	368275		4-Cl	0.092 ± 0.023	> 30
NC117	368277		4-F	0.23 ± 0.06	> 30
NC141	667921		2-OH	0.34 ± 0.09	> 30
NC018	368267	—————	3,4-di-OCH <sub>3</sub>	0.96 ± 1.08	24.8 ± 1.2

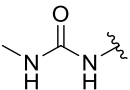
<b>NC015</b>	368253		3, 4, 5-tri-OCH <sub>3</sub>	0.70 ± 0.13	> 10
<b>NC022</b>	368274		4-OCH <sub>3</sub>	0.88 ± 0.36	28.3 ± 1.6
<b>NC020</b>	368273		4-N(CH <sub>3</sub> ) <sub>2</sub>	1.27 ± 0.34	24.7 ± 2.4
<b>NC024</b>	370278		2,4-di-OCH <sub>3</sub>	2.59 ± 1.84	> 30
<b>NC162</b>	368254		3,4-OCH <sub>2</sub> O-	0.35 ± 0.11	> 10
<b>NC116</b>	368276		4-F	0.27 ± 0.04	> 30
<b>NC120</b>	369090		4-OH	0.68 ± 0.35	> 30
<b>NC025</b>	370279		2,4-di-OCH <sub>3</sub>	0.36 ± 0.05	> 30
<b>NC026</b>	370281		4-OCH <sub>3</sub>	1.52 ± 0.02	22.6 ± 5.9
<b>NC027</b>	370283		4-N(CH <sub>3</sub> ) <sub>2</sub>	< 0.20	> 30
<b>NC028</b>	370285		2-OH, 3-OCH <sub>3</sub>	1.65 ± 0.65	> 10
<b>NC122</b>	370280		4-F	< 0.20	> 30
<b>NC123</b>	370282		3,4-OCH <sub>2</sub> O-	0.023 ± 0.017	> 30
<b>NC124</b>	370284		3,4,5-tri-OCH <sub>3</sub>	0.18 ± 0.02	24.2 ± 7.1

<sup>a</sup>Inhibition of PDI was assessed by PDI reductase assay. IC<sub>50</sub> values are indicated as the mean ± SD (standard deviation) of at least three independent experiments. <sup>b</sup>MTT cytotoxicity IC<sub>50</sub> values were determined in U87MG cells.

Table V-2 SAR of compounds with 5-hydroxy benzo[d][1,3]dioxole and other amine moieties



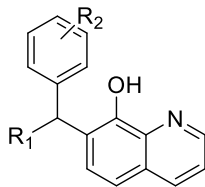
Compound	NSC Number	R <sub>1</sub>	R <sub>2</sub>	PDI IC <sub>50</sub> (μM) <sup>a</sup>	MTT IC <sub>50</sub> (μM) <sup>b</sup>
NC163	368255		3,4-OCH <sub>2</sub> O-	0.072 ± 0.017	> 10
NC300	368281		3,5-di-OCH <sub>3</sub> , 4-OH	0.17 ± 0.04	> 10
NC017	368265		3,4-OCH <sub>2</sub> O-	1.18 ± 0.11	> 10
NC019	368270		4-OCH <sub>3</sub>	1.30 ± 0.39	> 10
NC165	368268		2-OH, 3-OCH <sub>3</sub>	9.02 ± 4.61	> 10
NC299	368279		3,5-di-OCH <sub>3</sub> , 4-OH	2.20 ± 0.53	> 10
NC166	368278		4-F	12.72 ± 3.47	> 10
NC118	368280		4-F	0.67 ± 0.14	> 10
NC119	369087		4-OCH <sub>3</sub>	0.62 ± 0.04	> 10
NC023	-		4-OH	> 40	> 10
NC029	371006		3,4-OCH <sub>2</sub> O-	> 40	> 10

<b>NC030</b>	371007		3,4,5-tri-OCH <sub>3</sub>	> 40	> 10
<b>NC168</b>	371005		4-F	> 30	> 10

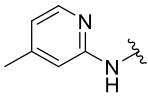
---

<sup>a</sup>Inhibition of PDI was assessed by PDI reductase assay. IC<sub>50</sub> values are indicated as the mean ± SD (standard deviation) of at least three independent experiments. <sup>b</sup>MTT cytotoxicity IC<sub>50</sub> values were determined in U87MG cells.

Table V-3 SAR of compounds with 8-hydroxyquinoline and 2-aminopyridine moieties

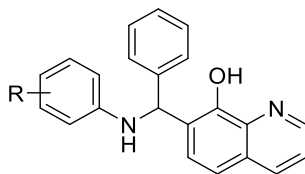


Compound	NSC Number	R <sub>1</sub>	R <sub>2</sub>	PDI IC <sub>50</sub>	MTT IC <sub>50</sub>
				( $\mu$ M) <sup>a</sup>	( $\mu$ M) <sup>b</sup>
CD528	G856-2528		3,5-di-OCH <sub>3</sub> , 4-OH	0.18 ± 0.06	7.4 ± 1.2
CD343	4896-2958	—————	4-Cl	0.17 ± 0.05	10.6 ± 0.7
CD345	4896-3004		2,6-di-Cl	1.89 ± 0.31	6.9 ± 1.6
CD639	7706-0076		2-Cl	0.50 ± 0.17	9.4 ± 0.6
CD611	4896-3086		4-CH <sub>3</sub>	0.46 ± 0.07	> 10
CD344	4896-3003		4-CH <sub>2</sub> CH <sub>3</sub>	0.17 ± 0.12	9.3 ± 5.9
CD346	4896-3082		2,5-di-CH <sub>3</sub>	0.73 ± 0.12	13.8 ± 5.9
CD355	4896-4013		2,4,6-tri-CH <sub>3</sub>	0.19 ± 0.09	10 ± 0.6
CD638	4896-3084		3-OCH <sub>3</sub>	2.86 ± 2.37	11.9 ± 0.4
CD626	G856-2546		2-F	0.47 ± 0.17	> 10
CD613	5994-0466		2-Cl, 3-OH	0.37 ± 0.03	> 10

<b>NC272</b>	1014	_____	-	< 0.20	> 10
<b>CD354</b>	4896-4000		2-CH <sub>3</sub>	> 40	> 10
<b>CD361</b>	5994-0131		2,5-di-CH <sub>3</sub>	> 40	> 10
<b>CD350</b>	4896-3501		4-F	0.14 ± 0.06	> 10
<b>CD377</b>	7706-0074		2-F	0.88 ± 0.23	13.1 ± 3.5
<b>CD341</b>	4896-0018		2-F, 6-Cl	> 40	20.6 ± 7.8
<b>CD373</b>	7033-0321		3-F	0.35 ± 0.07	9.2 ± 0.4
<b>CD348</b>	4896-3250		2-Cl	> 40	9.9 ± 1.4
<b>CD349</b>	4896-3254		2,6-di-Cl	> 40	7.2 ± 2.2
<b>CD352</b>	4896-3773		4-OBn	0.62 ± 0.29	9.3 ± 0.9
<b>CD362</b>	5994-0331		4-CH <sub>2</sub> CH <sub>3</sub>	5.39 ± 0.68	8.9 ± 2.2
<b>CD601</b>	G856-2531		4-CF <sub>3</sub>	26.50 ± 19.15	2.1 ± 0.1
<b>CD363</b>	5994-0397		4-NO <sub>2</sub>	0.53 ± 0.15	3.4 ± 0.6
<b>CD594</b>	5704-0657		3-OH, 4-OCH <sub>3</sub>	0.15 ± 0.02	> 10

<sup>a</sup>Inhibition of PDI was assessed by PDI reductase assay. IC<sub>50</sub> values are indicated as the mean ± SD (standard deviation) of at least three independent experiments. <sup>b</sup>MTT cytotoxicity IC<sub>50</sub> values were determined in U87MG cells.

Table V-4 SAR of compounds with 8-hydroxyquinoline and aniline moieties



Compound	NSC Number	R	PDI IC <sub>50</sub>	MTT IC <sub>50</sub>
			( $\mu\text{M}$ ) <sup>a</sup>	( $\mu\text{M}$ ) <sup>b</sup>
NC266	1008	-	0.11 ± 0.04	> 10
NC268	1010	4-NO <sub>2</sub>	0.15 ± 0.05	> 10
NC269	1011	4-COOH	0.30 ± 0.05	> 10
NC270	1012	2-COOH	1.48 ± 1.52	> 10
NC273	1015	2-COOC <sub>2</sub> H <sub>5</sub>	< 0.20	> 10
NC282	84087	2-OCH <sub>3</sub>	0.39 ± 0.11	> 10

<sup>a</sup>Inhibition of PDI was assessed by PDI reductase assay. IC<sub>50</sub> values are indicated as the mean ± SD (standard deviation) of at least three independent experiments. <sup>b</sup>MTT cytotoxicity IC<sub>50</sub> values were determined in U87MG cells.



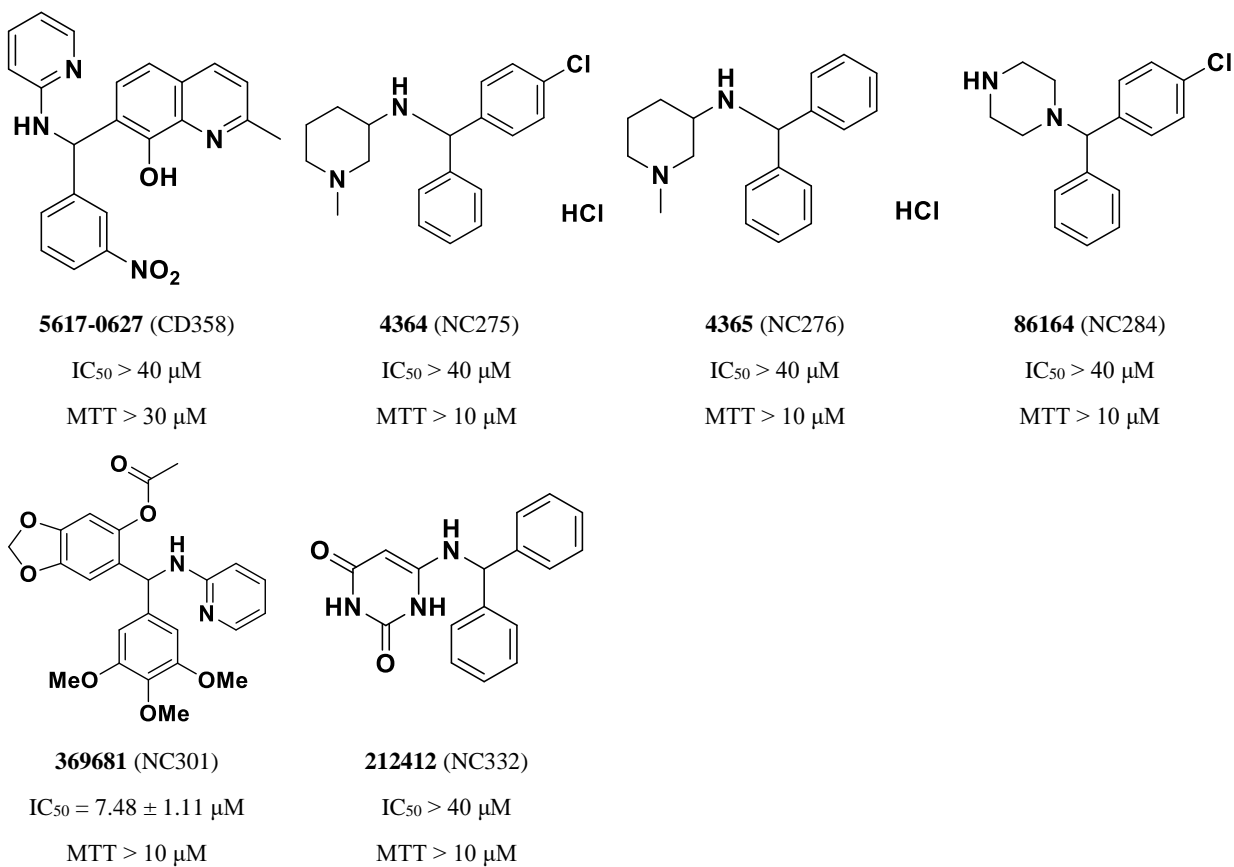
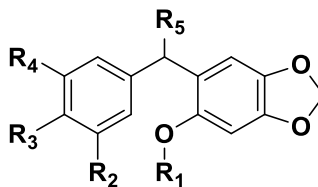


Figure V-5 Activity of additional **AS15** analogues in the PDI reductase assay (IC<sub>50</sub>) and MTT assay (in U87MG cells).

Table V-5 SAR of compounds lacking the tertiary amine



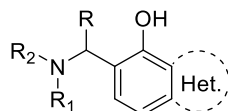
NSC		R1	R2	R3	R4	R5	PDI IC <sub>50</sub>	MTT IC <sub>50</sub>
Number	( $\mu\text{M}$ ) <sup>a</sup>						( $\mu\text{M}$ ) <sup>b</sup>	
NC002	269128	-H	-H	-OMe	-H	-H	> 40	> 10
NC003	269130	-Me	-H	-OMe	-H	-H	> 40	> 10
NC007	353647	-H	-H	-OMe	-H	-Me	> 40	> 10
NC008	353649	-Me	-H	-OMe	-OMe	-Me	> 40	> 10
NC013	363959	-H	-OMe	-OMe	-OMe	-Me	> 30	0.67 ± 0.46
NC006	352687	-CH <sub>2</sub> CH <sub>3</sub>	-H	-OMe	-OMe	-Me	> 40	9.6 ± 0.4
NC005	350123	-Me	-H	-OCH <sub>2</sub> O-		-H	> 40	> 10
NC010	355074	-Me	-H	-OCH <sub>2</sub> O-		-CH <sub>2</sub> COOH	> 40	> 10
NC011	358073	-Me	-Me	-OCH <sub>2</sub> CH <sub>3</sub>	-Me	-Me	> 40	> 10
NC012	363958	-H	-H	-OCH <sub>2</sub> CH <sub>3</sub>	-H	-Me	> 40	> 10

<sup>a</sup>Inhibition of PDI was assessed by PDI reductase assay. IC<sub>50</sub> values are indicated as the mean ± SD (standard deviation) of at least three independent experiments. <sup>b</sup>MTT cytotoxicity IC<sub>50</sub> values were determined in U87MG cells.

Having explored the SAR around the amino and phenyl moieties, which generally had a nominal impact on PDI inhibition, we synthesized and tested an additional 38 new compounds to diversify the phenolic moiety and probe the impact on PDI inhibition. Notably, this is, to our knowledge, the first comprehensive synthesis and biological study of diverse  $\alpha$ -aminobenzylphenol compounds that have distinct heterocyclic phenolic moieties other than phenols, hydroxy naphthalenes, hydroxybenzo[*d*][1,3]dioxoles, and hydroxyquinolines. Compounds were classified into three types based on the substitution pattern around the phenolic moiety. We speculated that the chelating 8-hydroxyquinoline in the **CD** series of compounds might improve PDI inhibition, acting as a H-bond donor-acceptor pair; thus, several other heterocyclic structures with similar characteristics were incorporated to yield Type I compounds (Table V-6). The PDI inhibitory effects of Type I compounds indicated that 8-hydroxyquinazoline, 5-hydroxyquinoxaline, 4-hydroxybenzothiazole, 7-hydroxybenzofuran, 4-hydroxybenzo[*d*][1,3]dioxole and 5-hydroxy-1,4-benzodioxane are all well tolerated. The 5-hydroxy-1,4-benzodioxane **DX1-114** inhibited PDI most potently with an IC<sub>50</sub> value of 290 ± 120 nM. The importance of the H-bond acceptor was further validated when replacement with a 4-indanol structure (**DX1-31**) resulted in a loss of potency. Interestingly, the position of the H-bond donor was flexible (**DX1-88**), indicating that binding may be supported by interactions with surrounding amino acids in the binding pocket. The fact that **DX1-113** lost its activity despite containing the H-bond donor-acceptor group suggested a bicyclic structure is necessary to fulfill the steric requirement around this moiety. Using **DX1-133** as a model compound, different substituents were introduced. All substituents were well-tolerated, and **DX1-202** and **DX1-203**

exhibited  $IC_{50}$  values below 0.2  $\mu$ M. For Type II compounds with a similar substitution pattern as **AS15** (Table V-7), both 5-hydroxybenzo[*d*][1,3]dioxole and 6-hydroxy-1,4-benzodioxane are preferred, with 6-hydroxyindoline leading to a moderate loss of activity (**DX1-158**). Adding a di-fluoro substitution to **DX1-1** improved activity, suggesting the di-fluoro analogue is a potential analogue to improve metabolic stability (**DX1-17**). Compound **DX1-69** and **DX1-97** lost activity completely, again demonstrating the importance of a H-bond acceptor on the bicyclic phenolic moiety. Type III compounds with substitution patterns different from **AS15** and **CD343** were also synthesized by incorporating different phenolic moieties (Table V-8). Most compounds lost their activity, suggesting an unfavorable binding mode. The exceptions contained a 5-hydroxyindole or 5-hydroxyindazole, with the latter leading to comparable inhibition of PDI at sub-micromolar  $IC_{50}$  values for all its analogues. This might be due to the -NH group of indole/indazole forming additional interactions with PDI as a H-bond donor. Most of the synthesized  $\alpha$ -aminobenzylphenols were not cytotoxic at 30  $\mu$ M, which was similar to the trend observed with the NC and CD series.

Table V-6 SAR of Type I compounds



Compound	R	R <sub>1</sub> -N-R <sub>2</sub>	Phenol Moiety	IC <sub>50</sub> (μM)	MTT (% inhibition at 30 μM)
<b>DX1-23</b>	2,3-OMe-Ph			0.39 ± 0.03	74
<b>DX1-24</b>	4-F-Ph			0.69 ± 0.13	54
<b>DX1-48</b>	4-F-Ph			4.86 ± 2.04	> 30
<b>DX1-58</b>	4-F-Ph			1.20 ± 0.51	> 30
<b>DX1-125</b>	4-F-Ph			0.66 ± 0.13	> 30
<b>DX1-116</b>	4-F-Ph			0.57 ± 0.25	> 30
<b>DX1-133</b>	4-F-Ph			0.56 ± 0.13	> 30
<b>DX1-114</b>	4-F-Ph			0.29 ± 0.12	> 30
<b>DX1-115</b>	4-F-Ph			2.83 ± 1.26	> 30
<b>DX1-88</b>	4-F-Ph			0.61 ± 0.20	> 30
<b>DX1-31</b>	4-F-Ph			> 10	> 30

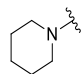
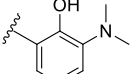
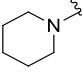
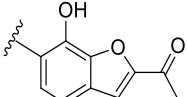
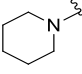
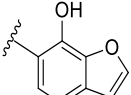
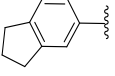
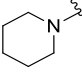
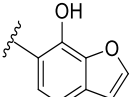
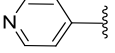
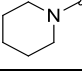
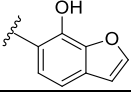
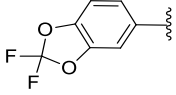
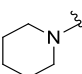
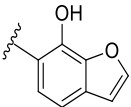
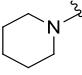
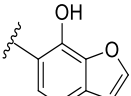
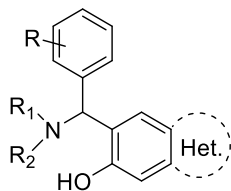
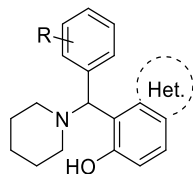
<b>DX1-113</b>	4-F-Ph			> 30	> 30
<b>DX1-187</b>	4-F-Ph			$1.23 \pm 0.23$	> 30
<b>DX1-199</b>	2-OH,4-F-Ph			$1.07 \pm 0.01$	> 30
<b>DX1-201</b>				$0.41 \pm 0.11$	> 30
<b>DX1-202</b>				< 0.2	> 30
<b>DX1-203</b>				< 0.2	> 30
<b>DX1-205</b>	4-CF <sub>3</sub> -Ph			$0.30 \pm 0.03$	> 30

Table V-7 SAR of Type II compounds



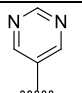
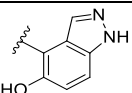
Compound	R	R <sub>1</sub> -N-R <sub>2</sub>	Phenol Moiety	IC <sub>50</sub> (μM)	MTT (% inhibition at 30 μM)
<b>DX1-1</b>	2,3-OMe			1.06 ± 0.31	66
<b>DX3-59B</b>	4-F			2.9 ± 2.4	> 30
<b>DX1-155</b>	4-F			0.67 ± 0.29	> 30
<b>DX1-158</b>	4-F			7.01 ± 1.39	> 30
<b>DX1-17</b>	2,3-OMe			0.51 ± 0.13	> 30
<b>DX1-69</b>	4-F			> 30	> 30
<b>DX1-97</b>	4-F			> 100	> 30

Table V-8 SAR of Type III compounds

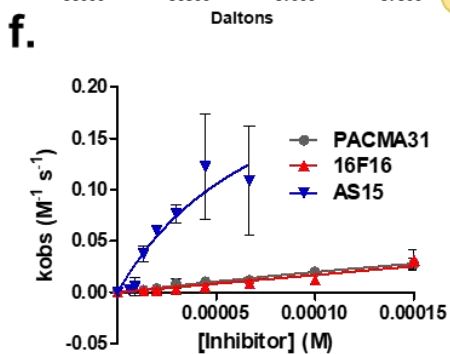
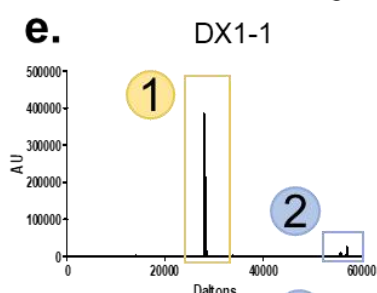
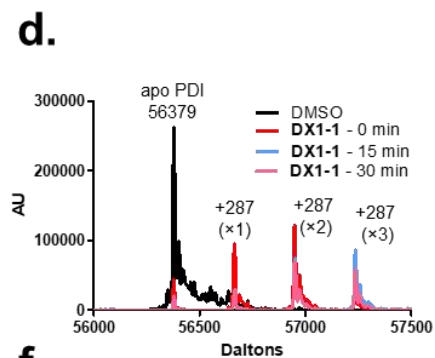
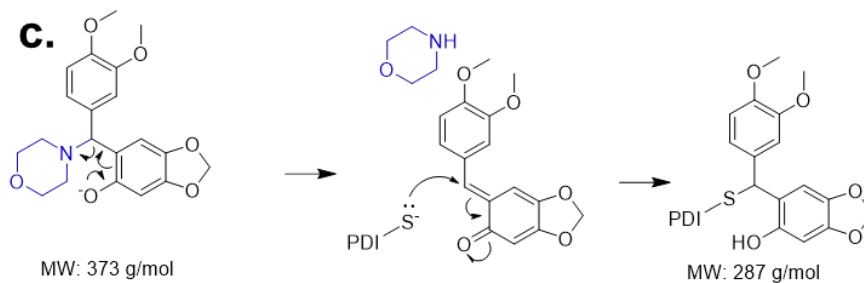
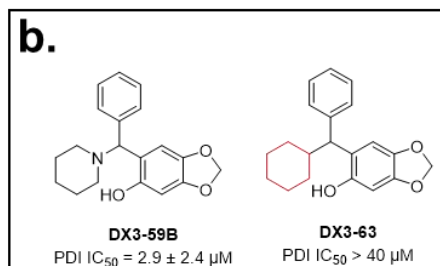
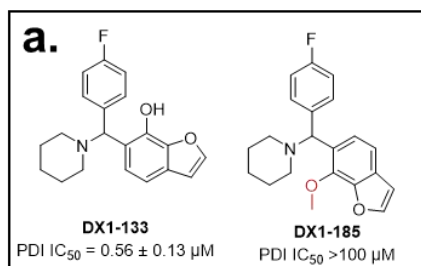


Compound	R	Phenol Moiety	IC <sub>50</sub> (μM)	MTT (% inhibition at 30 μM)
<b>DX-73</b>	4-F		> 30	> 30
<b>DX-96</b>	4-F		> 100	> 30
<b>DX1-101</b>	4-F		> 100	> 30
<b>DX1-137</b>	4-F		10.20 ± 2.88	> 30
<b>DX1-138</b>	4-F		> 100	> 30
<b>DX1-147</b>	4-F		1.81 ± 0.06	> 30
<b>DX1-98</b>	4-F		0.35 ± 0.14	87
<b>DX-142</b>	4-CF <sub>3</sub>		0.71 ± 0.10	> 30
<b>DX-143</b>	4-NO <sub>2</sub>		0.52 ± 0.36	> 30
<b>DX1-150</b>			0.34 ± 0.26	> 30
<b>DX1-152</b>			0.29 ± 0.13	> 30

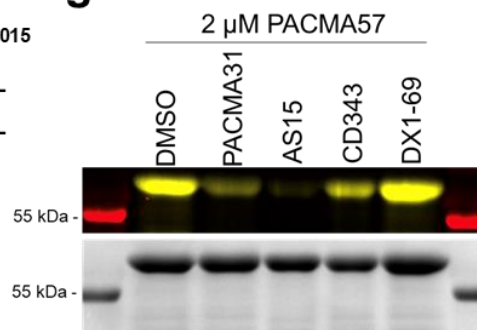
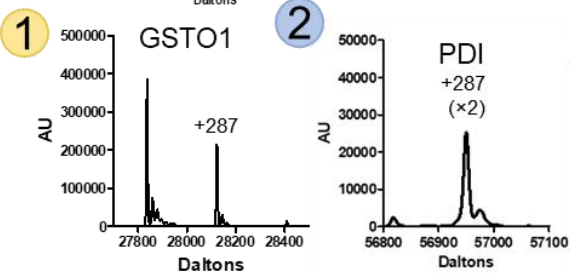


<b>DX1-153</b>			$0.83 \pm 0.29$	> 30
----------------	---	---	-----------------	------

**AS15 Analogues Covalently Bind to PDI.** We addressed the importance of the phenolic hydroxy and amine moiety of the series with two compounds; **DX1-185** lost activity with the replacement of the phenolic hydroxy (**DX1-133**) with a methoxy (Figure V-6). Similarly, replacing the piperidine in **DX3-59B** with a cyclohexane abolished its PDI inhibition. Both compounds demonstrated the importance of the  $\alpha$ -aminobenzylphenol core to the potency of this series of compounds.



ID	$K_{inact}/K_I$
16F16	170 ± 14
PACMA31	195 ± 9
AS15	2581 ± 258



Coomassie Stain

Figure V-6 SAR indicates that compounds are covalent PDI inhibitors. (A) Comparison of compounds with free hydroxy or methoxy on the bicyclic moiety. (B) Comparison of compounds with piperidine or cyclohexane moiety. (C) Proposed mechanism of inhibition via retro-Michael addition reaction. (D) **DX1-1** covalently binds to PDI. 100  $\mu\text{M}$  **DX1-1** was incubated with 10  $\mu\text{M}$  PDI for 30 minutes prior to injection. (E) **DX1-1** binds to PDI preferentially over GSTO1. 100  $\mu\text{M}$  **DX1-1** was incubated with a mixture of 10  $\mu\text{M}$  PDI and 10  $\mu\text{M}$  GSTO1 for 30 minutes prior to injection. (F) Concentration- and time-dependent PDI inhibition curves for  $k_{\text{inact}}/K_{\text{I}}$  determination of **PACMA31**, **16F16**, and **AS15**. Activity was measured using the PDI reductase assay. Absorbance was monitored over time at various concentrations and preincubation times with indicated compounds. (G) Gel-based competition with recombinant PDI and **PACMA57**. +: 20  $\mu\text{M}$ ; ++: 100  $\mu\text{M}$

The covalent disulfide bond is a reversible covalent interaction; thus, small molecules could also bind reversibly to the cysteine thiols. For example, a Michael-type conjugate addition of 2-cyanoacrylates to thiols was discovered to be a rapid reversible reaction at physiological pH.<sup>24</sup> Due to the nature of reversible disulfide bonds, we hypothesized that the **AS15** analogues, although demonstrating reversible inhibition, may be attacked by the nucleophilic cysteine thiols in the active sites of PDI. Upon base-mediated fragmentation to expose the Michael acceptor, the free thiol on PDI could react and form a covalent adduct (Figure V-6). This type of retro Michael addition to protein thiols has been observed with hydroxyquinolines like **CD343**. A zinc-dependent mechanism opened a quinone methide for selective reaction with HDAC5 and HDAC9<sup>15</sup>, another quinone methide intermediate was found to react with protein thiols over forming DNA adducts<sup>25</sup>, and co-crystallization confirmed pyridinylmethyl quinoline fragment binding to MIF tautomerase via a proline residue.<sup>16</sup> In the case of the pyridinylmethyl quinoline fragment, the compound bound via a retro Michael addition reaction that formed the quinone methide intermediate. This intermediate was primed to undergo the aza-Michael addition to covalently link to a proline residue in MIF tautomerase.

To confirm **AS15** analogues covalently label PDI, we incubated 10  $\mu\text{M}$  PDI with 100  $\mu\text{M}$  **DX1-1** or **DX1-69** and monitored adduct formation with quadrupole time-of-flight mass spectrometry (QTOF). The fragment matching the proposed mechanism of action was apparent

rapidly (< 5 minutes) after the compound was added. **DX1-1** bound oxidized PDI at three sites. When **DX1-1** was incubated in a mixture of 1:1 PDI:GSTO1, the mass of PDI increased by two equivalents of the fragment, demonstrating *in vitro* selectivity. An inactive analogue of **DX1-1** without the aromatic benzoxole (**DX1-69**) did not demonstrate covalent binding under the same conditions (Figure V-7).

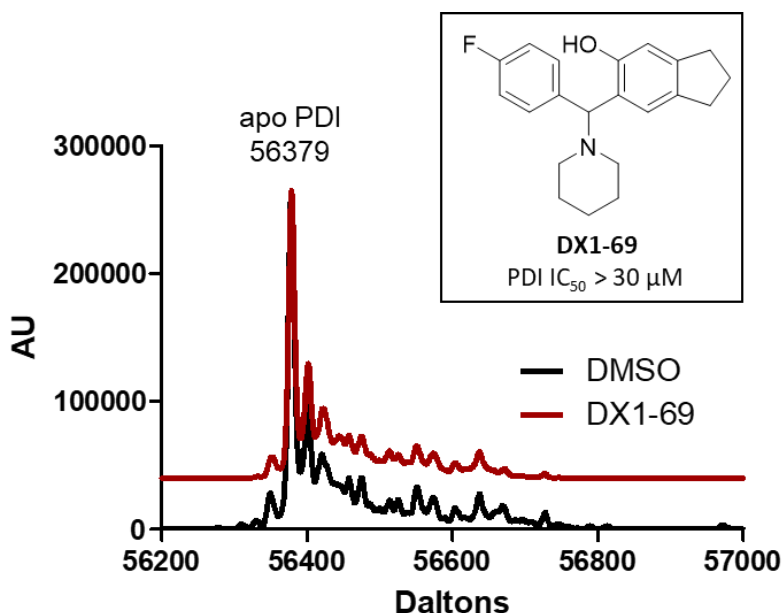


Figure V-7 Spectrum of inactive **AS15** analogue, **DX1-69**

To assess the covalent binding nature, we measured the  $k_{\text{inact}}/K_I$  of the lead compounds. For covalent inhibitors, the  $k_{\text{inact}}/K_I$  is the ratio of the observed rate of inactivation after a reversible reaction to form a protein-inhibitor (P-I) complex with all the protein molecules ( $k_{\text{inact}}$ ) to the concentration of inhibitor required to reach half of the maximum rate of covalent bond formation ( $K_I$ ). The kinetics of covalent PDI inhibitors **16F16**, **PACMA31**, and **AS15** were measured by assessing activity in the PDI reductase assay at incubation times from 5 to 60 minutes. **AS15** inhibited PDI with a  $k_{\text{inact}}/K_I$  of  $2.6 \times 10^3 \text{ M}^{-1}\text{s}^{-1}$  (Figure V-6).  $k_{\text{inact}}/K_I$  for **PACMA31** was  $2.0 \times$

$10^2 \text{ M}^{-1}\text{s}^{-1}$  and  $k_{\text{inact}}/K_{\text{I}}$  for **16F16** was  $1.7 \times 10^2 \text{ M}^{-1}\text{s}^{-1}$ . Thus, **AS15** more efficiently inhibited PDI than both covalent inhibitors **PACMA31** and **16F16**. Furthermore, a gel-based competition assay with the fluorescent probe of **PACMA31**, **PACMA57**, confirmed **AS15** analogues could compete with **PACMA57** to bind PDI.<sup>5</sup>

To address whether the **AS15** analogues targeted the active site cysteines of PDI, like **PACMA31**, we performed washout experiments with the PDI reductase assay. **AS15** (50  $\mu\text{M}$ ) was incubated with 40  $\mu\text{M}$  PDI for 3 hours at room temperature. After 3 hours, the PDI-**AS15** complex was diluted 100-fold into reaction buffer, the reaction was incubated for another hour at 37 °C, and insulin was added as a substrate to initiate the reaction. **PACMA31** (an irreversible inhibitor) at 1 and 100  $\mu\text{M}$  and **BAP2** (a reversible inhibitor) at 0.5 and 50  $\mu\text{M}$  were used as controls (Figure V-8). We found that both **AS15** and **CD343** did not maintain the characteristics of the high concentration of inhibitor after dilution to the low concentration. These results indicate that **AS15** and **CD343** behaved as reversible inhibitors in this wash out experiment. We further tested whether the compounds were binding in the **b'** domain with the ANS (anilinonaphthalene sulfonic acid) spectral scan.<sup>26</sup> ANS is a dye that fluoresces upon binding hydrophobic pockets and specifically targets the **b'** domain in PDI. **B'** domain-selective inhibitors of PDI such as estradiol and bepristat 1a compete with ANS.<sup>26</sup> **AS15** and **CD343** did not lower the fluorescence of ANS (Figure V-8). Our combined results from the thermal shift assay, washout experiment, and ANS spectral scan demonstrated that **AS15** and **CD343** are likely not substrate-binding domain inhibitors like estradiol and **BAP2**, but may be reversible covalent inhibitors of the active site cysteines.

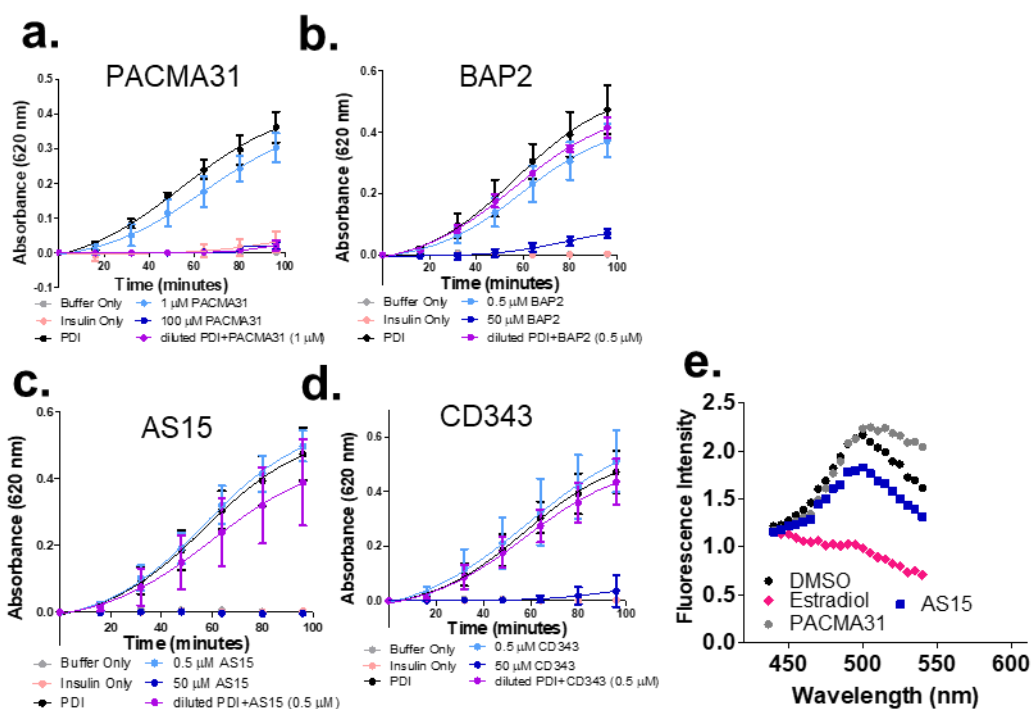


Figure V-8 Recovery of PDI activity upon treatment with **PACMA31** (A), **BAP2** (B), **AS15** (C), or **CD343** (D). (F) ANS spectral scan with 5  $\mu$ M PDI and 100  $\mu$ M **PACMA31**, estradiol, or **AS15**.

**AS15 Analogues Compete with Glutathione.** Because the **AS15** analogues seemed highly reactive toward nucleophilic attack, we hypothesized that glutathione may also react with the compounds. Glutathione is present in high concentrations in the cytoplasm and is an important redox regulator in the ER.<sup>27</sup> The oxidizing environment of the ER is maintained by the ratio of reduced to oxidized glutathione, which is lower than the ratio in the cytoplasm. Incubating the compounds with NAC before adding them to the PDI reductase assay rendered the compounds inactive (Figure V-9). **AS15** analogues were also inactivated with competing glutathione at physiological concentrations (5 mM) in the PDI reductase assay (Figure V-9). These results

provided further support that the **AS15** analogues act via addition to the active site cysteines in PDI.

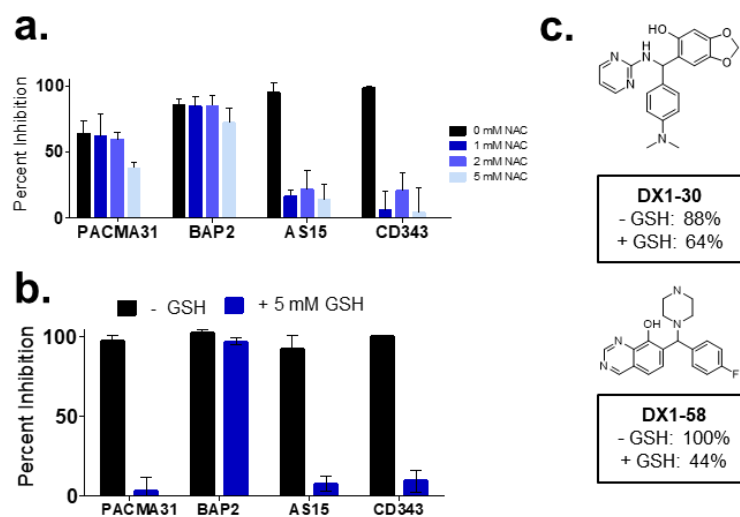


Figure V-9 N-Acetyl cysteine and glutathione inactivate **AS15** analogues. (A) N-Acetyl cysteine competition in PDI reductase assay. (B) Glutathione competition in PDI reductase assay. (C) Top two **AS15** analogues least sensitive to competition with 5 mM GSH in the PDI reductase assay.

To assess trends in the glutathione sensitivity of the **AS15** series, we screened all the analogues in the PDI reductase assay in the presence of 5 mM GSH. The high concentrations of glutathione in the cytoplasm may inactivate the compound *in vivo*; thus, the *in vitro* IC<sub>50</sub> value may not be a reliable indicator of *in vivo* activity.<sup>11</sup> Although the PDI reductase assay is performed at a relatively high concentration of DTT (500 μM), we added 5 mM glutathione to mimic a more physiological environment. This issue is particularly relevant because the analogues behave as reversible thiol adducts (Table V-9). Substrate-binding domain inhibitors isoquercetin and **BAP2** remained active in the presence of high GSH concentrations. We found two **AS15** analogues out of 93 that maintained potency in the presence of competing glutathione: **DX1-30** and **DX1-58**.

Table V-9 Percent inhibition of **AS15** analogues in the absence or presence of 5 mM GSH in the PDI reductase assay

	10 $\mu$ M			10 $\mu$ M			10 $\mu$ M	
	- GSH	+ GSH		- GSH	+ GSH		- GSH	+ GSH
<b>PACMA31</b>	95	-2	<b>DX1-114</b>	29	23	<b>NC108</b>	62	0
<b>isoquercetin</b>	54	42	<b>DX1-115</b>	53	31	<b>NC110</b>	86	5
<b>CD343</b>	100	15	<b>DX1-116</b>	42	20	<b>NC115</b>	85	3
<b>CD344</b>	97	3	<b>DX1-125</b>	86	30	<b>NC116</b>	98	9
<b>CD345</b>	-21	17	<b>DX1-133</b>	99	36	<b>NC117</b>	100	7
<b>CD346</b>	106	2	<b>DX1-137</b>	32	29	<b>NC118</b>	94	11
<b>CD350</b>	95	14	<b>DX1-147</b>	47	49	<b>NC119</b>	95	3
<b>CD352</b>	27	-2	<b>DX1-150</b>	79	32	<b>NC121</b>	100	20
<b>CD355</b>	90	14	<b>DX1-152</b>	72	47	<b>NC122</b>	97	27
<b>CD362</b>	98	1	<b>DX1-153</b>	79	55	<b>NC123</b>	100	21
<b>CD363</b>	-16	1	<b>DX1-155</b>	40	41	<b>NC124</b>	105	31
<b>CD373</b>	101	-3	<b>DX1-158</b>	40	43	<b>NC133</b>	96	19
<b>CD377</b>	101	7	<b>DX1-187</b>	99	46	<b>NC134</b>	87	20
<b>CD528</b>	98	-1	<b>DX1-199</b>	99	42	<b>NC141</b>	102	15
<b>CD594</b>	109	2	<b>DX1-201</b>	100	53	<b>NC161</b>	98	11
<b>CD601</b>	-22	-1	<b>DX1-202</b>	100	44	<b>NC162</b>	102	-1
<b>CD611</b>	102	3	<b>DX1-203</b>	99	47	<b>NC163</b>	99	10
<b>CD613</b>	123	10	<b>DX1-205</b>	100	52	<b>NC165</b>	0	-1
<b>CD626</b>	101	9	<b>NC014</b>	100	52	<b>NC166</b>	0	23
<b>CD638</b>	93	5	<b>NC015</b>	101	55	<b>NC266</b>	101	19
<b>CD639</b>	30	3	<b>NC016</b>	100	63	<b>NC268</b>	0	21
<b>CD640</b>	101	4	<b>NC017</b>	60	56	<b>NC269</b>	97	15
<b>DX1-001</b>	58	29	<b>NC018</b>	95	13	<b>NC270</b>	98	18
<b>DX1-017</b>	101	34	<b>NC019</b>	27	13	<b>NC272</b>	33	13
<b>DX1-023</b>	93	23	<b>NC021</b>	97	13	<b>NC273</b>	61	15
<b>DX1-024</b>	41	33	<b>NC022</b>	100	9	<b>NC282</b>	65	35
<b>DX1-030</b>	55	21	<b>NC024</b>	95	12	<b>NC299</b>	0	18
<b>DX1-048</b>	37	21	<b>NC025</b>	-17	11	<b>NC300</b>	97	22
<b>DX1-058</b>	100	44	<b>NC026</b>	98	23	<b>NC301</b>	0	23
<b>DX1-088</b>	98	12	<b>NC027</b>	96	4			
<b>DX1-098</b>	73	20	<b>NC028</b>	92	7			
<b>DX1-101</b>	28	31	<b>NC055</b>	97	8			
<b>DX1-113</b>	30	31	<b>NC107</b>	98	2			



We observed that **DX1-58** spontaneously formed a dimer after long-term storage, so we repurified the monomeric and dimeric forms of **DX1-58** and tested each form in the PDI reductase assay in the presence of glutathione (Figure V-10). The dimeric form of **DX1-58** was less sensitive to glutathione competition than the monomer (Figure V-10). Furthermore, we found that both the monomer and dimer of **DX1-58** bound to PDI (Figure V-10). Incubation with the **a'c** domain gave a species with two fragments of **DX1-1** bound, suggesting the compound binds two sites in the **a'c** domain, likely at least at the N-terminal redox-active cysteine Cys397 (Figure V-10). Furthermore, when we incubated the monomer and dimer of **DX1-58** with a C53S mutant of PDI, we observed only one species bound, suggesting that Cys53 is likely one of the key residues for binding (Figure V-10).

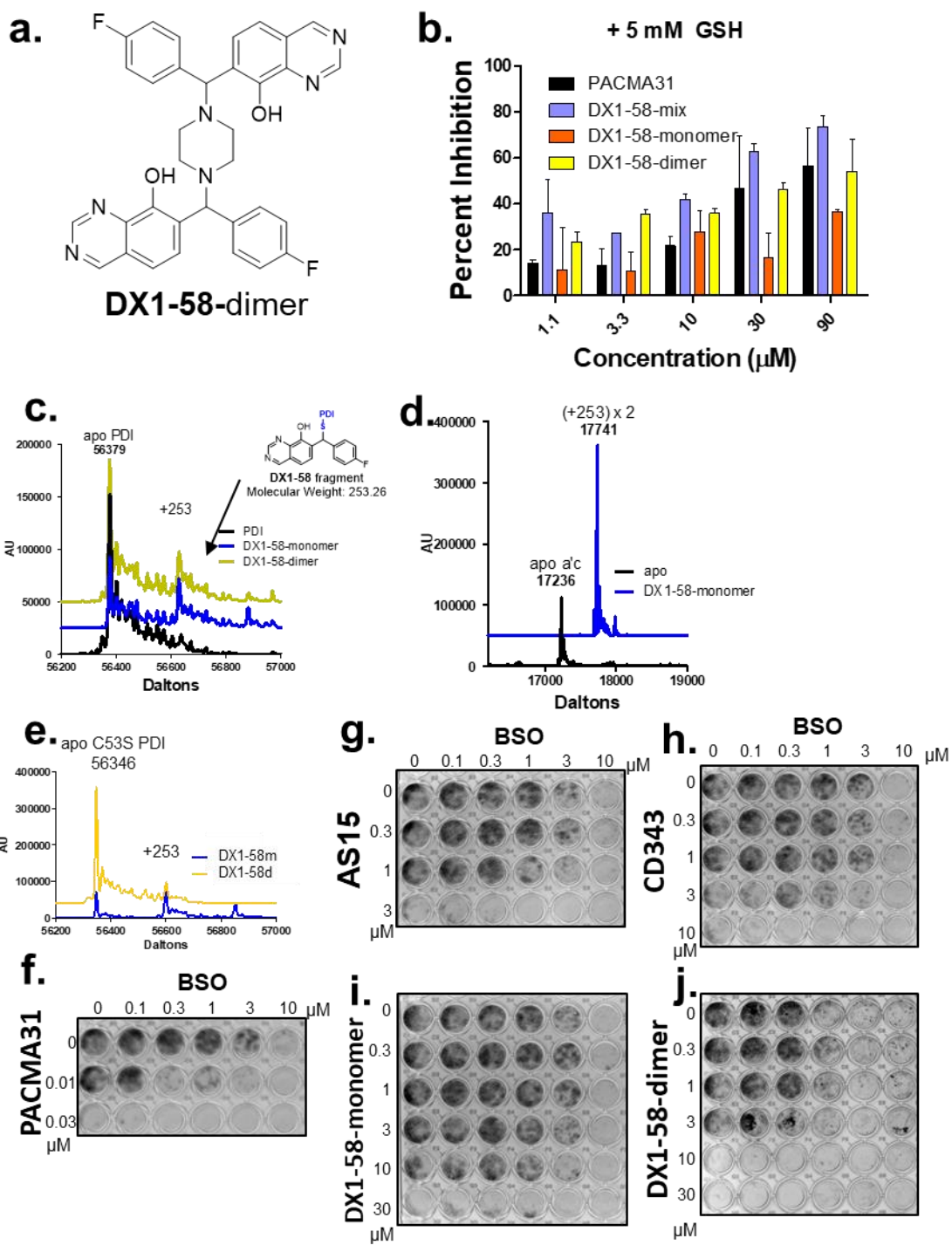


Figure V-10 Dimerized analogue is less sensitive to GSH treatment. (A) Structure of DX1-58 dimerization. (B) Percent inhibition of DX1-58 monomer and dimer in the PDI reductase assay in competition with 5 mM glutathione. (C) Protein mass spectrometry

confirms fragment of **DX1-58** binds to PDI. (D) One fragment of **DX1-58** binds the a'c domain. (E) **DX1-58** and **DX1-58** dimer bind C53S mutant PDI. Toxicity of **PACMA31** (F), **AS15** (G), **CD343** (H), **DX1-58** monomer (I), and **DX1-58** dimer (J) in the colony formation assay in the absence or presence of BSO. U118MG cells were pretreated with BSO for 24 h prior to compound addition.

Although the PDI disulfides are 500-fold more reactive than glutathione<sup>28</sup>, we hypothesized that glutathione may be inactivating the **AS15** analogues and contributing to lower their potency. Pretreatment of GBM cells with BSO for 24 hours before adding the compounds increased potency in the colony formation assay (Figure V-10; Figure V-11). While the monomer of **DX1-58** was more sensitive to BSO addition, the **DX1-58** dimer was more potent, and its potency was not dependent on BSO addition. These results support the hypothesis that glutathione depletion sensitizes GBM cells to PDI inhibition.

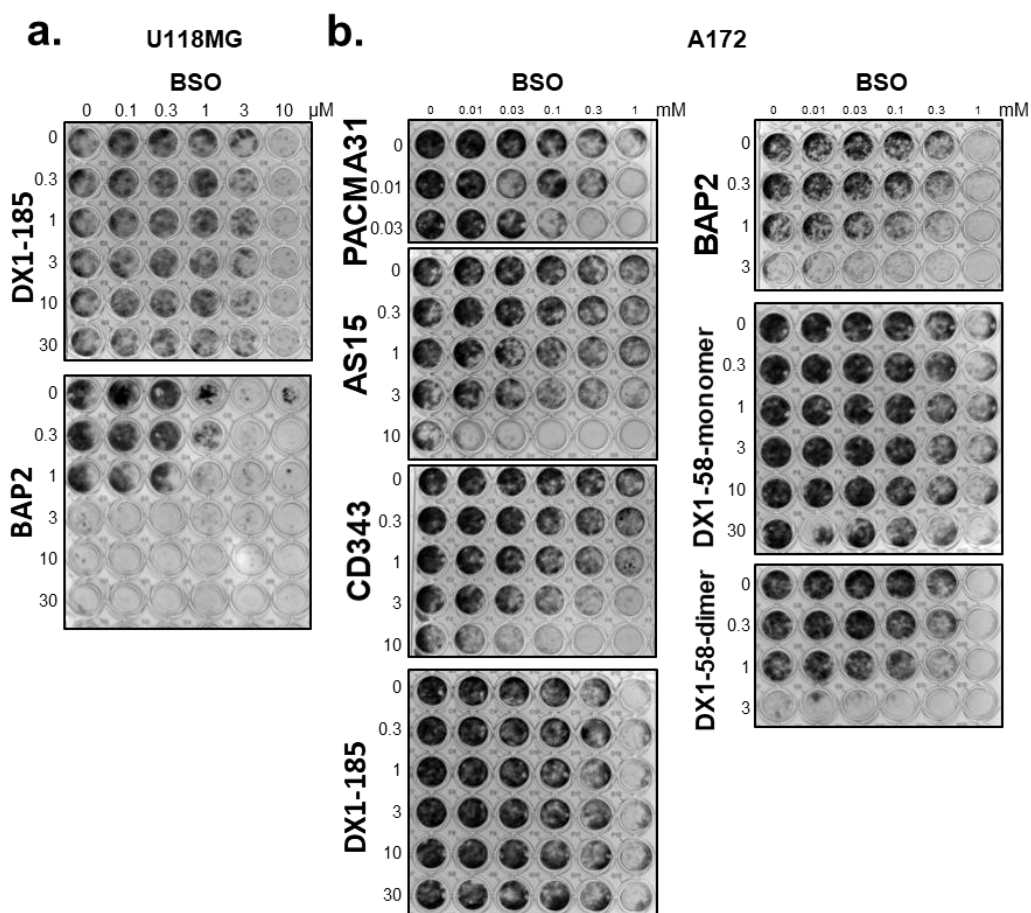


Figure V-11 Colony formation assay of PDI inhibitors in combination with BSO in (A) U118MG and (B) A172 cells. Cells were pretreated with BSO for 24 h prior to compound addition.

**AS15 Analogue Target Identification.** We sought to confirm whether the **AS15** analogues could target PDI in the cells by synthesizing two analogues of **DX3-59** with a BODIPY fluorescent tag on the phenyl ring (Figure V-12). The BODIPY-labeled compounds differed in the linker length between the parent compound and the tag. **DX3-173B** contained a two-carbon linker separating the amide groups on the BODIPY structure. The first BODIPY analogue did not inhibit PDI activity in the PDI reductase assay (Figure V-13). However, it did covalently bind proteins around 55-70 kDa when added to cells (Figure V-12). Incubation of both **DX3-159** and **DX3-173B** with

cell-free medium supplemented with fetal bovine serum demonstrated that the compounds bound to serum albumin (Figure V-12). Although **DX3-173B** bound to serum albumin, it inhibited PDI activity with an  $IC_{50}$  value comparable to the unlabeled analogue of  $1.37 \pm 0.23 \mu\text{M}$  (Figure V-12). To verify the band from **DX3-159** was not PDI, a Western blot was run with cells treated with **DX3-159** and **DX3-173B**. The GFP band from the **DX3-159**-treated cells runs closer to the molecular weight of albumin (69 kDa) than the PDI band around 55 kDa (Figure V-14). Additionally, when the cells are treated with **DX3-159** after serum starvation, the band disappears (Figure V-14). Furthermore, treatment with **DX3-173B** results in several bands, suggesting the compound may have more than one target. With recombinant PDI, **DX3-173B** covalently binds, and binding can be blocked with DTT, further supporting the mechanism of inhibition of this series (Figure V-15).

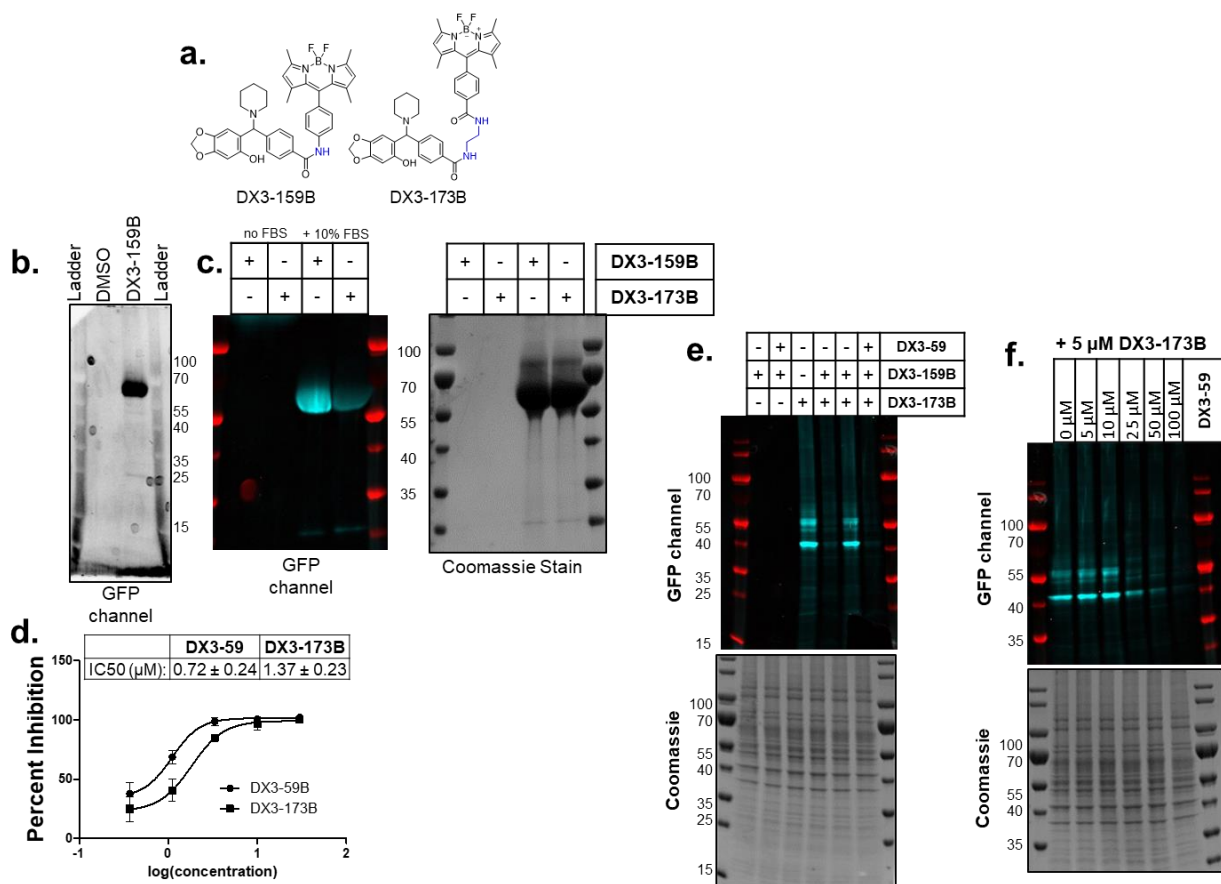


Figure V-12 **AS15** analogues bind serum albumin. (A) Structures of BODIPY-labeled **AS15** analogues (B) U118MG cells treated with 40 μM **DX3-159B** overnight (C) Cell-free DMEM treated with 20 μM **DX3-159B** or **DX3-173B** overnight at 37 °C. (D) **DX3-173B** dose-response curve in the PDI reductase assay. (E) Cell lysates incubated with indicated compounds for 24 h at room temperature after cell lysis. (F) Cell lysates treated with increasing concentrations of parent compound **DX3-59** before addition of BODIPY-labeled **DX3-173B**.

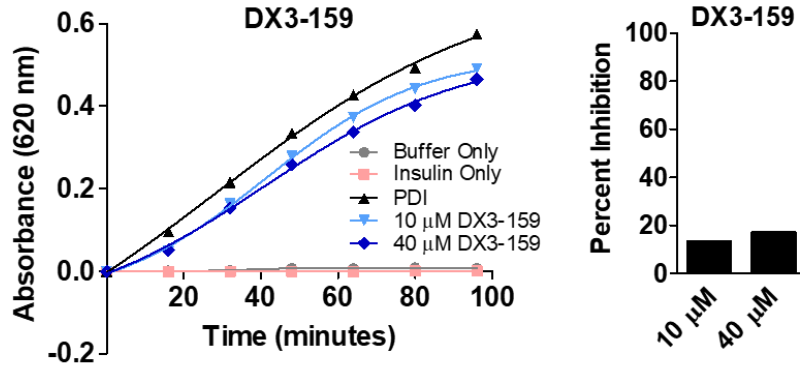


Figure V-13 Activity of **DX3-159** against wild-type PDIA1 in the PDI reductase assay

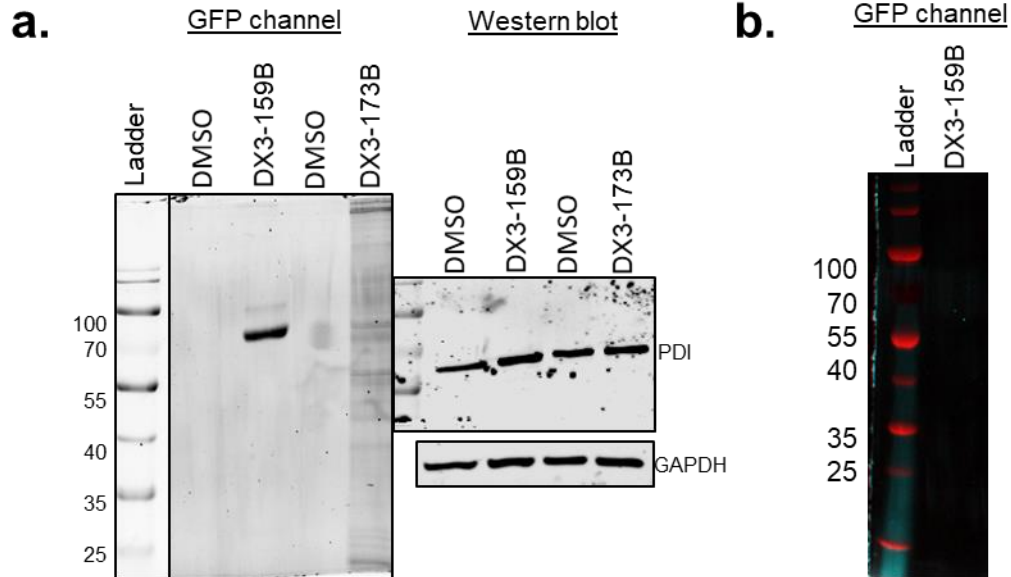


Figure V-14 **DX3-159B** protein band migrates higher than PDI (A) U118MG cells (in medium supplemented with 10 % FBS) incubated with DMSO, 40  $\mu$ M **DX3-159B** or 2  $\mu$ M **DX3-173B** for 24 hours before being collected in Cell Lytic M buffer and run on a 10 % polyacrylamide gel. The gel was imaged in the GFP channel prior to probing for PDI and GAPDH in Western blot analysis. (B) U118MG cells were serum starved overnight before incubation with 10  $\mu$ M **DX3-159B** for 24 hours before being collected in Cell Lytic M buffer, run on a 10 % polyacrylamide gel, and imaged in the GFP channel on the iBright (Thermo Fisher Scientific).

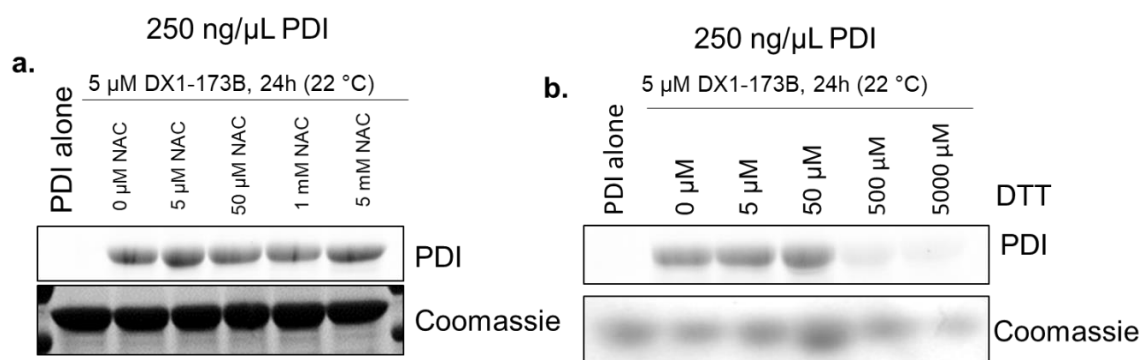


Figure V-15 DTT outcompetes **DX3-173B** for binding to PDI (A) 250 ng/μL recombinant PDI was incubated with indicated concentrations of N-acetyl cysteine (NAC) and **DX3-173B** at room temperature for 24 hours and run on a 10 % acrylamide gel. The PDI band was imaged with the GFP channel on the iBright (Thermo Fisher Scientific). (B) 250 ng/μL recombinant PDI was incubated with indicated concentrations of dithiothreitol (DTT) and **DX3-173B** at room temperature for 24 hours and run on a 10 % acrylamide gel. The PDI band was imaged with the GFP channel on the iBright.

To further investigate whether the BODIPY-labeled **AS15** analogues can target PDI, we treated cell lysates with the compounds for 24 hours. **DX3-159** did not covalently label proteins in the cell lysate, however, **DX3-173B** bound in two major bands around 55 and 40 kDa, and a minor band below 55 kDa (Figure V-12; Figure V-16). In addition, the unlabeled, parent compound competed for labeling both bands in a dose-dependent manner, but seemed to compete off the 55 kDa band at a lower concentration (5x [probe]) than the 40 kDa band (20x [probe]). In addition to inhibiting PDIA1 activity, **AS15** could also inhibit PDIA3 activity; thus, the band around 55 kDa could contain both PDIA1 and PDIA3. Additionally, **DX3-173** bound PDIA1, PDIA2, and PDIA3, in addition to BSA, and was competed off by the parent compound. Competition was not observed for binding to BSA, likely due to multiple binding sites for **DX3-173** on BSA (Figure V-17). **DX3-59** dose-dependently competed off **DX3-173B** for binding PDIA2 and PDIA3 (Figure V-18). Combining BSA with PDIA1 for 24 hours with **DX3-159** or **DX3-173B** did not improve binding to PDIA1 (Figure V-19). Because glutathione inactivated the compounds *in vitro*, cells were pre-



incubated with BSO prior to BODIPY-labeled compound treatment to determine whether depleting the cells of glutathione would improve on-target binding. BSO addition improved binding for **DX3-159**, however, binding was non-selective. Furthermore, addition of 10 % FBS decreased binding, further confirming the interaction between this series and serum albumin (Figure V-20). Incubation of the cell lysate with **DX3-173B** consistently resulted in three major bands (Figure V-20).

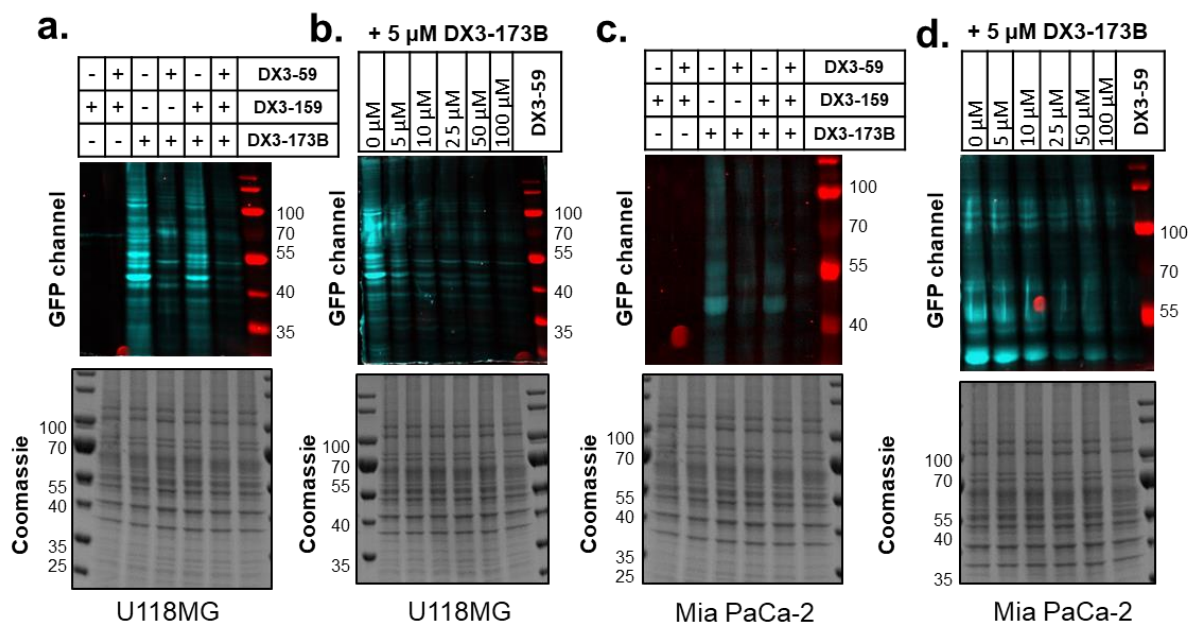


Figure V-16 **AS15** analogues bind multiple proteins. (A) U118MG cell lysates (30  $\mu$ g) incubated with 50  $\mu$ M **DX3-59** and 10  $\mu$ M **DX3-159** or **DX3-173B** for 24 h at room temperature after cell lysis. (B) U118MG cell lysates (30  $\mu$ g) treated with increasing concentrations of parent compound **DX3-59** before addition of BODIPY-labeled **DX3-173B**. (c) MiaPaCa-2 cell lysates (30  $\mu$ g) incubated with 50  $\mu$ M **DX3-59** and 10  $\mu$ M **DX3-159** or **DX3-173B** for 24 h at room temperature after cell lysis. (D) MiaPaCa-2 cell lysates (30  $\mu$ g) treated with increasing concentrations of parent compound **DX3-59** before addition of BODIPY-labeled **DX3-173B**. Samples were prepared under reducing conditions and BODIPY labeling was imaged with the iBright on the GFP channel.

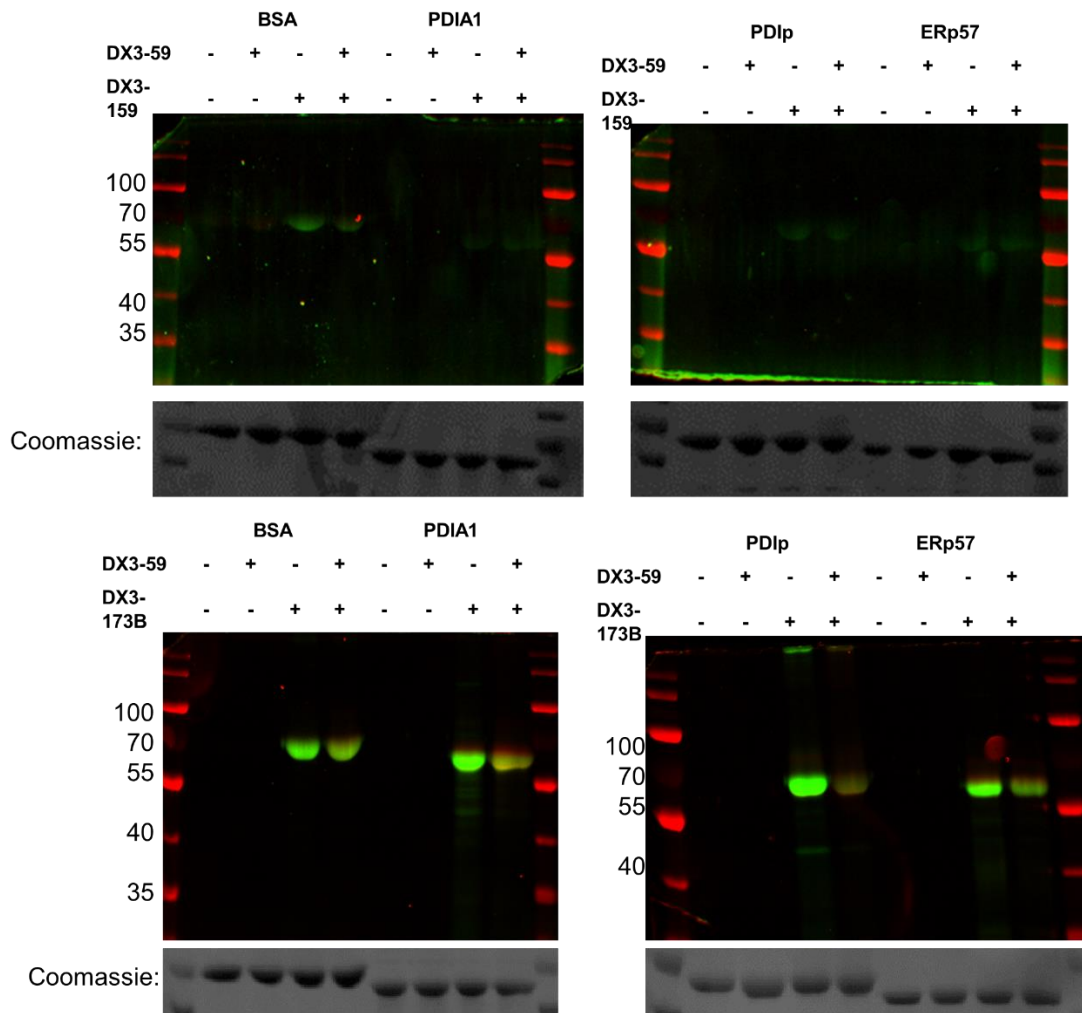


Figure V-17 **DX3-59** competition with BODIPY-labeled probe. Fluorescence imaging of recombinant PDI family members and BSA at 3.5  $\mu$ M treated with 100  $\mu$ M **DX3-59** overnight at room temperature. The samples were then treated for 30 minutes at room temperature with 20  $\mu$ M **DX3-159** (top) or **DX3-173B** (bottom). Samples were prepared under reducing conditions and BODIPY labeling was imaged with the iBright on the GFP channel.

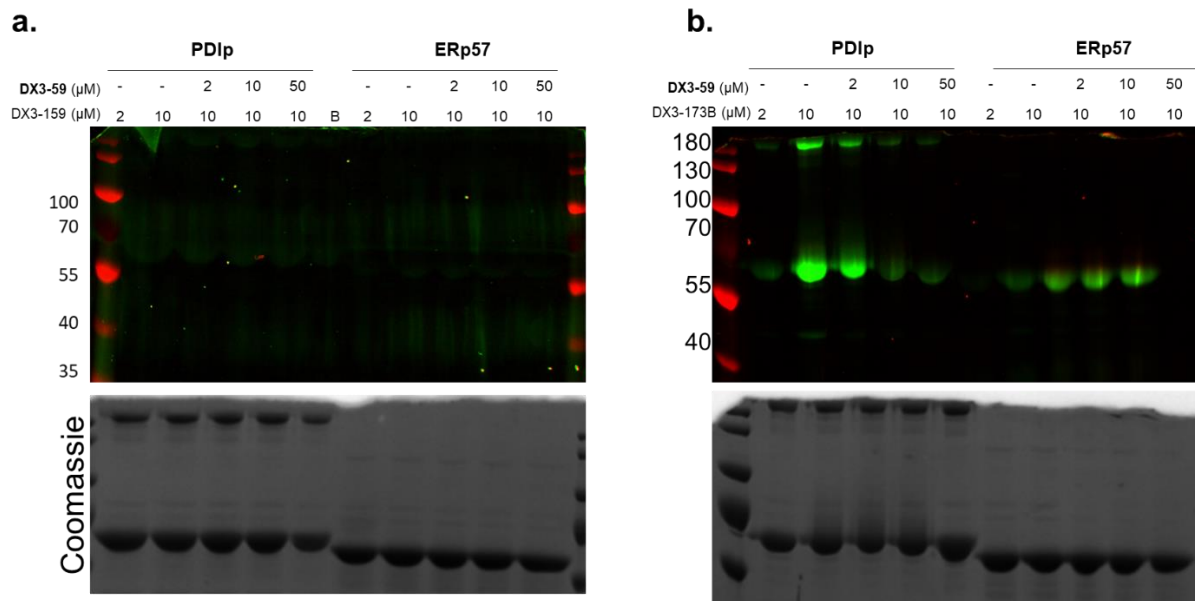


Figure V-18 Competitive inhibition of BODIPY-labeled AS15 analogue (A) **DX3-159** or (B) **DX3-173B** binding to 10  $\mu\text{M}$  PDip or ERp57 was assessed by in-gel fluorescence imaging. Recombinant protein was incubated with compounds for 24 h at room temperature before being analyzed by SDS PAGE.

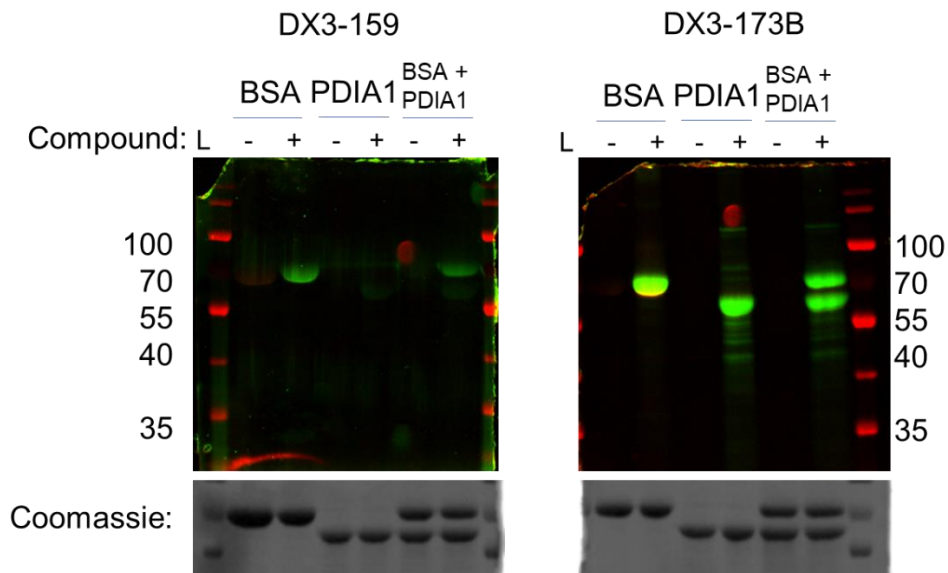


Figure V-19 Competitive inhibition of 20  $\mu\text{M}$  BODIPY-labeled AS15 analogue in BSA. **DX3-159** (left) or **DX3-173B** (right) binding to 3.5  $\mu\text{M}$  BSA or PDIA1 was assessed by in-gel fluorescence imaging. Recombinant protein was incubated with compounds for 24 h at room temperature before being analyzed by SDS PAGE.

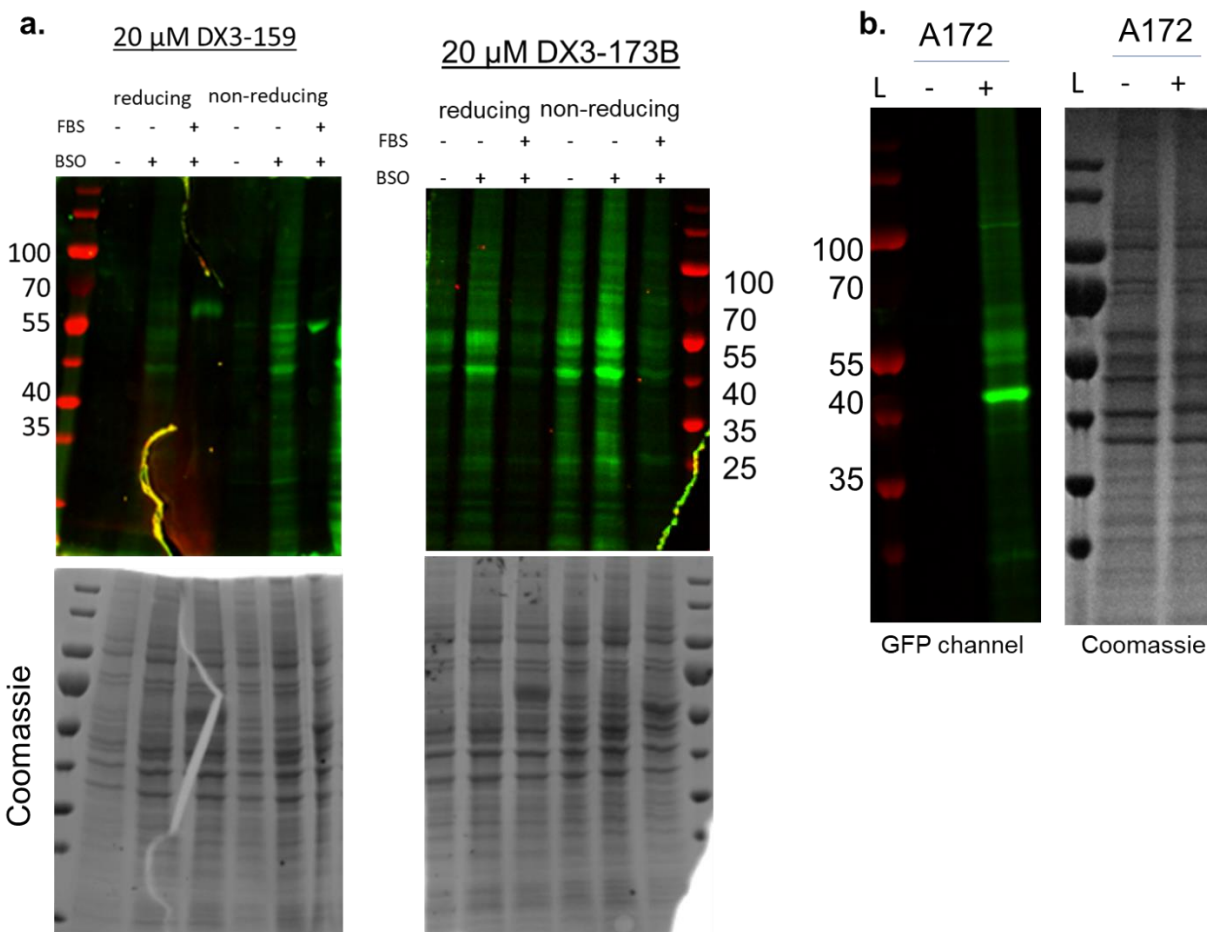


Figure V-20 Cell-based binding of BODIPY-labeled **AS15** analogues **DX3-159** (left) or **DX3-173B** (right) in U118MG cells in the presence of 20  $\mu$ M BSO or 10 % FBS. Cells were serum-starved and/or treated with BSO for 24 hours before compound addition. Cells were treated with compounds for 24 hours, then lysed and binding was assessed by in-gel fluorescence imaging under reducing or non-reducing conditions. (b) A172 cells were serum-starved 24 hours prior to addition of 20  $\mu$ M **DX3-173B** (+). After 24 hours, cells were lysed in Cell Lytic M buffer, and 40  $\mu$ g was subjected to SDS-PAGE under reducing conditions. Bands were submitted for proteomic analysis. L: protein ladder

Proteomic analysis of each of the bands revealed lists of potential target proteins (Table V-10; Table V-11; Table V-12). Several PDI family members have a molecular weight around 40 kDa, including ERp44, PDIA6, and TXNDC5, which could be responsible for the lower band (Table V-13). Reported targets of similar scaffolds include MIF tautomerase, HDAC5/9, and BRAF<sup>V600E</sup>. We did not observe bands at the molecular weights of those three targets, suggesting

that the **AS15** analogues do not bind these proteins, or the proteins have low abundance in the cell lines tested (Table V-14). Furthermore, those known targets, as well as STAT3, STAT5, Mcl-1, frataxin, and P2Y12 were not found in the bands analyzed with the proteomics experiment. In addition, confocal microscopy revealed that the BODIPY-labeled analogues mainly reside in the cytoplasm and ER, not in the nucleus with HDAC5/9 (Figure V-21).

Table V-10 Most abundant proteins around 40 kDa in A172 cells

Accession	Description	# cysteines	Location	Coverage [%]	# Peptides	# PSMs <sup>a</sup>	# Unique Peptides	MW <sup>b</sup> [kDa]
P60709	Actin, cytoplasmic 1 (ACTB)	6	cytoskeleton; cytosol; membrane; nucleus	74	21	184	9	41.7
P00558	Phosphoglycerate kinase 1 (PGK1)	7	cytosol; membrane	69	24	84	20	44.6
P68133	Actin, alpha skeletal muscle (ACTA1)	6	cytoskeleton; cytosol	53	15	115	5	42
P04075	Fructose-bisphosphate aldolase A (ALDOA)	8	cytoskeleton; cytosol; extracellular; membrane; nucleus	72	21	67	18	39.4
P05783	Keratin, type I cytoskeletal 18 (KRT18)	0	cytosol; nucleus	70	29	113	28	48
O43852	Calumenin (CALU)	2	endoplasmic reticulum; extracellular; Golgi; membrane	59	19	48	19	37.1
P05787	Keratin, type II cytoskeletal 8 (KRT8)	0	cytoskeleton; cytosol; membrane; nucleus	71	32	155	27	53.7
P08670	Vimentin (VIM)	1	cytoskeleton; cytosol; membrane	76	36	225	33	53.6
P04406	Glyceraldehyde-3-phosphate dehydrogenase (GAPDH)	3	cytoskeleton; cytosol; membrane; nucleus	57	16	54	16	36
O15260	Surfeit locus protein 4 (SURF4)	4	endoplasmic reticulum; Golgi; membrane	18	4	42	4	30.4
P04439	HLA class I histocompatibility antigen, A-3 alpha chain (HLA-A)	5	cell surface; endoplasmic reticulum; Golgi; membrane	53	15	28	2	40.8
Q15293	Reticulocalbin-1 (RCN1)	0	endoplasmic reticulum	57	15	30	15	38.9
P23526	Adenosylhomocysteinase (AHCY)	10	cytosol; nucleus	47	19	44	19	47.7
O75874	Isocitrate dehydrogenase [NADP] cytoplasmic (IDH1)	5	cytosol; extracellular; mitochondrion	53	19	33	17	46.6
P00505	Aspartate aminotransferase, mitochondrial (GOT2)	7	cell surface; membrane; mitochondrion	38	15	31	15	47.5
P04264	Keratin, type II cytoskeletal 1 (KRT1)	3	cytoskeleton; cytosol; extracellular; membrane; nucleus	57	33	101	29	66
P24752	Acetyl-CoA acetyltransferase, mitochondrial (ACAT1)	5	membrane; mitochondrion	37	12	18	12	45.2
P07339	Cathepsin D (CTSD)	9	extracellular; membrane vacuole	44	14	32	14	44.5

Q99536	Synaptic vesicle membrane protein VAT-1 homolog (VAT1)	4	extracellular; membrane; mitochondrion	52	13	45	13	41.9
P30460	HLA class I histocompatibility antigen, B-8 alpha chain (HLA-B)	6	cell surface; endoplasmic reticulum; Golgi; membrane	40	11	20	4	40.3
Q01105	HLA-DR-associated protein II (SET)	0	cytosol; endoplasmic reticulum; nucleus	30	7	10	7	33.5
P17174	Aspartate aminotransferase, cytoplasmic (GOT1)	4	cytosol; mitochondrion; nucleus; vacuole	55	18	19	18	46.2
Q96I99	Succinate--CoA ligase [GDP-forming] subunit beta, mitochondrial (SUCLG2)	6	membrane; mitochondrion	46	17	18	17	46.5

---

<sup>a</sup>PSMs: post-translational modifications <sup>b</sup>MW: molecular weight

Table V-11 Most abundant proteins around 55 kDa in A172 cells

Accession	Description	# cysteines	Location	Coverage [%]	# Peptides	# PSMs	# Unique Peptides	MW [kDa]
P08670	Vimentin (VIM)	1	cytoskeleton; membrane	76	36	225	33	53.6
P06733	Alpha-enolase (ENO1)	6	cell surface; membrane; nucleus	66	20	79	16	47.1
P68104	Elongation factor 1-alpha 1 (EEF1A1)	6	cytoskeleton; extracellular; nucleus	55	16	82	7	50.1
P60709	Actin, cytoplasmic 1 (ACTB)	6	cytoskeleton; membrane; nucleus	74	21	184	9	41.7
P05787	Keratin, type II cytoskeletal 8 (KRT8)	0	cytoskeleton; membrane; nucleus	71	32	155	27	53.7
P05783	Keratin, type I cytoskeletal 18 (KRT18)	0	cytosol; nucleus	70	29	113	28	48
P04264	Keratin, type II cytoskeletal 1 (KRT1)	0	cytoskeleton; extracellular; nucleus	57	33	101	29	66
P07954	Fumarate hydratase, mitochondrial (FH)	3	cytoplasm; mitochondrion	54	17	34	17	54.6
Q15084	Protein disulfide-isomerase A6 (PDIA6)		cytosol; endoplasmic reticulum; membrane	39	13	25	13	48.1
P60842	Eukaryotic initiation factor 4A- I (EIF4A1)	4	cytosol; membrane; nucleus	53	18	37	10	46.1
P13645	Keratin, type I cytoskeletal 10 (KRT10)	4	cytoskeleton; membrane; nucleus	50	26	84	23	58.8
Q71U36	Tubulin alpha-1A chain (TUBA1A)	12	cytoskeleton; endosome; nucleus	53	17	82	1	50.1
O43852	Calumenin (CALU)	2	endoplasmic extracellular; membrane	59	19	48	19	37.1
P50454	Serpin H1 (SERPINH1)	2	cytoplasm; endoplasmic reticulum; membrane	55	18	29	18	46.4
P07099	Epoxide hydrolase 1 (EPHX1)	4	endoplasmic reticulum; membrane	56	20	49	20	52.9
O60664	Perilipin-3 (PLIN3)	3	cytosol; endosome; Golgi; membrane	63	19	41	19	47
P49411	Elongation factor Tu, mitochondrial (TUFM)	6	membrane; mitochondrion	54	19	41	19	49.5
O75390	Citrate synthase, mitochondrial (CS)	4	mitochondrion; nucleus	40	13	20	13	51.7



Q8NBS9	Thioredoxin domain-containing protein 5 (TXNDC5)	12	endoplasmic reticulum; extracellular	39	13	23	13	47.6
P35527	Keratin, type I cytoskeletal 9 (KRT9)	4	cytosol; membrane; nucleus	59	26	75	25	62
P26641	Elongation factor 1-gamma (EEF1G)	6	cytosol; endoplasmic reticulum; nucleus	32	14	24	14	50.1
P61158	Actin-related protein 3 (ACTR3)	8	cytoskeleton; membrane	53	17	24	17	47.3
Q12765	Secernin-1 (SCRN1)	11	cytoplasm; nucleus	39	14	30	14	46.4

---

<sup>a</sup>PSMs: post-translational modifications <sup>b</sup>MW: molecular weight

Table V-12 Most abundant proteins around 57 kDa in A172 cells

Accession	Description	# cysteines	Location	Coverage [%]	# Peptides	# PSMs	# Unique Peptides	MW [kDa]	
P08670	Vimentin (VIM)	1	cytoskeleton; membrane	cytosol;	76	36	225	33	53.6
Q71U36	Tubulin alpha-1A chain (TUBA1A)	12	cytoskeleton; endosome; nucleus	cytosol; membrane;	53	17	82	1	50.1
P04350	Tubulin beta-4A chain (TUBB4A)	8	cytoskeleton; nucleus	cytosol;	72	22	107	4	49.6
P27797	Calreticulin (CALR)	8	cytosol; reticulum; Golgi;	endoplasmic extracellular; membrane; nucleus	71	27	52	27	48.1
P05787	Keratin, type II cytoskeletal 8 (KRT8)	0	cytoskeleton; membrane;	cytosol; nucleus	71	32	155	27	53.7
P06576	ATP synthase subunit beta (ATP5F1B)	16	cell surface; mitochondrion;	membrane; nucleus	68	25	68	25	56.5
P07437	Tubulin beta chain (TUBB)	7	cytoskeleton; membrane;	extracellular; nucleus	67	21	134	4	49.6
P68104	Elongation factor 1-alpha 1 (EEF1A1)	6	cytoskeleton; extracellular;	cytosol; membrane; nucleus	55	16	82	7	50.1
P25705	ATP synthase subunit alpha (ATP5F1A)	2	membrane; mitochondrion		52	23	48	23	59.7
P60709	Actin, cytoplasmic 1 (ACTB)	6	cytoskeleton; membrane;	cytosol; nucleus	74	21	184	9	41.7
P68371	Tubulin beta-4B chain (TUBB4B)	8	cytoskeleton; extracellular;	cytosol; nucleus	67	21	118	1	49.8
P04264	Keratin, type II cytoskeletal 1 (KRT1)	3	cytoskeleton; extracellular;	cytosol; membrane; nucleus	57	33	101	29	66
P00352	Retinal dehydrogenase 1 (ALDH1A1)	11	cytosol		59	25	31	23	54.8
P35527	Keratin, type I cytoskeletal 9 (KRT9)	4	cytosol; membrane; nucleus		59	26	75	25	62
P00367	Glutamate dehydrogenase 1 (GLUD1)	6	cytoplasm; mitochondrion		43	20	25	20	61.4
P13645	Keratin, type I cytoskeletal 10 (KRT10)	4	cytoskeleton; membrane;	cytosol; nucleus	50	26	84	23	58.8
P50995	Annexin A11 (ANXA11)	6	cytoskeleton; membrane;	cytosol; nucleus	33	16	18	16	54.4

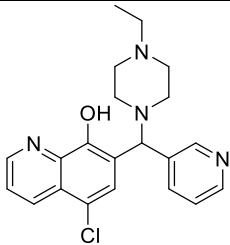
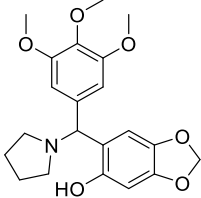
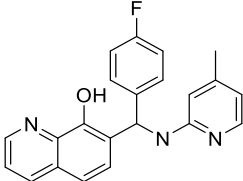
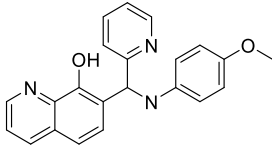
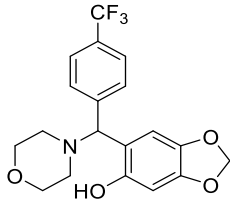
Q6NZI2	Caveolae-associated protein 1 (CAVIN1)	0	cytosol; endoplasmic reticulum; mitochondrion; nucleus	35	13	22	13	43.5
P09622	Dihydropyridine dehydrogenase (DLD)	10	mitochondrion	33	13	18	13	54.1
Q07960	Rho GTPase-activating protein 1 (ARHGAP1)	1	cytosol; membrane; endosome;	52	16	18	16	50.4
P06733	Alpha-enolase (ENO1)	6	cell surface; cytosol; membrane; nucleus	66	20	79	16	47.1
P43490	Nicotinamide phosphoribosyltransferase (NAMPT)	5	cytosol; nucleus; extracellular;	53	19	20	19	55.5
Q16658	Fascin (FSCN1)	11	cytoskeleton; cytosol	44	18	19	18	54.5
P54727	UV excision repair protein RAD23 homolog B (RAD23B)	1	cytosol; nucleus; proteasome	44	12	12	10	43.1
P68366	Tubulin alpha-4A chain (TUBA4A)	13	cytoskeleton; cytosol; extracellular	54	17	70	6	49.9

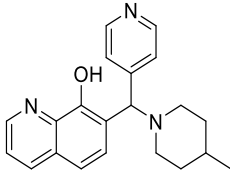
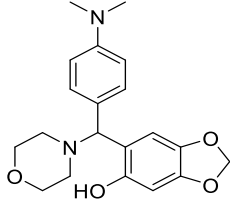
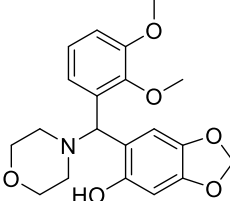
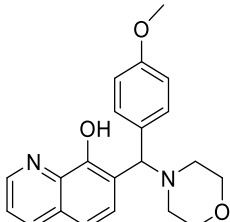
<sup>a</sup>PSMs: post-translational modifications <sup>b</sup>MW: molecular weight

Table V-13 PDI family members and molecular weight

Gene name	Size (kDa)	Gene name	Size (kDa)
P4HB	55	PDIA12 (TMX2)	34
PDIA2	55	PDIA13 (TMX3)	52
PDIA3 (ERp57)	54	PDIA14 (TMX4)	39
PDIA4 (ERp72)	71	(TMX5)	not reported
PDIA5 (PDIR)	57	PDIA15 (ERp46)	48
PDIA6 (P5)	46	PDIA16 (ERp19, AGR1)	18
PDIA7 (PDILT)	67	PDIA17 (AGR2, HAG-2)	20
PDIA8 (ERp27)	30	PDIA18 (AGR3, HAG-3)	19
PDIA9 (ERp29)	29	PDIA19 (ERdj5)	91
PDIA10 (ERp44)	44	PDIB1 (CASQ1)	45
PDIA11 (TMX1)	32	PDIB2 (CASQ2)	46

Table V-14 Known targets of similar inhibitors

Structure	Target	Size (kDa)	# of cysteines	cellular distribution
	HDAC5/HDAC9 <sup>15</sup>	122/111	14/11	nucleus
	STAT3/5 <sup>20</sup>	88/91	14/10	nucleus
	Mcl-1 <sup>29</sup>	37	2	nucleus
	MIF <sup>16-19</sup>	12.5	3	extracellular space
				

				
	P2Y12 <sup>30</sup>	39	10	cell membrane
	frataxin <sup>21</sup>	23	2	cytoplasm
	BRAF <sup>V600E</sup> 31	84	13	nucleus

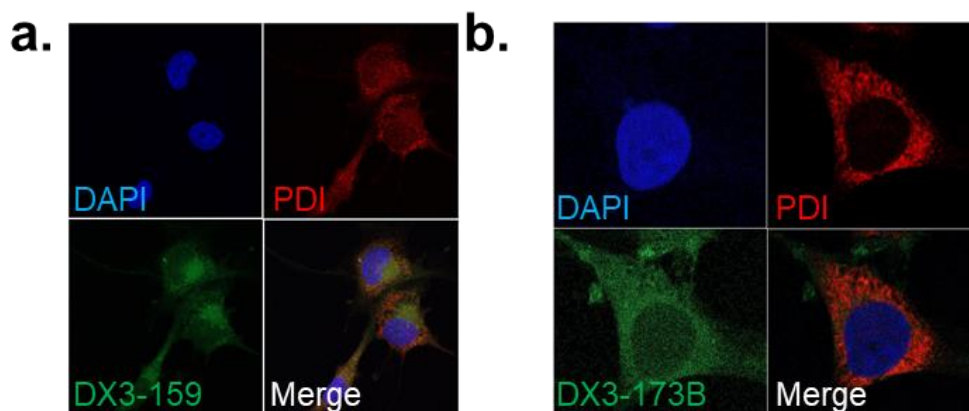


Figure V-21 Confocal microscopy images at 60X magnification of A172 cells treated with 10  $\mu\text{M}$  **DX3-159B** (A) or 2  $\mu\text{M}$  **DX3-173B** (B) for 24 h prior to fixation and staining for PDI

**AS15 Analogue Activates the Unfolded Protein Response.** We performed nascent RNA sequencing of one of the most potent analogues of **AS15**, **DX1-202**, to analyze changes in gene transcription in U87MG cells (Figure V-22).<sup>32</sup> Four hours after 20  $\mu\text{M}$  **DX1-202** treatment, 68 genes were upregulated at least two-fold and 12 genes were downregulated at least two-fold. We performed Gene Set Enrichment Analysis on the pre-ranked gene list of 7907 genes and identified that **DX1-202** upregulates transcription of genes involved in the unfolded protein response (Figure V-23). STRING (Search Tool for the Retrieval of Interacting Genes/Proteins) interactions of significant genes in the **DX1-202** Bru-seq dataset also demonstrated genes affected were involved in protein folding, ER stress, and response to ER stress (Figure V-22; Table V-15). Affected UPR genes included *CALR*, *HSPA5*, *MYZAP*, *NQO1*, and *SLC7A11*. Calreticulin (*CALR*) is an endoplasmic reticulum chaperone like PDI, specifically folds glycoproteins to be secreted, and mediates calcium homeostasis in the organelle.<sup>33</sup> Calreticulin acts as a sensor of ER stress because ER  $\text{Ca}^{2+}$  depletion triggers ER stress. Calreticulin has been demonstrated to bind to ERp57 and

regulate glycoprotein isomerization.<sup>34</sup> However, **DX1-202** treatment did not increase total cellular CALR expression in brain cancer cells (Figure V-22). *HSPA5* encodes for GRP78/BiP, an important chaperone responsible for promoting tumor growth.<sup>35</sup> Nascent polypeptides enter the endoplasmic reticulum and interact with GRP78/BiP to initiate protein folding. Increased transcription of GRP78/BiP indicates the cells are undergoing an unfolded protein stress response. NAD(P)H Quinone Dehydrogenase 1 (*NQO1*) is a cytosolic quinone reductase that promotes quinone-glutathione conjugation and removal from the cells. It is generally highly expressed in cancers and allows the tumor to cope with increased cytotoxic stress.<sup>36</sup> *SLC7A11* encodes for a cystine/glutamate antiporter protein that resides on the cell membrane. SLC7A11 is part of the system x<sub>c</sub><sup>-</sup> antiporter system that uptakes extracellular cystine as a precursor for GSH biosynthesis in exchange for glutamate.<sup>37</sup> Interestingly, we observed upregulated transcription of *SLC7A11* upon treatment with PDI inhibitor **35G8** as well.<sup>38</sup> Our results indicate that PDI inhibition may be synthetically lethal with system x<sub>c</sub><sup>-</sup> inhibition. Myocardial Zonula Adherens (*MYZAP*) is part of a transcriptional unit containing downstream gene POLR2M (polymerase (RNA) II (DNA directed) polypeptide M). MYZAP protein is expressed in cardiac tissue and is involved in signaling via Rho-related GTP-binding proteins. The Bru-seq RNA sequencing genes affected support **DX1-202**-mediated PDI inhibition in U87MG cells.



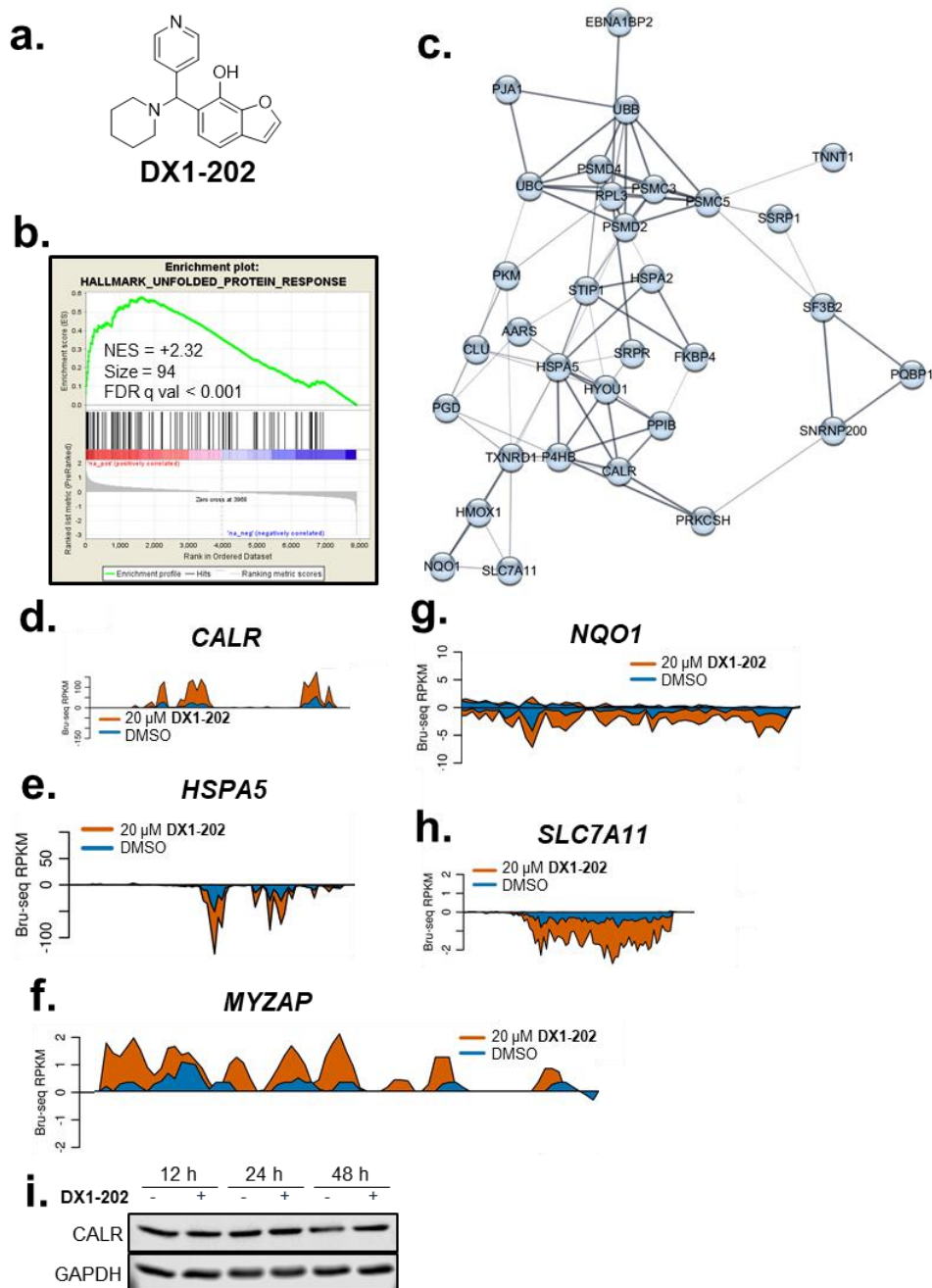
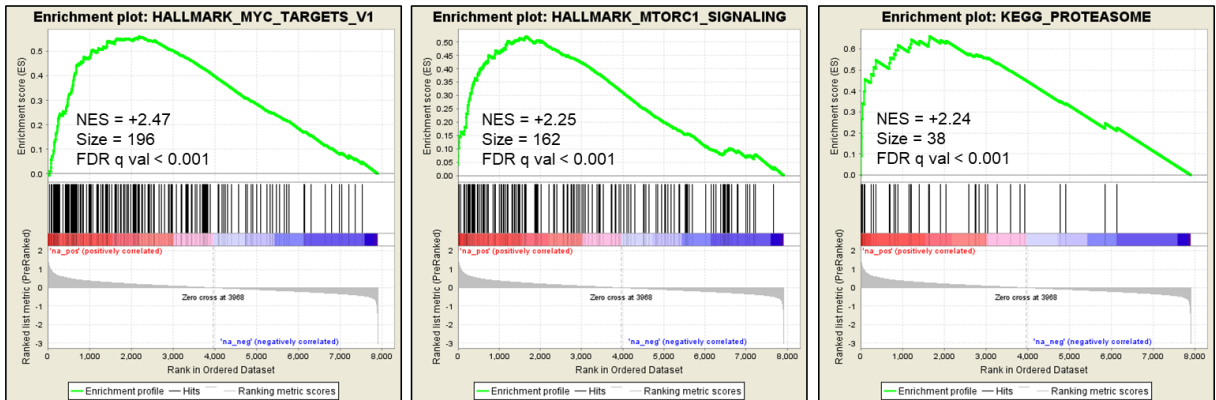


Figure V-22 **DX1-202** upregulates transcription of genes involved in the unfolded protein response. (A) Structure of **DX1-202**. (B) **DX1-202** promoted gene set enrichment similar to the unfolded protein response. NES: normalized enrichment score. FDR q val: false discovery rate q value. Criteria for GSEA was  $p < 0.05$  and false discovery rate  $< 25\%$ . (C) STRING interactions of significant genes in **DX1-202** Bru-seq dataset. Four-hour treatment with **DX1-202** increases transcription of representative unfolded protein response genes including *CALR* (D), *HSPA5* (E), *MYZAP* (F), *NQO1* (G), and *SLC7A11* (H). (I) U118MG cells were treated with 20  $\mu\text{M}$  **DX1-202** for 12, 24, or 48 h and probed for calreticulin protein expression. GAPDH is used as a loading control.

a.



b.

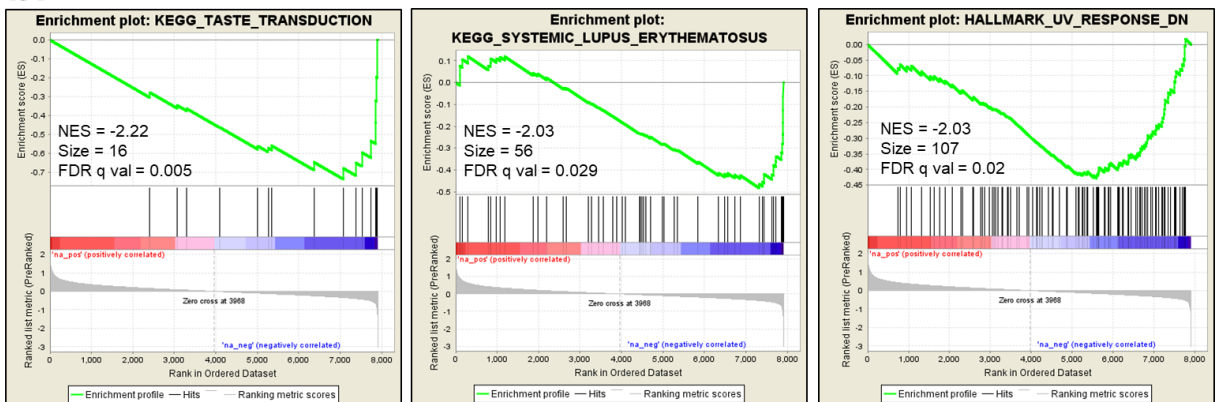


Figure V-23 Compound **DX1-202** treatment (20  $\mu$ M in U87MG cells) positively correlates with enrichment of (A) HALLMARK\_MYC\_TARGETS\_V1, HALLMARK\_MTORC1\_SIGNALING, and KEGG\_PROTEASOME, and negatively correlates with enrichment of (B) KEGG\_TASTE\_TRANSDUCTION, KEGG\_SYSTEMIC\_LUPUS\_ERYTHEMATOSUS, and HALLMARK\_UV\_RESPONSE\_DN. NES: normalized enrichment score; FDR q-val: false discovery rate q-value

Table V-15 STRING process terms for significantly affected genes upon **DX1-202** treatment.

term description	observed gene count	background gene count	false discovery rate	matching proteins in your network (labels)
protein folding	7	214	0.00021	CALR,CLU,FKBP4,HSPA2,HSPA5,P4HB,PIIB
response to endoplasmic reticulum stress	7	240	0.00022	CALR,HSPA5,HYOU1,P4HB,PSMC3,PSMC5,SRPR
proteasome-mediated ubiquitin-dependent protein catabolic process	7	257	0.00023	HSPA5,PSMC3,PSMC5,PSMD2,PSMD4,UBB,UBC

We further analyzed the Bru-seq signature of **DX1-202** with the Connectivity Map (Table V-16; Table V-17).<sup>39</sup> Because less than ten genes were significantly downregulated upon **DX1-202** treatment, the Connectivity Map analysis included only upregulated genes. **DX1-202** had a similar gene expression signature as the seleno-organic glutathione peroxidase mimetic ebselen.<sup>40</sup> Ebselen is an antioxidant that is known to react with cysteines, and it targets GTPase protein Rac1 in humans.<sup>41, 42</sup> Interestingly, ebselen inhibits MIF tautomerase activity as well.<sup>18</sup> This indicates that the signature of **DX1-202** may be an artifact of global cysteine reactivity rather than selective target inhibition. Furthermore, the signature of **DX1-202** demonstrated similarity with knockdown of *KDEL3* (KDEL endoplasmic reticulum protein retention receptor 3). *KDEL3* contains four cysteines and is upregulated as part of the unfolded protein response.<sup>43</sup> The protein is in a family of three KDEL receptors localized to the ER and Golgi complex. These results confirm that **DX1-202** exhibits a cysteine-reactive signature in brain cancer cells.

Table V-16 Top 25 compounds that positively correlate with **DX1-202** treatment in CMap.

<b>Name</b>	<b>Description</b>	<b>CMap Score</b>
avrainvillamide-analog-3	nucleophosmin inhibitor	99.47
BRD-K06817181	JAK inhibitor	99.40
perospirone	dopamine receptor antagonist	99.33
ebselen	GTPase inhibitor	99.33
hydroquinidine	antiarrhythmic	99.25
devazepide	CCK receptor antagonist	99.19
tosyl-phenylalanyl-chloromethyl-ketone	chymotrypsin inhibitor	98.84
erbstatin-analog	EGFR inhibitor	98.41
SA-792728	sphingosine kinase inhibitor	98.30
isoliquiritigenin	guanylate cyclase activator	98.17
sappanone-a	tyrosinase inhibitor	97.60
exemestane	aromatase inhibitor	96.86
CA-074-Me	cathepsin inhibitor	96.76
RITA	MDM inhibitor	96.62
penicillic-acid	other antibiotic	96.44
ABT-737	BCL inhibitor	96.30
tyrphostin-AG-82	EGFR inhibitor	95.36
NVP-AUY922	HSP inhibitor	95.35
capsazepine	TRPV agonist	94.82
INCA-6	calcineurin inhibitor	93.42
dihydro-7-desacetyldeoxygedunin	HSP inhibitor	93.30
etacrynic-acid	sodium/potassium/chloride transporter inhibitor	93.14
PD-160170	neuropeptide receptor antagonist	92.87
MNITMT	lymphocyte inhibitor	90.69
7b-cis	exportin antagonist	90.39

Table V-17 Top 25 compounds that negatively correlate with **DX1-202** treatment in CMap.

<b>Name</b>	<b>Description</b>	<b>CMap Score</b>
dexbrompheniramine	histamine receptor antagonist	-99.93
KU-C103428N	CDC inhibitor	-99.93
cabergoline	dopamine receptor agonist	-99.93
RO-90-7501	beta amyloid inhibitor	-99.93
calyculin	protein phosphatase inhibitor	-99.93
motesanib	KIT inhibitor	-99.89
L-745870	dopamine receptor antagonist	-99.89
TUL-XXI039	serine/threonine kinase inhibitor	-99.86
tandutinib	FLT3 inhibitor	-99.82
etilefrine	adrenergic receptor agonist	-99.82
telenzepine	acetylcholine receptor antagonist	-99.79
scopolamine	acetylcholine receptor antagonist	-99.79
erythromycin	NFkB pathway inhibitor	-99.79
rufloxacin	bacterial DNA gyrase inhibitor	-99.75
xanthoxyline	antifungal	-99.74
nefopam	cyclooxygenase inhibitor	-99.74
andarine	androgen receptor modulator	-99.72
mofezolac	cyclooxygenase inhibitor	-99.72
AR-A014418	glycogen synthase kinase inhibitor	-99.72
damnacanthal	SRC inhibitor	-99.71
tiaprofenic-acid	cyclooxygenase inhibitor	-99.69
axitinib	PDGFR receptor inhibitor	-99.68
NAS-181	serotonin receptor antagonist	-99.61
betaxolol	adrenergic receptor antagonist	-99.61
olanzapine	dopamine receptor antagonist	-99.59

## Discussion

Target engagement in cells is a critical aspect of preclinical targeted drug development. It is important to understand and verify that the compound can hit the target, and that interaction causes the observed phenotype. There are multiple techniques used to assess target engagement, including direct assays such as the cellular thermal shift assay (CETSA), drug affinity responsive target stability (DARTS), the NanoLuc thermal shift assay, and bioluminescence resonance energy transfer (BRET), or indirect methods such as knockdown effects or biomarker expression.<sup>44</sup> The core scaffold of **AS15** contains a phenolic Mannich base, which is a known promiscuous structure.<sup>45</sup> Thus, these compounds require careful assessment beyond lead discovery, especially in terms of selective target engagement. In order to determine on-target labeling of PDI in cells, we synthesized two variations of BODIPY-labeled **AS15** analogues. Our initial discovery upon treating cells with these compounds was that the compounds bind to serum albumin, an abundant protein containing 35 cysteine residues. When the **AS15** analogues were incubated with the cell lysates, we observed binding in three major bands, indicating that the compounds bound to proteins around 57 and 40 kDa. While plasma protein binding is a consideration for improvement of potency of this series, it will be important to establish whether one of the bands in the lysate contains PDIA1, and what the other targets of the compounds are. If the targets are identified, selectivity could be optimized to one or more of the targets.

These results corroborate previous findings with this Mannich base series. Targets identified for this series of compounds are summarized in Table V-14. The frataxin inhibitor, which differed from **AS15** by only an ortho methoxy that replaced the para methoxy, was non-

toxic up to 100  $\mu\text{M}$  in cells and dose-dependently prevented the ubiquitination of frataxin. The authors did not perform selectivity experiments since they were measuring a cellular protein function; however, they did show that the compound did not bind denatured protein. In the same year, another group reported a series of hydroxyquinolines similar to **CD343** as selective Mcl-1 inhibitors. With an SAR campaign, they demonstrated that the hydroxyl group and nitrogen were important for Mcl-1 activity. While we did not test their reported Compound 9, **DX1-23** and **DX1-24** are similar compounds, with the piperazine replaced by a morpholino group or pyrazine group. These compounds had submicromolar  $\text{IC}_{50}$  values in the PDI reductase assay, similar to the  $\text{IC}_{50}$  against Mcl-1 in the fluorescence polarization assay. In terms of selectivity, the researchers were able to demonstrate a correlation between a downstream response to Mcl-1 inhibition – cytochrome c release, and the extent of mitochondrial priming in cells.<sup>29</sup> Further targets of this series include HDAC5/9 and STAT3/5, BRAF<sup>V600E</sup>, and P2Y12. **NC124** was highly potent against leukemia cell lines (THP-1 and KASUMI-1), though it was much less potent against U87MG cells ( $\text{IC}_{50} = 24.2 \pm 7.1 \mu\text{M}$ ), possibly because TET1 expression is relatively lower.<sup>46</sup> Interestingly, several of the groups remarked that this series of compounds passed protein reactivity filters.

Because the analogues we tested were inactivated by GSH addition in the PDI reductase assay, we tested whether GSH depletion in a cell-based assay would influence potency. The compounds were all more potent when the cells were treated with non-toxic concentrations of BSO, the glutathione synthesis inhibitor. This result suggests that either the compounds are being sequestered by GSH in the cytoplasm and unable to reach the target protein, or that GSH depletion

prevents PDI from rescue. Thus, a potential strategy for further modification would include decreasing GSH reactivity of the series.

The glutathione-mediated antioxidant defense system is upregulated in cancer cells compared to normal cells to mitigate the harmful byproducts of increased cell metabolism.<sup>47</sup> Thus, increased concentrations of GSH are responsible for resistance to anti-cancer therapy. Temozolomide-resistant GBM tumors rely on glutathione antioxidant signaling pathways for survival.<sup>48</sup> Glutathione promotes metastasis in liver cancer and overexpression of glutathione synthesis enzymes has been linked with drug resistance.<sup>49, 50</sup>

Starting from a lead compound containing a benzobenzoxole scaffold and morpholine moiety, we investigated modifications around the core. The trends in the structure-activity relationships of the analogues that a tertiary amine and hydroxyl group were critical for activity demonstrated that the inhibitors likely bound to the active site cysteines of PDI. These results were validated by protein mass spectrometry that showed that **AS15** analogues bound in the active site of PDI. Though the compounds were potent *in vitro* inhibitors of PDI, glutathione inactivated the compounds, and target engagement will need optimization to move this series forward. The promiscuity of this series requires careful medicinal chemistry optimization to pursue as a target-based anti-cancer strategy. Because of the binding pattern of the **AS15** analogues and reactivity with glutathione, they have the potential to be optimized as *in vivo* thiol-reactive inhibitors.



## Experimental section

**Cell Culture.** Human glioblastoma cells U87MG, NU04 and A172 were obtained from the ATCC (Manassas, VA), and NU04 and A172 were maintained in RPMI-1640 (Thermo Fisher Scientific, Waltham, MA) supplemented with 10 % fetal bovine serum (FBS) (Thermo Fisher Scientific). Dulbecco's phosphate-buffered saline (DPBS) was purchased from Thermo Fisher Scientific. U87MG and HEK293T cells were maintained in DMEM supplemented with 10 % FBS. Cells were grown as monolayer cultures at 37 °C in a humidified atmosphere of 5 % CO<sub>2</sub> and tested for *Mycoplasma* contamination with the *Mycoplasma* detection kit, Plasmotest (InvivoGen, San Diego, California). All cell lines were authenticated with STR DNA profiling (University of Michigan, Michigan, USA) and matched to reference profiles from the AATC database. 3-(4,5-dimethylthiazol-2-yl)-2, 5-diphenyltetrazolium bromide (MTT) was purchased from Amresco (Solon, OH). Small molecule screening libraries were purchased from ChemDiv (San Diego, CA) or obtained from the National Cancer Institute through the Developmental Therapeutics Program.

**PDI protein purification.** PDI for this project was purified as reported in **Chapter 3**. PDIp, ERp57, and the a'c domain of PDI were purified as described previously.<sup>22</sup>

**Site-directed mutagenesis.** H256A and C53S mutants of PDI were obtained using wild-type PDI as the DNA template with the QuikChange II XL Site Directed Mutagenesis kit (Agilent Technologies, Santa Cruz, CA). Procedure was performed according to the manufacturer's protocol. All constructs were sequenced for verification and no additional mutations were

observed. Mutant PDI constructs were transformed into BL21 DE(3) cells and purified according to the wild-type PDI purification protocol.

**PDI reductase assay.** PDI activity was assessed by measuring the PDI-catalyzed reduction of insulin as described previously.<sup>17</sup> In brief, recombinant PDI protein (0.4  $\mu$ M or 50 nM for PDIA1, 1.6  $\mu$ M PDIp or ERp57) was incubated with indicated compounds at 37 °C for 1 hour in sodium phosphate buffer (100 mM sodium phosphate, 2 mM EDTA, 8  $\mu$ M DTT, pH 7.0). A mixture of sodium phosphate buffer, DTT (500  $\mu$ M or 125  $\mu$ M for 50 nM PDI reaction), and bovine insulin (130  $\mu$ M; Gemini BioProducts, West Sacramento, CA) was added to the incubated PDI protein. The reduction reaction was catalyzed by PDI at room temperature, and the resulting aggregation of reduced insulin B chains was measured at 620 nm. PDI activity was calculated with the formula, 
$$\text{PDI activity (\%)} = \frac{[(\text{OD}_{\text{T60}}[\text{PDI+DTT+compound}] - \text{OD}_{\text{T0}}[\text{PDI+DTT+compound}]) - (\text{OD}_{\text{T60}}[\text{DTT}] - \text{OD}_{\text{T0}}[\text{DTT}])]}{[(\text{OD}_{\text{T60}}[\text{PDI+DTT}] - \text{OD}_{\text{T0}}[\text{PDI+DTT}]) - (\text{OD}_{\text{T60}}[\text{DTT}] - \text{OD}_{\text{T0}}[\text{DTT}])]} \times 100$$
 (OD<sub>T0</sub> and OD<sub>T60</sub> were the absorbance values at 0 and 60 min after the reduction reaction, respectively). For reactions containing 50 nM PDI, PDI activity was measured at T180, or 180 min after insulin was added.

To determine the  $K_{\text{inact}}/k_{\text{I}}$  of covalent PDI inhibitors, the published procedure was adapted with the following modifications.<sup>8</sup> Compounds were incubated at 13.2  $\mu$ M, 19.8  $\mu$ M, 29.6  $\mu$ M, 44.4  $\mu$ M, 66.7  $\mu$ M, 100  $\mu$ M, and 150  $\mu$ M for 5, 15, 30, 45, or 60 min before addition of the insulin solution. The linear portions of the slopes of each kinetic curve obtained were used to calculate the  $K_{\text{obs}}$  in GraphPad Prism. The  $k_{\text{obs}}$  at each concentration was plotted to obtain the slope of the linear portion of the line as  $K_{\text{inact}}/k_{\text{I}}$ .

**Growth inhibition assay.** Cell growth inhibition was assessed by MTT assay as previously described in **Chapter 3**.<sup>61</sup> Cells were seeded in duplicate in 96-well plates at 3000 – 5000 cells/well. For glutathione depletion experiments, cells were pretreated for 24 h with buthionine sulfoximine (1 mM in A172 or 4  $\mu$ M in U118MG) before compound addition.

**Thermal shift assay.** Thermal shift of purified PDI (0.3 mg/ml in 100 mM NaPO<sub>4</sub>, pH 7.0) in the presence or absence of indicated compounds was determined as described.<sup>18</sup> Briefly, PDI, 100  $\mu$ M compound or DMSO as a vehicle control, 1X ROX dye, and 5  $\mu$ l Protein Thermal Shift Buffer were mixed to a 20  $\mu$ l total volume in a 384-well microplate. Each reaction was repeated in quadruplicate and reactions were mixed before measurements were taken. The plate was heated from 25 to 90 °C at 0.05 °C/second with the ViiA 7 Real-Time PCR System (Thermo Fisher Scientific, Waltham, MO). Melt curves were analyzed with the Protein Thermal Shift software (Thermo Fisher Scientific) and Boltzmann melting temperatures were reported.

**Reversibility Assay.** PDI activity was assessed by measuring the PDI-catalyzed reduction of insulin as described previously.<sup>17</sup> In brief, 0.4  $\mu$ M recombinant PDI was incubated with compounds at indicated concentrations at 37 °C for 1 hour in sodium phosphate buffer (100 mM sodium phosphate, 2 mM EDTA, 8  $\mu$ M DTT, pH 7.0). For samples containing diluted protein-compound complexes, 40  $\mu$ M PDI was incubated with 100  $\mu$ M **PACMA31**, 50  $\mu$ M **BAP2**, 50  $\mu$ M **AS15**, or 50  $\mu$ M **CD343** for 3 h at room temperature. The mixtures were diluted 100-fold into buffer (100 mM sodium phosphate, 2 mM EDTA, 8  $\mu$ M DTT, pH 7.0) and added to the 384-well, black, clear-bottom plate. A mixture of sodium phosphate buffer, DTT (500  $\mu$ M), and bovine insulin (130  $\mu$ M; Gemini BioProducts, West Sacramento, CA) was added to the incubated

PDI-compound samples. The reduction reaction was catalyzed by PDI at room temperature, and the resulting aggregation of reduced insulin B chains was measured at 620 nm. Absorbance at 620 nm was measured in a 384-well black-walled, clear-bottom plate.

**1-Anilinonaphthalene-8-sulfonic acid (ANS) Spectral Scan.** The ANS spectral scan was performed as previously described.<sup>26</sup> Briefly, 5  $\mu\text{M}$  PDI was incubated in the presence 100  $\mu\text{M}$  compounds or equivalent DMSO concentration in 50  $\mu\text{L}$  of TBS at 37  $^{\circ}\text{C}$  for 1 hour. Subsequently, 50 mM ANS was added and the mixture was incubated in the dark at 25  $^{\circ}\text{C}$  for 20 min. Fluorescence spectrum (Ex: 370 nm, Em: 400–700 nm) was measured in a 384-well black-walled, clear-bottom plate.

**Bromouridine RNA Sequencing (Bru-seq).** Bru-seq was performed as previously described.<sup>51</sup> U87MG cells were treated with DMSO or **DX1-202** (20  $\mu\text{M}$ ) for 4 h. 2 mM Bru was added in the last 30 min of treatment. Cells were collected, and total RNA was isolated with TRIzol reagent. Bru-labeled RNA was captured from total RNA by incubation with anti-BrdU antibodies (BD Biosciences) conjugated to magnetic beads (Dynabeads, goat anti-mouse IgG; Invitrogen). Bru-containing RNA population was isolated and sequenced. Sequencing reads were mapped to the hg38 reference genome. Pre-ranked gene lists were generated for each treatment ranking genes by fold change in transcription compared to control. Sequencing results were filtered using cutoff value of gene size > 300 bp and mean RPKM > 0.5.

The datasets were interrogated with Gene Set Enrichment Analysis (GSEA).<sup>52</sup> A log<sub>2</sub>(fold change) pre-ranked gene list of 7,908 genes was analyzed for gene enrichment using GSEA gene sets based

on the Kolmogorov-Smirnov statistic. For each gene set, an enrichment score (ES) was normalized to account for the difference in gene set size, and the false discovery rate (FDR) was calculated based on the normalized enrichment score (NES) values.

**Western blot.** Cells were harvested with a lysis buffer (25 mM tris(hydroxymethyl)aminomethane, 150 mM NaCl, 17 mM Triton X-100, 3.5 mM SDS, pH 7.4), lysed via sonication, and spun in a centrifuge at 13,500g at 4 °C for 10 min. Supernatant was collected and protein concentration determined with the BCA assay (Thermo Fisher Scientific, Waltham, MO). Samples were prepared with 30 µg protein and loaded onto 10 % acrylamide (Bio-Rad, Hercules, CA) gels. Protein from gels was electrotransferred to methanol-activated immobilon-FL PVDF membranes (EMD Millipore, La Jolla, CA). Membranes were blocked for 1 hour with Odyssey Blocking Buffer (LI-COR Biosciences, Lincoln, NE). Membranes were probed for proteins using primary antibodies (PDI, Cell Signaling, Danvers, MA, 1:1000) overnight at 4 °C. Membranes were incubated with secondary antibodies (anti-rabbit, Cell Signaling, 1:7500, or anti-mouse, Cell Signaling, 1:7500), and fluorescence was imaged by Odyssey imaging system (LI-COR Biosciences).

**Proteomics.** U118MG cells were seeded in a 6-well plate at  $0.5 \times 10^6$  cells/well in RPMI supplemented with 10 % FBS and allowed to attach overnight. Cells were treated with DMSO or 40 µM **DX3-159** overnight. Cells were washed with PBS and harvested with Cell Lytic M buffer (Sigma). The cells were lysed by incubation for 1 h on ice and spun in a centrifuge at 13,500g at 4 °C for 10 min. Supernatant was collected and protein concentration determined with the BCA assay (Thermo Fisher Scientific, Waltham, MO). For the proteomics experiment with A172 cells,

cell lysates in Cell Lytic M buffer were incubated with 10  $\mu$ M **DX3-173B** overnight at room temperature. Samples were prepared with 50  $\mu$ g protein boiled with Laemmli sample buffer and loaded onto 1 mm 10 % acrylamide gels. The gel was immediately imaged on the iBright with the GFP channel and stained with Coomassie. The band containing the BODIPY-labeled compound was cut out, digested, and analyzed at the University of Michigan Proteomics Resource Facility in the Department of Pathology.

**Confocal imaging.** A172 cells were treated with 10  $\mu$ M **DX3-159** or 2  $\mu$ M **DX3-173B** overnight. Cells were fixed in 4% paraformaldehyde for 15 minutes at room temperature and washed with 1X PBS before blocking in 10% fetal bovine serum for 60 minutes. PDI antibody (Cell Signaling; 3501S) was applied at 1:100 dilution in overnight at 4 °C. ProLong Diamond with DAPI (Invitrogen) was used to prepare the slides for analysis on the ZEISS Laser Scanning Microscope.

**Gel-based binding assays.** Gel-based binding assays were performed with recombinant protein and cell lysate, as indicated. Briefly, cells were coated in 6-well or 12-well plates. After overnight attachment, cells were either serum-starved, treated with BSO, or treated with test compounds at indicated concentrations overnight at 37 °C, 5 % CO<sub>2</sub>. Cells were then washed with PBS and lysed using Cell Lytic M buffer (Sigma) for 60 min on ice. A unit of 30-50  $\mu$ g of whole-cell protein was boiled with Laemmli sample buffer or non-reducing sample buffer (62.5 mM Tris-HCl, pH 6.8. 10% glycerol. 2% SDS. 0.05% bromophenol blue) and resolved on a 10% polyacrylamide gel. Gels were immediately imaged on an iBright imaging system (Thermo Fisher Scientific). For cell lysates, cells were harvested as above prior to compound treatment, then incubated with compounds overnight at room temperature before subjecting to SDS-PAGE. Similarly, *in vitro*

binding assays with recombinant PDIA1, PDIp, ERp57, and BSA were performed using 3.5  $\mu$ M protein in Cell Lytic M buffer incubated with compounds overnight at room temperature.

**Statistical analysis.** The IC<sub>50</sub> values were calculated using GraphPad Prism 7 software (GraphPad Software, Inc.). The error bars indicate mean  $\pm$  s.d. Bru-seq experiments were performed once.

## References

1. Wang, C.; Li, W.; Ren, J.; Fang, J.; Ke, H.; Gong, W.; Feng, W.; Wang, C. C. Structural insights into the redox-regulated dynamic conformations of human protein disulfide isomerase. *Antioxid Redox Signal* **2013**, *19*, 36-45.
2. Zou, H.; Wen, C.; Peng, Z.; Shao, Y.; Hu, L.; Li, S.; Li, C.; Zhou, H. H. P4HB and PDIA3 are associated with tumor progression and therapeutic outcome of diffuse gliomas. *Oncol Rep* **2018**, *39*, 501-10.
3. Lee, D.; Sun, S.; Ho, A. S.; Kiang, K. M.; Zhang, X. Q.; Xu, F. F.; Leung, G. K. Hyperoxia resensitizes chemoresistant glioblastoma cells to temozolomide through unfolded protein response. *Anticancer Res* **2014**, *34*, 2957-66.
4. Xu, S.; Sankar, S.; Neamati, N. Protein disulfide isomerase: A promising target for cancer therapy. *Drug Discov Today* **2014**, *19*, 222-40.
5. Xu, S.; Butkevich, A. N.; Yamada, R.; Zhou, Y.; Debnath, B.; Duncan, R.; Zandi, E.; Petasis, N. A.; Neamati, N. Discovery of an orally active small-molecule irreversible inhibitor of protein disulfide isomerase for ovarian cancer treatment. *Proc Natl Acad Sci U S A* **2012**, *109*, 16348-53.
6. Won, J. K.; Yu, S. J.; Hwang, C. Y.; Cho, S. H.; Park, S. M.; Kim, K.; Choi, W. M.; Cho, H.; Cho, E. J.; Lee, J. H.; Lee, K. B.; Kim, Y. J.; Suh, K. S.; Jang, J. J.; Kim, C. Y.; Yoon, J. H.; Cho, K. H. Protein disulfide isomerase inhibition synergistically enhances the efficacy of sorafenib for hepatocellular carcinoma. *Hepatology* **2017**, *66*, 855-68.
7. Lappi, A. K.; Lensink, M. F.; Alanen, H. I.; Salo, K. E.; Lobell, M.; Juffer, A. H.; Ruddock, L. W. A conserved arginine plays a role in the catalytic cycle of the protein disulphide isomerases. *J Mol Biol* **2004**, *335*, 283-95.
8. Cole, K. S.; Grandjean, J. M. D.; Chen, K.; Witt, C. H.; O'Day, J.; Shoulders, M. D.; Wiseman, R. L.; Weerapana, E. Characterization of an A-site selective protein disulfide isomerase A1 inhibitor. *Biochemistry* **2018**, *57*, 2035-43.
9. Chen, I. H.; Chang, F. R.; Wu, Y. C.; Kung, P. H.; Wu, C. C. 3,4-Methylenedioxy-beta-nitrostyrene inhibits adhesion and migration of human triple-negative breast cancer cells by suppressing beta1 integrin function and surface protein disulfide isomerase. *Biochimie* **2015**, *110*, 81-92.



10. Hoffstrom, B. G.; Kaplan, A.; Letso, R.; Schmid, R. S.; Turmel, G. J.; Lo, D. C.; Stockwell, B. R. Inhibitors of protein disulfide isomerase suppress apoptosis induced by misfolded proteins. *Nat Chem Biol* **2010**, 6, 900-6.
11. Foster, C. K.; Thorpe, C. Challenges in the evaluation of thiol-reactive inhibitors of human protein disulfide Isomerase. *Free Radic Biol Med* **2017**, 108, 741-9.
12. Ogunrinu, T. A.; Sontheimer, H. Hypoxia increases the dependence of glioma cells on glutathione. *J Biol Chem* **2010**, 285, 37716-24.
13. Lv, H.; Zhen, C.; Liu, J.; Yang, P.; Hu, L.; Shang, P. Unraveling the potential role of glutathione in multiple forms of cell death in cancer therapy. *Oxid Med Cell Longev* **2019**, 2019, 3150145.
14. Montero, D.; Tachibana, C.; Rahr Winther, J.; Appenzeller-Herzog, C. Intracellular glutathione pools are heterogeneously concentrated. *Redox Biol* **2013**, 1, 508-13.
15. Boskovic, Z. V.; Kemp, M. M.; Freedy, A. M.; Viswanathan, V. S.; Pop, M. S.; Fuller, J. H.; Martinez, N. M.; Figueroa Lazu, S. O.; Hong, J. A.; Lewis, T. A.; Calarese, D.; Love, J. D.; Vetere, A.; Almo, S. C.; Schreiber, S. L.; Koehler, A. N. Inhibition of zinc-dependent histone deacetylases with a chemically triggered electrophile. *ACS Chem Biol* **2016**, 11, 1844-51.
16. McLean, L. R.; Zhang, Y.; Li, H.; Li, Z.; Lukasczyk, U.; Choi, Y. M.; Han, Z.; Prisco, J.; Fordham, J.; Tsay, J. T.; Reiling, S.; Vaz, R. J.; Li, Y. Discovery of covalent inhibitors for MIF tautomerase via cocrystal structures with phantom hits from virtual screening. *Bioorg Med Chem Lett* **2009**, 19, 6717-20.
17. Zapatero, M. C.; Perez, P.; Vazquez, M. J.; Colmenarejo, G.; de Los Frailes, M.; Ramon, F. Discovery of novel inhibitors of the tautomerase activity of macrophage migration inhibitory factor (MIF). *J Biomol Screen* **2016**, 21, 446-58.
18. Ouertatani-Sakouhi, H.; El-Turk, F.; Fauvet, B.; Cho, M. K.; Pinar Karpinar, D.; Le Roy, D.; Dewor, M.; Roger, T.; Bernhagen, J.; Calandra, T.; Zweckstetter, M.; Lashuel, H. A. Identification and characterization of novel classes of macrophage migration inhibitory factor (MIF) inhibitors with distinct mechanisms of action. *J Biol Chem* **2010**, 285, 26581-98.
19. Cisneros, J. A.; Robertson, M. J.; Valhondo, M.; Jorgensen, W. L. Irregularities in enzyme assays: The case of macrophage migration inhibitory factor. *Bioorg Med Chem Lett* **2016**, 26, 2764-7.
20. Jiang, X.; Hu, C.; Ferchen, K.; Nie, J.; Cui, X.; Chen, C. H.; Cheng, L.; Zuo, Z.; Seibel, W.; He, C.; Tang, Y.; Skibbe, J. R.; Wunderlich, M.; Reinhold, W. C.; Dong, L.; Shen, C.; Arnovitz, S.; Ulrich, B.; Lu, J.; Weng, H.; Su, R.; Huang, H.; Wang, Y.; Li, C.; Qin, X.; Mulloy, J. C.; Zheng, Y.; Diao, J.; Jin, J.; Li, C.; Liu, P. P.; He, C.; Chen, Y.; Chen, J. Targeted inhibition

of STAT/TET1 axis as a therapeutic strategy for acute myeloid leukemia. *Nat Commun* **2017**, *8*, 2099.

21. Lavecchia, A.; Di Giovanni, C.; Cerchia, C.; Russo, A.; Russo, G.; Novellino, E. Discovery of a novel small molecule inhibitor targeting the frataxin/ubiquitin interaction via structure-based virtual screening and bioassays. *J Med Chem* **2013**, *56*, 2861-73.

22. Xu, S.; Liu, Y.; Yang, K.; Wang, H.; Shergalis, A.; Kyani, A.; Bankhead, A., 3rd; Tamura, S.; Yang, S.; Wang, X.; Wang, C. C.; Rehemtulla, A.; Ljungman, M.; Neamati, N. Inhibition of protein disulfide isomerase in glioblastoma causes marked downregulation of DNA repair and DNA damage response genes. *Theranostics* **2019**, *9*, 2282-98.

23. Yang, S.; Shergalis, A.; Lu, D.; Kyani, A.; Liu, Z.; Ljungman, M.; Neamati, N. Design, synthesis, and biological evaluation of novel allosteric protein disulfide isomerase inhibitors. *J Med Chem* **2019**, *62*, 3447-74.

24. Serafimova, I. M.; Pufall, M. A.; Krishnan, S.; Duda, K.; Cohen, M. S.; Maglathlin, R. L.; McFarland, J. M.; Miller, R. M.; Frodin, M.; Taunton, J. Reversible targeting of noncatalytic cysteines with chemically tuned electrophiles. *Nat Chem Biol* **2012**, *8*, 471-6.

25. Madonna, S.; Beclin, C.; Laras, Y.; Moret, V.; Marcowycz, A.; Lamoral-Theys, D.; Dubois, J.; Barthelemy-Requin, M.; Lenglet, G.; Depauw, S.; Cresteil, T.; Aubert, G.; Monnier, V.; Kiss, R.; David-Cordonnier, M. H.; Kraus, J. L. Structure-activity relationships and mechanism of action of antitumor bis 8-hydroxyquinoline substituted benzylamines. *Eur J Med Chem* **2010**, *45*, 623-38.

26. Bekendam, R. H.; Bendapudi, P. K.; Lin, L.; Nag, P. P.; Pu, J.; Kennedy, D. R.; Feldenzer, A.; Chiu, J.; Cook, K. M.; Furie, B.; Huang, M.; Hogg, P. J.; Flaumenhaft, R. A substrate-driven allosteric switch that enhances PDI catalytic activity. *Nat Commun* **2016**, *7*, 12579.

27. Go, Y. M.; Jones, D. P. Redox compartmentalization in eukaryotic cells. *Biochim Biophys Acta* **2008**, *1780*, 1273-90.

28. Walker, K. W.; Gilbert, H. F. Oxidation of kinetically trapped thiols by protein disulfide isomerase. *Biochemistry* **1995**, *34*, 13642-50.

29. Richard, D. J.; Lena, R.; Bannister, T.; Blake, N.; Pierceall, W. E.; Carlson, N. E.; Keller, C. E.; Koenig, M.; He, Y.; Minond, D.; Mishra, J.; Cameron, M.; Spicer, T.; Hodder, P.; Cardone, M. H. Hydroxyquinoline-derived compounds and analoguing of selective Mcl-1 inhibitors using a functional biomarker. *Bioorg Med Chem* **2013**, *21*, 6642-9.

30. Ahn, Y. H.; Lee, J. Y.; Park, H. D.; Kim, T. H.; Park, M. C.; Choi, G.; Kim, S. Identification of a new morpholine scaffold as a P2Y<sub>12</sub> receptor antagonist. *Molecules* **2016**, *21*, E1114.

31. Qin, J.; Xie, P.; Ventocilla, C.; Zhou, G.; Vultur, A.; Chen, Q.; Liu, Q.; Herlyn, M.; Winkler, J.; Marmorstein, R. Identification of a novel family of BRAF(V600E) inhibitors. *J Med Chem* **2012**, *55*, 5220-30.
32. Paulsen, M. T.; Veloso, A.; Prasad, J.; Bedi, K.; Ljungman, E. A.; Magnuson, B.; Wilson, T. E.; Ljungman, M. Use of Bru-Seq and BruChase-Seq for genome-wide assessment of the synthesis and stability of RNA. *Methods* **2014**, *67*, 45-54.
33. Wang, W. A.; Groenendyk, J.; Michalak, M. Calreticulin signaling in health and disease. *Int J Biochem Cell Biol* **2012**, *44*, 842-6.
34. Jessop, C. E.; Tavender, T. J.; Watkins, R. H.; Chambers, J. E.; Bulleid, N. J. Substrate specificity of the oxidoreductase ERp57 is determined primarily by its interaction with calnexin and calreticulin. *J Biol Chem* **2009**, *284*, 2194-202.
35. Wang, M.; Wey, S.; Zhang, Y.; Ye, R.; Lee, A. S. Role of the unfolded protein response regulator GRP78/BiP in development, cancer, and neurological disorders. *Antioxid Redox Signal* **2009**, *11*, 2307-16.
36. Oh, E. T.; Park, H. J. Implications of NQO1 in cancer therapy. *BMB Rep* **2015**, *48*, 609-17.
37. Koppula, P.; Zhang, Y.; Zhuang, L.; Gan, B. Amino acid transporter SLC7A11/xCT at the crossroads of regulating redox homeostasis and nutrient dependency of cancer. *Cancer Commun (Lond)* **2018**, *38*, 12.
38. Kyani, A.; Tamura, S.; Yang, S.; Shergalis, A.; Samanta, S.; Kuang, Y.; Ljungman, M.; Neamati, N. Discovery and mechanistic elucidation of a class of protein disulfide isomerase inhibitors for the treatment of glioblastoma. *ChemMedChem* **2018**, *13*, 164-77.
39. Lamb, J.; Crawford, E. D.; Peck, D.; Modell, J. W.; Blat, I. C.; Wrobel, M. J.; Lerner, J.; Brunet, J. P.; Subramanian, A.; Ross, K. N.; Reich, M.; Hieronymus, H.; Wei, G.; Armstrong, S. A.; Haggarty, S. J.; Clemons, P. A.; Wei, R.; Carr, S. A.; Lander, E. S.; Golub, T. R. The Connectivity Map: Using gene-expression signatures to connect small molecules, genes, and disease. *Science* **2006**, *313*, 1929-35.
40. Nakamura, Y.; Feng, Q.; Kumagai, T.; Torikai, K.; Ohigashi, H.; Osawa, T.; Noguchi, N.; Niki, E.; Uchida, K. Ebselen, a glutathione peroxidase mimetic seleno-organic compound, as a multifunctional antioxidant. Implication for inflammation-associated carcinogenesis. *J Biol Chem* **2002**, *277*, 2687-94.
41. Bender, K. O.; Garland, M.; Ferreyra, J. A.; Hryckowian, A. J.; Child, M. A.; Puri, A. W.; Solow-Cordero, D. E.; Higginbottom, S. K.; Segal, E.; Banaei, N.; Shen, A.; Sonnenburg, J. L.;

- Bogyo, M. A small-molecule antivirulence agent for treating *Clostridium difficile* infection. *Sci Transl Med* **2015**, *7*, 306ra148.
42. Beilhartz, G. L.; Tam, J.; Zhang, Z.; Melnyk, R. A. Comment on "A small-molecule antivirulence agent for treating *Clostridium difficile* infection". *Sci Transl Med* **2016**, *8*, 370tc2.
43. Trychta, K. A.; Back, S.; Henderson, M. J.; Harvey, B. K. KDEL receptors are differentially regulated to maintain the ER proteome under calcium deficiency. *Cell Rep* **2018**, *25*, 1829-40.e6.
44. Schurmann, M.; Janning, P.; Ziegler, S.; Waldmann, H. Small-molecule target engagement in cells. *Cell Chem Biol* **2016**, *23*, 435-41.
45. Baell, J. B.; Holloway, G. A. New substructure filters for removal of pan assay interference compounds (PAINS) from screening libraries and for their exclusion in bioassays. *J Med Chem* **2010**, *53*, 2719-40.
46. Fu, R.; Ding, Y.; Luo, J.; Yu, L.; Li, C. L.; Li, D. S.; Guo, S. W. TET1 exerts its tumour suppressor function by regulating autophagy in glioma cells. *Biosci Rep* **2017**, *37*, BSR20160523.
47. Bansal, A.; Simon, M. C. Glutathione metabolism in cancer progression and treatment resistance. *J Cell Biol* **2018**, *217*, 2291-8.
48. Zhu, Z.; Du, S.; Du, Y.; Ren, J.; Ying, G.; Yan, Z. Glutathione reductase mediates drug resistance in glioblastoma cells by regulating redox homeostasis. *J Neurochem* **2018**, *144*, 93-104.
49. Huang, Z. Z.; Chen, C.; Zeng, Z.; Yang, H.; Oh, J.; Chen, L.; Lu, S. C. Mechanism and significance of increased glutathione level in human hepatocellular carcinoma and liver regeneration. *FASEB J* **2001**, *15*, 19-21.
50. Lu, S. C. Regulation of glutathione synthesis. *Mol Aspects Med* **2009**, *30*, 42-59.
51. Paulsen, M. T.; Veloso, A.; Prasad, J.; Bedi, K.; Ljungman, E. A.; Tsan, Y. C.; Chang, C. W.; Tarrier, B.; Washburn, J. G.; Lyons, R.; Robinson, D. R.; Kumar-Sinha, C.; Wilson, T. E.; Ljungman, M. Coordinated regulation of synthesis and stability of RNA during the acute TNF-induced proinflammatory response. *Proc Natl Acad Sci U S A* **2013**, *110*, 2240-5.
52. Subramanian, A.; Tamayo, P.; Mootha, V. K.; Mukherjee, S.; Ebert, B. L.; Gillette, M. A.; Paulovich, A.; Pomeroy, S. L.; Golub, T. R.; Lander, E. S.; Mesirov, J. P. Gene set enrichment analysis: A knowledge-based approach for interpreting genome-wide expression profiles. *Proc Natl Acad Sci U S A* **2005**, *102*, 15545-50.

## CHAPTER VI

### Concluding Summary

#### Current state of glioblastoma drug discovery research

The aggressive nature and complex genetic origin of glioblastoma render most targeted therapies inactive against GBM tumor growth and underline the urgent need for research into new treatments. Even the current standard of care, temozolomide, a non-selective DNA alkylating agent, prolongs survival by only a few months before the tumor regains the ability to proliferate. Research into targeted agents has uncovered a variety of “driver” mutations and proteins, such as mTOR and BRAF V600 mutations, but the research has not yet resulted in targeted therapies for patients.<sup>1, 2</sup> Furthermore, brain cancer research should be built carefully on the foundation of neuroscience and an understanding of brain biology.

Several small molecules are undergoing clinical trials to treat glioblastoma. Ribociclib is a cyclin D1/CDK4 and CDK6 inhibitor approved to treat breast cancer that was tested in a Phase 0 study in patients with recurrent glioblastoma. Ribociclib was able to penetrate the blood-brain barrier, but exhibited limited efficacy in the small cohort (progression-free survival: 9.7 weeks, cohort size: 6 patients).<sup>3, 4</sup> Olaparib has also been tested in combination with the standard-of-care for GBM. Olaparib is a poly(ADP-ribose) polymerase (PARP) inhibitor that sensitizes tumors to radiation and chemotherapy. Olaparib typically causes hematological toxicity. However, patients in the OPARATIC trial tolerated intermittent dosing of olaparib with minimal dose-limiting

toxicity.<sup>5</sup> These results provided the rationale to continue into a randomized Phase II trial to further evaluate the efficacy of the combination. Dacomitinib, an irreversible EGFR tyrosine kinase inhibitor, was tested in patients with recurrent GBM with EGFR amplification in the GEINO11 trial.<sup>6</sup> Four of the 30 patients with EGFR amplification without EGFRvIII mutation were progression-free at 6 months; however, even though the study did not reach its endpoint, three patients were progression-free at 12 months. These results indicate that mutation status of other GBM drivers or outside factors may play a role in drug efficacy. Despite the low success rate of small molecules in GBM clinical trials, treatments based on the genetic characterization of the tumor may provide more promising results in future studies.

Small molecules are not the only glioblastoma treatment undergoing research. Extensive research is underway to study the efficacy of antibodies, vaccines, nanoparticles, stereotactic surgery and other types of radiotherapy on brain cancer prognosis. Of the eight completed Phase III trials from 2005 to 2016, only one had positive results.<sup>7</sup> The successful study used tumor-treating fields (TTF), or low-intensity, alternating electric fields administered on the scalp, to treat patients with glioblastoma who had completed concomitant chemotherapy following surgical resection. TTFs, when combined with temozolomide, significantly improved overall survival compared with patients receiving chemotherapy alone (20.9 months versus 16.0 months).<sup>8</sup> Immunotherapy has become another area of great interest for glioblastoma treatment, even though the tumor microenvironment enlists immunosuppressive mechanisms to limit drug efficacy.<sup>9</sup> For example, a dendritic cell vaccine generated with autologous tumor lysate, DCVax-L, was effective and preliminary results from the ongoing trial reported that early median survival of patients receiving the vaccine was 23.1 months.<sup>10</sup> The dendritic cell vaccine works by activating the natural

killer cells to destroy the tumor. An autologous dendritic cell vaccine is prepared by isolating the dendritic cells from a patient's blood and stimulating the cells with a cancer associated antigen. Dendritic cell vaccines represent a potential novel immune-oncology therapeutic strategy to treat glioblastoma, in addition to peptide vaccines and checkpoint inhibition. Furthermore, the oncolytic adenovirus DNX-2401, developed from the cold virus, showed promising activity in a Phase I trial in patients with recurrent malignant glioma. Of the 25 patients who received treatment, 20 % survived over 3 years after treatment.<sup>11</sup> Thus, the rationale for treating brain tumors with immune and viral therapy is growing. In the future, it could be possible that small molecules could be harnessed to hijack the complex pathways activated by these macromolecular therapies, to improve drug delivery and efficacy.

In addition to the novel types of glioblastoma therapies being explored, it will be likely that single agent targeted therapy would be ineffective at wiping out glioblastoma. Unlike the success of imatinib in chronic myeloid leukemia – a cancer that originates from a specific chromosomal abnormality – targeted therapies have had limited efficacy in glioblastoma. More likely, an arsenal of specific targeted agents will be able to selectively attack the tumor cells. Synthetic lethal screening campaigns, discussed in detail in Chapter 1, have attempted to identify potent combination therapies. Interestingly, a genome-wide CRISPR-Cas9 lethality screen revealed no synthetic lethal targets for common alterations including *RBI*<sup>mut</sup>, *TERT* expression, or *TP53*<sup>loss/mut</sup>.<sup>12</sup> This suggests that the cancer cell growth is either mediated by different pathways, or inhibition is more complex than the knockout of just two genes. While their results were not published, Hoellerbauer, et al. indicate that GBM cell growth is mediated by the RTK/Ras and PI3K pathway or amplification of *MYC* and *MYCN*.<sup>12</sup> Further questions must be addressed as well,

including clinical trial design, better preclinical models, and the involvement of the tumor microenvironment.<sup>13</sup>

### **Challenges of developing PDI inhibitors**

Developing effective PDI inhibitors requires careful consideration; thiol-reactive compounds are common pan-assay interference compounds because of their promiscuity. The mainstay of PDI inhibitor development is the PDI reductase assay because it is amenable to high throughput screening. However, because the assay requires the reducing agent dithiothreitol, redox cycling compounds can be false positives, as well as reactive electrophiles. The PDI reductase assay uses insulin as a substrate. Under reducing conditions, PDI reduces the disulfide bonds in insulin to break apart the a chain and b chain. In the PDI reductase assay, the b chain aggregates. Thus, thiol-reactive compounds can inhibit PDI activity, but thiol reactive compounds can be promiscuous, as demonstrated by the **AS15** analogues that inhibit PDI, but also MIF tautomerase, HDACs, STATs, and other targets. Thus, it is critical to validate PDI inhibitors with orthogonal assays during the initial phase of lead discovery to rule out promiscuous hits. To confirm PDI inhibition, we used multiple assays including the thermal shift assay, ANS spectral scan, drug affinity responsive stability (DARTS), and the cellular thermal shift assay. Furthermore, the endoplasmic reticulum as an organelle and its effects on small molecules should be considered. Firstly, the ER is a highly oxidizing environment that could modify reactive small molecules, especially substituents that are prone to oxidation. Additionally, phase I metabolic enzymes such as cytochrome P450 reside in the endoplasmic reticulum of various tissues including the liver, kidney, and brain, and could block a small molecule from reaching its target.



Because of the potential issues for selectivity with thiol directed PDI inhibitors, b' domain inhibitors represent a more selective approach for PDI inhibition. The b' domain is specific to PDI family members, and each b' domain of the PDI family members is unique for diverse substrate recognition. Several inhibitors have been characterized to bind in the substrate-binding pocket, including estradiol<sup>14</sup>, bepristat 1a<sup>15</sup>, isoquercetin<sup>16</sup>, and **BAP2**<sup>17</sup>. With the exception of **BAP2**, these inhibitors are less toxic than active site PDI inhibitors. For example, isoquercetin analogues are in clinical trials for thrombosis-related indications<sup>16</sup>. The low cytotoxicity of substrate-binding domain inhibitors may be related to their low binding affinity. For example, the  $K_d$  of quercetin, measured by isothermal calorimetry, is 18.3  $\mu\text{M}$ , and the binding  $K_d$  for **BAP2** is 9.4  $\mu\text{M}$ .<sup>18</sup> The low binding affinity for small molecules in the substrate-binding domain may be explained by the mechanism of PDI substrate proteins associating and dissociating with the pocket. If substrate-binding domain inhibitors were optimized for binding affinity, we may find a more potent cytotoxic PDI inhibitor that is ideally more selective.

### Summary of the dissertation

In this dissertation, a detailed preclinical evaluation of an extensive library of PDI inhibitors was carried out with a focus on scaffolds of three lead compounds: **35G8**, **BAP2**, and **AS15**. PDI plays a critical role in the proper disulfide bond formation of nascent polypeptides in the ER, and brain cancer cells are highly addicted to PDI. PDI knockdown is lethal to cancer cells, and PDI inhibition prevents neurosphere formation in patient derived GBM cells. Thus, PDI inhibition represents a potential anti-cancer strategy. Major strategies for small molecule inhibitor develop focus on thiol-directed inhibitors of the active site cysteines or hydrophobic reversible inhibition by binding in the b' domain. Through rigorous biochemical analysis, **BAP2** was

demonstrated as a b' domain inhibitor, while **AS15** was revealed to covalently bind to PDI to inhibit its function.

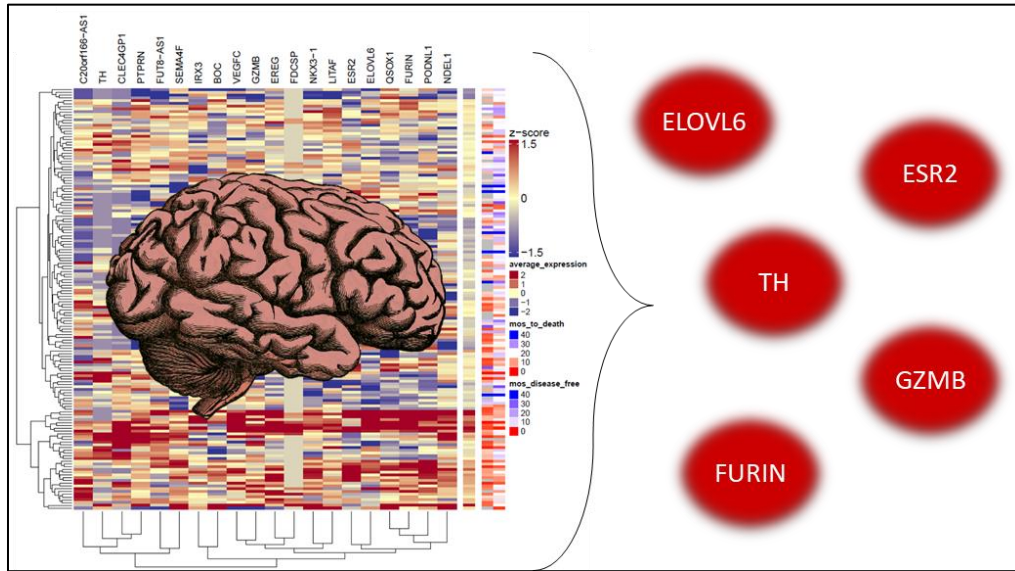


Figure VI-1 Potential drivers of GBM tumors based on TCGA analysis

Chapter 1 of this dissertation provides an overview of the research on small molecule treatment of glioblastoma (Figure VI-1). Importantly, we used a bioinformatics approach to probe the TCGA survival data and identify potential drivers of disease. In this review, we found 20 genes associated with reduced survival, 5 of which (ELOVL6, ESR2, TH, FURIN, and GZMB) are druggable protein targets. This study demonstrated a bioinformatics approach to generating hypotheses about previously unknown genes that may be responsible for disease progression. Further experimental validation of the role these proteins play in glioblastoma is warranted.

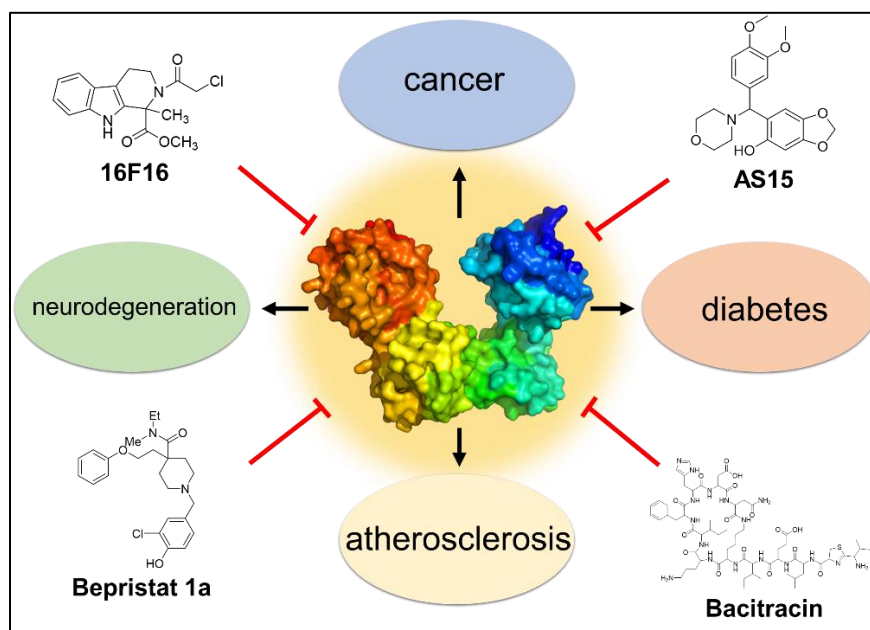


Figure VI-2 PDI modulators in different diseases

Chapter 2 of this dissertation provides an overview of PDI function and the unique roles it plays in different disease states (Figure VI-2). Because PDI has numerous substrates, its function or dysfunction has been reported in neurological disorders, atherosclerosis, and diabetes, as well as in cancer. Thus, PDI inhibitors, or modulators, may be useful in a wide range of indications. With respect to cancer, PDI has been demonstrated to play a role in glioblastoma, multiple myeloma, ovarian cancer, and non-small cell lung cancer. The importance of PDI in the progression of these diseases emphasizes the need for a potent, selective small molecules inhibitor of the enzyme.

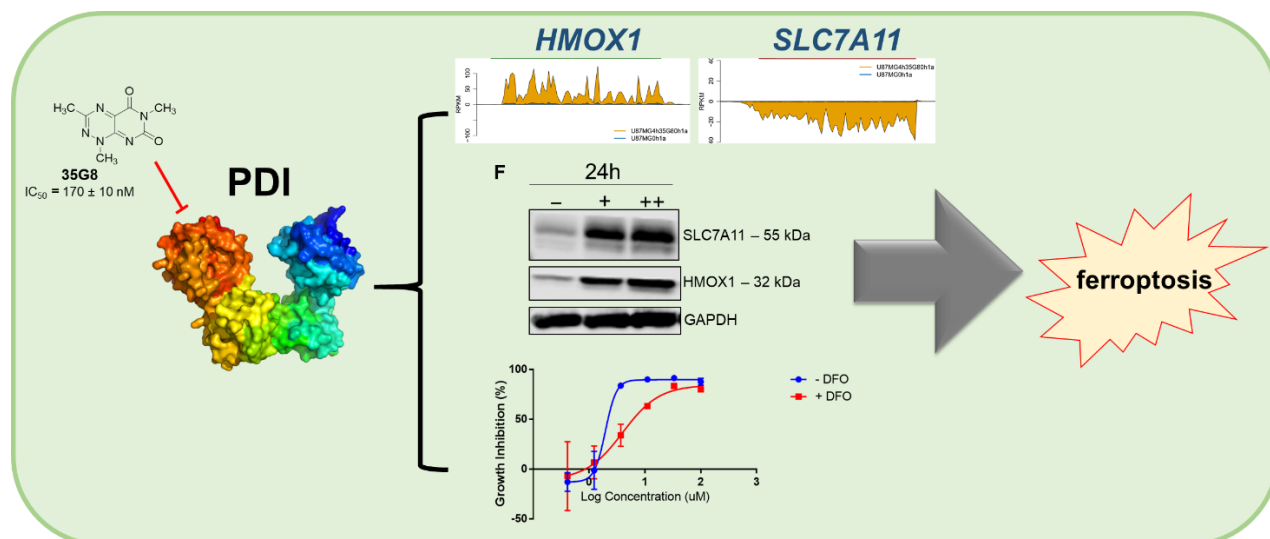


Figure VI-3 Discovery of **35G8** as a PDI inhibitor

In Chapter 3, we characterized **35G8** as a novel, potent PDI inhibitor (Figure VI-3). Much effort was involved in validating that the compound did not exhibit its PDI inhibition via its PAINS redox cycling properties before pursuing this scaffold as a *bona fide* PDI inhibitor. After confirming **35G8** inhibited PDI activity and destabilized PDI in the cells, we compared its transcriptomic profile with that of PDI knockdown. **35G8** induced an ER stress response and a ferroptosis cell death signature. To confirm this, we rescued cell death with iron chelator DFO. This study was the first to link PDI inhibition to ferroptosis, an iron-dependent form of cell death.

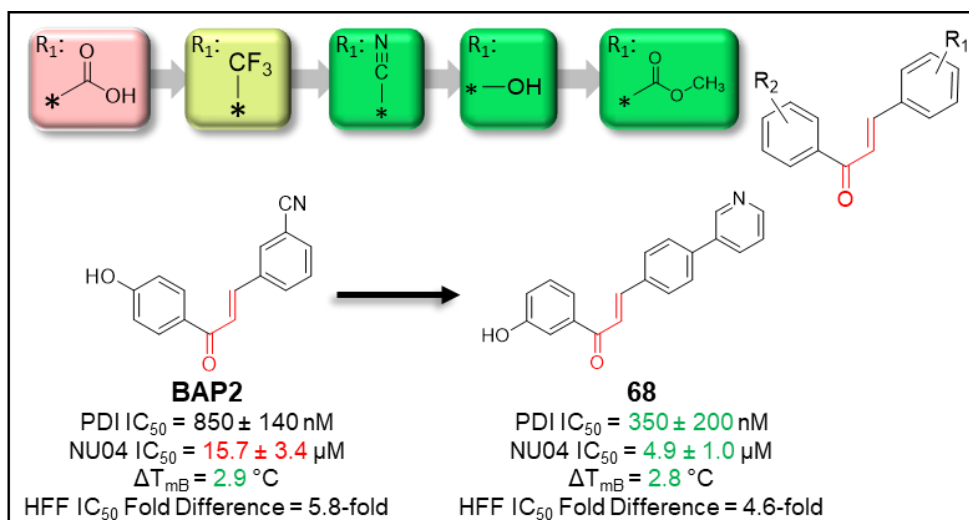


Figure VI-4 Lead compound **BAP2** optimization

In Chapter 4, we detail an extensive structure-activity relationship campaign of 67 chalcone analogues that supported the identification of the binding pocket of the lead compound to further structure-based drug design and optimization (Figure VI-4). Although **BAP2** and optimized analogue **59** have modest thiol reactivity, mutation of His256 to Ala abolishes **BAP2** analogue activity. Importantly, analogues inhibit glioblastoma cell growth, induce ER stress, increase expression of G2M checkpoint proteins, and reduce expression of DNA repair proteins. Cumulatively, our results support inhibition of PDI as a novel strategy to treat glioblastoma.

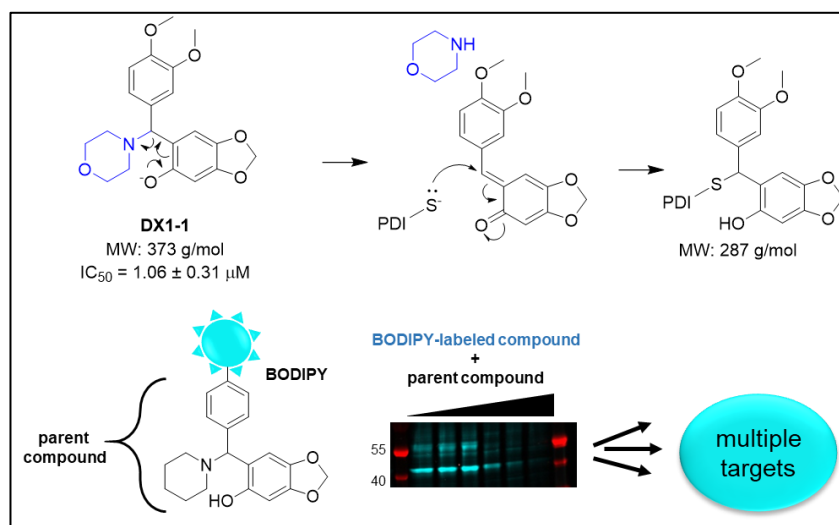


Figure VI-5 Identification of **AS15** analogues that covalently bind PDI

Lastly, Chapter 5 details yet another potent PDI inhibitor series (Figure VI-5). We report the benzyl-benzodioxole **AS15** analogues as potent PDI inhibitors and investigate modifications to the scaffold to optimize PDI inhibition and target engagement. We performed the first systematic synthesis of diverse  $\alpha$ -aminobenzylphenol modifications to the hydroxybenzo[*d*][1,3]dioxole core. Furthermore, we were able to identify the binding mechanism as a retro Michael addition to thiolate anions in the a' and a domains, though the compounds likely bind other sites in the protein as well. Nascent RNA sequencing revealed that an active analogue of **AS15** triggers the unfolded protein response in glioblastoma cells. Based on the mechanism of action of the **AS15** analogues, we confirmed that the compounds are sensitive to glutathione *in vitro*, and glutathione blocks target binding. Additionally, glutathione synthesis inhibitor BSO sensitized glioblastoma cells to **AS15** analogue treatment. However, the compounds likely have more than one target in the cells and are not selective for PDI. Thus, this series would require further medicinal chemistry optimization to produce potent, selective PDI inhibitors.

## Significance of the study

This work details the successful preclinical evaluation of several small molecules as inhibitors of PDI. These molecules were identified through both phenotypic and target-based screens. The lead compounds are potent at inhibiting PDI reductase activity and bind to PDI in the in-cell target engagement assays. Furthermore, we identified PDI inhibitors that sensitized GBM cells to radiation and had *in vivo* efficacy in a subcutaneous xenograft. Collectively, this dissertation provides further evidence for PDI as a target in GBM and rationalizes the pursuit of combinations of PDI inhibitors with the standard-of-care in more robust preclinical models, and finally, clinical trials.

## Future Directions

Validation of PDI as a target in brain cancer

Although glioblastoma is not a secretory cancer, PDI expression correlates with GBM disease progression, and PDI knockdown inhibits patient derived neurosphere formation. These observations provide strong initial validation to target PDI in glioblastoma. Further validation could include more robust models of glioblastoma and CRISPR/Cas9-mediated PDI knockout. Using the limiting dilution method in Cas9-expressing cells, we used CRISPR RNA targeting exon 2 of PDI to knockout the gene. By using this method, we selected for cells that survived gene knockout, and the cells had a similar doubling time as the wild-type cells. Extensive characterization of the RNA profile of three PDI knockout clones is underway to determine how the cells are able to survive without PDI. It is possible that the cells have established a mechanism

of resistance to promote survival. It is also possible that transient transfection of cells with PDI crRNA provides a more realistic response that would mimic the effect of a potent PDI inhibitor.

### Structure-based drug design

Because of the complexity and flexibility of PDI, binding should be the first priority after identifying a potent lead compound in order to rationally optimize the compound as a PDI inhibitor. The substrate-binding domain offers opportunities for structure-guided design because there are several residues available for hydrophobic and electrostatic interactions. Ideally, an active site inhibitor could also be modified to make critical non-covalent interactions with residues around the CGHC motif to improve selectivity and binding. NMR studies with PDI fragments may be the most efficient strategy for structure-based drug design. A PDI crystal structure has eluded researchers for over 30 years, potentially because we do not fully understand the complex oligomerization of the protein, its flexibility, and presence as a mixture of multiple oxidized/reduced conformations. Hopefully researchers will continue to pursue this challenge and solve a co-crystal structure with PDI and its inhibitors.

### Novel assay development and the limit of detection

To characterize the inhibition of PDI, we used one enzymatic activity assay– the PDI reductase assay. This assay measures the ability of PDI to reduce disulfide bonds in insulin over a period of a few hours. The assay is a standard PDI activity assay because of its ease of use and robust applicability for high throughput screening. However, the standard protocol requires a relatively high concentration of PDI (400 nM), especially when we are reaching the limit of detection with the PDI inhibitors we have discovered, with  $IC_{50}$  values around 200 nM. As part of



my dissertation project, I was able to optimize the reductase assay to run with 50 nM PDI, and with the optimized assay we could characterize IC<sub>50</sub> values down to 25 nM. However, another important issue remains. PDI catalyzes reactions on nascent polypeptides in its oxidized state. Therefore, the ability of PDI to oxidize thiols should be tested to mimic the physiological environment as closely as possible. PDI oxidase assays do exist, but they are complex and require the observation of multiple folding intermediates of substrates such as BPTI via mass spectroscopy. Thus, they are typically set aside for the more convenient alternative. However, in the future it will be critical to develop a robust PDI oxidase assay, both in vitro and cell-based, to identify PDI inhibitors that would inhibit PDI in cells.

## References

1. Toll, S. A.; Tran, H. N.; Cotter, J.; Judkins, A. R.; Tamrazi, B.; Biegel, J. A.; Dhall, G.; Robison, N. J.; Waters, K.; Patel, P.; Cooper, R.; Margol, A. S. Sustained response of three pediatric BRAF(V600E) mutated high-grade gliomas to combined BRAF and MEK inhibitor therapy. *Oncotarget* **2019**, *10*, 551-7.
2. Franz, D. N. Everolimus in the treatment of subependymal giant cell astrocytomas, angiomyolipomas, and pulmonary and skin lesions associated with tuberous sclerosis complex. *Biologics* **2013**, *7*, 211-21.
3. Tien, A. C.; Li, J.; Bao, X.; Derogatis, A.; Kim, S.; Mehta, S.; Sanai, N. A phase 0 trial of ribociclib in recurrent glioblastoma patients incorporating a tumor pharmacodynamic- and pharmacokinetic-guided expansion cohort. *Clin Cancer Res* **2019**, *25*, 5777-86.
4. Miller, T. W.; Traphagen, N. A.; Li, J.; Lewis, L. D.; Lopes, B.; Asthagiri, A.; Loomba, J.; De Jong, J.; Schiff, D.; Patel, S. H.; Purow, B. W.; Fadul, C. E. Tumor pharmacokinetics and pharmacodynamics of the CDK4/6 inhibitor ribociclib in patients with recurrent glioblastoma. *J Neurooncol* **2019**, *144*, 563-72.
5. Chalmers, A. J.; Short, S.; Watts, C.; Herbert, C.; Morris, A.; Stobo, J.; Cruickshank, G.; Dunn, L.; Erridge, S.; Godfrey, L.; Jefferies, S.; Lopez, J. S.; McBain, C.; Pittman, M.; Dillon, S.; James, A.; Nowicki, S. A.; Williamson, A.; Kelly, C.; Halford, S. E. R. Phase I clinical trials evaluating olaparib in combination with radiotherapy (RT) and/or temozolomide (TMZ) in

glioblastoma patients: Results of OPARATIC and PARADIGM phase I and early results of PARADIGM-2. *J Clin Oncol* **2018**, 36, 2018.

6. Sepulveda-Sanchez, J. M.; Vaz, M. A.; Balana, C.; Gil-Gil, M.; Reynes, G.; Gallego, O.; Martinez-Garcia, M.; Vicente, E.; Quindos, M.; Luque, R.; Ramos, A.; Ruano, Y.; Perez-Segura, P.; Benavides, M.; Sanchez-Gomez, P.; Hernandez-Lain, A. Phase II trial of dacomitinib, a pan-human EGFR tyrosine kinase inhibitor, in recurrent glioblastoma patients with EGFR amplification. *Neuro Oncol* **2017**, 19, 1522-31.

7. Vanderbeek, A. M.; Rahman, R.; Fell, G.; Ventz, S.; Chen, T.; Redd, R.; Parmigiani, G.; Cloughesy, T. F.; Wen, P. Y.; Trippa, L.; Alexander, B. M. The clinical trials landscape for glioblastoma: Is it adequate to develop new treatments? *Neuro Oncol* **2018**, 20, 1034-43.

8. Stupp, R.; Taillibert, S.; Kanner, A.; Read, W.; Steinberg, D.; Lhermitte, B.; Toms, S.; Idbaih, A.; Ahluwalia, M. S.; Fink, K.; Di Meo, F.; Lieberman, F.; Zhu, J. J.; Stragliotto, G.; Tran, D.; Brem, S.; Hottinger, A.; Kirson, E. D.; Lavy-Shahaf, G.; Weinberg, U.; Kim, C. Y.; Paek, S. H.; Nicholas, G.; Bruna, J.; Hirte, H.; Weller, M.; Palti, Y.; Hegi, M. E.; Ram, Z. Effect of tumor-treating fields plus maintenance temozolomide vs maintenance temozolomide alone on survival in patients with glioblastoma: A randomized clinical trial. *JAMA* **2017**, 318, 2306-16.

9. Lynes, J.; Sanchez, V.; Dominah, G.; Nwankwo, A.; Nduom, E. Current options and future directions in immune therapy for glioblastoma. *Front Oncol* **2018**, 8, 578.

10. Liao, L. M.; Ashkan, K.; Tran, D. D.; Campian, J. L.; Trusheim, J. E.; Cobbs, C. S.; Heth, J. A.; Salacz, M.; Taylor, S.; D'Andre, S. D.; Iwamoto, F. M.; Dropcho, E. J.; Moshel, Y. A.; Walter, K. A.; Pillainayagam, C. P.; Aiken, R.; Chaudhary, R.; Goldlust, S. A.; Bota, D. A.; Duic, P.; Grewal, J.; Elinzano, H.; Toms, S. A.; Lillehei, K. O.; Mikkelsen, T.; Walbert, T.; Abram, S. R.; Brenner, A. J.; Brem, S.; Ewend, M. G.; Khagi, S.; Portnow, J.; Kim, L. J.; Loudon, W. G.; Thompson, R. C.; Avigan, D. E.; Fink, K. L.; Geoffroy, F. J.; Lindhorst, S.; Lutzky, J.; Sloan, A. E.; Schackert, G.; Krex, D.; Meisel, H. J.; Wu, J.; Davis, R. P.; Duma, C.; Etame, A. B.; Mathieu, D.; Kesari, S.; Piccioni, D.; Westphal, M.; Baskin, D. S.; New, P. Z.; Lacroix, M.; May, S. A.; Pluard, T. J.; Tse, V.; Green, R. M.; Villano, J. L.; Pearlman, M.; Petrecca, K.; Schulner, M.; Taylor, L. P.; Maida, A. E.; Prins, R. M.; Cloughesy, T. F.; Mulholland, P.; Bosch, M. L. First results on survival from a large Phase 3 clinical trial of an autologous dendritic cell vaccine in newly diagnosed glioblastoma. *J Transl Med* **2018**, 16, 142.

11. Lang, F. F.; Conrad, C.; Gomez-Manzano, C.; Yung, W. K. A.; Sawaya, R.; Weinberg, J. S.; Prabhu, S. S.; Rao, G.; Fuller, G. N.; Aldape, K. D.; Gumin, J.; Vence, L. M.; Wistuba, I.; Rodriguez-Canales, J.; Villalobos, P. A.; Dirven, C. M. F.; Tejada, S.; Valle, R. D.; Alonso, M. M.; Ewald, B.; Peterkin, J. J.; Tufaro, F.; Fueyo, J. Phase I study of DNX-2401 (Delta-24-RGD) oncolytic adenovirus: Replication and immunotherapeutic effects in recurrent malignant glioma. *J Clin Oncol* **2018**, 36, 1419-27.

12. Hoellerbauer, P.; Arora, S.; Feldman, H.; Carter, L.; Girard, E. J.; Corrin, P.; Olson, J. M.; Paddison, P. Gene-12. Emerging principles of synthetic lethality in glioblastoma. *Neuro Oncol* **2017**, 19, vi95-vi95.

13. Aldape, K.; Brindle, K. M.; Chesler, L.; Chopra, R.; Gajjar, A.; Gilbert, M. R.; Gottardo, N.; Gutmann, D. H.; Hargrave, D.; Holland, E. C.; Jones, D. T. W.; Joyce, J. A.; Kearns, P.; Kieran, M. W.; Mellingerhoff, I. K.; Merchant, M.; Pfister, S. M.; Pollard, S. M.; Ramaswamy, V.; Rich, J. N.; Robinson, G. W.; Rowitch, D. H.; Sampson, J. H.; Taylor, M. D.; Workman, P.; Gilbertson, R. J. Challenges to curing primary brain tumours. *Nat Rev Clin Oncol* **2019**, *16*, 509-20.
14. Fu, X. M.; Wang, P.; Zhu, B. T. Characterization of the estradiol-binding site structure of human pancreas-specific protein disulfide isomerase: Indispensable role of the hydrogen bond between His278 and the estradiol 3-hydroxyl group. *Biochemistry* **2011**, *50*, 106-15.
15. Bekendam, R. H.; Bendapudi, P. K.; Lin, L.; Nag, P. P.; Pu, J.; Kennedy, D. R.; Feldenzer, A.; Chiu, J.; Cook, K. M.; Furie, B.; Huang, M.; Hogg, P. J.; Flaumenhaft, R. A substrate-driven allosteric switch that enhances PDI catalytic activity. *Nat Commun* **2016**, *7*, 12579.
16. Zwicker, J. I.; Schlechter, B. L.; Stopa, J. D.; Liebman, H. A.; Aggarwal, A.; Puligandla, M.; Caughey, T.; Bauer, K. A.; Kuemmerle, N.; Wong, E.; Wun, T.; McLaughlin, M.; Hidalgo, M.; Neuberg, D.; Furie, B.; Flaumenhaft, R.; Investigators, C. Targeting protein disulfide isomerase with the flavonoid isoquercetin to improve hypercoagulability in advanced cancer. *JCI Insight* **2019**, *4*, 125851.
17. Xu, S.; Liu, Y.; Yang, K.; Wang, H.; Shergalis, A.; Kyani, A.; Bankhead, A., 3rd; Tamura, S.; Yang, S.; Wang, X.; Wang, C. C.; Rehemtulla, A.; Ljungman, M.; Neamati, N. Inhibition of protein disulfide isomerase in glioblastoma causes marked downregulation of DNA repair and DNA damage response genes. *Theranostics* **2019**, *9*, 2282-98.
18. Lin, L.; Gopal, S.; Sharda, A.; Passam, F.; Bowley, S. R.; Stopa, J.; Xue, G.; Yuan, C.; Furie, B. C.; Flaumenhaft, R.; Huang, M.; Furie, B. Quercetin-3-rutinoside inhibits protein disulfide isomerase by binding to its b'x domain. *J Biol Chem* **2015**, *290*, 23543-52.